The National Geospatial-Intelligence Agency (NGA)
Collaborative Atmospheric Measurement Program (CAMP)

February 28, 2014
Final Report

Authors:
Ms. Gail Anderson NOAA; Steve Broberg NASA/JPL; Dr. Christy L. Crosiar NGA; Dr. Robert Kroutil; Mr. Paul E. Lewis NGA; Mr. David P. Miller; Dr. Ed Olsen NASA/JPL; Tom Pagano NASA/JPL; Mr. Luc Rochette LR-Tech; Dr. Sylvia S. Shen The Aerospace Corporation; Dr. W. L. Smith Sr. Hampton University; Dr. Mark Thomas EPA; Dr. Sun Wong NASA/JPL

Special Thanks To: Ms. Arlyn Andrews NOAA; Mr. Jonathan Kofler NOAA; Ryan J. Ippolito DIA; Mr. Andre Lanouette LR-Tech; Ms. Jeannette Van Den Bosch AFRL

In Fondest Memory of Our Colleague Dr. Sylvia S. Shen,
Distinguished Scientist of The Aerospace Corporation and Fellow of SPIE

Paul E. Lewis NGA/IB
Editor
CAMP Program Manager

Executive Summary

The goal of the Collaborative Atmospheric Measurement Program (CAMP) activity and this final report is to provide a compendium to the literature on the relative accuracy, estimation retrieval methodologies, and technical issues of quantitative greenhouse gas (GHG) estimation (with emphasis on Carbon Dioxide (CO_2) estimation) from remotely sensed passive longwave infrared (LWIR) spectral data. Due to the profound effect of water vapor on the absorption and trapping of infrared energy and on the accuracy of remotely sensed infrared data, the authors have chosen to treat water vapor as a GHG and address its measurement and accuracy for the reasons outlined in Appendix D 1.1. This report also presents the utility and value of space and ground based remotely sensed passive LWIR measurements for future global monitoring of GHG, CO_2 sources and sinks, characterization of the atmosphere, and climate prediction.

Spatially and temporally concurrent ground and space based LWIR hyperspectral and supporting data were collected during 2012 and 2013 and used to determine quantitative GHG estimations and seasonal characterization of the atmospheric column in the Dallas/Fort Worth TX, Moody TX, and Lamont OK regional areas.

This report compares the relative accuracy of space and ground based remotely sensed passive LWIR measurements and the Moody, TX tower based Carbon Tracker single point measurements of CO_2 using average parts per million (PPM) and measurement correlation in terms of standard deviation on a monthly average. Additionally, this approach to comparison facilitates correlation of these vastly different measurements and techniques with other historical point measurement records such as the Mauna Loa CO_2 record of measurement trends from their beginning in 1958 to present.

Spatially and temporally concurrent quantitative CO_2 retrieval estimations were obtained in PPM of the atmosphere over Moody, TX and the surrounding region during 2012 and April and May of 2013 from the NASA Atmospheric Infrared Sounder AIRS and the LR Tech ASSIST-II spectrometers. Spatially and temporally concurrent AIRS and ASSIST-II retrieved CO_2 estimations were examined and compared with measurements in PPM from the NOAA Carbon Tracker instrumentation on the 1499 ft. KWKT-TV tower located in Moody, TX.

The AIRS and ASSIST-II reported CO_2 retrieval numbers in PPM represent an average of the atmospheric column below or above the spectrometer respectively. The reported Carbon Tracker measurements represent a single point at a specific altitude. Although each of these three instruments is making a simultaneous measurement in roughly the same location, all three instruments are measuring very different temporally concurrent samples of the atmospheric column. The correlation between these measurements depends strongly on the homogeneity of CO_2 in the atmosphere. For this reason a statistical comparison of the retrieval results for CO_2 estimations from the AIRS and ASSIST-II spectrometers and Carbon Tracker instrument measurements is reported in terms of monthly averages and standard deviations and the reader should avoid making comparisons of temporally concurrent single measurements from the graphical presentations in this report.

In order to characterize the atmospheric homogeneity of CO_2 and correlate it in a statistically significant manner with the AIRS and ASSIST-II spectrometer measurements a procedure for using cost effective small aircraft to collect and measure Carbon Dioxide and water vapor as a function of altitude up to 10,000.0 feet was developed and implemented. Obstacles to the development and verification of the small aircraft collection and measurement procedure prohibited the subsequent collection of a statistically significant number of concurrent aircraft atmospheric CO_2 measurements before the study concluded. Nevertheless, the limited concurrent aircraft atmospheric CO_2 measurements are reported and suggest in-homogeneity in atmospheric $CO_{2.}$ A documented aircraft collection and measurement procedure is included in this report in support of future work. It is recommended that a follow on to the CAMP activity and report be conducted using the same approach documented in this report and include a statistically significant number of concurrent aircraft collection data using the documented collection and measurement procedure.

Comparison of the AIRS and ASSIST-II monthly average CO_2 estimations with the Moody, TX tower based Carbon Tracker single point measurements indicate that remotely sensed and tower based instruments are capturing similar concentration trends. Comparisons of monthly standard deviation estimates indicate remotely sensed and tower based sensitivities are of the same order of magnitude. These findings suggest the suitability and synergistic use of both remotely sensed passive LWIR and tower based measurements for monitoring atmospheric CO_2 on a global scale and providing added insight into its variability. The reported averages from the Mauna Loa record show a steady 0.53% or two parts per million increase per year in CO_2 from the beginning of these measurements to the present, roughly 50 years. Passive LWIR instrumentation and measurement is able to verify this trend and in fact does using AIRS data from 2002 to the present on a global scale (see Figure 6).

The CAMP final report replete with supporting data is offered as scientific evidence in support of the next generation passive LWIR remote sensing technologies needed by GHG/Climatology modelers and our policy and decision makers in addressing global climate change.

Additionally: The atmospheric modeling and simulation techniques developed for the CAMP activity and used to simulate the measured at sensor passive infrared radiances from the AIRS-space based, the ASSIST-ground based, and aircraft infrared spectrometers (see section 5.0) are universally applicable in applying a correction for the effect of atmosphere to multispectral, hyperspectral and ultraspectral data from radiometrically calibrated infrared spectrometers. Furthermore, the accuracy of a correction for the effect of atmosphere is quantifiable through comparison of the simulated at sensor radiance to the measured at sensor radiance. The successful use of these atmospheric modeling and simulation techniques with the CAMP AIRS and ASSIST-II data suggests a practical operational methodology for obtaining quantifiably accurate corrections for multi., hyper., and ultraspectral data operationally on a global scale.

1.1 CAMP Activity Overview

A thorough assessment of the accuracy and utility of using remotely sensed infrared spectral data to estimate the concentration of GHG along with its feasibility, relative cost to implement on a regional and global scale, and benefit is urgently needed by policy makers. Models used to predict the effects of GHG on global climate change are in need of more detailed atmospheric information including the contribution of regional CO_2 sources and sinks. Without this information, policy makers will have little tangible criteria upon which they can assess the effectiveness of future GHG reduction efforts, treaties, or agreements.

The National Geospatial-Intelligence Agency (NGA) believes that the CAMP collaborative approach focused on the four LWIR measurement areas addressed in this document (i.e., ground based, aircraft based, space based, and supporting validation technologies) will provide a comprehensive understanding and a valuable contribution to the literature on the utility of remotely sensed LWIR spectral data and associated supporting measurement methodologies for GHG estimation needed by GHG/Climatology modelers and policy and decision makers in addressing global climate change (see Appendix A 1.0 for additional objective details).

In order to accomplish this critical task, NGA has supported the CAMP activity, an autonomous civil participant committee led and NGA/IB supported project. The committee/authors are subject area expert practitioners, participants and principal investigators from each of the measurement areas addressed.

The NGA CAMP activity provided resources to cover the operation of its committee to include: meeting costs, consulting costs for identified expertise working on the tasks of this committee, data collection costs including travel, the final report, and honorarium for travel where appropriate.

The committee directed the collection and data analysis needed to provide and deliver this comprehensive report on the quantitative accuracy associated with GHG estimation derived from LWIR remotely sensed data, and recommended approaches for regional source and sink GHG measurement methodologies.

Due to the profound effect of water vapor on the absorption and trapping of infrared energy and on the accuracy of remotely sensed infrared data, the committee has chosen to treat water vapor as a GHG and address its measurement and accuracy for the reasons outlined in Appendix D 1.1.

Table of Contents

1.1 CAMP Activity Overview 4

2 **Space Based Passive LWIR Measurements 15**

2.1 Introduction 15

2.2 CO_2 product development 16

2.3 Product Validation 18

2.4 Science findings using AIRS CO_2 data 21

2.5 AIRS Data Holdings 22

2.6 AIRS and the CAMP CO_2 field campaign 23

2.6.1 CO_2 Climatology for the CAMP field campaign 23

2.6.2 Co-located Retrievals 24

2.7 CAMP Spring 2013 Campaign at Moody, TX 27

2.7.1 Overview 27

2.8 CAMP Sonde and AIRS Temperature and Specific Humidity Comparison 29

2.8.1 Temperatures: 30

2.8.2 Specific Humidity: 30

2.8.3 Biases: 30

2.9 Seasonal Variation of AIRS CO_2 data vs. WKT in situ tower 32

2.10 References (Space Based Passive LWIR Measurements) 34

3 **Ground Based Passive LWIR Measurements 36**

3.1 Summary: 36

3.2 Background 37

3.2.1 Radiance Sensitivity to Atmospheric Profiles: 37

3.3 Optimal Estimation Retrieval 38

3.3.1 Retrieval of Atmospheric Profiles from ASSIST Radiance Measurements: 38

3.3.2 Statistical Bias Correction: 40

3.4 Physical Retrieval 42

3.4.1 Matrix Inverse Solution. 42

3.5 Temperature-Relative Humidity, Trace Gas Retrieval Results April 19, 2013 44

3.6 CO_2 Concentration Retrieval Results for Planetary Boundary Layer (PBL) April 19, 2013 46

3.7 CAMP April and May ASSIST Vs. Carbon Tracker Results April-May 2013 47

3.7.1 Daily Comparisons: 47

3.7.2 Statistical Results 50

3.8 Summary and Conclusions 51

3.9 References (Ground Based Passive LWIR Measurements): 52

4 Aircraft Support: Instrumentation, Sonde Calibration-Collection, CO2-Water vapor/humidity Collection and Measurement Procedure 54

4.1 Aircraft Support Overview 54

4.2 Calibration of Analogue and Digital Radiosondes 54

4.2.1 Limitations of the RS80 Series Radiosonde 54

4.2.2 Development of a Radiosonde Calibration Chamber 55

4.2.3 Digital Radiosonde System 58

4.3 Aircraft (in-Situ altitude) CO_2 and Water Vapor (Humidity) Instrumentation, Collection, and Measurement Procedures 59

4.3.1 In Situ Sampling General Concept 59

4.3.2 Sampling System 60

4.3.3 Sample Preparation 62

4.3.4 Sample Collection 62

4.3.5 Laboratory Analysis 63

4.4 Radiosonde and Aircraft Humidity Modeling and Comparison 65

4.5 References Aircraft Support: Instrumentation, Sonde Calibration-Collection, CO2-Water vapor/humidity Collection and Measurement Procedure 68

5 Atmospheric Modeling and Simulation Support 69

5.1 Planet Boundary Layer (PBL) At-Sensor Radiance Modeling Support 69

5.1.1 INTRODUCTION 69

5.1.2 OVERALL MODEL 70

5.1.3 ESTIMATION OF WATER VAPOR AMOUNT 73

5.1.4 Estimation of Saturation Water Vapor Concentration At the Surface 74

5.1.5 Estimation of Saturation Water Vapor Concentration for Each of the Ten 100-meter Atmospheric Intervals 77

5.1.6 Estimation of Actual Water Vapor Concentration for Each of the Ten 100-meter Atmospheric Intervals 79

5.1.7 SUMMARY 80

5.2 INTRODUCTION OF SECOND RADIATIVE TRANSFER MODEL 81

5.2.1 Overview of MODTRAN®: CODE DESCRIPTION 82

5.2.2 Radiance Equation in MODTRAN5®5 83

5.2.3 Comparison for paired AIRS and ASSIST Calculations based on MODTRAN5®5: Input Specifications 86

5.2.4 Comparison for paired AIRS and ASSIST Calculations based on MODTRAN5®5: Output Specifications 88
5.2.5 Sensitivity Studies for paired AIRS and ASSIST Calculations based on MODTRAN5®5: 4/16/2013 and 5/20/2013 88
5.2.6 Conclusions for MODTRAN simulations of paired AIRS and ASSIST Measurements 89
5.2.7 References (Section 5.2) 96
6 Assessment of Instrument Accuracy Requirement For Greenhouse Gas Concentration Retrieval 98
6.1 INTRODUCTION 98
6.2 BACKGROUND 98
6.3 EFFECT OF INSTRUMENT ERROR ON CO_2 CONCENRATION RETRIEVAL 99
6.3.1 Summary 102
6.4 References (Atmospheric Modeling and Simulation Support section 5.1 and section 6) 102

List of Figures

Figure 2.1 NASA's Atmospheric Infrared Sounder Instrument on the EOS Aqua Spacecraft observes the infrared spectrum globally every day to obtain accurate measurements of temperature, water vapor and trace gases in the atmosphere. 15
Figure 2.2 Un-normalized weighting functions for channels used in AIRS CO2 retrievals 17
Figure 2.3 AIRS yields about 15,000 Mid-Tropospheric CO_2 measurements per day. 18
Figure 2.4 AIRS Mid-Tropospheric CO_2 is a tracer for atmospheric motion particularly in the vertical direction, July, 2010 Monthly average. 19
Figure 2.5 Month in which the peak in the seasonal cycle occurs. (left) CO_2 from AIRS and the NOAA Carbon Monitoring Diagnostic Laboratory (CMDL), (right) Temperatures from AIRS, and MODIS Gross Primary Productivity (GPP) 20
Figure 2.6 Amplitude of the seasonal cycle for (left) AIRS CO_2 and CMDL, (right) AIRS Temperature at 500 mb and the surface. 20
Figure 2.7 AIRS reveals a depression of Mid-Tropospheric CO_2 in the South Atlantic (July Climatology). 21
Figure 2.8 Hovmöller Diagram of AIRS Mid-Tropospheric CO_2 shows seasonal cycle and annual trend. In this Figure we can also see the flow of CO_2 from the Northern Hemisphere to the Southern Hemisphere. 23
Figure 2.9 (Top Left) Sample Monthly Gridded AIRS CO_2 data product for July 2003. (Top Right) AIRS measured Mid-Tropospheric CO_2 over the Houston area from 2003-2011, overlaid with reconstructed climatology. (Bottom Left) Climatology of the seasonal behavior of mid-tropospheric CO_2 over the Houston area. (Bottom Right) Anomaly of Mid-Tropospheric CO_2 over the Houston area (difference of two curves in (Top Right). 24
Figure 2.10 (left). AIRS CO_2 vs. cloud fraction. (right). CO_2 amount vs. O3, CO, Temperature and Water Vapor (Top Left, Top Right, Bottom Left, Bottom Right respectively). 26

Figure 2.11 (left). Overpass times for the AIRS over McKinney Texas. (top) am, (bottom) pm. 26
Figure 2.12 CAMP Spring Campaign CO_2 data sets from Moody, Tx; WKT tower in situ measurements at 3 heights (meters above ground level), AIRS retrievals within 200 km of the tower, and aircraft in-flight samples at 5 elevations above ground level (ft. AGL) 27
Figure 2.13 April CAMP Spring Campaign CO_2 data sets from Moody, Tx; WKT tower in situ measurements at 3 heights (meters above ground level), AIRS retrievals within 200 km of the tower, and aircraft in-flight samples at 5 elevations above ground level (ft. AGL) 28
Figure 2.14 April 15-25 CAMP Spring Campaign CO_2 data sets from Moody, Tx; WKT tower in situ measurements at 457 m AGL (above ground level), AIRS retrievals within 200 km of the tower, and aircraft in-flight samples at 5 heights above ground level (ft. AGL) 28
Figure 2.15 May CAMP Spring Campaign CO_2 data sets from Moody, Tx; WKT tower in situ measurements at 457 m AGL (above ground level), AIRS retrievals within 200 km of the tower, and aircraft in-flight samples at 5 heights above ground level (ft. AGL) 29
Figure 2.16 The AIRS sounding temperature (in K) profiles (blue lines) and the corresponding CAMP sonde temperature profiles (red lines). The upper panel shows the AIRS temperatures at levels flagged as “good” quality (Quality flag ≤ 1), and the lower panel shows the AIRS temperatures at levels flagged as “best” quality (Quality flag = 0). 31
Figure 2.17 Similar to Fig. 1, but for the AIRS sounding specific humidity (in g/kg) profiles and the corresponding CAMPS sonde specific humidity profiles. 31
Figure 2.18 Biases in AIRS temperatures (upper panel) and specific humidity (lower panel) compared to the CAMP sonde measurements. The red lines show the biases of direct comparison, while the blue lines show the biases with the CAMP sonde profiles being smoothed by the corresponding AIRS temperature or specific humidity averaging kernels. .. 32
Figure 2.19 WKT (457m) CO_2 data from Moody, Tx, with monthly means overlaid. 33
Figure 2.20 AIRS CO_2 data from Moody, Tx (200 km radius), with monthly means. 33
Figure 2.21 shows the monthly mean data for both the AIRS and WKT 457m data sets. 34
Figure 3.1 ASSIST brightness temperature (Left) and radiance spectra (Right) showing the spectral regions where specific gases are optically active. 37
Figure 3.2 ASSIST radiance Jacobians (i.e., Sensitivity functions) for temperature, water vapor, ozone, methane, nitrous oxide, carbon monoxide, carbon dioxide, and aerosol. 39
Figure 3.3 ASSIST temperature (top) and relative humidity (bottom) retrieval time-cross-section for the period April 19 (17 UTC) to April 21 (00 UTC), 2012 for the surface to 4-km layer of the atmosphere over McKinney Texas. The left hand panels show the retrieval results obtained solely from the optimal estimations algorithm whereas the middle panel shows the result after bias correction. The right hand panel shows the RAQMS analysis. 41
Figure 3.4 Same as Figure 3 but for ozone (top) and carbon monoxide (bottom) 41
Figure 3.5 Same as Figure 3 but for methane (top) and nitrous oxide (bottom) 42
Figure 3.6 Flow diagram for the ALOSE-5 sounding retrieval algorithm. 44
Figure 3.7 ASSIST temperature (top left), relative humidity (top right), water vapor mixing ratio (bottom left), and total precipiTable water (bottom right) retrieval time cross-sections for April 19, 2013 for the surface to 4-km layer of the atmosphere over Moody Texas. 45

Figure 3.8 ASSIST carbon monoxide(top left), ozone (top right), methane (bottom left), and nitrous oxide (bottom right) retrieval time cross-sections for April 19, 2013 for the surface to 4-km layer of the atmosphere over Moody Texas. 46
Figure 3.9 ASSIST carbon dioxide (black dots), carbon tracker measurements (red curve), and aircraft measurements (open red circles) for the atmospheric column over Moody Texas during for April 19, 2013. 47
Figure 3.10 100 minute mean clear sky ASSIST surface to 2 km layer carbon dioxide (blue dots) overlaying 30 second interval carbon tracker measurements at ~250 meters (solid line) for the atmospheric column over Moody Texas for NGA selected days during April, 2013. 48
Figure 3.11 100 minute mean clear sky ASSIST surface to 2 km layer carbon dioxide (blue dots) overlaying 30 second interval carbon tracker measurements at ~250 meters (solid line) for the atmospheric column over Moody Texas for NGA selected days during May, 2013. 50
Figure 3.12 Scatter between 100-minute average clear sky ASSIST carbon dioxide (blue dots) overlaying 30-second interval carbon tracker measurements for the atmospheric column over Moody Texas for selected days during May, 2013. Results are shown for the raw unfiltered measurements (top panels) and for employing a statistical filter using 1 sigma (middle row) and ½ sigma (lower panels) filtering criteria, respectively. 51
Figure 4.2.1 Radiosonde Calibration Chamber and System Controller 57
Figure 4.2.2 Radiosonde Flight Data Output Example with Humidity Correction Applied....... 58
Figure 4.2.3 iMet 1 A/B Digital Radiosonde 59
Figure 4.3.1. Rotometer and Sampling Manifold with Aluminized Bag Whole Gas Sampling System. 61
Figure 4.3.2. Vaisala M170/HMP77 Temperature/Humidity Probe 61
Figure 5.1 Modeling of At-Sensor Radiance 71
Figure 5.2.1 MODTRAN 5 Equivalent Width Formulation 84
Figure 5.2.2 MODTRAN output mode for derivative cooling rates. Ref: (Bernstein, L. S., A. Berk, P. K. Acharya, D. C. Robertson, G. P. Anderson, J. H. Chetwynd, L. M. Kimball, 1996: Very Narrow Band Model Calculations of Atmospheric Fluxes and Cooling Rates. *J. Atmos. Sci.*, 53, 2887–2904.) 86
Figure 5.2.3 The pair of slides demonstrate how the detailed structure of the fine scale sonde can overlap with the default values provided within MODTRAN. The upper atmosphere is defined by built-in MOD5 profiles (ref 4, Section 5.) 87
Figure 5.3.3 The two H2O continua (CKD and MT-CKD, in units of Optical Depth) are plotted over a broader spectral range and logarithmic optical depth. The relative magnitude differences between 500 and 2000 cm-1 will be critical to improving the correlation between model prediction and measurement. 89
Figure 5.2.4 For May 20, 2013, both AIRS and ASSIST measurements for the same time and location. The MODTRAN simulations used the sonde data for May 20, as described earlier in Section 5, and the T-skin retrieved by the AIRS team. 90
5.3.1 For April 16, 2013, only the ASSIST measurements were simulated, using the ASSIST retrieved atmospheric components. The residuals for both May 20 (multiplied by '-1') and April 16 are plotted at the bottom. 91

Figure 5.3.2a Transmittances for a number of atmospheric gases, between 0 and 100km, are plotted in Fig. a. In both Figs. a and Fig. b, the 'CKD' H2O continuum contribution is denoted in red. 92
Figure 5.3.2bTResiduals: A scaled 'CKD' H2O continuum contribution is again denoted in red. Since the 'full path' transmittance is identical in the up (ASSIST) and down (AIRS) looking modes, the envelope of the CKD continuum has the highest correlation with the shape of the residual misfits between measurement and MODTRAN5. Of course there are other molecular sources for the finer scale misfits, including some due to wavelength alignment differences. 93
Figure 5.3.4a Figure a. shows the results of an inconsistent sensitivity test, where each molecule was perturbed uniquely within a pair of up-down MODTRAN simulations, with each such calculation subtracted from the two (up & down) control cases. 94
Figure 5.3.4b In Figure b. the unique sensitivity curves in Figure a. were convolved with the H2O continuum transmittance, to further demonstrate the importance of updating the current CKD implementation. Any change is the H2O continuum will impact the accuracy of MODTRAN........ 95
Figure 6.1 CO_2 Absorbance vs. Wavelength 101
Figure 6.2 CO_2 Absorbance vs. Wavelength (Different y-Scale) 101
Figure B-1. CAMP Regional Study Area........ 109
Figure B-2a. CO_2 emission sources, locations, sizes for the Dallas-Fort Worth, TX (DFW) area. Courtesy EPA Climate Change Division-Office of Atmospheric Programs........ 110
Figure B-2b. CO_2 emission sources, locations, sizes for the Grant County, OK area. Courtesy EPA Climate Change Division-Office of Atmospheric Programs 110
Figure B-3 Data collection and synchronization process for the regional area measurement data 111
Figure C-1. Earth's global annual mean energy budget (Wm^{-2}) for March 2000 to May 2004. Illustration from Trenberth, Fasullo, and Kiehl[9]........ 112
Figure D-1 Modeled 5250 deg. C solar radiance and atmospheric absorption by water vapor (H_2O),Carbon Dioxide(CO_2) [11]. 114
Figure E-1a (top) E-1b (bottom). ENSO model calculation of factors influencing temperature[12] 116
Figure E-2 Mauna Loa Carbon Dioxide Record from the beginning of measurements to present 117
Figure G-1. Temperature vs altitude US Standard Atmosphere 119
Figure G-2 Verticle profile of pressure in millibars(---), density in grams per cubic meter(—), plotted on a logarithmic scale [18 P-F193]........ 120
Figure G-3 The plot of the blackbody spectra representative of the sun (5780 deg K) and earth (286 deg K) on a logarithmic wavelength scale[20 P4] 122
Figure G-4 Spatially and Temporally concurrent AIRS/AERI atmospheric spectra over Lamont, OK........ 128
Figure G-5 MODTRAN®5 generated spectra of major atmospheric GHG constituents 129
Figure G-6 AIRS/AERI spatially and temporally concurrent atmospheric spectra Region 1... 130
Figure G-7 AIRS/AERI spatially and temporally concurrent atmospheric spectra Ozone region 131

Figure G-8 AIRS/AERI spatially and temporally concurrent atmospheric spectra Region 3... 133
Figure I-4 Summary Average Annual Precipitation.. 158
Figure I-5. Average daily maximum temperature 159
Figure I-6. Summary Relative Humidity 160
Figure I-7. Upper Level Wind Directions and Velocities.. 163
Figure J-8. Mean and near-maximum wind speeds by atmospheric pressure level – January168
Figure J-9. Mean and near-maximum wind speeds by atmospheric pressure level – February 168
Figure J-10. Mean and near-maximum wind speeds by atmospheric pressure level – March169
Figure J-11. Mean and near-maximum wind speeds by atmospheric pressure level – April . 169
Figure J-12. Mean and near-maximum wind speeds by atmospheric pressure level – May.. 170
Figure J-13. Mean and near-maximum wind speeds by atmospheric pressure level – June.. 170
Figure J-14. Mean and near-maximum wind speeds by atmospheric pressure level – July... 171
Figure J-15. Mean and near-maximum wind speeds by atmospheric pressure level – August 171
Figure A16. Mean and near-maximum wind speeds by atmospheric pressure level – September 172
Figure J-17. Mean and near-maximum wind speeds by atmospheric pressure level – October 172
Figure J-18. Mean and near-maximum wind speeds by atmospheric pressure level – November 173
Figure J-19. Mean and near-maximum wind speeds by atmospheric pressure level – December.. 173
Figure J-20. Cloud ceiling < 3,000ft and horizontal visibility of 3.0 miles............................ 174
Figure J-21. Cloud ceiling < 1,500ft and horizontal visibility of 3.0 miles............................ 174
Figure J-22. Cloud ceiling < 1,000ft and horizontal visibility of 2.0 miles............................ 175
Figure J-23. Cloud ceiling < 200ft and horizontal visibility of 0.5 miles 175

Table of Tables

Table 2.1. Co-located AIRS CO_2 Soundings for McKinney Texas Only first 10 lines of the file are shown 25
Table 2.2. Co-located AIRS Ancillary Products for McKinney Texas include Mid-Tropospheric and Surface Temperature, Water Vapor, Cloud Fraction, Cloud Top Pressure, Total Ozone and Carbon Monoxide 25
Table 2.3 (right) Table of overpass times projected for AIRS by day. 26
Table 2.3. AIRS files matched up with the CAMP sondes and distances and time spans between the AIRS soundings and the sonde launches. 29
Table 4.2.1 Initial RS80L Radiosonde Humidity Readings 55
Table 4.2.2 Calibration Matrix Program 57
Table 4.2.3 iMet 1 A/B Sonde Specifications 59
Table 4.2.4 Trip Blank Sample Results 65
Table 4.2.5 Ascent 002, Release 001, 19 April 2013 66
Table 4.2.6 Ascent 004, Release 001, 18 May 2013 67
Table 4.2.7 Ascent 006, Release 001, 20 May 2013 67
Table 6.1 Input Parameter Values for At-Sensor Radiance 100
Table 6.2 Temperature Values Calculated from Modeled Radiance Spectra 102

List of Appendices

Appendices A-J contain relevant background and supplementary information 103
Appendix A Issues surrounding data collection-analysis and reducing emissions of greenhouse gases (GHG) 103
Appendix A-1.0 CAMP data collection analysis objective 103
Appendix A-1.1 Issues surrounding reducing emissions of greenhouse gases (GHG) 104
Appendix A-1.2 Intergovernmental Panel on Climate Change (IPCC) 106
Appendix B Overview of CAMP atmospheric measurement campaign, regional study areas, and schedule 106
Appendix B-1.0 Atmospheric measurement campaign 106
Appendix B-1.1 Regional study areas 107
Appendix B-1.2 Collection schedule 110
Appendix C What constitutes the "greenhouse effect" 110
Appendix C-1.0 Temperature and heat transfer 110
Appendix C-1.1 Earth's energy budget 111
Appendix C-1.2 The greenhouse effect 112
Appendix D The solar radiation spectrum and greenhouse gases (GHG) 113
Appendix D-1.0 The solar radiation spectrum 113
Appendix D-1.1 Greenhouse gasses (GHG) 113
Appendix E Scientific observations indicating global temperature change 114
Appendix E-1.0 Historical observation records 114
Appendix F Overview of GHG global grid measurement data 116
Appendix F-1.0 Global Atmospheric Watch 116
Appendix F-1.1 Carbon Tracker 117
Appendix G Fundamental properties for LWIR measurement of the atmosphere 117
Appendix G-1.0 Atmospheric temperature structure 117
Appendix G-1.1 Analysis of pressure and density 118
Appendix G-1.10 A detailed look at spatially and temporally concurrent upward looking and downward looking passive LWIR hyperspectral atmospheric spectra 127
Appendix G-1.11 Atmospheric Region "1" 6.2-8.8 um 128
Appendix G-1.12 Atmospheric Region "2" 8.7-12.2 um 130
Appendix G-1.13 Atmospheric Region "2" (9.3-10.18 um) Ozone 131
Appendix G-1.14 Atmospheric Region "3" 12.2-13.2um 132
Appendix G-1.2 Ozone 119
Appendix G-1.3 Atmospheric processes 120
Appendix G-1.4 Solar vs terrestrial radiation 121
Appendix G-1.5 Optical density Beer's law 122
Appendix G-1.6 Transmissivity, absorptivity, and Schwartzchild's equation 123
Appendix G-1.8 Absorption characteristics of optical depth σ in the vertical profile of the atmosphere 124
Appendix G-1.9 Remote sensing of temperature 125
Appendix H Complete documentation of the ASTM Standard laboratory methodologies D1945 and D3416 outlined in section 4.3.5 for measurement of CO_2 samples collected from the aircraft. 135
Appendix H-1.0 ASTM D1945-(03)Primary Methodology 136
Appendix H-1.1 ASTM D3416 Redundant Methology 153

Appendix I Study Area Climatology 156
Appendix J Acknowledgements 180
Appendix J Dallas, TX (DFW) Climatology 166
I 1.4 Surface and upper level winds 160
References (Appendices A-G) 133

2 Space Based Passive LWIR Measurements

2.1 Introduction

The space segment of the CAMP is achieved with NASA's Atmospheric Infrared Sounder (AIRS), shown in Figure 2.1. AIRS is a hyperspectral infrared instrument on the EOS Aqua Spacecraft, launched on May 4, 2002. AIRS has 2378 infrared channels ranging from 3.7 µm to 15.4 µm and a 13.5 km footprint at nadir. The AIRS is a "facility" instrument developed by NASA as an experimental demonstration of advanced technology for remote sensing and the benefits of high resolution infrared spectra to science investigations. AIRS, in conjunction with the Advanced Microwave Sounding Unit (AMSU), produces quality controlled temperature profiles with 1K/km accuracy on a global scale, as well as water vapor profiles and trace gas amounts for CO_2, CO, SO_2, O_3 and CH_4. AIRS data are used for weather forecasting, climate process studies and validating climate models.

Figure 2.1 NASA's Atmospheric Infrared Sounder Instrument on the EOS Aqua Spacecraft observes the infrared spectrum globally every day to obtain accurate measurements of temperature, water vapor and trace gases in the atmosphere.

All AIRS products used in this campaign are derived using the AIRS Science Team Version-5 retrieval algorithm [1]. The AIRS products are divided into three types. Level 1B products are calibrated and geolocated upwelling radiances from the four major subsystems on the AIRS/AMSU system. There are 2378 infrared AIRS spectral channel radiances, 4 Vis/NIR AIRS spectral channel radiances, and 15 microwave channels from the AMSU. Level 2 products are retrieved geolocated cloud-cleared radiances and geophysical quantities, usually offered on the scale of the AMSU footprint which is approximately 45 km at nadir. This is due to the cloud clearing methodology involving observations in a 3x3 array of raw AIRS footprints and one AMSU footprint. The cloud clearing procedure generates the derived product cloud cleared radiances, which represent the set of channel radiances AIRS would have observed if the entire 3x3 array of AIRS footprints were completely cloud free. Level 3 products are gridded spatially (1 degree latitude and longitude bins for most products; 2 degrees latitude and 2.5 degrees longitude for the mid-tropospheric CO_2 products) and temporally (1 day, 8 day and monthly) and are available for most of the same products as in the standard level 2. There are a number of research products from AIRS including CH_4, Dust, and HNO_3, and SO_2. Recently Outgoing Longwave Radiation (OLR), CO and CO_2 were added to the core products due to their maturity and value to the scientific community. CO_2 data are post processed and resident in a separate file. All AIRS products are available at the Goddard Earth Sciences Data and Information Services Center (GES/DISC) at http://disc.sci.gsfc.nasa.gov. In addition to data products, data readers, user guides and verification/validation reports are also available at this location. Additional information on the AIRS Project and science applications can be found at the AIRS home page http://airs.jpl.nasa.gov.

2.2 **CO_2 product development**

Originally designed for temperature and water vapor profiles, the high information content in the AIRS spectra enabled scientists to extract other trace gas species. Extraction of carbon dioxide is problematic in that the carbon dioxide concentration in the atmosphere is high compared to its variability of only a few percent. To complicate matters, the carbon dioxide absorption features at 4.3 µm and 15 µm are used in the retrieval of temperature; however valuable unused channels remain among the 2378 channels available that can be used for CO_2 retrieval.

Multiple researchers have demonstrated the ability to retrieve CO_2 concentrations using AIRS data. Crevoisier et al. used a non-linear regression inference method to retrieve CO_2 in the mid troposphere in the tropics (20S-20N) on a 15 x 15 degree horizontal grid with a precision of 2.5 ppm[2]. In a more recent effort, researchers at ECMWF assimilated AIRS radiances in a 4D VAR radiance assimilation system to constrain the CO_2 mixing ratios[3]. In this latter study, a 50% reduction in CO_2 differences between model and aircraft measurements was achieved. AIRS CO_2 retrievals were also successfully demonstrated at NOAA using a regularized nonlinear least squares solution to minimize the RMS differences between the observed radiances and those calculated for the AIRS Rapid Transmittance Algorithm (RTA)[4]. The NOAA retrievals utilize cloud cleared radiances which enable global coverage under most cloud conditions twice daily. Comparisons with NOAA ESRL/GMD flask measurements using this method over a 2 week average and 200 km radius demonstrate the ability to measure large scale changes in atmospheric CO_2 concentrations of 2 ppmv. Researchers at UMBC derived low to mid-tropospheric CO_2 in clear ocean regions between ±60° latitude by minimizing the residuals between the computed radiances and the observed radiances through scaling the CO_2 concentrations[5]. To mitigate complications with temperature sensitivity, they used ECMWF temperatures. They demonstrated accuracies of 0.5-1.0 ppm compared to aircraft. While all of these methods have been extraordinarily successful, the AIRS project has selected a new retrieval methodology that provides the highest accuracy, yield, and coverage under most cloud conditions, day and night, for land and ocean fields.

The CO_2 retrieval method selected for routine production by the AIRS Project is called the method of Vanishing Partial Derivatives (VPD)[6]. The VPD method, which employs the least squares minimization method developed by Carl Friedrich Gauss in 1795, iteratively minimizes the difference between the observed cloud cleared radiances and calculated radiances for AIRS where the calculated radiances employ the AIRS RTA. The VPD method applies the minimization independently and sequentially to all geophysical parameters that impact the radiance of a given channel used to retrieve CO_2, i.e. atmospheric temperature, water vapor, ozone, and carbon dioxide. The retrieval starts with the AIRS cloud cleared radiances for CO_2 channels with peak weighting functions in the mid-troposphere, or about 5-8 km in altitude (See Figure 2.2). Channels also exist that have sensitivity to the stratosphere and near surface, and they will be used for retrievals in these regions at a later time. The retrieval also requires atmospheric temperature, water vapor, and ozone from the AIRS standard product (45 x 45 km). These products are retrieved again using the VPD method and specially selected channels prior to optimization of the CO_2 and the process is iterated until the radiance residuals for all parameters are minimized or the change in CO_2 falls below 0.25 ppm. Extensive quality control is applied during the retrieval including: quality of the AIRS geophysical products, monotonically decreasing radiance residuals from one iteration to the next, and spatial homogeneity of a 2x2 set of retrievals (clusters) is required to be within 2 ppm in an RMS sense. The resulting product achieves a yield over 15,000 mid-tropospheric CO_2 retrievals per 24-hour period (see Figure 2.3), each with a horizontal footprint of 100x100 km and an accuracy better than 2 ppm.

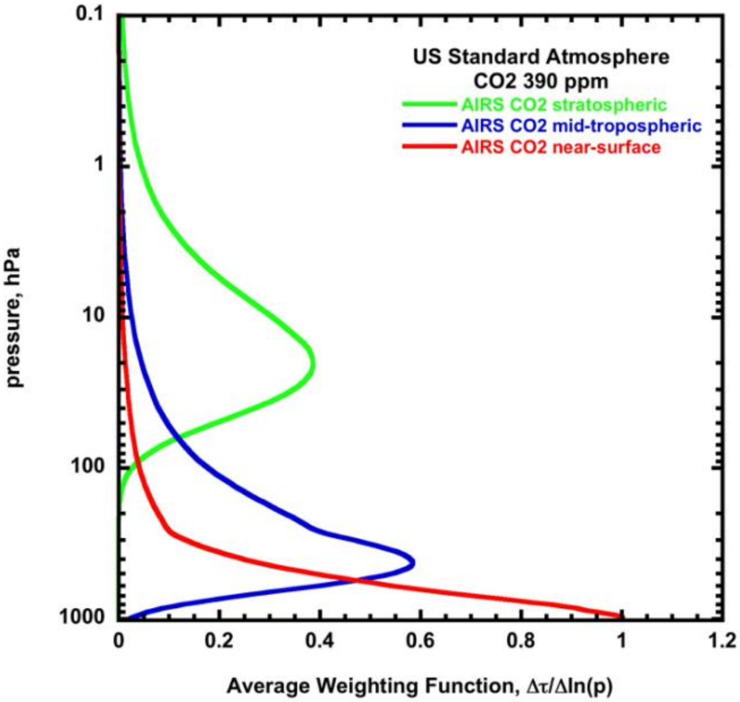

Figure 2.2 Un-normalized weighting functions for channels used in AIRS CO2 retrievals

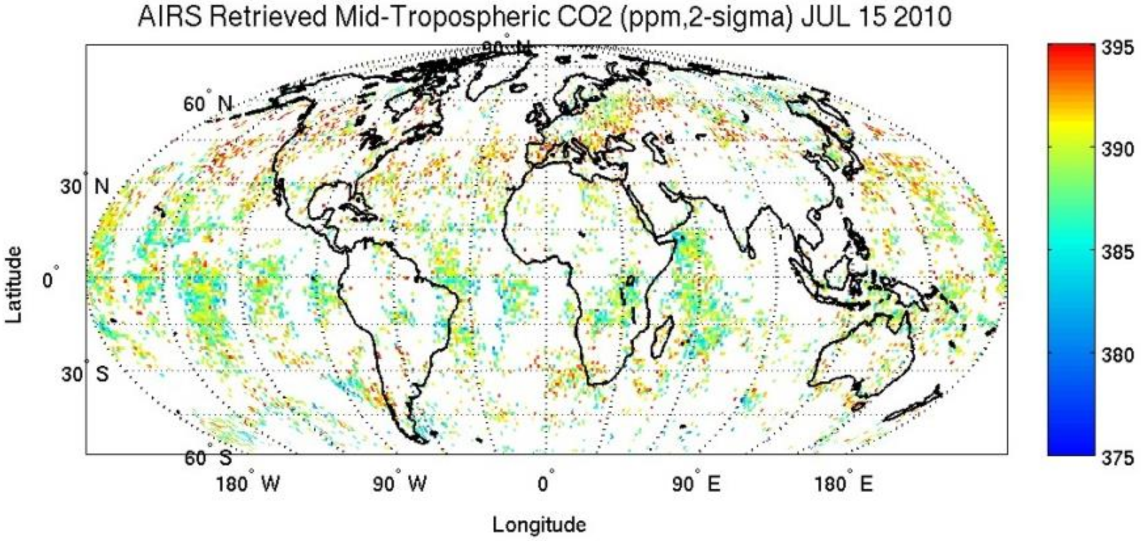

Figure 2.3 AIRS yields about 15,000 Mid-Tropospheric CO_2 measurements per day.

2.3 Product Validation

AIRS VPD CO_2 retrievals were compared to aircraft measurements made in the mid-troposphere by Matsueda, taken over the Pacific Ocean at ≥10 km altitude between Australia and Japan from Sept. 2002 to March 2004[6]. Of the 402 available flask measurements, 223 are co-located with AIRS data within a radius of 150 km and ±4 hours. We exclude from consideration any of the 223 clusters that contain less than three AIRS retrievals and reject all AIRS retrievals that do not seek a minimum during the iteration process. As a result, the 223 clusters and collocated Matsueda measurements are reduced to 103 containing 927 AIRS retrievals. The comparison results in a bias difference of 1.2 ppmv and a standard deviation of 3.1 ppmv. With the addition of QC on the uniformity of the clusters, the result improves slightly to a bias of 1.0 ppmv, and standard deviation of 3.0 ppmv. Of most interest to note is that the distribution of the difference between the Matsueda aircraft observations and the AIRS CO_2 measurements is highly Gaussian. This implies that monthly averages (see Figure 2.4) have lower standard deviation. In fact, comparison with 14 months of Matsueda data and AIRS data yielded a mean bias of 0.43 ppmv and a standard deviation of 1.2 ppmv. Additional validation data now exists for other aircraft comparisons that will be presented in a subsequent paper by the authors.

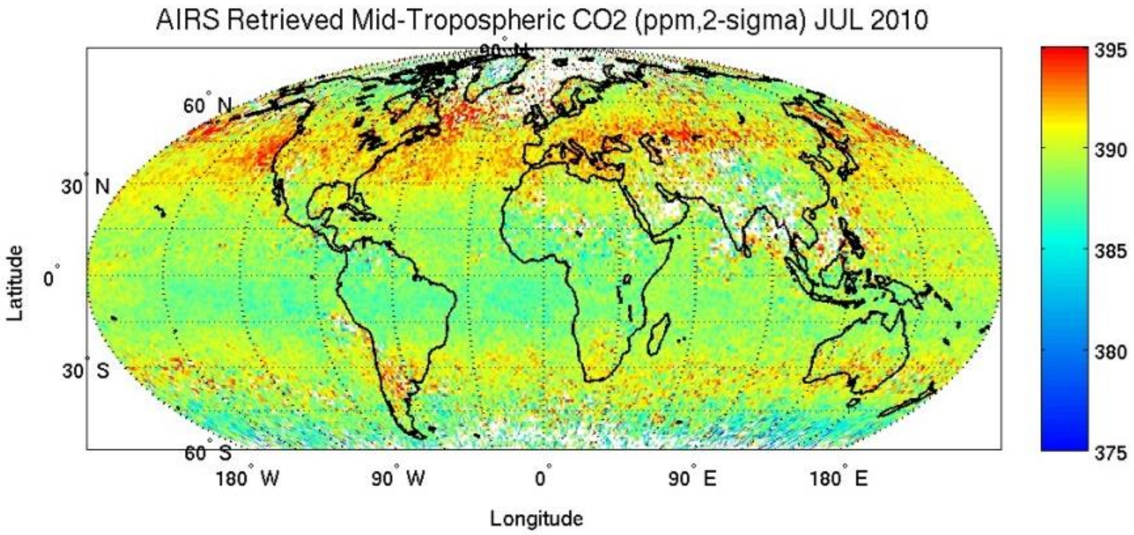

Figure 2.4 AIRS Mid-Tropospheric CO_2 is a tracer for atmospheric motion particularly in the vertical direction, July, 2010 Monthly average.

Comparisons have also been made between the AIRS VPD CO_2 retrievals and ground based measurements using an upward looking Fourier Transform Infrared Radiometer (FTIR) at Park Falls Wisconsin between July 2004 and March 2006[7]. Comparisons are made on monthly average CO_2 retrievals from both sets of data over a 19 month time span. Both data sets agree extremely well with differences as expected. In the winter months, the AIRS and FTIR data agree to better than 2 ppm. However, in the summer months the FTIR data show much lower CO_2 concentrations than observed by AIRS, with differences ranging from 0 to 7 ppm. The difference is explainable since the FTIR measures the total column whereas the AIRS measures only the mid-troposphere. The increased sensitivity to the near surface of the FTIR means the FTIR measurements are more sensitive to the drawdown of CO_2 from the biomass that occurs in the spring and summer. The levels observed in the difference meet expectations for CO_2 uptake from the surface.

AIRS data have been compared to ground based measurements of CO_2. A time series of AIRS Level 3 CO_2 retrievals were used to compute the peak of the CO_2 seasonal cycle and the amplitude. To compute the peak of the seasonal cycle, the data were first fit to a cubic spline, then the peak and minimum for each year are determined. These were compared to similar calculations on a global set of CO_2 observations from NOAA CMDL [8]. Results are shown in Figure 2.5 for the peak month and Figure 2.6 for the amplitude. In these Figures we also show the seasonal metrics for AIRS mid-tropospheric and surface temperatures and Gross Primary Productivity (GPP) derived from MODIS Enhanced Vegetation Index (EVI). GPP is a measure of the rate at which photosynthesis occurs in global land vegetation. Results show that CO_2 in the mid-troposphere lags the surface by about a month but the uncertainties grow as we go pole-ward. We see good correlation in the GPP and temperature for most latitudes. In Figure 2.6 we see a significant difference in the amplitude of the seasonal cycle at the surface and in the mid-troposphere. Both, the delay in the peak of the seasonal cycle and the decreased amplitude of the mid-tropospheric CO_2 compared to the surface are evident in our comparisons with the Moody, TX site discussed in section 2.3.3.

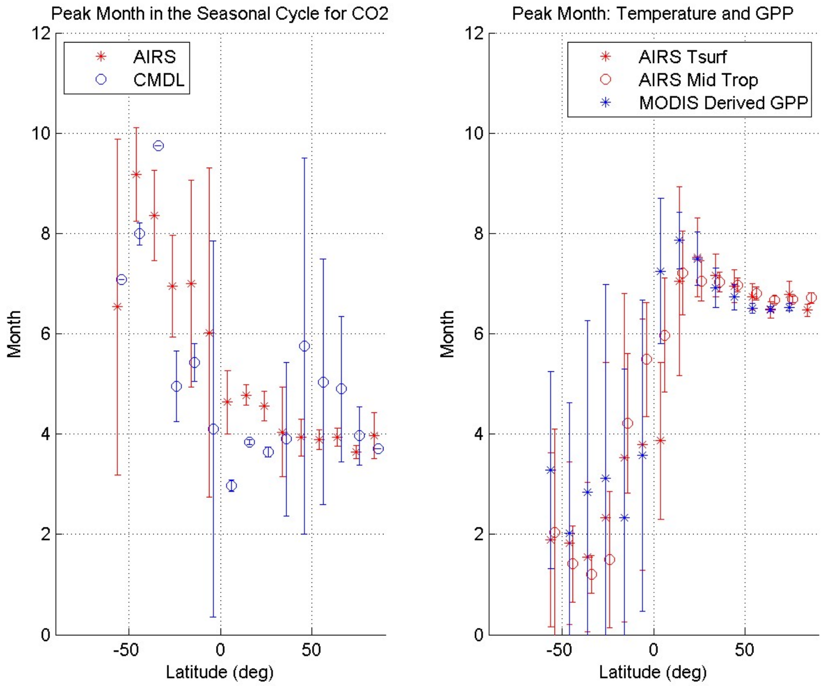

Figure 2.5 Month in which the peak in the seasonal cycle occurs. (left) CO$_2$ from AIRS and the NOAA Carbon Monitoring Diagnostic Laboratory (CMDL), (right) Temperatures from AIRS, and MODIS Gross Primary Productivity (GPP)

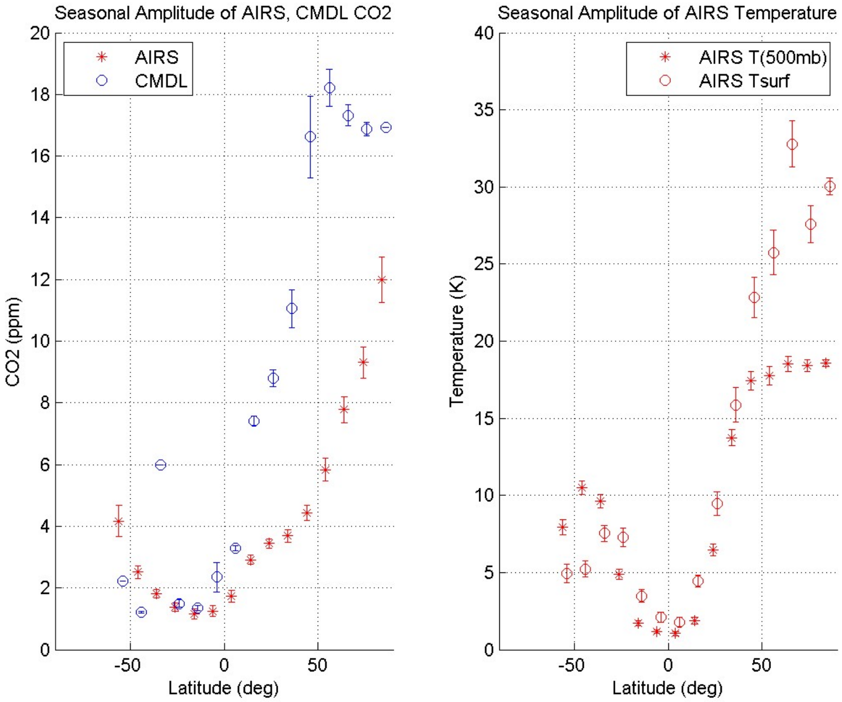

Figure 2.6 Amplitude of the seasonal cycle for (left) AIRS CO$_2$ and CMDL, (right) AIRS Temperature at 500 mb and the surface.

2.4 Science findings using AIRS CO_2 data

Carbon dioxide turns out to be an excellent tracer gas since it does not react with other gases in the atmosphere. We are finding that the AIRS Mid-tropospheric CO_2 is a good indicator of vertical motion in the atmosphere. We know the majority of atmospheric CO_2 is produced and absorbed near the surface and that there are no sources or sinks in the free troposphere. Thus elevated levels of mid-tropospheric CO_2 are the result of airflow into the mid-troposphere from the near surface.

The most obvious finding from the AIRS retrievals is that the distribution of CO_2 is not uniform in contrast to what is found in the models[9]. Strong Latitudinal and Longitudinal gradients exist particularly over the large land masses in the Northern Hemisphere. This phenomenon is referred to in the referenced publication as "CO_2 weather". The large variability in atmospheric circulation due to convection and global and mesoscale transport is responsible for most of the variability seen in the AIRS data. Another example of CO_2 horizontal variability can be seen in Figure 2.7 where the AIRS CO_2 data show a prominent, seasonally persistent depression in concentrations in the south Atlantic [10]. This depression is associated with a strong downward flow of the Atlantic Walker Circulation. These early qualitative assessments were indicative of several investigations to follow that show the AIRS CO_2 data are extremely useful for understanding global scale transport processes and validating Global Circulation Models.

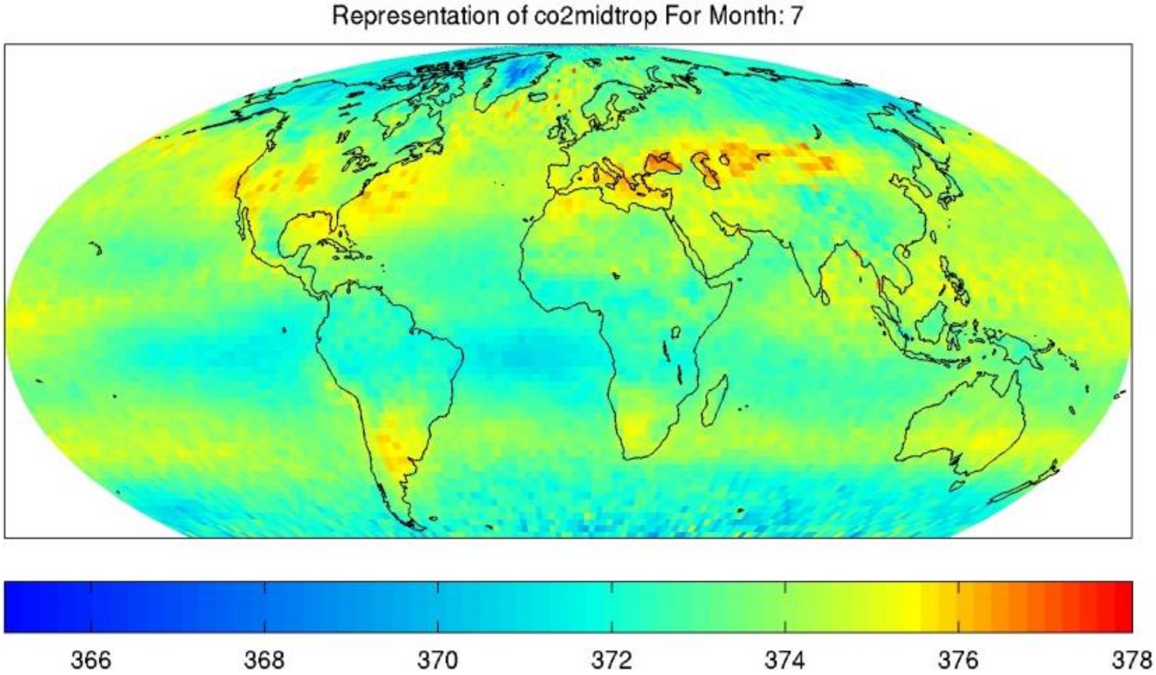

Figure 2.7 AIRS reveals a depression of Mid-Tropospheric CO_2 in the South Atlantic (July Climatology).

In one of the first circulation studies using AIRS CO_2, researchers observed the response of the atmosphere during the El Nino Southern Oscillation [10]. In this study, the AIRS data are de-trended to remove the ~2ppm/year increase and the average horizontal distributions plotted for 11 El Nino months and 17 La Nina months. During El Nino, the CO_2 concentration over the Central Pacific region is enhanced while it is reduced over the Western Pacific. The same paper also identifies that CO_2 concentrations in the polar regions are diminished if the polar vortex is strong. The AIRS mid-tropospheric CO_2 product has been used to study the Madden-Julian Oscillation (MJO) and Tropical Interseasonal Oscillations, and as such provides a unique constraint as well as a robustness test for coupled carbon-climate models [11, 12, 13]. Scientists in China compared the AIRS product to ground-based and aircraft measurements, concluding that the AIRS product is consistent with both sets of in situ measurements and is able to capture the seasonal variations [14].

Finally, scientists are using the AIRS CO_2 data to improve vertical and horizontal transport in GCM's. Scientists have developed techniques to assimilate AIRS CO_2 data in GCM's and early results show an improvement in the retrieval of surface fluxes [15]. In a study led by researchers at the University of Edinburgh, CO_2 concentrations calculated by the NASA GEOS-Chem GCM were compared to several data sets including the AIRS mid-tropospheric CO_2 over the period of 2004–2006 [16]. AIRS data compare well with the GEOS-Chem model with small biases observed in the mid-tropospheric CO_2 trends.

2.5 **AIRS Data Holdings**

All data from the AIRS mission have now been processed to retrieve mid-tropospheric CO_2. A contiguous 10 year record now exists for AIRS starting in September 2002 to the present. Figure 2.8 shows a Hövmoller diagram of the monthly and zonal average CO_2 concentrations for an 8 year period starting in September 2002. This Figure was created by averaging the monthly data sets (Figure 2.4) into 5 degree latitude bins for all longitudes. The data contain 90 months from September 2002 to February 2010. We see several expected and unexpected features in the data set. First we see the annual increase of 2 ppm/year in the data. A linear fit to the global averages for all months and years yields approximately 2.07 ppm/year from the AIRS CO_2 data. Secondly, the strong seasonal cycle caused by the production and uptake of CO_2 primarily in the northern hemisphere is readily apparent. A third observation is the presence of the depression in the Southern Hemisphere around 10°S. Closer inspection of the Hövmoller diagram leads the authors to believe there is a continuous flow of CO_2 from the Northern Hemisphere to the Southern Hemisphere with a time scale from 6-8 months.

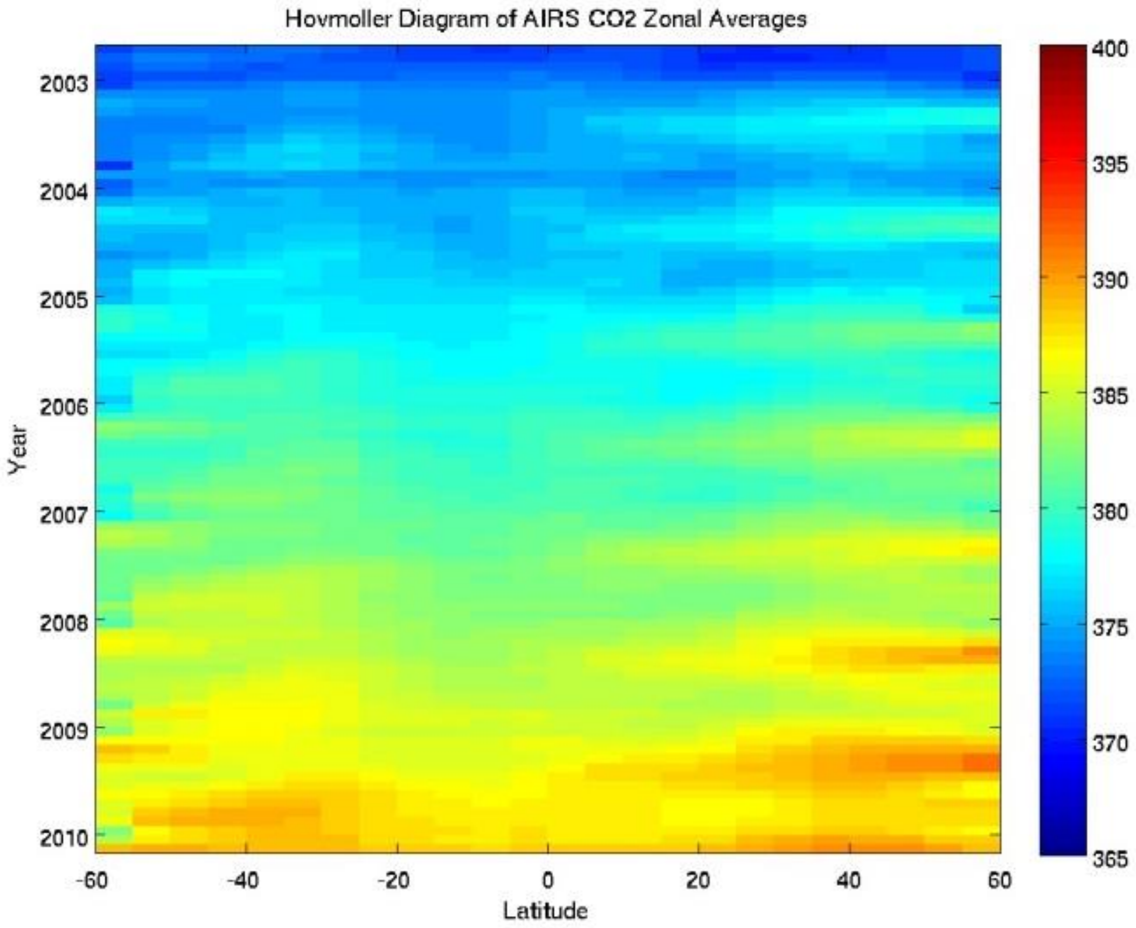

Figure 2.8 Hovmöller Diagram of AIRS Mid-Tropospheric CO_2 shows seasonal cycle and annual trend. In this Figure we can also see the flow of CO_2 from the Northern Hemisphere to the Southern Hemisphere.

2.6 AIRS and the CAMP CO_2 field campaign

2.6.1 CO_2 Climatology for the CAMP field campaign

The AIRS CO_2 measurements were first used to create a climatology of the mid-tropospheric concentrations of carbon dioxide over the campaign area (see Figure 2.9). This climatology assisted the team by providing the nominal background levels of CO_2 that are present in the mid-troposphere as a function of the time of year and in defining the best time of year for measuring the seasonal fluctuations in CO_2. The optimal times for the campaign were decided to be near the peak of the seasonal cycle, May, and the minimum, November, to capture the seasonal signal in CO_2. Flights occurred in September 2012, and April/May 2013.

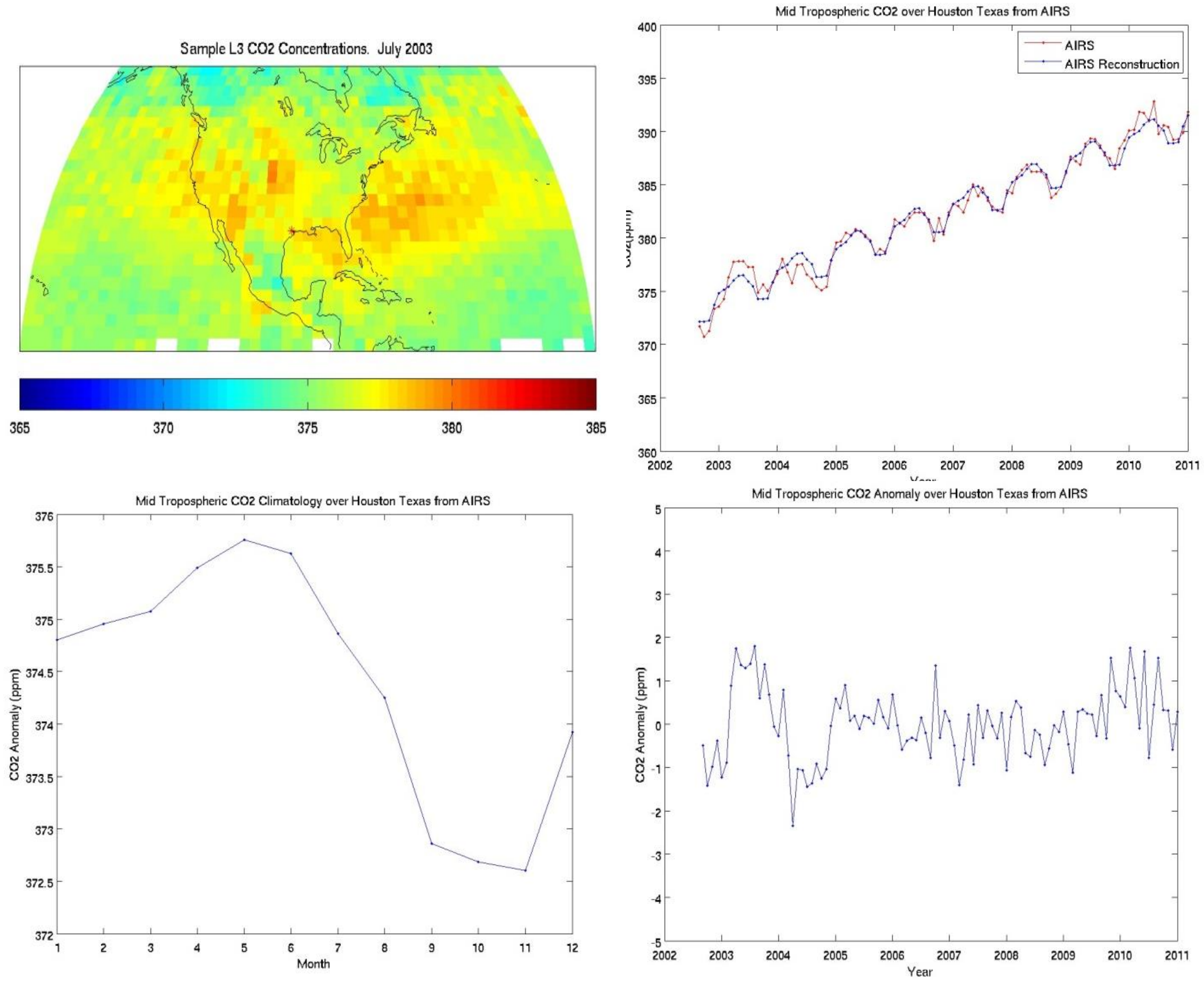

Figure 2.9 (Top Left) Sample Monthly Gridded AIRS CO_2 data product for July 2003. (Top Right) AIRS measured Mid-Tropospheric CO_2 over the Houston area from 2003-2011, overlaid with reconstructed climatology. (Bottom Left) Climatology of the seasonal behavior of mid-tropospheric CO_2 over the Houston area. (Bottom Right) Anomaly of Mid-Tropospheric CO_2 over the Houston area (difference of two curves in (Top Right).

2.6.2 Co-located Retrievals

Individual AIRS CO_2 soundings were co-located with several locations relevant to the campaign so that comparisons can be made with other data sets in this region and the CO_2 mid-tropospheric anomalies can be determined. Co-located data sets were provided for Houston Tx, McKinney Tx, Moody Tx, Lamont OK, and Quebec City. The co-locations started March 16, 2012 and continue on through the end of the campaign. Table 2.1 shows an example of the co-located data. Co-located data sets for Temperature, Water Vapor, and other “ancillary” data products from AIRS were also provided for these sites (see Table 2.2 for an example).

Table 2.1. Co-located AIRS CO_2 Soundings for McKinney Texas Only first 10 lines of the file are shown

% CO2 Data from AIRS for:												
% McKinney_Tx Lat: 33.18 Lon: -96.59												
% Within: 200.0 km												
Year	Month	Day	Hr	Min	Sec	Lat	Lon	FOV	LandFrc	CO2	CO2_std	SolZen
2012	3	16	8	25	36	33.48	-95.11	6	0.98	388.05	1.82	138.1
2012	3	16	8	25	36	33.61	-96.01	7	0.98	395.4	1.09	138.5
2012	3	16	8	25	36	33.73	-96.88	8	0.93	396.39	1.23	138.9
2012	3	16	8	25	36	32.56	-96.23	7	0.91	392.11	1.11	139.3
2012	3	16	8	25	36	31.88	-97.32	8	0.95	397.7	1.8	140.4
2012	3	19	8	55	28	33.92	-95.88	1	0.96	394.18	1.98	132.3
2012	3	19	19	56	48	31.9	-97.75	11	0.97	388.44	1.95	37
2012	3	19	19	57	52	33.07	-95.58	13	0.95	397.9	1.05	39.1
2012	3	24	20	16	0	31.9	-96.68	15	0.96	390.74	1.24	38.6
2012	3	24	20	16	0	32.86	-96.85	15	0.94	391.27	0.89	39.2

Table 2.2. Co-located AIRS Ancillary Products for McKinney Texas include Mid-Tropospheric and Surface Temperature, Water Vapor, Cloud Fraction, Cloud Top Pressure, Total Ozone and Carbon Monoxide

% Ancillary Data from AIRS for:															
% McKinney_Tx Lat: 33.18 Lon: -96.59															
% Within: 75.0 km															
%yr mo day hr min sec Lat Lon fov# T(500mb) TSurf q(500mb) CldFrc CldTopPres TotO3(DU) TotCO(mol/cm^2)															
Year	Month	Day	Hr	Min	Sec	Lat	Lon	FOV	T(500mb)	Tsurf	q(500mb)	CldFrc	CldTopP	TotO3	CO
2012	3	16	8	25	18.92	33.4	-96.3	14	258.07	289.4	0.18	0	-9999	273.85	2.45E+18
2012	3	16	8	25	18.99	33.46	-96.73	15	258.31	288.47	0.2	0	-9999	278.27	2.41E+18
2012	3	16	8	25	19.06	33.52	-97.17	16	259.01	289.44	0.26	0	-9999	290.29	2.35E+18
2012	3	16	8	25	26.86	32.86	-96	13	258.8	290.58	0.63	0	454.75	279.97	2.15E+18
2012	3	16	8	25	26.92	32.92	-96.43	14	259.06	288.88	0.91	0.94	725.59	280.97	2.14E+18
2012	3	16	8	25	26.99	32.98	-96.87	15	259.16	291.8	1.08	0	258.37	279.26	2.11E+18
2012	3	16	19	26	38.52	32.89	-96.67	8	258.35	298.35	0.89	0.1	203.09	277.98	2.07E+18
2012	3	16	19	26	38.59	32.98	-96.15	9	257.72	295.73	0.93	0	219.15	285.5	2.00E+18
2012	3	16	19	26	46.52	33.36	-96.82	8	258.89	297.44	0.85	0.05	205.93	292.13	2.13E+18
2012	3	16	19	26	46.59	33.46	-96.3	9	258.73	298.22	1.07	0.13	241.26	283.96	2.04E+18
2012	3	17	20	9	27.86	32.52	-96.72	28	259.23	292.64	0.72	0.3	257.42	308.79	1.91E+18
2012	3	17	20	9	35.86	33.01	-96.82	28	259.96	284.52	0.72	0.04	235.32	333.94	1.91E+18
2012	3	17	20	9	43.86	33.49	-96.91	28	259.01	291.92	0.51	0.53	215.82	-9999	1.74E+18

Having all the data from a single site in one file gives an opportunity to examine correlations amongst the data sets. In particular, we wanted to identify the correlation of temperature, water vapor, clouds and other trace gases on CO_2. Figure 2.10 shows dependence on cloud fraction. Most AIRS CO_2 retrievals occur in clear regions, but there is no bias with cloud fraction. Similarly we see no dependence of CO_2 with ozone, or carbon monoxide within the statistical significance of the data set (~3ppm). Temperature and water vapor dependence of the CO_2 is also unbiased, however we see most retrievals obtained in warm, dry conditions.

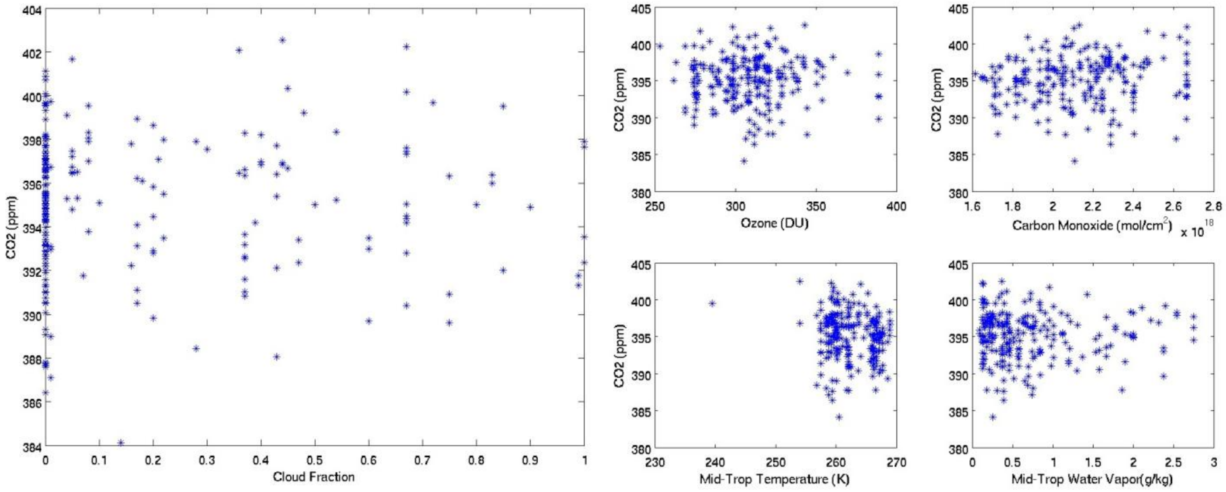

Figure 2.10 (left). AIRS CO_2 vs. cloud fraction. (right). CO_2 amount vs. O3, CO, Temperature and Water Vapor (Top Left, Top Right, Bottom Left, Bottom Right respectively).

With the co-located data products were stored the time of acquisition for that site, latitude, longitude and which of the 90 fields of view (FOV's) acquired by AIRS. The team needed to know when the AIRS would overpass the acquisition sites. Since the AIRS orbit repeats every 16 days, we binned the co-location times into 16 bins, shown in Figure 2.11. Not all days have an am and pm overpass. The resulting pattern has excellent consistency to within a few minutes of every overpass. The pattern was projected forward to the time of the CAMP flights and used in scheduling the data collection activities (Table 2.3).

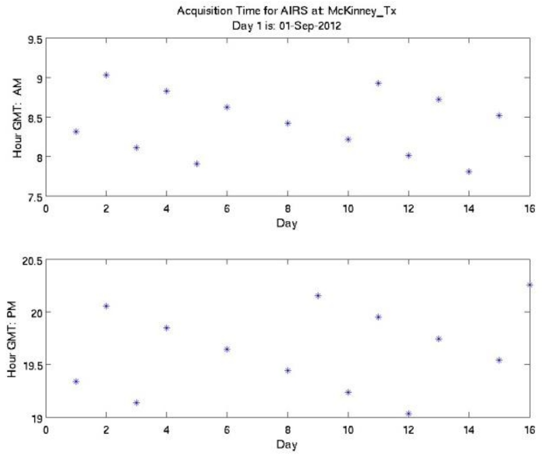

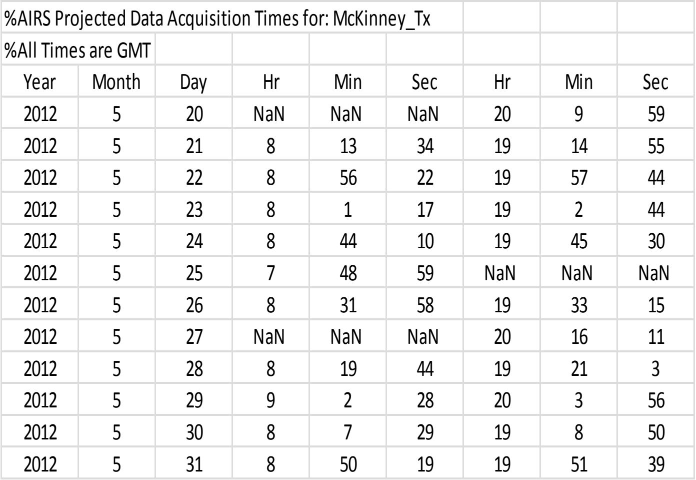

%AIRS Projected Data Acquisition Times for: McKinney_Tx								
%All Times are GMT								
Year	Month	Day	Hr	Min	Sec	Hr	Min	Sec
2012	5	20	NaN	NaN	NaN	20	9	59
2012	5	21	8	13	34	19	14	55
2012	5	22	8	56	22	19	57	44
2012	5	23	8	1	17	19	2	44
2012	5	24	8	44	10	19	45	30
2012	5	25	7	48	59	NaN	NaN	NaN
2012	5	26	8	31	58	19	33	15
2012	5	27	NaN	NaN	NaN	20	16	11
2012	5	28	8	19	44	19	21	3
2012	5	29	9	2	28	20	3	56
2012	5	30	8	7	29	19	8	50
2012	5	31	8	50	19	19	51	39

Figure 2.11 (left). Overpass times for the AIRS over McKinney Texas. (top) am, (bottom) pm.

Table 2.3 (right) Table of overpass times projected for AIRS by day.

2.7 CAMP Spring 2013 Campaign at Moody, TX

2.7.1 Overview

Figures 2.12 through 2.15 below illustrate the CO_2 data sets from the CAMP Spring 2013 Campaign which were examined. The CAMP aircraft flights took place on 4/16, 4/19, 5/18, and 5/19 and the five samples from each flight are represented as the large circles, with color coding for sample heights (feet Above Ground Level). The "WKT" data set is a subset of the data available from the NOAA Earth System Research Laboratory's (ESRL) Tall Tower Greenhouse Gas Observing Network[17]. WKT tower CO_2 measurements are made at heights of 30, 122, and 457 meters above ground level (at the time the data was acquired, only the 457 m data was available after 4/15). The AIRS data presented are all matchups located within 200 km of the WKT tower. Figure 2.12 shows all the data from 3/10 through 6/1. Figure 2.13 has the time axis limited to April to allow a finer view of the relationship between the various data sets. Figure 2.14 zooms in further to a 10 day window that encompasses the 4/16 and 4/19 flights. Figure 2.15 shows the May portion of the data set.

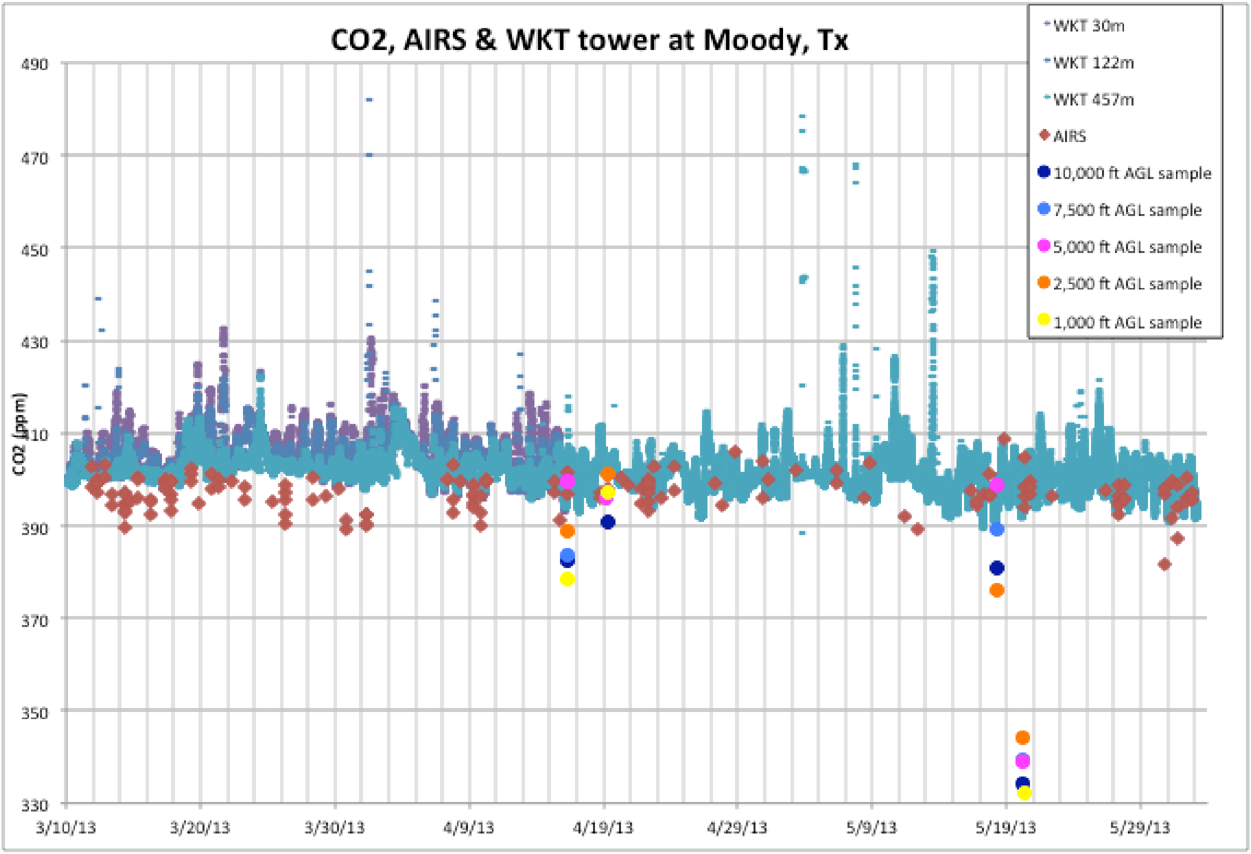

Figure 2.12 CAMP Spring Campaign CO_2 data sets from Moody, Tx; WKT tower in situ measurements at 3 heights (meters above ground level), AIRS retrievals within 200 km of the tower, and aircraft in-flight samples at 5 elevations above ground level (ft. AGL)

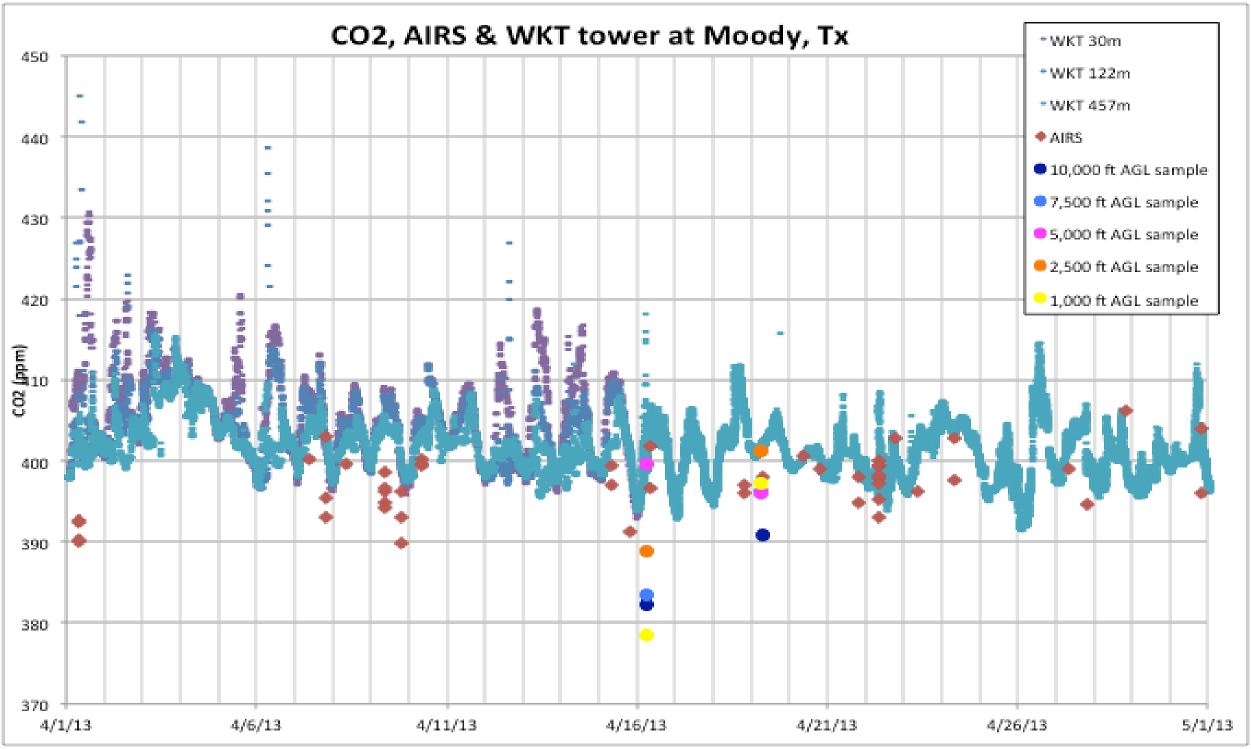

Figure 2.13 April CAMP Spring Campaign CO$_2$ data sets from Moody, Tx; WKT tower in situ measurements at 3 heights (meters above ground level), AIRS retrievals within 200 km of the tower, and aircraft in-flight samples at 5 elevations above ground level (ft. AGL)

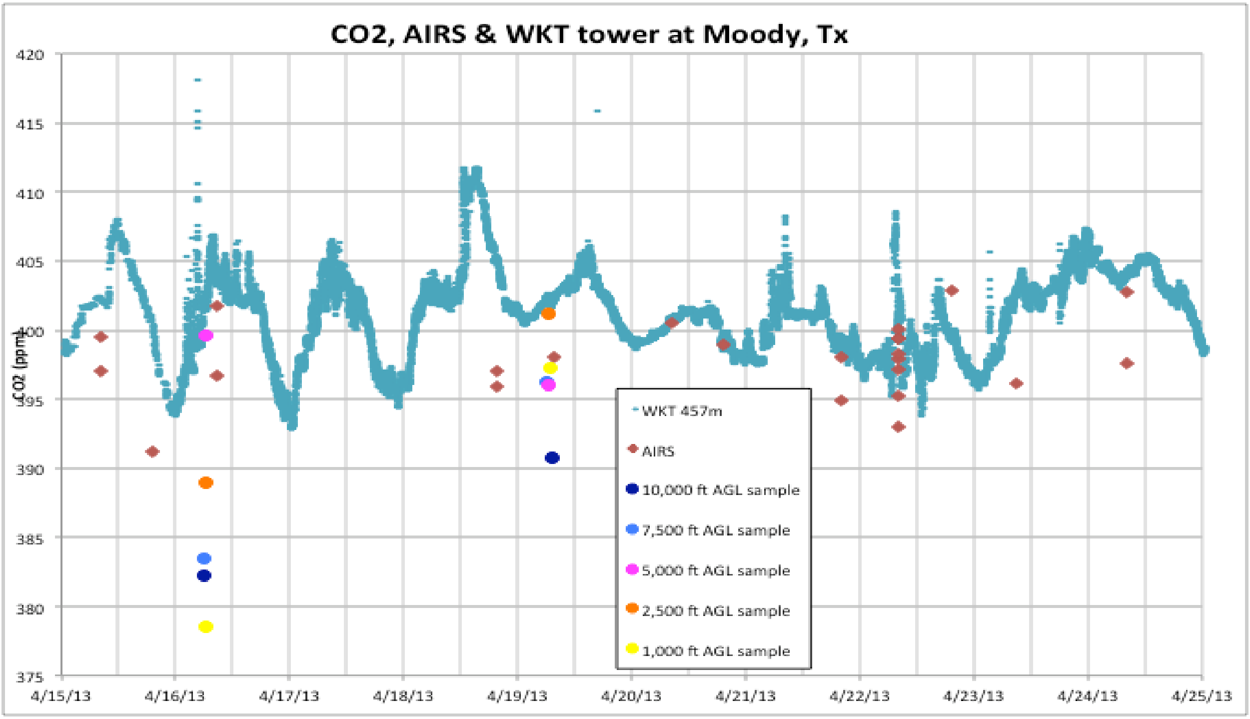

Figure 2.14 April 15-25 CAMP Spring Campaign CO$_2$ data sets from Moody, Tx; WKT tower in situ measurements at 457 m AGL (above ground level), AIRS retrievals within 200 km of the tower, and aircraft in-flight samples at 5 heights above ground level (ft. AGL)

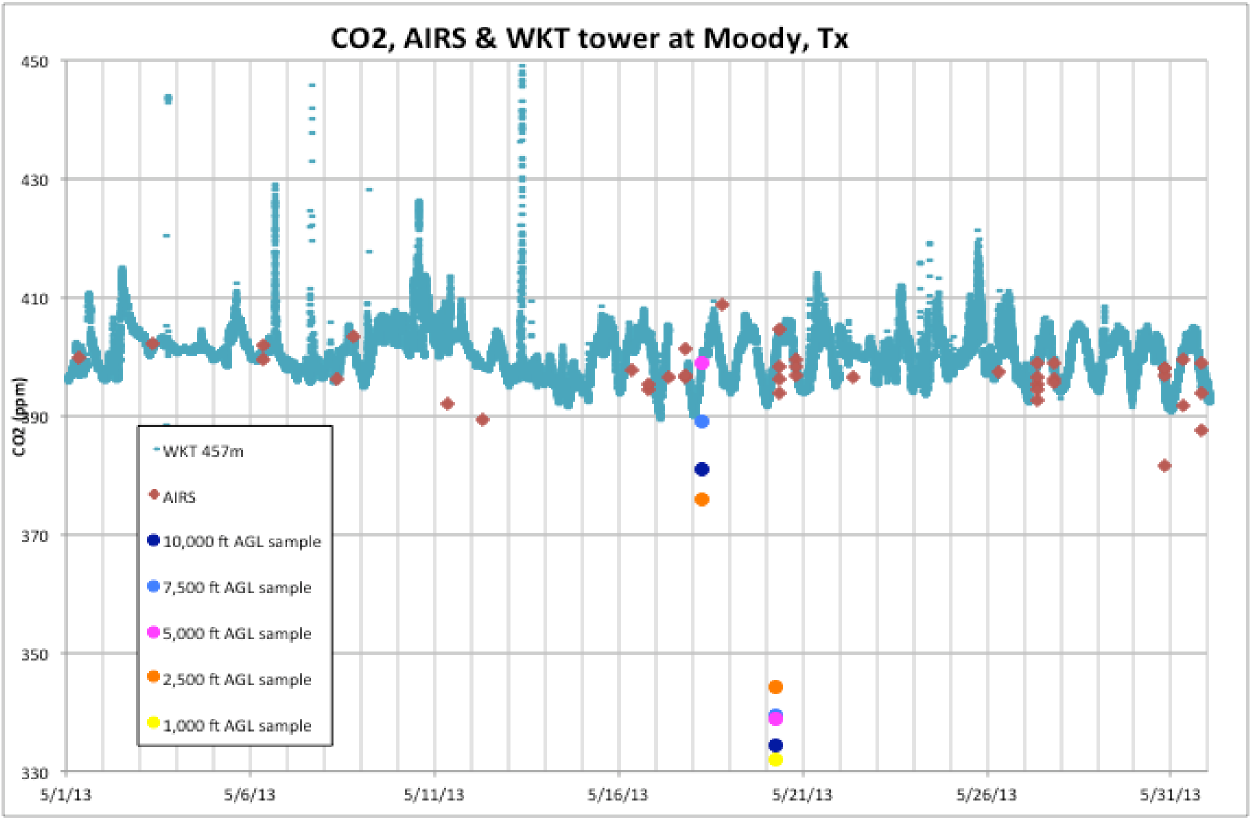

Figure 2.15 May CAMP Spring Campaign CO_2 data sets from Moody, Tx; WKT tower in situ measurements at 457 m AGL (above ground level), AIRS retrievals within 200 km of the tower, and aircraft in-flight samples at 5 heights above ground level (ft. AGL)

2.8 CAMP Sonde and AIRS Temperature and Specific Humidity Comparison

Sondes were launched during the CAMP campaign at site (97.31°W, 31.21°N) on April 19 (18:53 UTC), May 18 (15:53 UTC), and May 20 of 2013 (16:46 UTC). The data files used were obtained from the epaaspect2.net ftp server. The files used were from the directory named "ASPECT-Moody-Radiosonde-Data-For-Silvia", and had the suffix "Flt_1_basic.txt.

AIRS sounding retrievals (Version 6 Level-2 support product) were matched up with these sonde launches for the closest location and time. Table 2.4 shows the distances and time spans between the matched-up AIRS soundings and the sonde launches as well as the corresponding AIRS file names.

Table 2.3. AIRS files matched up with the CAMP sondes and distances and time spans between the AIRS soundings and the sonde launches.

Dates	Distances	Time Span	AIRS files
Apr. 19	33 km	1.5 hr	AIRS.2013.04.19.203.L2.RetSup.v6.0.7.0.G13110124705.hdf
May 18	19 km	4.0 hr	AIRS.2013.05.18.198.L2.RetSup.v6.0.7.0.G13139140429.hdf
May 20	6.2 km	2.9 hr	AIRS.2013.05.20.196.L2.RetSup.v6.0.7.0.G13141125534.hdf

2.8.1 Temperatures:

For temperature comparison, CAMP sonde temperatures are linearly interpolated in log-pressure scale onto the AIRS support product pressure levels. Figure 2.16 compares the AIRS sounding temperature profiles to the corresponding CAMP sonde temperature profiles. Above 600-700 hPa AIRS temperature profiles are consistent with CAMP's temperature profiles. Below 600-700 hPa AIRS temperatures deviate from CAMP's; however, these data are not flagged as the "best" quality in AIRS retrievals.

2.8.2 Specific Humidity:

AIRS retrievals use the Murphy-Koop algorithm to calculate saturation water vapor mixing ratio. Using other algorithms to convert any measurements of relative humidity to specific humidity may introduce significant differences when comparing the measurements with AIRS specific humidity. Therefore, we use the CAMP sonde relative humidity and then apply the Murphy-Koop algorithm to convert the data to specific humidity, instead of directly using the CAMP calculated specific humidity in the enhanced files.

CAMP sonde specific humidity data within two AIRS support product pressure levels are averaged as to compare with the AIRS layer specific humidity. Comparison of AIRS specific humidity to CAMP sonde specific humidity is shown in Fig. 2.17. AIRS retrievals generally capture the sonde specific humidity profiles, although the detailed vertical structures are smoothed in the AIRS profiles.

2.8.3 Biases:

As retrievals of temperature/water vapor at a particular altitude are sensitive to the temperatures/water vapor at other altitudes, such inter-altitude dependence of retrievals is summarized in AIRS retrievals' averaging kernels. A more fair comparison between any measurements and AIRS data should apply these averaging kernels to the measured profiles before the comparison. The blue lines in Fig. 2.18 show the biases of temperatures and specific humidity with the sonde measurements smoothed by the corresponding AIRS averaging kernels, while the red lines show the direct comparisons. The temperature biases between the AIRS and the sonde measurements are within 1 K in altitudes when quality flags equal to 0 (the "best" quality). The specific humidity biases are also small in altitudes when quality flags are equal to 0.

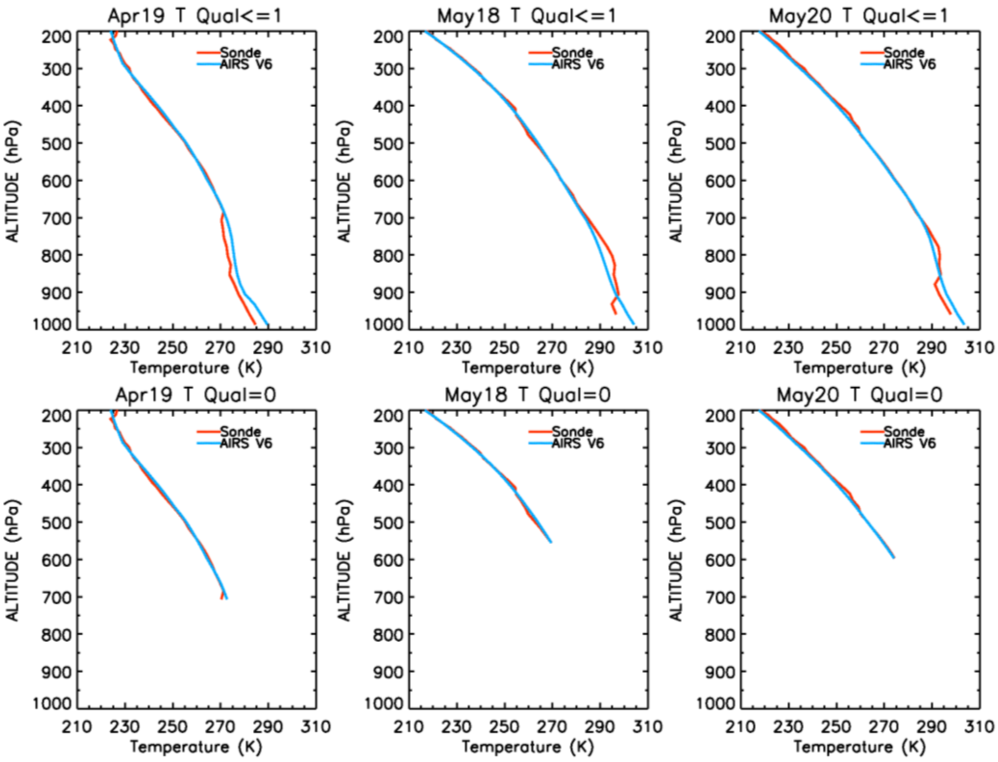

Figure 2.16 The AIRS sounding temperature (in K) profiles (blue lines) and the corresponding CAMP sonde temperature profiles (red lines). The upper panel shows the AIRS temperatures at levels flagged as "good" quality (Quality flag ≤ 1), and the lower panel shows the AIRS temperatures at levels flagged as "best" quality (Quality flag = 0).

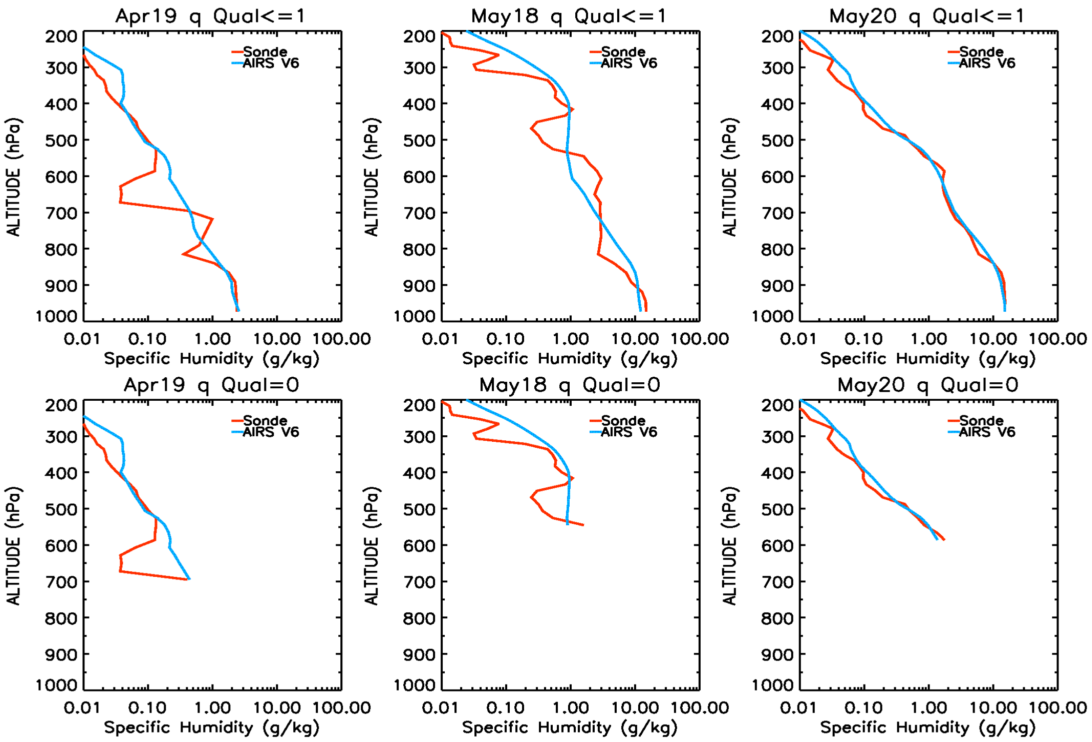

Figure 2.17 Similar to Fig. 1, but for the AIRS sounding specific humidity (in g/kg) profiles and the corresponding CAMPS sonde specific humidity profiles.

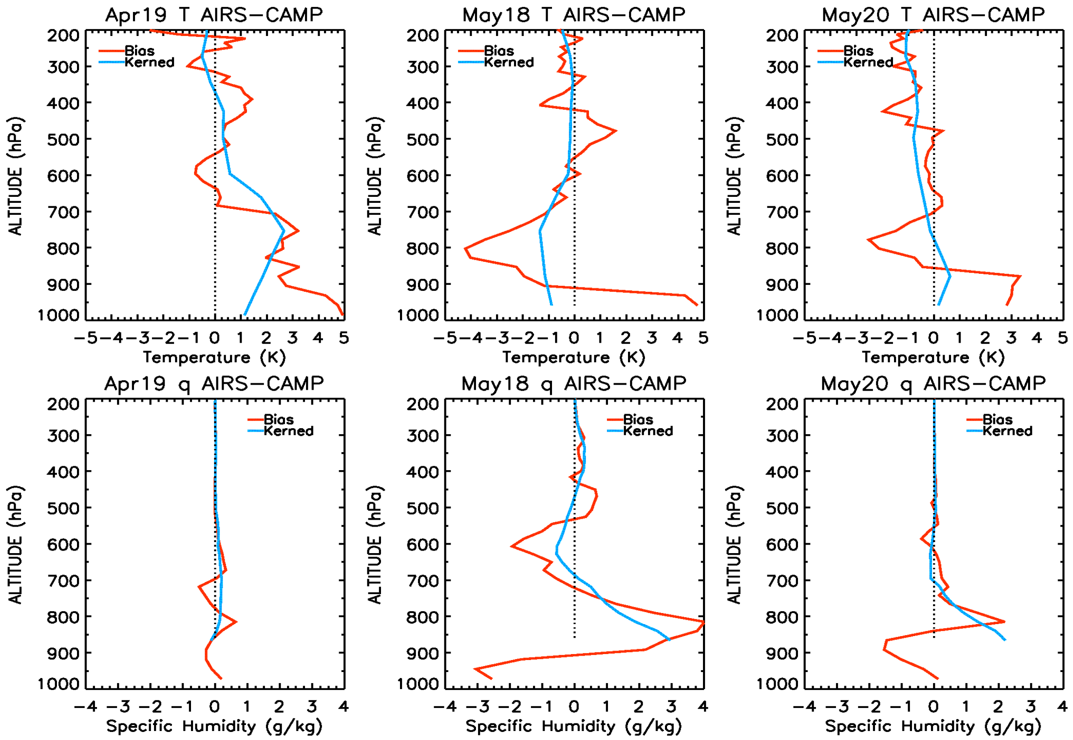

Figure 2.18 Biases in AIRS temperatures (upper panel) and specific humidity (lower panel) compared to the CAMP sonde measurements. The red lines show the biases of direct comparison, while the blue lines show the biases with the CAMP sonde profiles being smoothed by the corresponding AIRS temperature or specific humidity averaging kernels.

2.9 Seasonal Variation of AIRS CO_2 data vs. WKT in situ tower

In order to see the seasonal variability of the differences between the AIRS and the WKT CO_2 measurements, data from 2010-Jan-01 through 2013-Jun-30 were compared. Monthly means were calculated for both the WKT data and the AIRS data. Figure 2.19 shows the WKT data with monthly means and error bars overlaid (error bar is one standard deviation). Figure 2.20 shows the corresponding AIRS data with monthly means overlaid. Figure 2.21 shows the monthly mean data for both the AIRS and WKT data sets. The WKT data set is a subset of the data available from the NOAA Earth System Research Laboratory’s (ESRL) Tall Tower Greenhouse Gas Observing Network[17]. WKT tower CO_2 measurements are made at heights of 30, 122, and 457 meters above ground. The data shown below are the 457m data. The AIRS data presented are all matchups located within 200 km of the WKT tower.

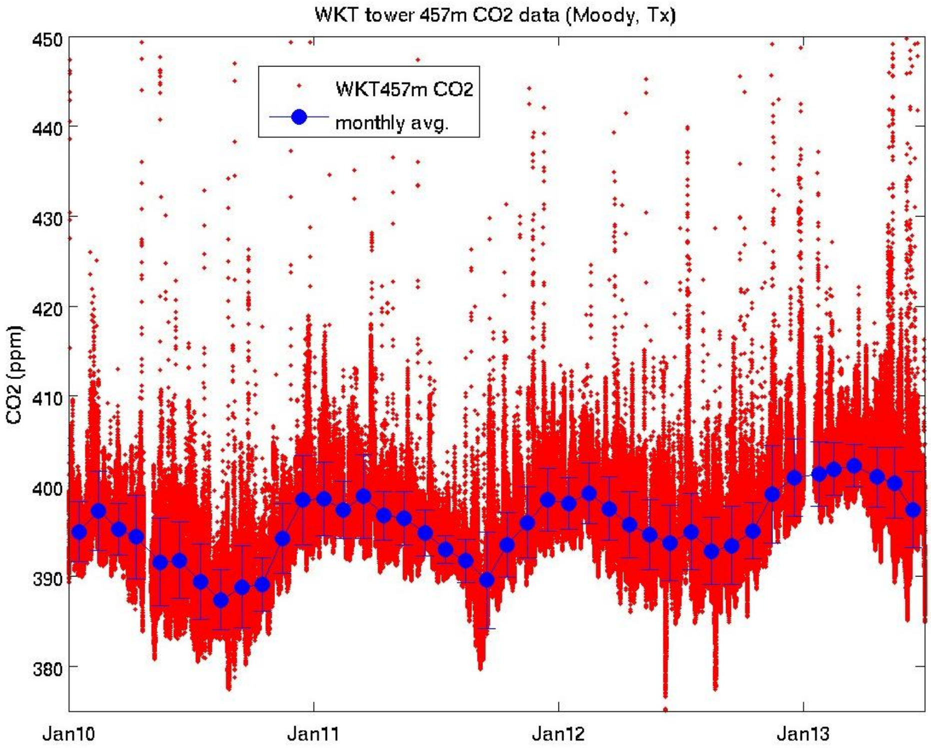

Figure 2.19 WKT (457m) CO_2 data from Moody, Tx, with monthly means overlaid.

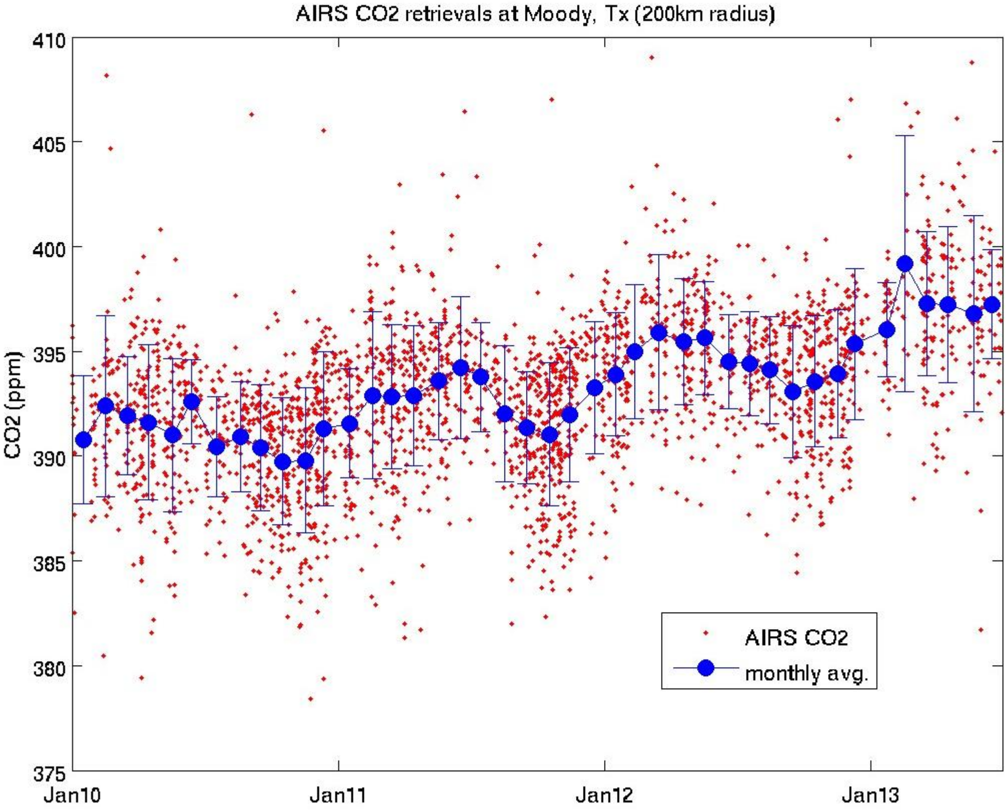

Figure 2.20 AIRS CO_2 data from Moody, Tx (200 km radius), with monthly means.

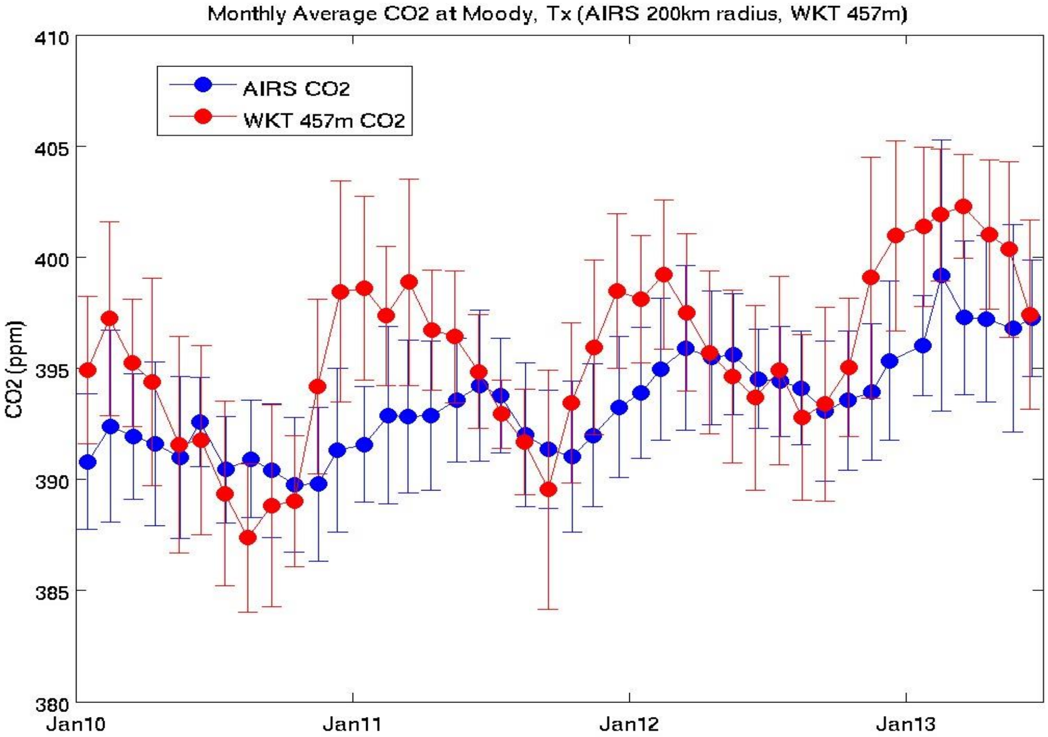

Figure 2.21 shows the monthly mean data for both the AIRS and WKT 457m data sets.

As discussed in section 1.3, Product Validation, there is an evident phase shift in the maxima and minima of the seasonal cycle and a decreased amplitude of the AIRS mid-tropospheric CO_2 as compared to the (near) surface WKT tower data.

2.10 References (Space Based Passive LWIR Measurements)

[1] Susskind, J.; Blaisdell, J.M.; Iredell, L.; and Keita, F. (2010), Improved Temperature Sounding and Quality Control Methodology Using AIRS/AMSU Data; The AIRS Science Team Version 5 Retrieval Algorithm, IEEE Transactions on Geoscience and Remote Sensing, Volume 49, Issue: 3, DOI: 10.1109/TGRS.2010.2070508, 1-25.

[2] Crevoisier C., S. Heilliette, A. Chedin, S. Serrar, R. Armante, N. A. Scott (2004), Midtropospheric CO_2 concentration retrieval from AIRS observations in the tropics, Geophys. Res. Lett., 31, L17106, doi:10.1029/2004GL020141

[3] Engelen, R. J., S. Serrar, and F. Chevallier (2009), Four-dimensional data assimilation of atmospheric CO_2 using AIRS observations, J. Geophys. Res., 114, D03303, doi:10.1029/2008JD010739

[4] Maddy, E. S., C. D. Barnet, M. Goldberg, C. Sweeney, and X. Liu (2008), CO_2 retrievals from the Atmospheric Infrared Sounder: Methodology and validation, J. Geophys. Res., 113, D11301, doi:10.1029/2007JD009402

[5] Strow, L. L., and S. E. Hannon (2008), A 4-year zonal climatology of lower tropospheric CO_2 derived from ocean-only Atmospheric Infrared Sounder observations, J. Geophys. Res., 113, D18302, doi:10.1029/2007JD009713

[6] , M., C. Barnet, E. T. Olsen, L. Chen, and E. Maddy (2005), On the determination of atmospheric minor gases by the method of vanishing partial derivatives with application to CO_2, Geophys. Res. Lett., 32, L22803, doi:10.1029/2005GL024165

[7] Chahine, M. T., L. Chen, P. Dimotakis, X. Jiang, Q. Li, E. T. Olsen, T. Pagano, J. Randerson, and Y. L. Yung (2008), Satellite remote sounding of mid-tropospheric CO_2, Geophys. Res. Lett., 35, L17807, doi:10.1029/2008GL035022

[8] Conway, T.J., P.M. Lang, and K.A. Masarie (2011), Atmospheric Carbon Dioxide Dry Air Mole Fractions from the NOAA ESRL Carbon Cycle, Cooperative Global Air Sampling Network, 1968-2010, Version: 2011-10-14, Path: ftp://ftp.cmdl.noaa.gov/ccg/co2/flask/event/.

[9] Pagano, T. S., Chahine, M. T., Olsen, E. T., "Seven Years of Observations of Mid Tropospheric CO_2 from the Atmospheric Infrared Sounder," Proc. International Astronautical Congress, IAC-10.B1.6.3, Prague, CZ (2010b).

[10] Jiang, X., M. T. Chahine, E. T. Olsen, L. L. Chen, and Y. L. Yung (2010), Interannual variability of mid-tropospheric CO_2 from Atmospheric Infrared Sounder, Geophys. Res. Lett., 37, L13801, doi:10.1029/2010GL042823

[11] Li, K. F., Tian, B., Waliser, D. E., Yung, Y. L., "Tropical mid-tropospheric CO_2 variability driven by the Madden-Julian oscillation," PNAS 107(45), 19171–19175, doi:10.1073/pnas.1008222107, (2010).

[12] Jiang, X., M. T. Chahine, Q. Li, M. Liang, E. T. Olsen, L. L. Chen, J. Wang, and Y. L. Yung (2012), CO_2 semiannual oscillation in the middle troposphere and at the surface, Global Biogeochem. Cycles, 26, GB3006, doi:10.1029/2011GB004118.

[13] Wang, J., X. Jiang, M. T. Chahine, M.-C. Liang, E. T. Olsen, L. L. Chen, S. J. Licata, T. S. Pagano, and Y. L. Yung (2011), The influence of tropospheric biennial oscillation on mid-tropospheric CO_2, Geophys. Res. Lett., 38, L20805, doi:10.1029/2011GL049288.

[14] Bai, W., Ziang, X. Y., Ziang, P., "Temporal and spatial distribution of tropospheric CO_2 over China based on satellite observations," Chinese Science Bulletin 55(31), 3612–3618, doi:10.1007/s11434-010-4182-4, (2011).

[15] Feng, L., Palmer, P. I., Yang, Y., Yantosca, R. M., Kawa, S. R., Paris, J.-D., Matsueda, H., Machida, T., "Evaluating a 3-D transport model of atmospheric CO_2 using ground-based, aircraft, and space-borne data,", Atmospheric Chemistry and Physics 11(6), 2789–2803, Copernicus Gesellschaft MBH, Gottingen; Bahnhofsallee 1e, Gottingen, 37081, Germany, http://atmos-chem-phys.net/11/2789/2011/acp-11-2789-2011.pdf, (2011).

[16] Liu, J., I. Fung, E. Kalnay, J.-S. Kang, E. T. Olsen, and L. Chen (2012), Simultaneous assimilation of AIRS XCO_2 and meteorological observations in a carbon climate model with an ensemble Kalman filter, J. Geophys. Res., 117, D05309, doi:10.1029/2011JD016642.

[17] Andrews, A. E., Kofler, J. D., Trudeau, M. E., Williams, J. C., Neff, D. H., Masarie, K. A., Chao, D. Y., Kitzis, D. R., Novelli, P. C., Zhao, C. L., Dlugokencky, E. J., Lang, P. M., Crotwell, M. J., Fischer, M. L., Parker, M. J., Lee, J. T., Baumann, D. D., Desai, A. R., Stanier, C. O., de Wekker, S. F. J., Wolfe, D. E., Munger, J. W., and Tans, P. P.: CO_2, CO and CH4 measurements from the NOAA Earth System Research Laboratory's Tall Tower Greenhouse Gas Observing Network: instrumentation, uncertainty analysis and recommendations for future high-accuracy greenhouse gas monitoring efforts, Atmos. Meas. Tech. Discuss., 6, 1461-1553, doi:10.5194/amtd-6-1461-2013, 2013.

3 Ground Based Passive LWIR Measurements

3.1 Summary:

This section describes the algorithm used to define the thermodynamic and chemistry retrievals from an upward looking passive infrared Atmospheric Sounder Spectrometer by Infrared Spectral Technology (ASSIST) instrument[1]. The ASSIST instrument was operated during April and May 2013 at the NOAA Carbon Tracker Facility in Moody, TX and McKinney, TX as part of the National Geospatial-Intelligence Agency (NGA) Collaborative Atmospheric Measurement Program (CAMP). The purpose of this research was to determine if the accuracy expressed in terms of mean and standard deviation of the retrieved CO_2 data compares sufficiently with the Carbon Tracker data at Moody and Mona Loa historical measurements to be used for future global GHG measurement tracking which depends on the correlation between these physical and remotely sensed measurements.

The ASSIST radiance spectra are transformed into vertical profiles of temperature, humidity, carbon monoxide, ozone, methane, and nitrous oxide. The vertical mean mixing ratio of carbon dioxide for the Planetary Boundary Layer (PBL) is also retrieved. The entire data set produced for CAMP is available for access through the LRTech web-site http://www.lrtech.ca/. This report presents a comparison between the ASSIST CO_2 PBL mean column mixing ratio (0-2-km) retrievals, obtained for an NGA selection of a subset of days during April and May 2013, with the Moody Texas ~250 meter altitude carbon tracker tower measurements. The mean and standard deviation of both measurements are similar. However, there is poor correlation between the two sets of raw measurements before statistical filtering. This poor correlation between the raw data sets for the two instruments is attributed to the fact that the tower measurements are a point measurement near the surface (~250 meter altitude) whereas the ASSIST measurement is a column concentration measurement for lowest 2-km layer of the atmosphere. Thus, the correlation between these two sets of data depends strongly on the homogeneity of the CO_2 within the surface to 2-km layer of atmosphere. Limited aircraft measurements (see section ###) obtained during this period for the CAMP suggest that the vertical variability of CO_2 is larger than the disagreement between the ASSIST retrievals and the Carbon Tracker Tower measurements, indicating that large ASSIST/Tower discrepancies are due to the vertical inhomogeneity of the carbon dioxide mixing. Small discrepancies can be attributed to random measurement errors and they also contribute to the poor correlation.
However, once an objective Gaussian statistical filter (http://en.wikipedia.org/wiki/Gaussian_filter) is employed to remove differences, which exceed one standard deviation (σ) and one-half a standard deviation (0.5σ) between the two sets of measurements, a good correlation (correlation coefficients of 0.72 and 0.94, for a 1 σ and 0.5 σ filter, respectively) is obtained for the two sets of observations.

3.2 **Background**

3.2.1 Radiance Sensitivity to Atmospheric Profiles:

The radiance spectra measured with the ASSIST instrument are sensitive to atmospheric profile features caused by the absorption and re-emission of the radiation emitted by atmospheric gases. Figure 3.1 shows the regions of the spectrum measured by ASSIST that are optically active to the trace gases retrieved.

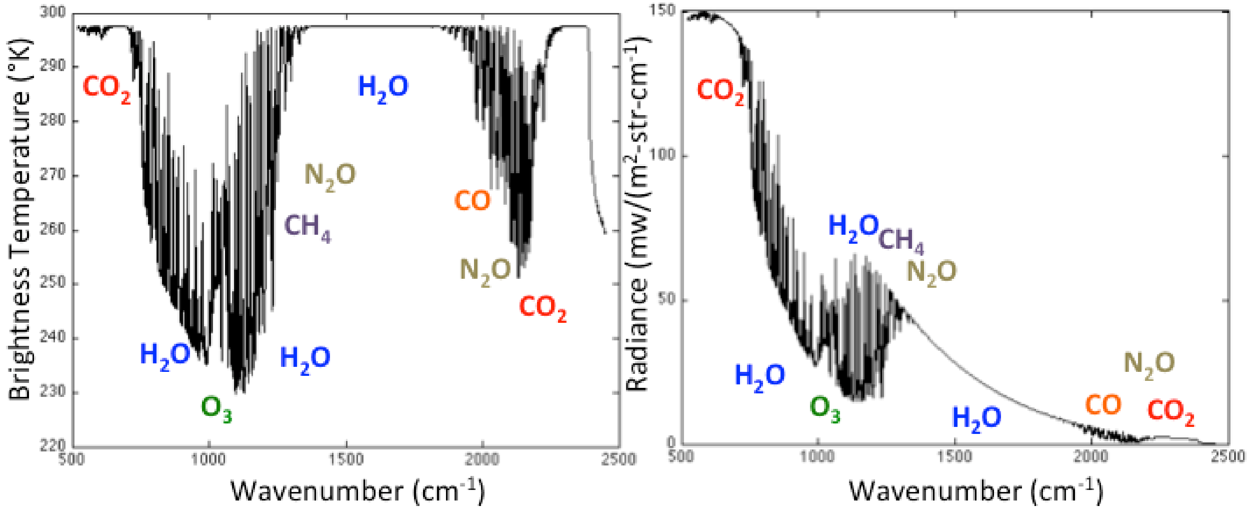

Figure 3.1 ASSIST brightness temperature (Left) and radiance spectra (Right) showing the spectral regions where specific gases are optically active.

With the exception of the opaque region from about 1400 cm-1 to 1700 cm-1, most of the infrared spectrum observed with the ASSIST instrument provides useful information on the trace gas structure of the atmosphere. Additional insight into the column density structure of these gases in the atmosphere can be gleaned from Figure 3.1 right, which plots the radiance

$$J_{ij} = (dR_i / dQ_j) \tag{1}$$

sensitivity to trace gas profile variations in terms of the change in radiance with respect to temperature and gaseous mixing ratio as a function of altitude[2]. The Jacobian, J, is defined in equation (1), where R is the radiance, Q is temperature or gaseous mixing ratio and the subscripts i and j refer to spectral wavenumber and atmospheric level, respectively. It can be seen from Figure 3.1 that the altitude region of the highest sensitivity of the ASSIST radiances to optically active gases resides in the Planetary Boundary Layer (PBL), which occupies the lowest 2-km of atmosphere. However, ozone, methane, and nitrous oxide also provide contributions from higher altitude layers in the stratosphere as well. Carbon dioxide sensitivity is seen to be largely restricted to the lowest 2 km of atmosphere.

3.3 Optimal Estimation Retrieval

3.3.1 Retrieval of Atmospheric Profiles from ASSIST Radiance Measurements:

The retrieval of atmospheric profiles from ASSIST radiance measurements is performed using a physically based optimal estimation[3] (see: http://en.wikipedia.org/wiki/Optimal_estimation) procedure followed by a direct simultaneous numerical inversion of the radiative transfer equation using the optimal estimation profile as the initial condition and constraint for the matrix inversion process[4]. Specifically, the optimal estimation solution is defined in equation (2) as

$$q_r = q_o + (r_m - r_o)C \qquad (2)$$

where q is a vector containing the atmospheric profile quantities, r is a vector containing the radiance spectrum and C is the solution matrix, which is comprised of the statistical covariance of radiance spectra, profile quantities, and radiance observation error about the statistical sample mean or initial guess condition. The subscripts r, o, and m refer to the retrieval, initial condition or mean of the profiles comprising the statistical sample utilized, and the measurement, respectively. The solution matrix, C, is computed using equation (3)

$$C = R'^T R' + \lambda E^T E^{-1} R'^T Q' \qquad (3)$$

where Q and R are climatological matrices whose elements consist of a climatological ensemble of atmospheric profile values and ASSIST spectral radiances calculated using a Line-By-Line Radiative Transfer Model (LBLRTM). The prime symbol indicates the deviation from the climatological mean profile or initial profile conditions, q_o and r_o. The error covariance matrix, E^TE, is diagonal assuming random spectral measurement noise with the Lagrangian multiplier, λ, used to stabilize the matrix inversion.

The statistical sample of atmospheric profiles used to generate the matrix C is generally determined from a global set of climatological profiles generated by the NOAA Real-time Air Quality Modeling System (RAQMs)[5]. However, for the CAMP study, a subsample of atmospheric profiles for the Texas and Oklahoma region for the months of April and May, 2010 were used as the statistical data base.

After the statistical optimal estimation profile is derived, two additional physical steps, described below, are utilized to insure that the final profiles for atmospheric temperature, water vapor, and all the trace gases satisfy ASSIST radiance measurements to within their measurements error.

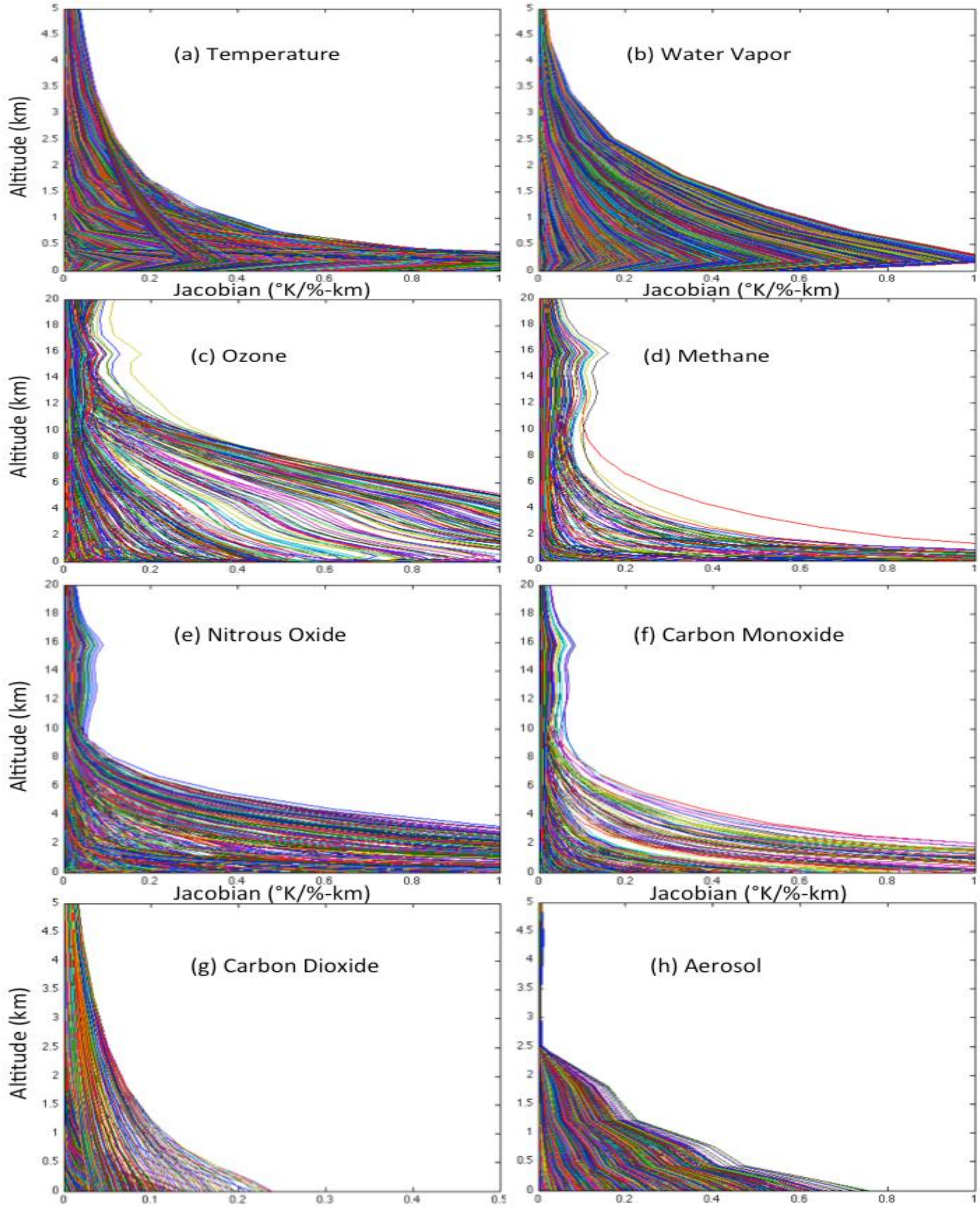

Figure 3.2 ASSIST radiance Jacobians (i.e., Sensitivity functions) for temperature, water vapor, ozone, methane, nitrous oxide, carbon monoxide, carbon dioxide, and aerosol.

3.3.2 Statistical Bias Correction:

The statistical bias correction is a technique to alleviate the vertical feature bias of the retrieval to the mean profile of the statistical ensemble used to derive the C matrix defined by equation 3 . Because of the limited vertical resolving power of the radiance measurements, as shown in Figure 3.2, the vertical structure of the retrieved profile will bias towards the mean of the statistical ensemble of soundings used to produce the C-matrix. This bias can be eliminated by using a much better estimate of the actual vertical structure characteristics of the profile for any particular location and time that is provided by a real-time dynamic forecast model. The procedure, as employed here, is to obtain the forecast profiles using the real-time hourly interval 13.5 km resolution NOAA RApid Update Profile (RAP) forecast for atmospheric temperature and water vapor and the 6-hour interval 111-km resolution RAQMS profiles for the trace gas profile estimates. The bias error produced by the climatological sample used in the optimal estimation procedure is determined by producing another retrieval of the atmospheric profiles from ASSIST radiances calculated from these profiles using the LBLRTM. Since in this simulated radiance condition, the so-called “Truth” is known, since the simulated radiances were produced from it, the statistically induced bias is merely the difference between the simulated radiance retrieval and the forecast profiles used to simulate them. This bias error profile can then be subtracted from the original optimal estimation profiles obtained from the actual ASSIST radiance measurements.

An example of results obtained with and without the bias correction for ASSIST measurements made at McKinney Texas during the 2012 CAMP are shown in Figures 3.3, 3.4 and 3.5. It can be seen from these Figures that the ASSIST bias corrected results possess the most detailed vertical structure and as such presumably represent the best estimate of the actual temperature and gas structure for this altitude region. The white stripes in these Figures represent voids due to interference of the ASSIST radiometric signal produced by clouds, the retrieval being obtained below, but not above, each respective cloud base level.

Several additional references to papers reviewing the methods of retrieving atmospheric profiles from interferometer spectrometer measurements[6-8] are provided in the reference section of this report.

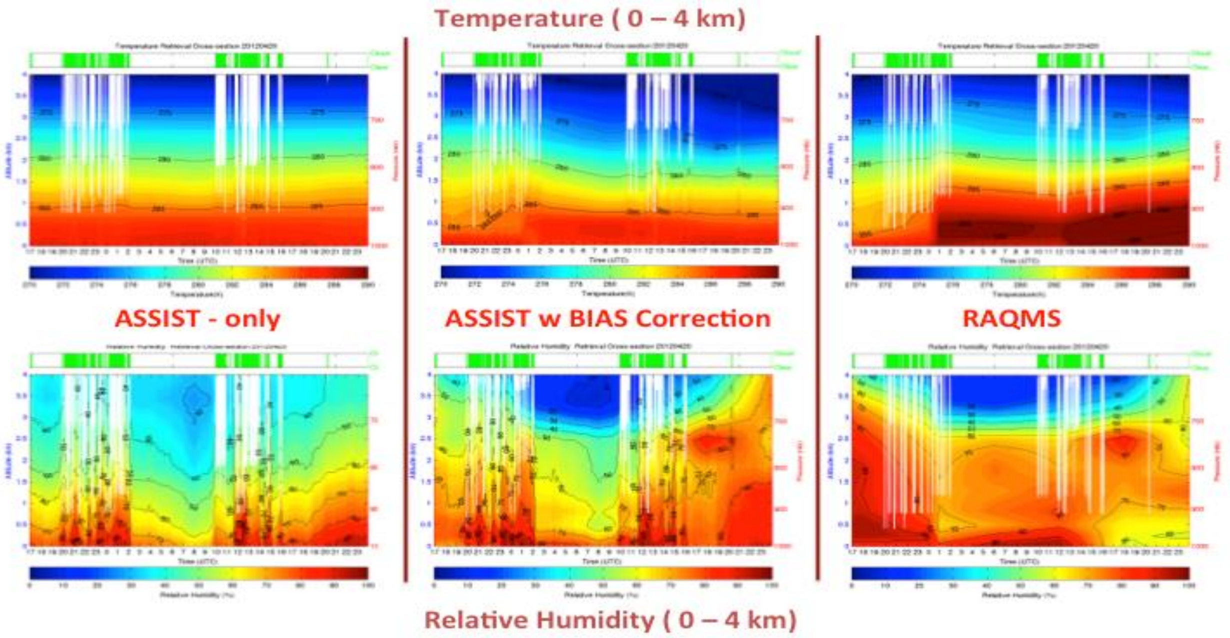

Figure 3.3 ASSIST temperature (top) and relative humidity (bottom) retrieval time-cross-section for the period April 19 (17 UTC) to April 21 (00 UTC), 2012 for the surface to 4-km layer of the atmosphere over McKinney Texas. The left hand panels show the retrieval results obtained solely from the optimal estimations algorithm whereas the middle panel shows the result after bias correction. The right hand panel shows the RAQMS analysis.

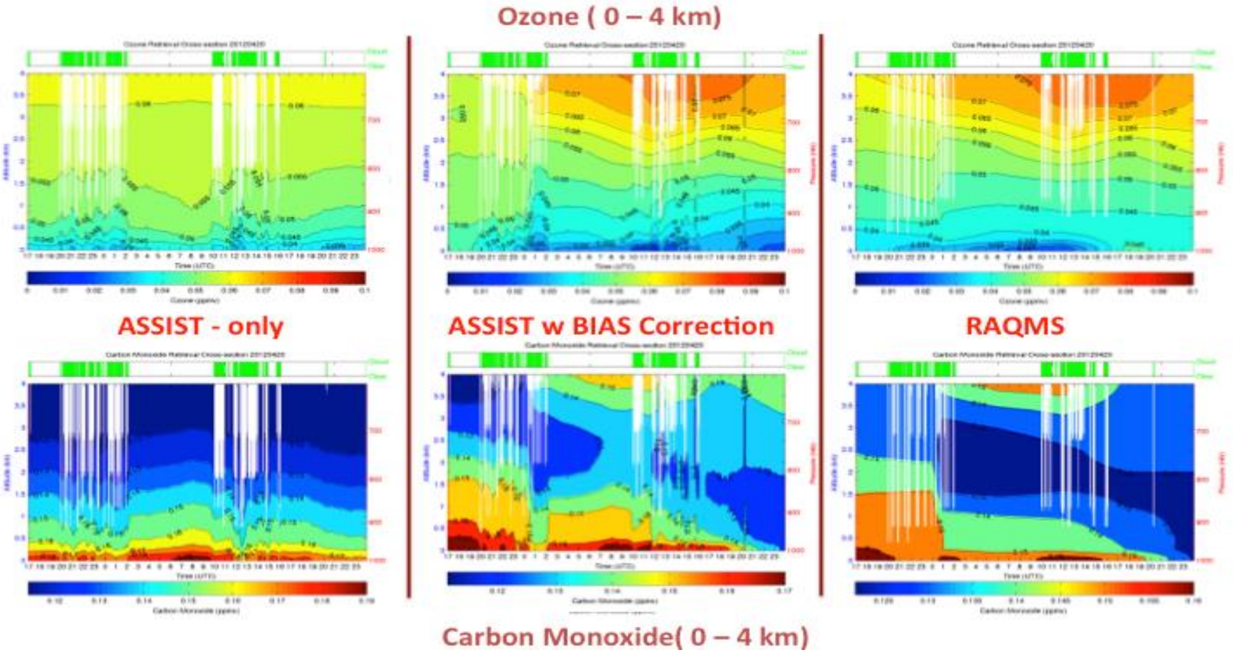

Figure 3.4 Same as Figure 3 but for ozone (top) and carbon monoxide (bottom)

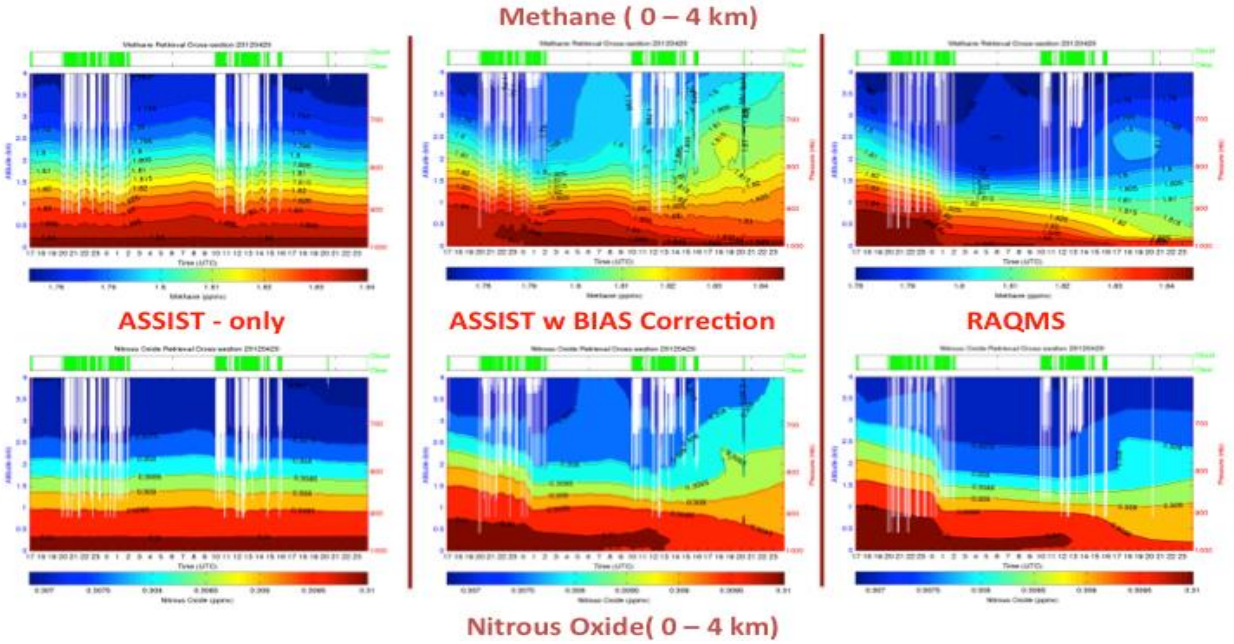

Figure 3.5 Same as Figure 3 but for methane (top) and nitrous oxide (bottom)

3.4 Physical Retrieval

3.4.1 Matrix Inverse Solution.

The last step of the retrieval process is to apply a direct mathematical inverse solution so as to guarantee that the radiances calculated from the final profile retrievals satisfy the radiance measurements to within their experimental error. This inverse solution is actually an inversion of equation (1) where the Jacobians for temperature and all of the trace gases are generated by taking the bias corrected optimal estimation profiles and scaling them by factors of 1.5 and 0.75 to estimate the Jacobian about that profile. Thus, in this case the final matrix inverse solution is merely the bias corrected optimal estimation profiles scaled by those factors required to produce agreement between the observed and calculated radiances. Mathematically, the solution is

$$f_q = 1 + (J^T J + \lambda E^T E)^{-1} J^T (r_m - r_o)/r_o \qquad (4)$$

where f_q is a vector of profile scale factors, J is the Jacobian matrix and r_m is the vector of measured spectral radiances and r_o the vector of calculated radiances corresponding to the bias corrected optimal estimation retrieval. Once f_q is determined the final temperature and mixing ratio retrieved values are given by

$$q(p) = f_q \, q_o(p) \qquad (5)$$

It is noted that the matrix inverse step of the retrieval process is only applied to the average of all clear sky radiance measurements obtained within each 100 minute time interval of the ASSIST radiance measurements. The differences between the clear sky physical matrix inverse retrieval and the bias corrected optimal estimation retrieval obtained at the average time of the clear sky radiances are then time interpolated to provide physical retrieval corrections for the optimal estimation retrievals for every ASSIST observation.

Figure 3.6 shows the flow diagram for the CAMP sounding retrieval algorithm. Basically, a statistical database, based on the output of the Real-time Air Quality Modeling System (RAQMS) and radiances computed for eleven different cloud base altitude classes, one of them being clear, is used within a statistical regression retrieval algorithm to provide eleven different initial estimates of the thermodynamic and trace gas profiles, dependent upon cloud base altitude. For each retrieval, an improved estimate is obtained by performing another retrieval for each cloud base class using a radiance calculated from a RAP plus RAQMS background profile. The difference between the synthetic radiance regression retrieval and the background profile used to calculate the synthetic radiance spectrum used for the retrieval is assumed to be the retrieval error induced by the statistics employed (i.e., the “Statistical Bias Correction” referred to above). This error is removed from each of the eleven real ASSIST data regression retrievals. The final optimal estimation ASSIST retrieval is then obtained by choosing that one of eleven profiles which agrees best, in an RMSD sense, with the independent RAP plus RAQMS profile.

Finally, the bias corrected optimal estimation retrieval is used as the background profile for the direct physical matrix inverse solution of profile scale factors (equation 4) required to make the final solution radiatively consistent with the measured radiances. As noted above, only clear sky measurements averaged over a 100 minute time intervals are used to determine these scale factors, which are subsequently linearly interpolated across cloudy periods to provide a quasi-continuous final solution for the entire time period of measurement.

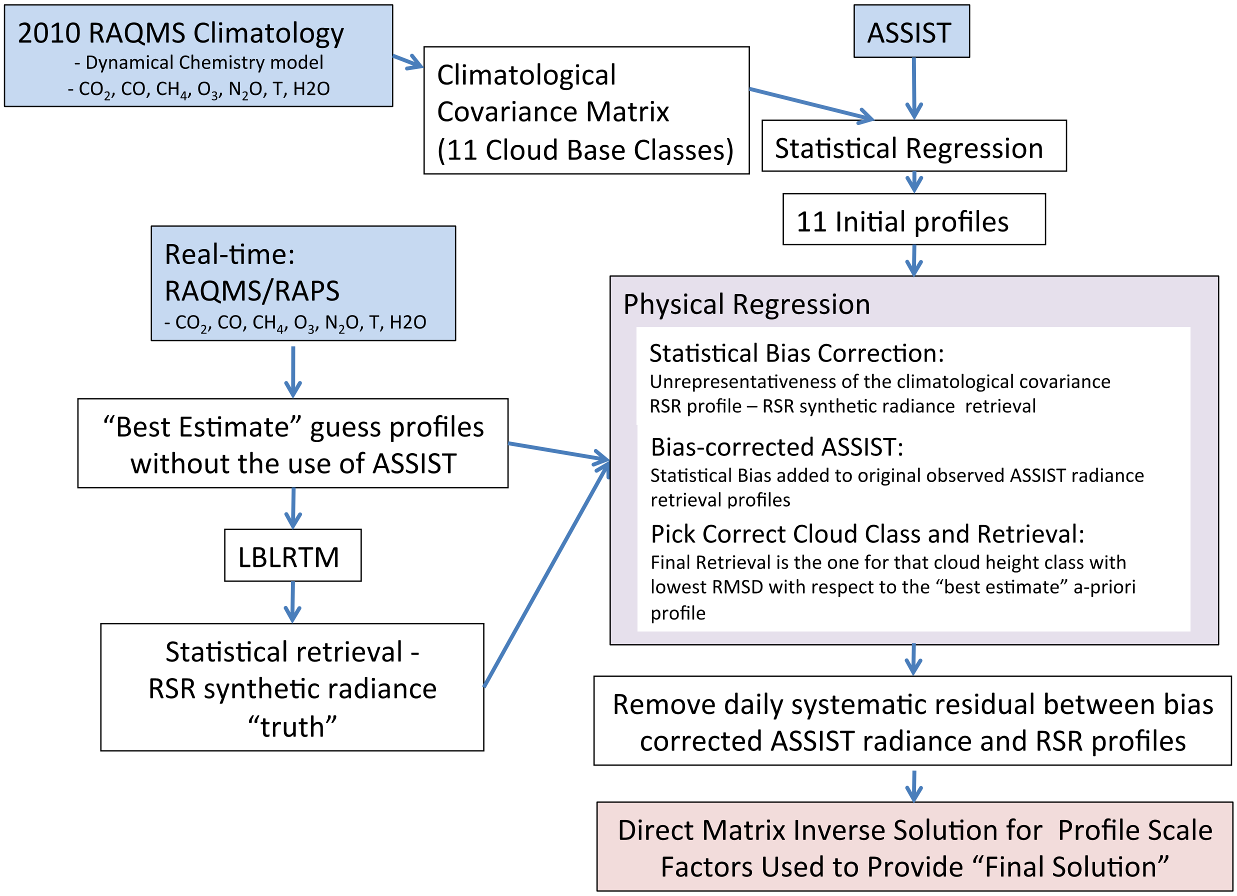

Figure 3.6 Flow diagram for the ALOSE-5 sounding retrieval algorithm.

3.5 Temperature-Relative Humidity, Trace Gas Retrieval Results April 19, 2013

Figures 3.7 and 3.8 show the temperature, relative humidity, and trace gas retrieval results for April 19, 2013, which was one of the clearest days of all the CAMP study days. As can be seen, the time variation of the atmospheric structure for all the retrieved variables is very coherent, indicating little noise in the retrieved products. Also, the diurnal variation of the retrieved atmospheric temperature and relative humidity structure shows the expected variations within the PBL. Minimum temperature and maximum relative humidity occur during the night-time early morning hours of 8 – 14 UTC whereas a maximum temperature and minimum relative humidity occurs during the day-time late afternoon (20 – 22 UTC) period of this clear spring day. It is also interesting to note from Figure 3.8 that the mixing ratio minimum of the pollutant gases, carbon dioxide and ozone, also occur during the nighttime early morning hours (8 – 14 UTC) when there is a minimum of anthropogenic sources of these pollutants.

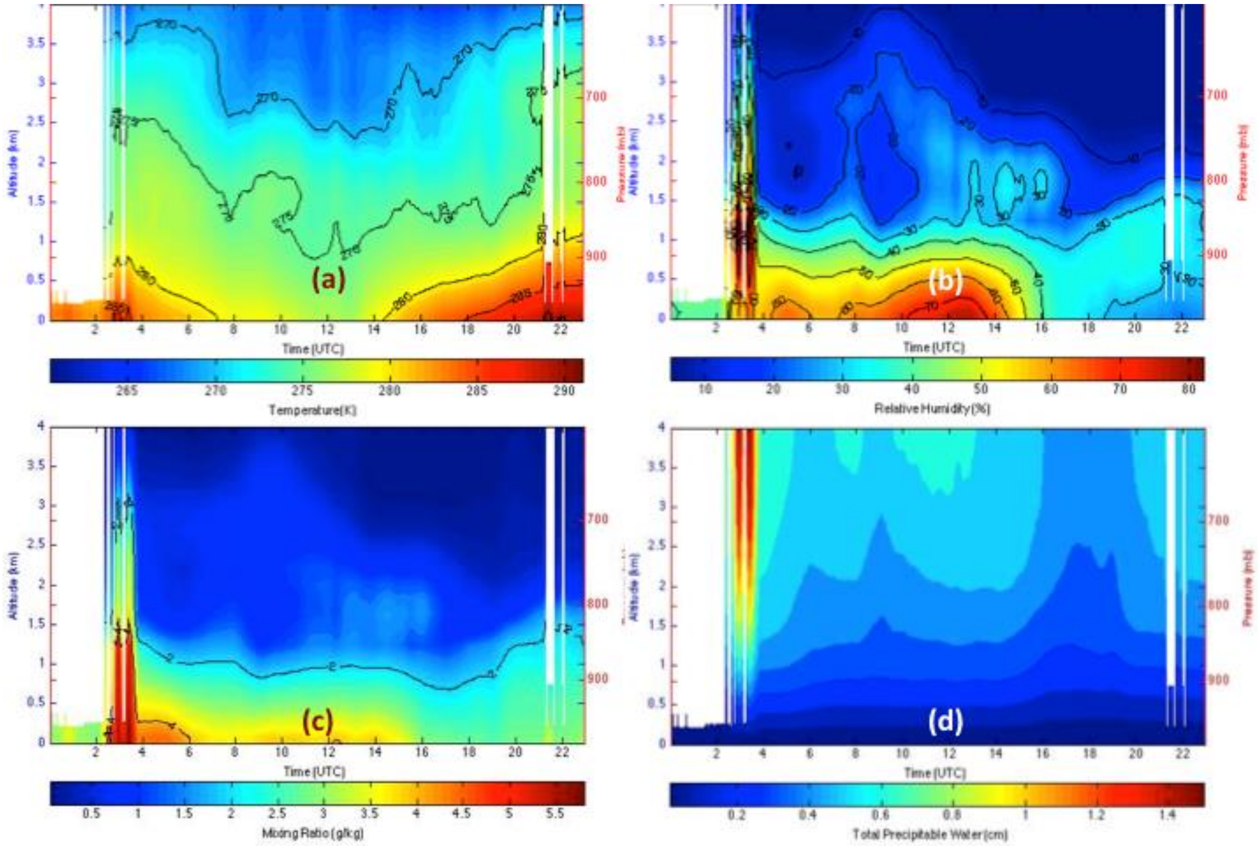

Figure 3.7 ASSIST temperature (top left), relative humidity (top right), water vapor mixing ratio (bottom left), and total precipiTable water (bottom right) retrieval time cross-sections for April 19, 2013 for the surface to 4-km layer of the atmosphere over Moody Texas.

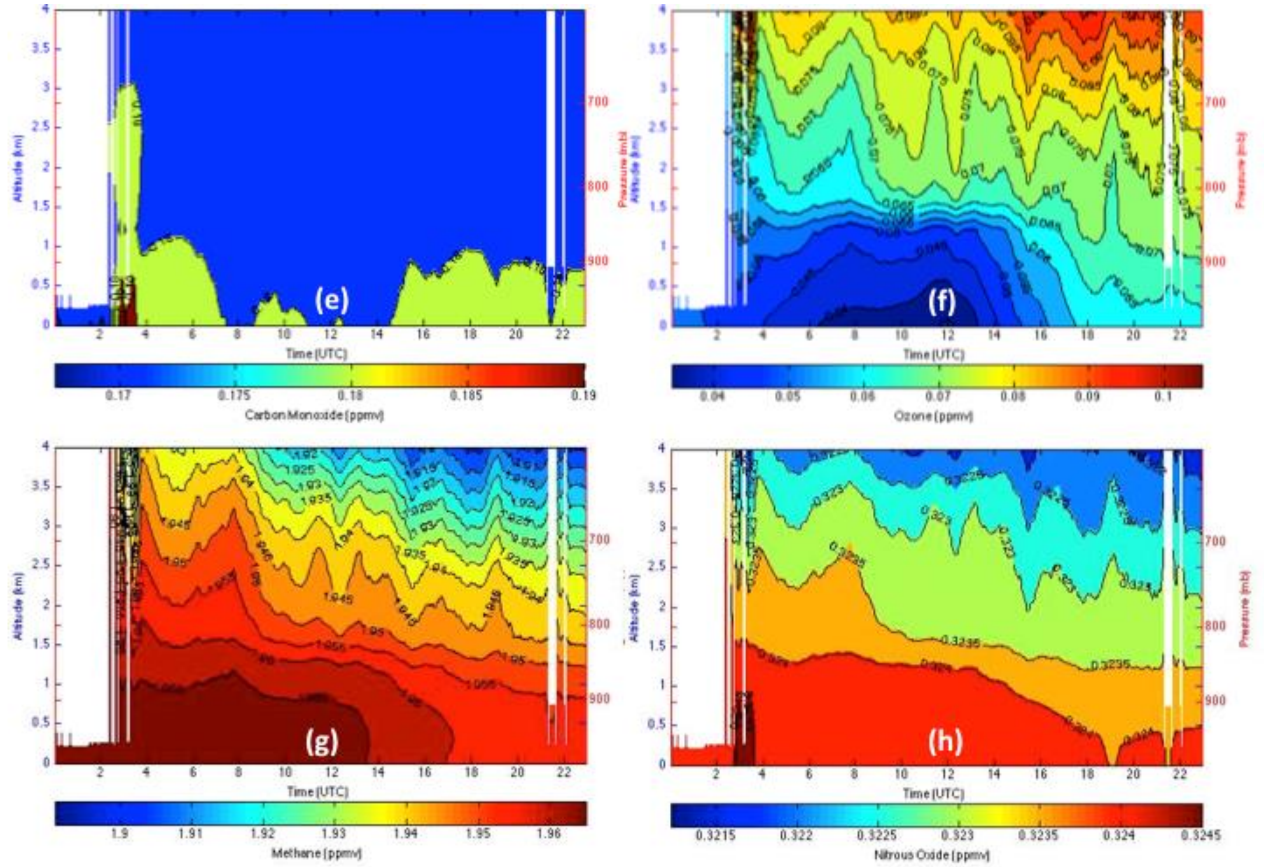

Figure 3.8 ASSIST carbon monoxide(top left), ozone (top right), methane (bottom left), and nitrous oxide (bottom right) retrieval time cross-sections for April 19, 2013 for the surface to 4-km layer of the atmosphere over Moody Texas.

3.6 CO_2 Concentration Retrieval Results for Planetary Boundary Layer (PBL) April 19, 2013

Figure 3.9 shows the results obtained for the CO_2 concentration retrieved for the PBL from the ASSIST data. Also shown are the measurements from the carbon tracker tower and from flask samples of the atmospheric carbon dioxide concentration at altitudes of 1000, 2500, 5000, 7500, and 10,000 feet (i.e., 300, 760, 1620, 2290, and 3000 meters) altitude. As can be seen, there is excellent agreement between the ASSIST and the carbon tracker tower measurements during the first half of the day but then a discrepancy develops during the afternoon hours (i.e., after 17 UTC, or 12 noon local time). However, the ASSIST measurements are in relatively good agreement with the aircraft flask measurements during this time period, indicating that the afternoon discrepancy between the ASSIST retrievals and the carbon tracker tower data is due to the vertical inhomogeneity of the carbon dioxide above Moody Texas. Thus, the correspondence between the ASSIST data and the carbon tracker data depends greatly on the vertical distribution of CO_2 mixing ratio.

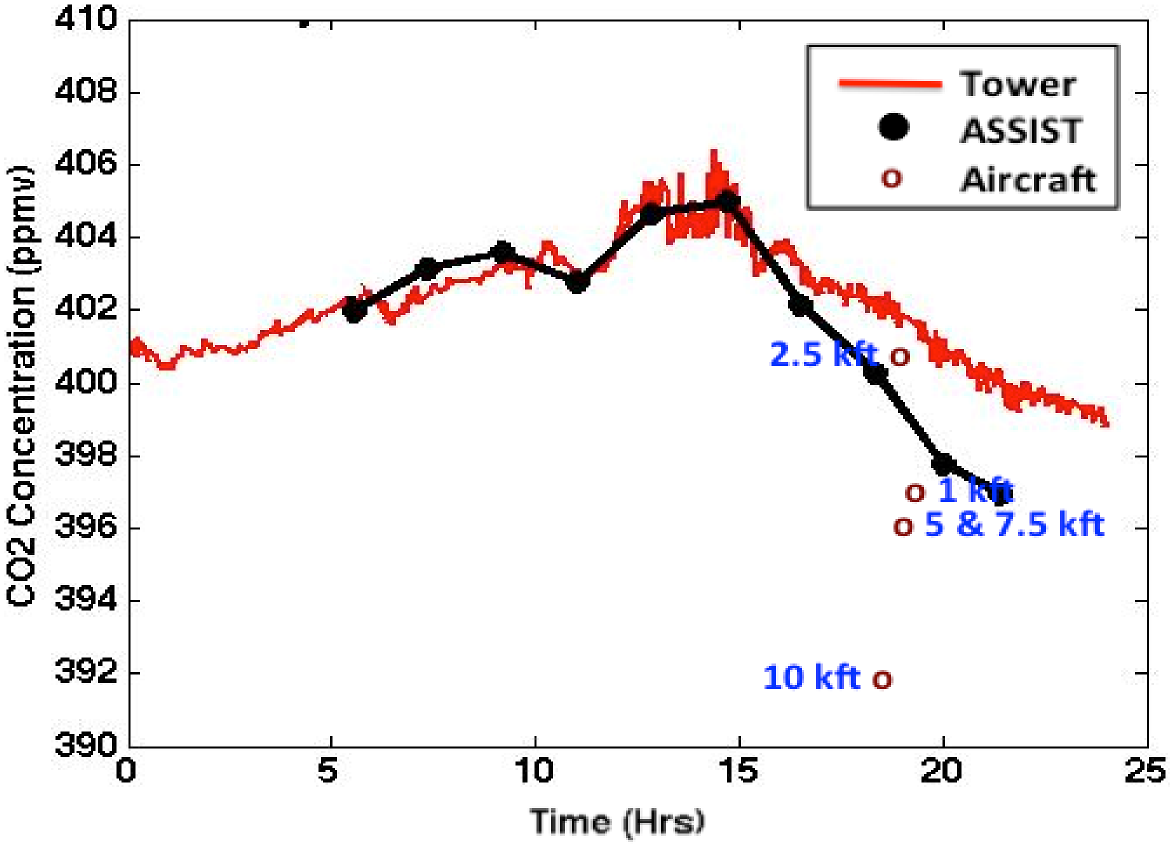

Figure 3.9 ASSIST carbon dioxide (black dots), carbon tracker measurements (red curve), and aircraft measurements (open red circles) for the atmospheric column over Moody Texas during for April 19, 2013.

3.7 CAMP April and May ASSIST Vs. Carbon Tracker Results April-May 2013

3.7.1 Daily Comparisons:

Results for eleven days during April 2013 (i.e., 16, 18 ,19, 20, 21, 22, 23, 24, 27, 28, and 30 April 2013) and thirteen days during May 2013 (i.e., 1, 3, 6, 8, 11, 12, 16, 17, 18, 20, 22, 26, and 27 May 2013) were selected by NGA for ASSIST CO_2 retrievals and comparison with the carbon tracker tower data. Figures 3.10 and 3.11 show time sections of the clear sky 100 minute average ASSIST CO_2 concentration retrievals (dots) overlaying the 30 second interval carbon tracker tower data for April and May, respectively. One can see that there is generally good agreement for many of the observations but poor agreement on other occasions. Fine time scale variations resolved by the 30 second interval tower data cannot be captured by the 100 minute interval clear sky ASSIST retrievals.

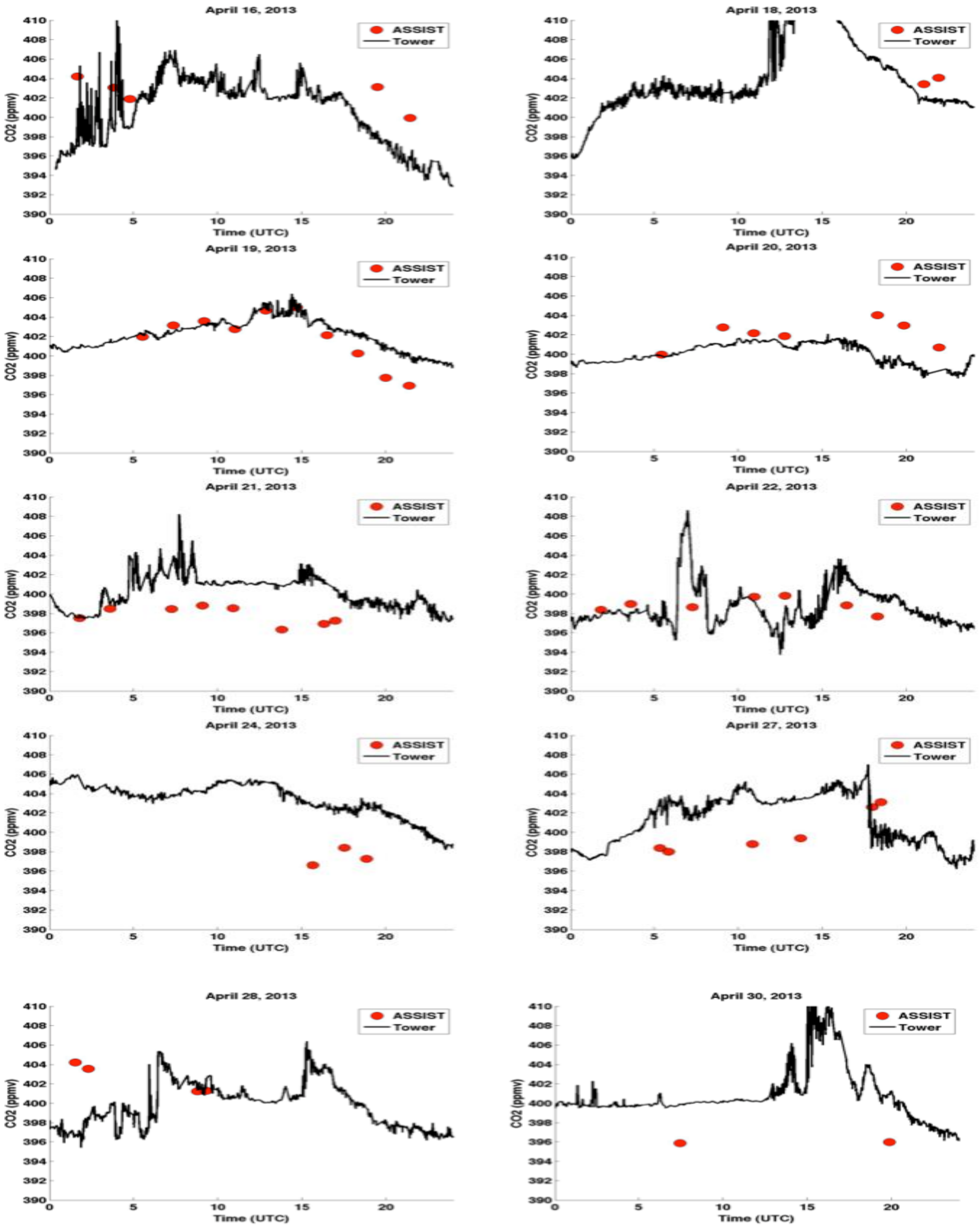

Figure 3.10 100 minute mean clear sky ASSIST surface to 2 km layer carbon dioxide (blue dots) overlaying 30 second interval carbon tracker measurements at ~250 meters (solid line) for the atmospheric column over Moody Texas for NGA selected days during April, 2013.

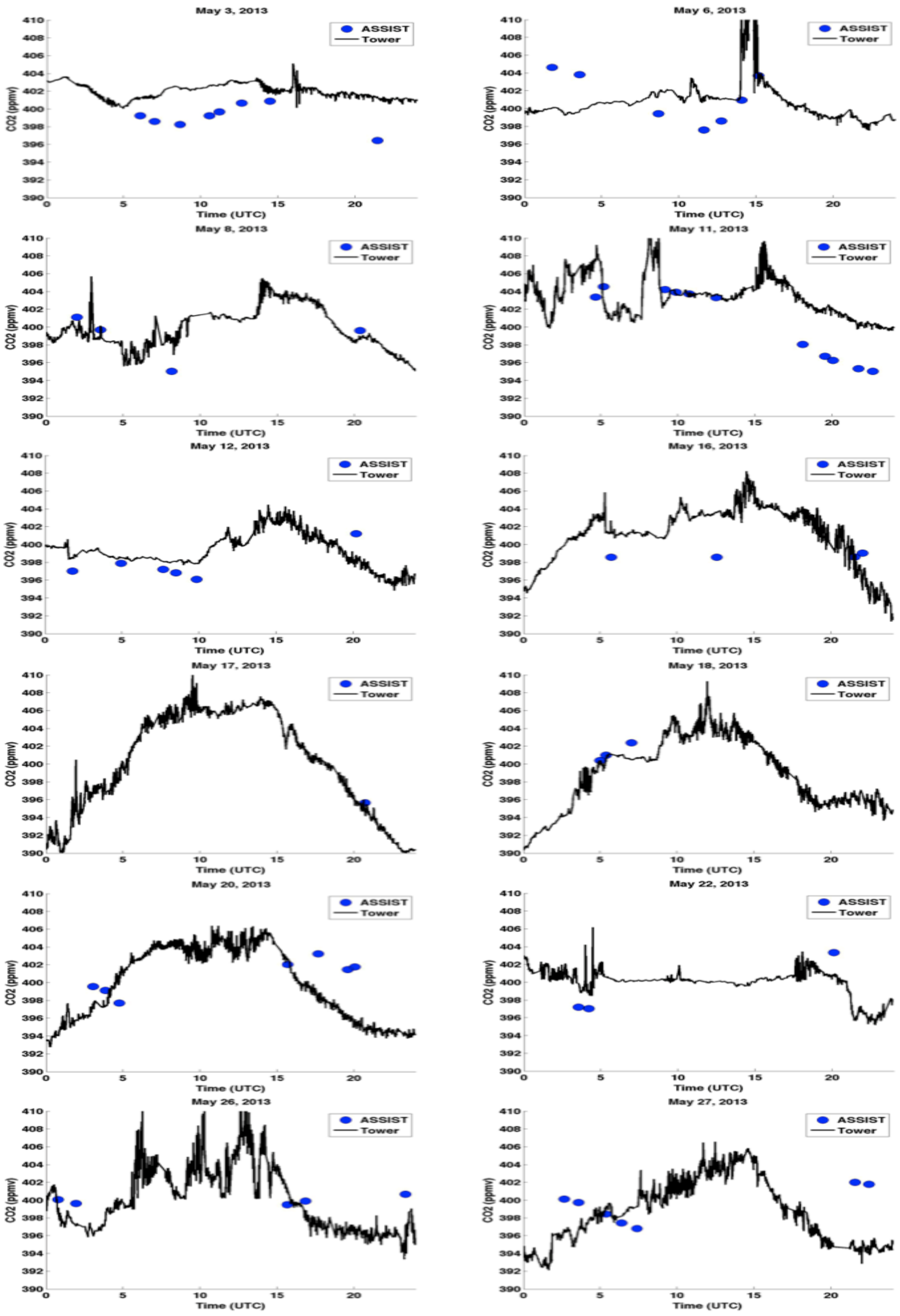
May 3, 2013
May 6, 2013
May 8, 2013
May 11, 2013
May 12, 2013
May 16, 2013
May 17, 2013
May 18, 2013
May 20, 2013
May 22, 2013
May 26, 2013
May 27, 2013
ASSIST
Tower
CO2 (ppmv)
Time (UTC)
390
392
394
396
398
400
402
404
406
408
410
0
5
10
15
20

Figure 3.11 100 minute mean clear sky ASSIST surface to 2 km layer carbon dioxide (blue dots) overlaying 30 second interval carbon tracker measurements at ~250 meters (solid line) for the atmospheric column over Moody Texas for NGA selected days during May, 2013.

3.7.2 Statistical Results

Figure 3.12 shows scatter plots of the ASSIST and carbon tracker tower data for April and May, 2013 obtained before and after statistical filtering. For these comparisons the 30 second tower data was averaged to the 100 minute time intervals of the ASSIST data. One sigma and one half sigma standard deviation statistical filters were employed to exclude outliers due to random differences produced from vertical non homogeneities of the CO_2 mixing and to random measurement errors in the ASSIST and tower data.

As can be seen from Figure 3.12, there is little correlation between the two sets of raw measurements before statistical filtering of the data. This poor correlation between the raw data from these two instruments is attributed to the fact that the tower measurements are a point measurement near the surface (~250 meter altitude) whereas the ASSIST measurement is a column average mixing ratio from the surface to ~ 2000 meters in altitude. Nevertheless, after applying a Gaussian statistical filter (http://en.wikipedia.org/wiki/Gaussian_filter) to the data, the correlation between the two sets of measurements is quite good considering the very different nature of the two measurements (i.e., the tower being a point measurement and the ASSIST being a column average). The mean values of the two sets of data are 400.23 ppmv and 400.75 ppmv for the ASSIST and tower data, respectively. Also, the standard deviations of the two sets of data compare favorably being 2.3 ppmv and 2.2 ppmv for the ASSIST and tower data, respectively. It is important to note that the Gaussian statistical filter is a purely objective one so that residual mismatch noise will remain even after the filtering is performed. Statistical filtering would only improve the correlation of the two data sets if there were a true physically driven relation between the two sets of measurements. If the two sets of measurements were totally random relative to one another, the correlation between the two data sets would be zero and there would be no improvement obtained by employing the statistical filter.

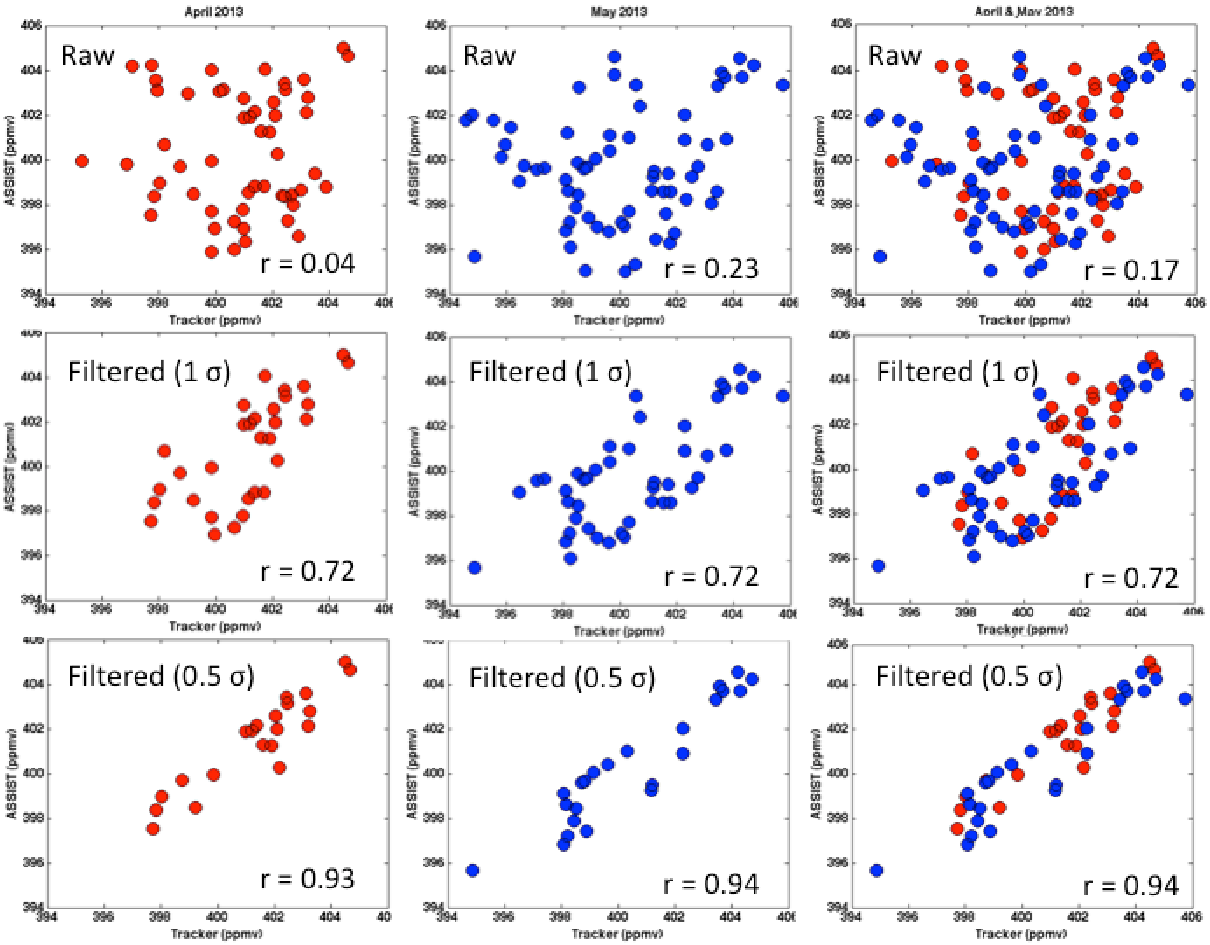

Figure 3.12 Scatter between 100-minute average clear sky ASSIST carbon dioxide (blue dots) overlaying 30-second interval carbon tracker measurements for the atmospheric column over Moody Texas for selected days during May, 2013. Results are shown for the raw unfiltered measurements (top panels) and for employing a statistical filter using 1 sigma (middle row) and ½ sigma (lower panels) filtering criteria, respectively.

3.8 Summary and Conclusions

This algorithm used to define the thermodynamic and chemistry retrievals from an upward looking passive infrared Atmospheric Sounder Spectrometer by Infrared Spectral Technology (ASSIST) instrument operated at the NOAA Carbon Tracker Facility in Moody, TX and McKinney, TX as part of the National Geospatial-Intelligence Agency (NGA) Collaborative Atmospheric Measurement Program (CAMP) is described. The ASSIST radiance spectra are transformed into vertical profiles of temperature, humidity, carbon monoxide, ozone, methane, and nitrous oxide. The vertical mean mixing ratio of carbon dioxide for the Planetary Boundary Layer (PBL) is also retrieved. A comparison between the ASSIST CO_2 PBL mean column mixing ratio (0-2-km) retrievals, obtained for an NGA selection of a subset of days during April and May 2013, with the Moody Texas ~250 meter altitude carbon tracker tower measurements was presented. The mean and standard deviation of both measurements are shown to be similar. However, a poor correlation between the two sets of raw measurements resulted before statistical filtering. This poor correlation between the raw data sets for the two instruments is attributed to the fact that the tower measurements are a point measurement near the surface (~250 meter altitude) whereas the ASSIST measurement is a column concentration measurement for lowest 2-km layer of the atmosphere. Thus, the correlation between these two sets of data depends strongly on the homogeneity of the CO_2 within the surface to 2-km layer of atmosphere. Limited aircraft measurements obtained during this period for the CAMP suggest that the vertical variability of CO_2 is larger than the disagreement between the ASSIST retrievals and the Carbon Tracker Tower measurements, indicating that large ASSIST/Tower discrepancies are due to the vertical inhomogeneity of the carbon dioxide mixing. However, once an objective Gaussian statistical filter (http://en.wikipedia.org/wiki/Gaussian_filter) is employed to remove differences, which exceed one standard deviation (σ) and one-half a standard deviation (0.5σ) between the two sets of measurements, a good correlation (correlation coefficients of 0.72 and 0.94, for a 1 σ and 0.5 σ filter, respectively) is obtained for the two sets of observations. These excellent correlations between the PBL column ASSIST retrievals and the near surface point observations from the carbon tracker tower were obtained after applying an objective statistical filtering of the data. This result indicates that both sets of measurements are consistent and accurate for use in determining the CO_2 concentration for the partial volume of atmosphere being measured by each device.

3.9 References (Ground Based Passive LWIR Measurements):

[1]Rochette, Luc, William L. Smith, Michael Howard, Tim Bratcher, "ASSIST, Atmospheric Sounder Spectrometer for Infrared Spectral Technology: latest development and improvement in the atmospheric sounding technology", in Imaging Spectrometry XIV, Sylvia S. Shen; Paul E. Lewis, Editors, Proceedings of SPIE Vol. 7457 (SPIE, Bellingham, WA 2009)

[2]Smith, W.L, W.F. Feltz, R.O. Knuteson, H.E. Revercomb, H.B. Howell, and H.M. Woolf, 1999: The retrieval of planetary boundary layer structure using ground-based infrared spectral radiance measurements. *J. Atmos. Oceanic Technol.*, 16, 323-333.

[3]Clive D. Rodgers (1976). "Retrieval of Atmospheric Temperature and Composition From Remote Measurements of Thermal Radiation". *Reviews of Geophysics and Space Physics* **14** (4). p. 609.

[4]Smith, W. L., L. Rochette, R. B. Pierce, "Determination of Greenhouse Gas Profiles From Ground based Infrared Radiance Measurements", SPIE 2012 Optics and Photonics, 12-16 August, 2012, Dan Diego CA.

[5]Pierce, R. B.; Al-Saadi, J. A.; Schaack, T.; Lenzen, A.; Zapotocny, T.; Johnson, D.; Kittaka, C.; Buker, M.; Hitchman, M. H.; Tripoli, G.; Fairlie, T. D.; Olson, J. R.; Natarajan, M.; Crawford, J.; Fishman, J.; Avery, M.; Browell, E.; Crielson, J.; Kondo, Y. and Sandholm, S. T. Regional Air Quality Modeling System (RAQMS) predictions of the tropospheric ozone budget over east Asia. Journal of Geophysical Research, Volume 108, 2003

[6]Feltz, W. F., H. B. Howell, R. O. Knuteson, H. M. Woolf, and H E. Revercomb, 2003: Near Continuous Profiling of Temperature, Moisture, and Atmospheric Stability using the Atmospheric Emitted Radiance Interferometer (AERI). *J. Appl. Meteor.*, 42, 584-597.

[7]Smith, W. L. Sr.; Revercomb, H.; Bingham, G.; Larar, A.; Huang, H.; Zhou, D.; Li, J.; Liu, X. and

Kireev, S. Evolution, current capabilities, and future advances in satellite nadir viewing ultra-spectral IR sounding of the lower atmosphere. Atmospheric Chemistry and Physics, Volume 9, Issue 15, 2009, pp.5563-5574.

[8] Smith, William L. Sr.; Weisz, Elisabeth; Kireev, Stanislav V.; Zhou, Daniel K.; Li, Zhenglong and Borbas, Eva E. Dual-regression retrieval algorithm for real-time processing of satellite ultraspectral radiances. Journal of Applied Meteorology and Climatology, Volume 51, Issue 8, 2012, 1455–1476.

4 Aircraft Support: Instrumentation, Sonde Calibration-Collection, CO2-Water vapor/humidity Collection and Measurement Procedure

4.1 Aircraft Support Overview

The goal of this support activity was to provide a statistically significant amount of cost effective calibrated concurrent Sonde releases and aircraft measurements of CO2 and water vapor for the PBL up to the reasonable operational safety limits of available operationally cost effective aircraft. Calibration procedures for Sonde releases have been developed for both analog and digital Sondes as well as their cross calibrated usage. Collection and measurement procedures for CO2 and water vapor as a function of altitude up to 10,000.00 ft. were also developed and validated. These procedures are documented in this section. Note: Although all procedures were developed and validated during the CAMP activity; statistically significant numbers of concurrent Sonde releases were not achieved due to catastrophic failure of the program's only transceiver, statistically significant aircraft measurements of CO_2 and water vapor were not obtained due to the significant time required for development, modeling, and validation. With this said concurrent Sonde and aircraft measurement data was collected referenced in this report. The aircraft-Sonde-instrumentation collection, measurement, and modeling procedures documented in this report should facilitate collection of statistically significant collections of these data in the future through the use of cost effective small aircraft. Therefore, for the purposes of definitively addressing the homogeneity of CO_2 and its correlation with measurements from passive LWIR and tower instrumentation the following recommendation is made for a follow on study: Repeat the CAMP Moody, TX collection for two months in the winter and spring using AIRS, ASSIST-II and NOAA's Carbon Tracker instrumentation. Using the procedures documented in this report obtain approximately 30 concurrent Sonde releases and aircraft measurements of CO_2 and water vapor as a function of altitude.

4.2 Calibration of Analogue and Digital Radiosondes

A requirement of the CAMP program was the accurate and repeaTable measurement of tropospheric and stratospheric temperature and humidity values using a method independent of the radiometric remote sensing techniques used in the program. A meteorological radiosonde was a logical choice since the method directly measures the pressure, temperature, and humidity values at a regular interval as the radiosonde is lifted by a gas filled balloon. At the start of the CAMP program, The US EPA ASPECT program utilized a Vaisala PP15 processor and UR15 upper air receiver suiTable for use with Vaisala RS80 analogue probes. While the RS80 probes were used by a number of weather organizations for several years, these probes suffer from humidity sensor errors due to long-term degradation of the sensor and have been replaced by RS90 series digital radiosondes. As part of the CAMP project, a study was conducted to determine how surplus RS80L probes could be recalibrated and used as an inexpensive component to provide upper air data for the program.

4.2.1 Limitations of the RS80 Series Radiosonde

The Vaisala RS80 radiosonde was the most commonly used analogue radiosonde since introduction to the weather services in the late 1970s. The RS80 series probes consisted of separate temperature (0.1 ^{o}C resolution) and humidity (1% RH resolution) capacitive sensing elements located on a flexible arm which was positioned into the slip stream as the sensor was carried aloft. An internal micro-barometric sensor provided pressure reading to a resolution of 0.1 hPa. Pressure, temperature, and humidity (PTU) readings were transmitted on the standard meteorological frequencies using a multi-tone modulation scheme. Each radiosonde was equipped with a calibration tape which was used to “program” the processor at the time of launch.

While the RS80 was extensively used, problems with the probe, namely the humidity sensor, were documented. Specifically, investigations tended to show that the humidity sensor was prone to under-reporting high humidity (such as when passing through a cloud) and tended to show long-term degradation with older probes result in progressively lower humidity readings. For this reason, the RS80 series of probes were vacuum sealed at the time of manufacture and had a specific shelf life after which the probe was discarded.

In addition to the humidity limitations, the probes had a certain hysteresis lag due to the way that the capacitive sensors responded to both temperature and humidity. This lag in response limited how fast the probes were normally sampled and limited the vertical resolution that could be measured with a stock upper air decoder. Normal default sampling intervals of 5 seconds was common and corresponded to a vertical resolution of about 25 meters assuming a normal assent rate of 5 meters/second.

4.2.2 Development of a Radiosonde Calibration Chamber

A study was developed to investigate the possibility of using a large stock of out-of-date RS80L radiosondes if: 1) A calibration correction could be applied to the factory calibration coefficients to compensate for humidity drift/degradation, 2) the sampling rate of the probe could be increased to provide a higher vertical resolution without introducing unwanted sampling hysteresis and noise, and 3) to develop a robust ground check method to determine how the probe behaved at high and low humidity levels.

The initial step in this study was determining the magnitude of drift/degradation that was present in the stock of surplus RS80L probes. A series of measurements were conducted that compared the reference humidity (developed with a sling psychrometer) to those of the sonde humidity reading obtained during the ground check procedure. Table 4.2.1 shows start readings for eight sondes randomly selected from the stock of probes.

Table 4.2.1 Initial RS80L Radiosonde Humidity Readings

Date of Measurement	Reference Humidity (%RH)	Radiosonde Humidity (%RH)	Difference (%RH) Sonde - Reference	Percent of Reference (%)
5 July 2012	68	56	-12	82.3
6 July 2012	60	50	-10	83.3
9 July 2012	58.6	52	-6.6	88.7
10 July 2012	80.0	69	-11	86.2
11 July 2012	69.6	61	-8.6	87.6
12 July 2012	40	37	-3	92.5
31 July 2012	40.5	35	-5.5	86.4
8 Aug 2012	66.9	66	-3.9	98.7

Examination of the data does show a low sonde humidity bias of about 85% to the reference in each of the sondes with exception of two samples. None of the sondes tested in the study showed humidity greater than the reference. This limited data set supported observations given in the literature that the RS80L sonde does have a humidity bias by design or by age. In addition, the above data does show that while the sondes consistently under report humidity, the degree of bias is not consistent and a simple scaling factor would not be appropriate to correct the indicated humidity. A concept was developed to investigate whether the observed bias was linear in both temperature and humidity. Such a finding would permit a straightforward correction factor that could be applied to sondes flight data to adjust humidity back to proper values.

A typical radiosonde flight will generate temperature readings ranging from a high of 35 ^{o}C to lows near -80 ^{o}C with concurrent humidity measurements ranging from near saturation to lows often approaching 0% relative humidity. A chamber was designed that permitted a range of temperatures from – 40 ^{o}C to +40 ^{o}C with a programmable humidity level ranging from near 0 % RH to saturation. The chamber enclosure consisted of a large Pelican shipping container enclosed in three inches of high density foam insulation (Figure 4.2.1). Internal circulation was maintained by using frequency controlled box fans. Cooling and resistive heating elements were contained in an internal duct with liquid nitrogen being used as the refrigerant. A proportional-integral-differential (PID) control loop was used to maintain a given temperature based on a programmed temperature set point. Levels of humidity were controlled using a combination of a dry nitrogen carrier gas flowing through a heated water bubbler flask coupled with a flow control valve and PID controller. Both the temperature and humidity PID controllers were interfaced to a Vaisala HMP60L high resolution temperature/humidity cell located inside the calibration chamber.

Figure 4.2.1 Radiosonde Calibration Chamber and System Controller

At the initiation of a sonde data collection sequence, the sonde was programmed in a normal fashion using the paper calibration tape and the processing unit was referenced to the station (chamber) pressure, temperature and humidity (PTU). Since the enclosure was constructed from plastic, the transmitted PTU signal from the radiosonde was received using the UR15 receiver remotely. The processing unit was operated in research mode and data collection was manually started since no true flight (steadily decreasing pressure) was conducted. A six point temperature/humidity calibration sequence was conducted and is given in Table 4.2.2.

Table 4.2.2 Calibration Matrix Program

Condition	Temperature oC	Humidity %
1	30	50
2	30	0
3	-30	0
4	-30	50
5	-30	100
6	30	100

Each calibration sequence required about 2 hours to complete. A sampling interval of 1 second was used for each calibration run. Results for each calibration run were then analyzed to determine the linearity of the 30 ^{o}C and -30 ^{o}C humidity measurements (ranging from 0% to 100% and including the 50% point). If the results showed an R value exceeding 0.9, the probe was accepted and linear correction confidents were developed to compensate any observed degradation in the humidity sensor and to make the probe serviceable. A two dimensional correction matrix was generated and then applied to the sonde during the actual flight. An example of a radiosonde flight with humidity correction factors applied is given in Figure 4.2.2.

```
                              Station  :McKinney
Sounding : 1
RS-number: 148900144

Started manually by operator
Started at:      10 JUL 12 17:47 GMT
Time   AscRate  Hgt/MSL   Pressure Temp  RH  RHcor  VP  Dewp  Abs Hum  MixRatio
 min sec   m/s     m      ft        mb        C      %     %     mb    C       g/m3       g/kg
  0    0    0.0   178    583      993    30.0    61    70    29.8  24.0   21.32       19.26
  0    1    0.8   179    587      992    29.9    61    70    29.7  23.9   21.21       19.15
  0    2    0.8   180    590      992    29.8    61    70    29.5  23.8   21.09       19.04
  0    3    0.8   180    590      992    29.7    61    70    29.3  23.7   20.98       18.93
  0    4    0.8   181    593      992    29.6    61    70    29.2  23.6   20.87       18.82
  0    5    0.8   182    597      992    29.5    61    70    29.0  23.5   20.75       18.72
  0    6    1.1   183    600      992    29.4    61    70    28.8  23.4   20.64       18.61
  0    7    1.1   185    606      992    29.2    61    70    28.5  23.2   20.42       18.39
  0    8    1.1   186   610       992    29.1    62    71    28.8  23.4   20.65       18.60
  0    9    1.1   188   616       991    28.9    62    71    28.5  23.2   20.43       18.39
  0   10    1.1   189   620       991    28.8    62    71    28.3  23.1   20.32       18.28
```

Figure 4.2.2 Radiosonde Flight Data Output Example with Humidity Correction Applied

While this approach was found to be possible, three problems prevented implementation of the RS80L radiosondes in the CAMP project. First, the method was best conducted in a controlled laboratory setting due to external heat loading to the chamber. Tests conducted in an uncontrolled hanger exhibiting ambient temperatures of 35 °C showed very slow response in chamber temperatures below -20 °C forcing the set points to be changed to -20 °C. This eliminated the use of the chamber at the point of launch and required that probes be calibrated days in advance and then resealed in plastic bags with desiccant packets since the factory vacuum packing was compromised. Secondly, the recalibration method was very time consuming and only permitted two probes to be processed in a given day. Finally, the RS80L radiosonde was designed to use the Omega navigation system to provide wind finding during a given flight. The Omega system was primarily used by the US Navy and is no longer in use so wind-finding data could not be extracted during a given flight. Since the radiosonde moves with the wind, upper air data could not be back correlated to exact positions which complicated integrating this data into the CAMP dataset. Based on these limitations a decision was made to investigate the use of a digital radiosonde system.

4.2.3 Digital Radiosonde System

A literature search of available digital radiosonde systems indicated that a relatively new entry into the upper air market by International Meteorological Systems provided a cost effective solution for a digital PTU sensor with full GPS wind-finding capabilities. The system chosen for the CAMP program consisted of iMet 1 A/B digital radiosondes (Figure 4.2.3) coupled to an iMet 3050 sounding system. Radiosonde specifications are given in Table 4.2.3.

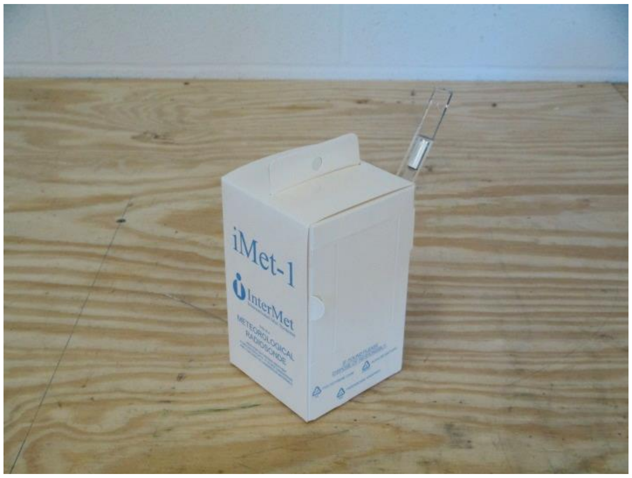

Figure 4.2.3 iMet 1 A/B Digital Radiosonde

Table 4.2.3 iMet 1 A/B Sonde Specifications

Sonde Element	Sensor Type	Range	Accuracy	Resolution
Temperature	Bead Thermistor	-90 to 50 oC	0.3 oC	0.01 oC
Humidity	Capacitive	0 to 100% RH	5% RH	1% RH

All radiosonde flights were conducted using 350 gram natural rubber balloon filled with hydrogen. A unique feature of the iMet radiosondes is no need to ground reference the sonde prior to flight. However, prior to each flight, station temperature, humidity and pressure were noted and compared to the pre-flight quality control data provided by the sounding system.

During each flight, two types of data were processed and reported to the CAMP team including a raw, un-interpolated PTU data file and a processed World Meteorological Organization (WMO) standard report. Data recording was started automatically once the balloon was released (by the measured decrease in pressure) and was updated every two seconds up to 120 minutes or balloon burst. Based on a standard ascent rate of 5 m/s, this provided a vertical resolution of about 10 meters. In addition, since the iMet radiosonde provides GPS wind finding, the height above geoid is given in the raw and processed data set. This useful feature provides an independent determination of altitude for each PTU reading.

4.3 Aircraft (in-Situ altitude) CO_2 and Water Vapor (Humidity) Instrumentation, Collection, and Measurement Procedures

4.3.1 In Situ Sampling General Concept

The measurement of CO_2 and water vapor at specific altitudes was of primary importance to the CAMP study. Accordingly, a collection system was designed that based on the following criteria:

1. The system must physically fit in the ASPECT aircraft.
2. The system must permit the controlled collection of undisturbed air at specific altitudes, at specific geographical locations and over a specific amount of time.
3. Permit a representative whole gas collection of air (for subsequent CO2 analysis) and a concurrent high accuracy measurement of sample temperature and relative humidity.
4. Permit a controlled and repeaTable sample preparation, handling, and shipping methodology.
5. Provide for a certified and repeaTable analytical method for determining total CO2 content within each sample.

The overall concept of collection consisting of four elements which included:

1. Sample preparation which included triple flushing/evaluation each sampling bag with dry nitrogen followed by installation of all sample bags into the aircraft.
2. The active collection of each sample at the pre-designated altitude.
3. Post collection sample manage including preparing each sample for shipment and the inclusion of a trip blank.
4. The analysis of each sample for CO_2 at a certified laboratory.

4.3.2 Sampling System

The CAMP whole gas sampling system consisted of a low pressure, high flow rate pump directly filling 20 liter aluminized Tedlar bags (Figure 4.3.1). Inlet air was extracted from the undisturbed bulk atmosphere using a ram tube located under the right wind of the aircraft (Figure 4.3.2). Since the ASPECT Aero Commander 680 F/L aircraft is a twin engine, this sampling location allowed air to be sampled without any influence from engine exhaust. The ram tube was constructed of 3/8 inch 316 stainless steel using Swagelok type fittings. Pumping of air was accomplished using a dry piston high volume pump conFigured to operate from an independent 12vdc gel cell battery. A Visalia M170 control head coupled to a HMP77 temperature/relative humidity sensor (Figure 4.3.2) was installed in series between the sampling inlet port and the suction port on the pump using a Swagelok “Tee” fitting utilizing Teflon ferrules to seal the probe body within the fitting. A continuous record of temperature and humidity was recorded on the humidity sensor and downloaded after the flight. A flow rate of 7 liters/min was used for all sample collection and was controlled using a needle valve rotometer calibrated from 0 to 10 liter/min. Five sample bags were installed in the system corresponding to the five altitudes selected for the study. Selection of the appropriate sample bags was accomplished using a multi-valve manifold that permitted a continuous flow of air through the sampling pump by wasting flow when a bag was not being filled (Figure 4.3.1). Due to changes in volume due to altitude, a standard sample volume of 14 liters (indicated at altitude) was collected for each sample. This allowed expansion of the high altitude samples without over pressuring the sample bag.

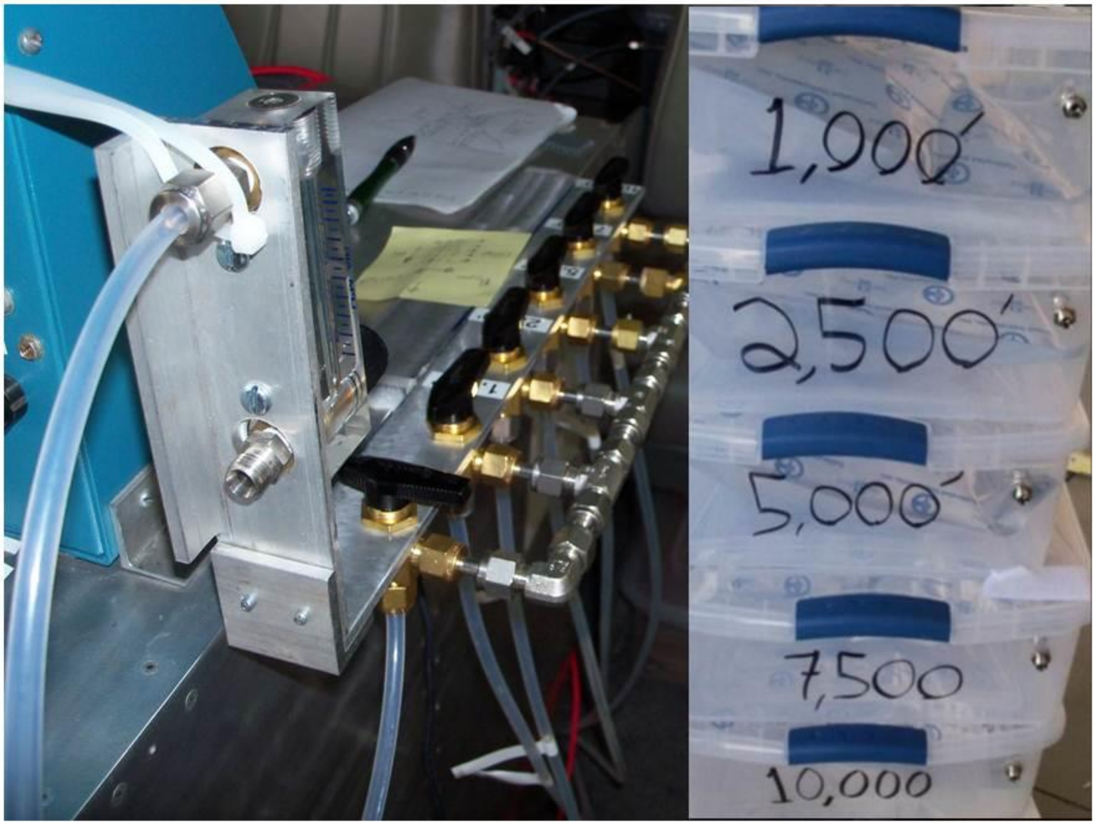

Figure 4.3.1. Rotometer and Sampling Manifold with Aluminized Bag Whole Gas Sampling System.

Figure 4.3.2. Vaisala M170/HMP77 Temperature/Humidity Probe

4.3.3 Sample Preparation

Prior to all collections, all sample bags (six in total for each flight) were conditioned to reduce the influence of residual CO_2 in the sample. The initial step consisted of a visual inspection of each bag to make certain that holes or tears were not present. The condition of the sample valve was checked with attention given to the fitting to bag interface to make certain that the interface was tight and leak free. Each bag was then filled with approximately 20 liters of dry high purity nitrogen and then evacuated using a vacuum pump. This process was repeated two times. The bag was filled a third time and then allowed to sit for a period of 12 hours (overnight) at which time the volume of gas within each bag was visually inspected to find leaks. Any bag showing a reduction in volume was removed from inventory. Bags passing the leak down test were then attached to the vacuum pump and pumped down for a period of five minutes, and sealed using the bag valves. A trip blank sample was then prepared by back filling the bag with approximately 14 liters of dry nitrogen and then sealed with a Swagelok cap. All other sample bags were loaded into flight containers consisting of plastic snap lock lid storage boxes equipped with a Swagelok bulkhead fitting. A sample label was attached to each bag having a unique sample number. A short run of ¼ Teflon tubing was used to connect the sample bag to the bulkhead fitting.

Approximately 20 minutes prior to take off, the temperature/humidity sensor was checked and installed in the sample collection system. The system was cross checked by comparing the temperature and relative humidity reading within the hanger with that obtained with a standard sling psychometer. Each sample bag was then installed in the aircraft and attached to the appropriate port on the sampling manifold using ¼ Teflon tubing. All interconnection fittings consisted of 316 stainless Swagelok fitting. Just prior to take-off, the bag valve for each sample was opened and visually checked by the system operator. The sample pump was then briefly activated and visually checked to make sure that a flow rate of 7 liters/min was achievable.

4.3.4 Sample Collection

Active sample collection was conducted at five standard altitudes consisting of 1000, 2500, 5000, 7500, and 10000 feet MSL (mean sea level reference). A single flight line approximately four miles in length and located ½ mile south of the Moody tower was used for all collections. Selection of which altitude to start the collection was dependent on other project tasks concurrently being conducted on the project. Typically, collections were conducted from high altitude toward the lower altitudes. Irrespective of the order, each collection was accomplished using the same process. Approximately 10 minutes from the initiation of sample collection, the crew activated the sampling pump and started recording inlet temperature/humidity data. In coordination with the flight crew, a 2 minute warning was issued as the aircraft approached the collection line. During this time the aircraft was flown level at the designated collection altitude and the flow rate of the system was adjusted for 7 l/min flow. When instructed by the flight crew and at the start of the collection line, the system operator opened the appropriate sample port valve while simultaneously closing the flow bypass valve. The operator immediately noted the sample flow reading and if necessary readjusted the rotometer for a standard flow of 7 L/min. The start time and flow rate of the system was logged by the system operator in the flight data sheet. The sampling system was then monitored for a period of 2 minutes (timed by the operators) and then stopped by simultaneously closing the sample port valve and opening the sample bypass valve. The stop time of the sample was also logged in the flight data sheet. This process was repeated for each altitude.

At the completion of all active sampling, the system operator stopped the temperature/humidity collection and turned off the sample pump. The aircraft then returned to base. Immediately upon landing and taxi, a member of the CAMP ground team visually inspected each sample bag for proper volume and then closed the bag valves. Each sample container was then removed from the aircraft.

4.3.4.1 Post Sampling Procedures

The post sampling procedures were initiated by examining each bag and visually correlating the sample volume to the altitude collected. Samples collected at the higher altitudes had a smaller volume when observed at surface pressure. A Swagelok cap was then affixed to each sample bag. Relevant information including the sample number, date and time of collection, sample location, and sample volume was recorded on a sample documentation sheet, signed by the CAMP member and then copied. A formal chain of custody form was prepared and in addition to a copy of the sample collection sheets was included with the samples prior to shipping. Three to four sample bags were then loaded into shipping containers (large Coleman Coolers) and shipped using Fed-Ex to the laboratory.

4.3.5 Laboratory Analysis

All whole gas samples collected at part of the CAMP project were analyzed offsite by an independent certified laboratory (Environmental Analytical Services, Inc., San Luis Obispo, CA). Each sample was analyzed using two ATSM methods including ASTM D1945 (primary method) and D3416 (redundant analysis method). In general, both methods share common techniques consisting of chromatographic gas species separation followed by a catalyst and detection.

Method D1945 is equivalent to EPA method 3C (Permanent Gases also known as Fixed Gases). This method can use passivated canisters and/or Tedlar type bags. Samples are analyzed by gas chromatography followed by a thermal conductivity detector. A detailed description and procedure form Method ASTM D1945 is contained in Appendix H.

4.3.5.1 Comparison of Whole Gas Bags to Passivated Canisters

In the design phase of developing a whole gas sampling technique to support the CAMP project, both passivated canisters and whole gas bags were considered. Canister sampling systems utilized a passivated coating (typically nickel) on the inside of a stainless steel vessel which prevents sampled gases from reacting with surface of the vessel. Canisters are typically prepared by high vacuum pumping of the contents often with concurrent baking of the entire container to aid in releasing any high molecular weight compounds condensed on the canister interior. Since canisters are cleaned using high vacuum techniques, valving and other plumbing is constructed of vacuum tight fittings. The collection of samples can be achieved by allowing the vacuum to pull in a sample through a flow control device or by active pressurization again with some form of flow control device. Canisters offer an ideal sampling method since once a gas is collected, leakage out or infusion of gas into the canister is effectively zero. Canisters do have disadvantages with the three biggest being the cost of procurement or leasing, the complexity of the cleaning and/or sampling system, and the physical size and weight of the device.

Whole gas sampling bags share many of the attributes of canisters with additional advantages of a smaller footprint, greatly reduced weight and reduced costs as compared to corresponding canisters. Sampling systems for bags are typically much simpler in design. Sampling bags do have negative attributes with the most serious being infusion and/or leakage through the bag membrane. Specialty bags are manufactured that limit membrane transfer by using thin layers of aluminum in addition to the synthetic bag material. A secondary negative attribute of the whole gas bag is the fragile nature of the construction. Bags can be torn with rough handling and can easily be "popped" if filled beyond the rated capacity. In the end, limitations of available space and gross weight influenced a decision to use whole gas bags for the CAMP project.

Prior to the execution of active sampling, the performance of whole gas (Tedlar) were examined. Published data for the permeability of CO_2 through this brand of bag shows rates of up to 172 cc/m^2/day. If one considers the surface area of a 20 liter bag (approximately 0.46 m^2) the potential diffusion rate of the bag is 80 cc/day. If a two day delay from collection to analysis is assumed, this rate of diffusion would potentially result in 160 cc of CO_2 transfer into/out of the bag or approximately 1 percent of the collected bag volume. If a 5 ppm CO_2 atmospheric difference is to be observed (approximately 1.25 percent of the total CO_2 atmospheric concentration) then this diffusion rate represents that magnitude of error. While this diffusion rate is a worse case situation requiring a large concentration driving force, it was determined that a standard Tedlar bag was not the best choice.

A similar analysis was conducted using published data for multi-layer aluminized bags. This type of bag has low CO_2 permeability; values are on the order of 0.80 cc/m^2/day or for a 20 liter bag approximately 0.40 cc/day. Again using a two day delay this corresponds to about 0.001 percent of the atmospheric average concentration which is well within the error limits to support CAMP. The CAMP team determined that if aluminized bags were utilized and the delay time from collection to analysis was minimized, accepTable detection resolution could be obtained with these systems.

During each of the CAMP sampling events, a trip blank sample was processed and provided to the laboratory for reference. These samples were purged in the same fashion as all of the flight samples but were back-filled with 14 liter or more of dry nitrogen. Results for these samples are given in Table 4.2.4.

Table 4.2.4 Trip Blank Sample Results

Sample	Date	Collection to Analysis Delay (Days)	Laboratory Result (CO_2 ppmV)	Sample/Atmospheric CO_2 Percent (Assuming 440 ppmV atmospheric CO_2 Concentration)
006	16 April 2013	0.86	16.41	4.11
012	19 April 2013	2.84	8.89	2.22
018	18 May 2013	----	Lost sample	---
024	20 May 2013	0.92	57.8	14.45

An examination of these results shows significant variation in the blank CO_2 concentration for each of the sample events. With this small sample size the reason for the blank concentration variance is not known but may be a result of diffusion, CO_2 contamination within the dry nitrogen or laboratory error. Most likely, the most significant influence on error is the laboratory uncertainty. In general methods D1945 and D3616 tend to have detection limits of about 5% or 20 ppmV assuming an atmospheric sample. Accordingly, all of the blank samples fell within this quality control parameter even though there is sample to sample variance.

In summary, laboratory detection limit is most likely the limiting factor on the ultimate resolution of an atmospheric CO_2 sample. The sampling vessel has an impact but the magnitude is not fully understood. Improvement in CO_2 measurements can be made including the use of canisters which effectively removes diffusion as an error, the use of high purity nitrogen as a purge/cleaning gas, and finally an increase in the sample sizes for each at altitude collection event and an increase in the number of total flights. These improvements would permit a complete assessment of measurement error to be established.

4.4 Radiosonde and Aircraft Humidity Modeling and Comparison

A direct comparison of the radiosonde and aircraft humidity measurements was not possible due to the different environments in which the two systems measured relative humidity namely the difference in temperature. The radiosonde utilized a thin-wire thermistor and capacitive humidity probe to measure air temperature and humidity levels directly during the ascension. The ASPECT aircraft utilized a similar type of probe for temperature and humidity measurement that was integrated within the flow stream of the whole gas sampling system. Sampled air was drawn into the system from under the aircraft wing and was heated by the sensible heat of the aircraft interior and sampling equipment within the aircraft. In order to directly compare these measures of humidity, a temperature correction was made to the aircraft measurement.

Humidity comparisons were computed at the 5 standard altitudes that the aircraft flew over the Moody tower site. These altitudes consisted of 1000 Ft Above Ground Level (AGL), 2500 Ft AGL, 5000 Ft AGL, 7500 Ft AGL, and 10,000 Ft AGL. Each standard altitude was converted to a Mean Sea Level altitude (MSL) by adding the ground surface elevation of 770 Ft to each AGL altitude resulting in 1770 Ft MSL (539.4 M), 3270 Ft MSL (997 M), 5770 Ft MSL (1758 M), 8270 Ft MSL (2521 M) and 10770 Ft MSL (3283 M). Measured aircraft relative humidity was converted to equivalent slip-stream humidity by first computing the saturation vapor pressure of the gas stream passing by the aircraft probe using the following equation:

$$P_{ws} = 6.1162*10^{(7.5892*T/(T+240.71)} \quad (1)$$

Where P_{ws} = Water Saturation Vapor Pressure (in mb)

T = Gas Temperature at the point of measurement (in ^{o}C)

Bounds on the saturation vapor pressure were computed by including the stated measurement accuracy for both the relative humidity measurement (1%) and the temperature measurement (0.1 ^{o}C). The water vapor pressure was next computed using the measured relative humidity and saturation vapor pressure using the following equations:

$$P_w = RH*100/P_{ws} \quad (2)$$

Where Pw = Water Vapor Pressure (in mb)

The slip stream relative humidity was next computed by dividing the aircraft derived vapor pressure by the sonde derived saturation vapor pressure (computed using the sonde temperature and relative humidity at the same MSL altitude and equation 1). The associated errors of the sonde temperature (0.1 ^{o}C) and humidity (5%) measurements in addition to the bounds generated for the aircraft vapor pressures were used to generate an overall error bound for the corrected aircraft humidity. Sonde and Aircraft humidity comparisons are given in Tables 4.2.5, 4.2.6, and 4.2.7.

Table 4.2.5 Ascent 002, Release 001, 19 April 2013

Altitude (AGL) in Feet	Radiosonde (%)	Aircraft (%)
10000	1.26 ± 5	11.3 ± 3.46
7500	19.2 ± 5	9.3 ± 2.78
5000	6.61 ± 5	14.9 ± 2.33
2500	38.6 ± 5	41.3 ± 2.18
1000	31.9 ± 5	28.2 ± 1.84

Table 4.2.6 Ascent 004, Release 001, 18 May 2013

Altitude (AGL) in Feet	Radiosonde (%)	Aircraft (%)
10000	20.5 ± 5	21.5 ± 2.91
7500	19.2 ± 5	19.6 ± 1.71
5000	21.0 ± 5	19.9 ± 1.32
2500	70.8 ± 5	78.5 ± 2.11
1000	66.5 ± 5	69.0 ± 1.84

Table 4.2.7 Ascent 006, Release 001, 20 May 2013

Altitude (AGL) in Feet	Radiosonde (%)	Aircraft (%)
10000	10.9 ± 5	19.5 ± 2.60
7500	23.3 ± 5	25.8 ± 1.76
5000	21.6 ± 5	27.8 ± 1.41
2500	81.4 ± 5	88.1 ± 2.23
1000	66.4 ± 5	74.0 ± 1.86

Note on comparisons. While the agreement between the aircraft and sonde relative humidities show differences, humidity trend and magnitude agree well. A source of unqualified error resides in the fact that distances between the sonde and the aircraft progressively increase with altitude due to the flight of the balloon. The comparison becomes a synoptic comparison with increasing altitude (and corresponding distance).

Future Improvements

While the intercomparison of relative humidity between the aircraft and the radiosonde tend to show good agreement in the lower atmosphere and reasonable agreement in the upper atmosphere, changes can be implemented to further improve this intercomparison throughout the atmospheric column. The primary limiting factor corresponds to the fact radiosondes released near the study area have the possibility of traveling large distances prior to reaching the corresponding flight levels of the research aircraft. This results in the aircraft and the radiosonde measuring two distinct locations of the atmosphere and two different air parcels. Provisions can be made to conduct multiple radiosonde releases in a timed fashion and released from upwind locations to result in a respective radiosonde traveling through the same altitude and accordingly same air as the aircraft and at the same time. Such a design will entail the necessity to use at least 3 radiosonde ground stations (which can be collected) and at least one preview radiosonde flight to determine the general upper air winds and the corresponding approximate upwind release points.

4.5 References Aircraft Support: Instrumentation, Sonde Calibration-Collection, CO2-Water vapor/humidity Collection and Measurement Procedure

Ciesielski, Paul E., Richard H. Johnson, Junhong Wang, 2009: Correction of Humidity Biases in Vaisala RS80-H Sondes during NAME. *J. Atmos. Oceanic Technol.*, **26**, 1763–1780.

Wierenga, Rodney, Joe Parini. Intermet 403 Mhz Radiosonde System, World Meteorological Organization from http://www.wmo.int.

5 Atmospheric Modeling and Simulation Support

5.1 Planet Boundary Layer (PBL) At-Sensor Radiance Modeling Support

5.1.1 INTRODUCTION

This report describes the theory and process developed to estimate the LWIR radiance spectrum reaching to a sensor on-board an aircraft. This at-sensor radiance modeling capability is being developed in support of NGA's Collaborative Atmospheric Measurement Program (CAMP). The goal of the CAMP program is to obtain a thorough understanding of the quantitative accuracy of boundary layer greenhouse gas (GHG) estimation derived from passive infrared remotely sensed measurement data. The CAMP study utilized spaceborne and airborne down-looking, as well as ground-based up-looking passive infrared instruments to collect near simultaneous data for quantitative GHG estimation in the lower troposphere.

Essential parameters such as ground temperature, total pressure near the ground, relative humidity, and ground emissivity can be readily measured. Using these measured parameters, a model has been developed to generate an estimated at-sensor LWIR radiance spectrum as a function of the concentration values for four major atmospheric constituents (water vapor, CO_2, ozone, and methane). For the initial testing and evaluation, the study aircraft is assumed to be at 1000 meters AGL. The at-sensor radiance spectrum is modeled by propagating the ground radiance through 10 intervals of 100 meters of atmosphere above ground and also propagating the atmospheric radiance in each 100-meter atmospheric interval through all intervals above that interval reaching the sensor.

Using known or measured ground temperature, total pressure near the ground, and relative humidity, this model estimates the water vapor concentration in each of the 10 atmospheric intervals based on the Clausius-Clapeyron equation and the ideal gas law. The concentrations of ozone and methane are assumed to be relatively unchanged in these 10 intervals. The objective is to use this model iteratively to estimate the at-sensor LWIR radiance spectrum by varying the concentration of CO_2 until the modeled at-sensor spectrum matches the spectrum sensed by the nadir looking Fourier transform infrared spectrometer (FTIS) on-board the study aircraft. The gas concentration of CO_2 used in the model that produces a match provides an estimate of the amount of CO_2 in the column of atmosphere at the time of data collection. The CO_2 estimates derived using this method can then be compared to the estimates generated from atmospheric profile retrievals from ground-based upward looking and spaceborne downward looking infrared data, thereby providing additional insights into the boundary layer greenhouse gas estimation problem.

Note: This revised report describes the process to estimate the LWIR radiance spectrum reaching to a sensor on-board an aircraft when the necessary ancillary information is provided by the radiosonde data. More specifically, this revision describes the process to estimate the water vapor amount in each of the 100-meter atmospheric intervals from the ground to the airborne sensor when the air temperature, total pressure, and relative humidity for each 100-meter atmospheric interval are provided by the radiosonde data. In section 5.1.5 and 5.1.6, the modifications to the calculations are made in each necessary step immediately below the original calculation descriptions and they are written in red color.

5.1.2 OVERALL MODEL

The following basic radiance equation is used in the model (Equation 1).

$$L(\lambda) = \tau_a(\lambda)\varepsilon_g(\lambda)B(\lambda, T_g) + \varepsilon_a(\lambda)B(\lambda, T_a) \tag{1}$$

where

L is the observed radiance
λ is the wavelength
τ_a is the atmospheric transmittance
ε_g is the emissivity of the ground
B(λ,T) is the Planck function at temperature T
ε_a is the emissivity of the atmospheric constituents
T_g is the ground temperature
T_a is the air temperature

For the initial testing and evaluation, the study aircraft is assumed to be at 1000 meters AGL. The at-sensor radiance spectrum is modeled by propagating the ground radiance through 10 intervals of 100 meters of atmosphere above ground and also propagating the atmospheric radiance in each 100-meter atmospheric interval through all intervals above that interval reaching the sensor. Figure 5.1 illustrates how the at-sensor radiance spectrum is modeled as the sum of the ground radiance spectrum and the atmospheric radiance spectrum reaching to the sensor after they pass through 10 intervals of 100 meters of atmosphere.

The atmospheric transmittance τ_a (hence the emissivity of the atmospheric constituents ε_a), the air temperature T_a, and the Planck function $B(\lambda, T_a)$ at temperature T_a are modeled and estimated separately for each of the 10 intervals. The emissivity of the ground ε_g is assumed to be a constant value (i.e. do not vary as a function of wavelength).

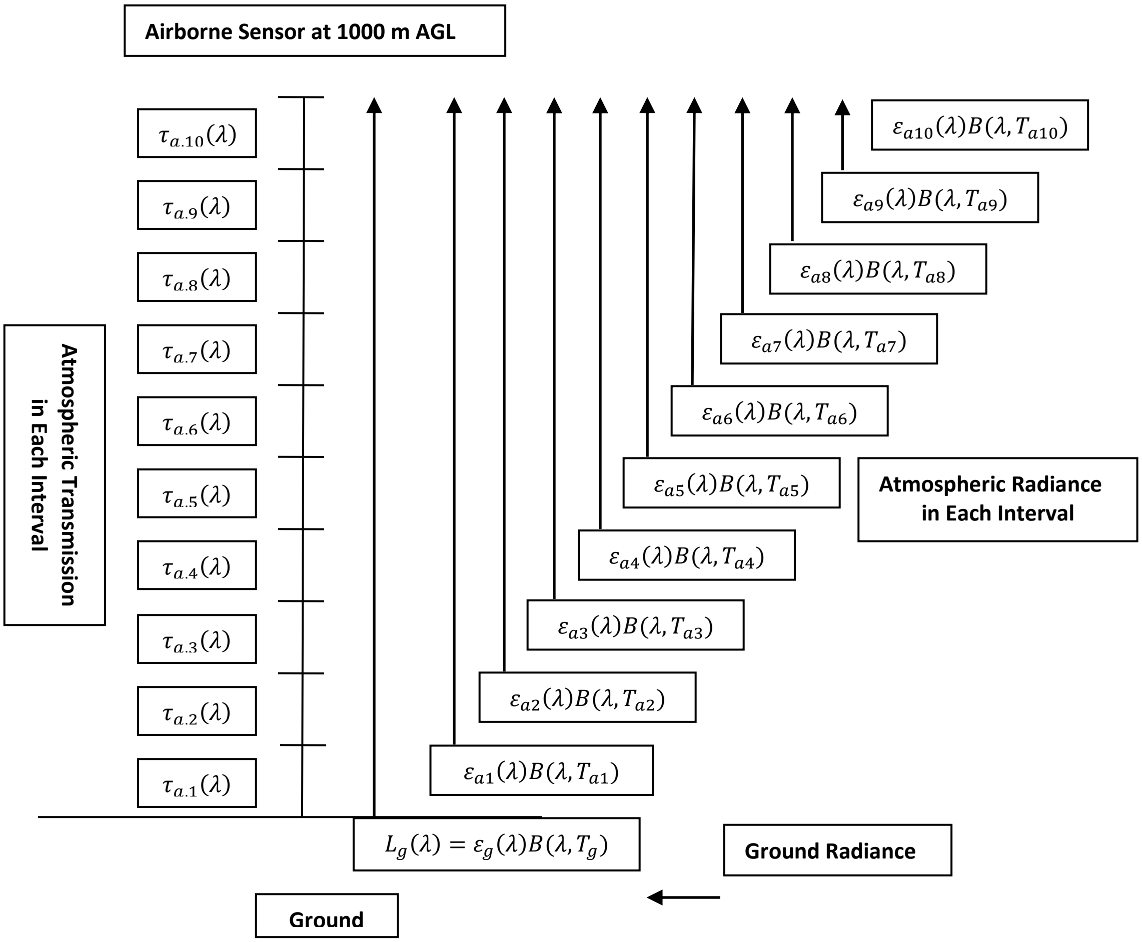

Figure 5.1 Modeling of At-Sensor Radiance

The at-sensor radiance spectrum is modeled using the following Equation (Equation 2).

$$\begin{aligned} L(\lambda) = {} & \tau_{a10}(\lambda)\tau_{a9}(\lambda)\tau_{a8}(\lambda)\tau_{a7}(\lambda)\tau_{a6}(\lambda)\tau_{a5}(\lambda)\tau_{a4}(\lambda)\tau_{a3}(\lambda)\tau_{a2}(\lambda)\tau_{a1}(\lambda)\varepsilon_g(\lambda)B\big(\lambda,T_g\big) \\ & + \tau_{a10}(\lambda)\tau_{a9}(\lambda)\tau_{a8}(\lambda)\tau_{a7}(\lambda)\tau_{a6}(\lambda)\tau_{a5}(\lambda)\tau_{a4}(\lambda)\tau_{a3}(\lambda)\tau_{a2}(\lambda)\varepsilon_{a1}(\lambda)B(\lambda,T_{a1}) \\ & + \tau_{a10}(\lambda)\tau_{a9}(\lambda)\tau_{a8}(\lambda)\tau_{a7}(\lambda)\tau_{a6}(\lambda)\tau_{a5}(\lambda)\tau_{a4}(\lambda)\tau_{a3}(\lambda)\varepsilon_{a2}(\lambda)B(\lambda,T_{a2}) \\ & + \ldots\ldots\ldots\ldots\ldots \\ & + \tau_{a10}(\lambda)\varepsilon_{a9}(\lambda)B(\lambda,T_{a9}) \\ & + \varepsilon_{a10}(\lambda)B(\lambda,T_{a10}) \end{aligned} \qquad (2)$$

where
L is the observed radiance (in units of W/μm-cm^2-str)
λ is the wavelength (in units of μm)
τ_{ai} is the atmospheric transmittance in the ith interval
ε_g is the emissivity of the ground
B(λ,T) is the Planck function at temperature T
ε_{ai} is the emissivity of the atmospheric constituents in the ith interval

T_g is the ground temperature
T_{ai} is the air temperature of the ith interval

And the atmospheric transmittance in the ith interval is given by

$$\tau_{ai}(\lambda) = e^{-[c_{1i}lk_1(\lambda)+c_{2i}lk_2(\lambda)+c_{3i}lk_3(\lambda)+c_{4i}lk_4(\lambda)]} \qquad \text{for i=1, …. , 10} \qquad (3)$$

where
$\tau_{ai}(\lambda)$ is the atmospheric transmittance in the ith interval
c_{1i} is the concentration (in units of ppm) of water vapor in the ith interval
l is the path length of the ith interval (i.e. 100 meters in this study)
$k_1(\lambda)$ is the absorption coefficients of water vapor at 1 ppm-m
c_{2i} is the concentration (in units of ppm) of CO_2 in the ith interval
$k_2(\lambda)$ is the absorption coefficients of CO_2 at 1 ppm-m
c_{3i} is the concentration (in units of ppm) of ozone in the ith interval
$k_3(\lambda)$ is the absorption coefficients of ozone at 1 ppm-m
c_{4i} is the concentration (in units of ppm) of methane in the ith interval
$k_4(\lambda)$ is the absorption coefficients of methane at 1 ppm-m

and the emissivity of the atmospheric constituents in the ith interval is

$$\varepsilon_{ai}(\lambda) = 1 - \tau_{ai}(\lambda) \qquad \text{for i=1, …. , 10} \qquad (4)$$

and the Planck function B(λ,T) is defined as follows.

$$B(\lambda, T) = \frac{A_1}{\lambda^5\left(e^{\frac{A_2}{\lambda T}} - 1\right)}$$

where
A_1=11910 W-μm^4/cm^2-str
A2=14388 μm ^{o}K
T is temperature in ^{o}K

Equation 2 shows how the at-sensor radiance spectrum is modeled. The first term in Equation (2) represents the portion of the modeled at-sensor radiance contributed by the ground radiance $\varepsilon_g(\lambda)B(\lambda, T_g)$ as it transmits through 10 intervals of 100 meters of atmosphere above it. Each of the second through the eleventh terms in Equation (2) represents the portion of the at-sensor radiance contributed by the atmospheric radiance $\varepsilon_{ai}(\lambda)B(\lambda, T_{ai})$ of a 100-meter interval as it transmits through all 100-meter intervals above that interval.

In order to use Equation (2) to estimate the at-sensor radiance spectrum $L(\lambda)$, the individual terms in Equation (2) need to be estimated. The following sections describe the theory and methodology used to model and estimate these terms.

As can be seen in Equation (3), the atmospheric transmittance (and hence the emissivity of the atmospheric constituents) in each interval is a function of the concentrations of the four major atmospheric constituents (i.e. water vapor, CO_2, ozone, and methane) in that interval. Thus the concentrations of the four gases need to be estimated or assumed to be of certain values. Of these four major constituents, the amount of water vapor in the atmosphere has the most significant impact on atmospheric transmittance. The amount of water vapor in the atmosphere is a function of the air temperature, pressure, and relative humidity. Given the ground temperature, total pressure near the ground, and relative humidity, the methodology used to estimate the air temperature and pressure for each of the 10 intervals, and hence the water vapor concentration in each interval is described in detail in Section 5.1.5 and 5.1.6. Or alternatively, if the air temperature, pressure, and relative humidity for each of the 10 intervals are available from radiosonde data, they can be used in place of the estimated air temperature and pressure for each interval in the model. These measured values from radiosonde data can also be used to determine the accuracy of the saturation water vapor pressure and the dry air pressure estimated from using the Clausius-Clapeyron equation and the Barometric Model.

For initial development of the model, the concentrations of CO_2, ozone, and methane are assumed to be well mixed gases and therefore are the same for all 10 intervals. Their concentrations are assumed to be:

Concentration for CO_2: $C_{2i} = 387$ ppm for i=1, …. , 10
Concentration for ozone: $C_{3i} = 0.01$ ppm for i=1, …. , 10
Concentration for methane: $C_{4i} = 2.8$ ppm for i=1, …. , 10

This model will be used iteratively to estimate the at-sensor LWIR radiance spectrum by varying the concentration of CO_2 until the modeled at-sensor spectrum matches the spectrum sensed by the nadir looking Fourier transform infrared spectrometer (FTIS) on-board the study aircraft. The gas concentration of CO_2 used in the model that produces a match provides an estimate of the amount of CO_2 in the column of atmosphere at the time of data collection.

5.1.3 ESTIMATION OF WATER VAPOR AMOUNT

The actual concentration of water vapor is determined by first estimating the concentration of saturation water vapor at the surface for a given temperature. The Clausius-Clapeyron equation is used to compute the saturation water vapor pressure at the surface. The ideal gas law is used to compute the saturation water vapor density and dry air density at the surface. These values are used to compute the saturation water vapor concentration at the surface. The steps to estimate the concentration of saturation water vapor at the surface is described in detail in Section 3.1.4.

Next, the concentration of saturation water vapor in each of the ten 100-meter atmospheric intervals is estimated. The lapse rate is used to estimate the temperature for each of the 10 intervals. The Clausius-Clapeyron equation is used to compute the saturation water vapor pressure for each of the 10 intervals. And the Barometric Model is used to compute the dry air pressure for each of the 10 intervals. The ideal gas law is used to compute the saturation water vapor density and dry air density for each interval. The concentration of saturation water vapor for each interval is then computed. Section 5.1.4 describes the steps to estimate the concentration of saturation water vapor for each of the ten 100-meter atmospheric intervals.

Relative humidity is then used in combination with the estimated saturation water vapor concentration to produce an estimate of the actual water vapor concentration for each interval. Section 5.1.5 describes the steps to estimate the actual water vapor concentration for each of the ten 100-meter atmospheric intervals.

5.1.4 Estimation of Saturation Water Vapor Concentration At the Surface

If the energy of random motion of a water molecule at the surface of liquid water is great enough, the water molecule will break its electrostatic bonds with other water molecules, and enter the gas phase. That is, it will become a water vapor molecule with no electrostatic bonds to other water molecules. This process is called evaporation.

Water vapor molecules also exhibit a range of energies of random motions. Water vapor molecules that collide with the liquid or ice surface and lack sufficient energy will be held at the liquid or ice surface by electrostatic bonds with other molecules there, that is, they will stick and become part of the liquid or ice. This process is called condensation. In contrast, molecules that are sufficiently energetic will bounce off the surface and remain in the gas state.

As long as there are some water vapor molecules present, evaporation and condensation will occur simultaneously. In other words, some water vapor molecules will always be colliding with the liquid or ice surface and some will be sticking while other sufficiently energetic molecules will be breaking away from the surface and entering the gas state. When evaporation and condensation occur at the same rate, then the liquid or ice will experience no net gain or loss of water molecules. This state is called the state of equilibrium. When a liquid or ice surface is in equilibrium with the water vapor next to it, the space adjacent to the liquid or ice is saturated with water vapor.

To estimate the water vapor concentration in each atmospheric interval, the water vapor concentration at saturation is first estimated at the surface. In order to estimate the saturation water vapor concentration at the surface, the saturation water vapor pressure at the surface needs to be computed first. The Clausius-Clapeyron equation is used to compute the saturation water vapor pressure at the surface.

The Clausius-Clapeyron equation for equilibrium between liquid and vapor is

$$\frac{dP}{dT} = \frac{L}{T(V_v - V_l)} \tag{5}$$

where P is saturation water vapor pressure
T is temperature
L is the latent heat of vaporization (i.e. enthalpy of vaporization)
V_v is the volume at temperature T of the vapor phase
V_l is the volume at temperature T of the liquid phase

Since $V_v >> V_l$, Equation (5) becomes

$$\frac{dP}{dT} = \frac{L}{TV_v}$$

Use the following equation from the ideal gas law:

$$PV_v = RT$$

where R is gas constant for water vapor=461.491 J/(kg * ^{o}K)

Then the Clausius-Clapeyron equation becomes

$$\frac{dP}{dT} = \frac{L}{\frac{RT^2}{P}}$$

We can re-write it as

$$\frac{1}{P}dP = \frac{L}{R}\frac{1}{T^2}dT$$

Or equivalently

$$\mathrm{d}(\ln \mathrm{P}) = \frac{\mathrm{L}}{\mathrm{R}}\left(\mathrm{d}\left(-\frac{1}{\mathrm{T}}\right)\right)$$

Therefore

$$\ln \mathrm{P} = \mathrm{c} - \frac{\mathrm{L}}{\mathrm{RT}}$$

where L is heat of vaporization=2.257x10^{6}J/kg
R is gas constant for water vapor=461.491 J/(kg * ^{o}K)
c is a constant

When the above equation is evaluated at two different temperatures T_1 and T_2, we get

$$\ln \mathrm{P}_1 = \mathrm{c} - \frac{\mathrm{L}}{\mathrm{RT}_1}$$

$$\ln \mathrm{P}_2 = \mathrm{c} - \frac{\mathrm{L}}{\mathrm{RT}_2}$$

If we subtract the above two equations, we have

$$\ln\frac{P_1}{P_2} = \frac{L}{R}\left(\frac{1}{T_2} - \frac{1}{T_1}\right)$$

where $\frac{L}{R} = \frac{2.257\text{x}10^6\text{J/kg}}{461.491\ \text{J/(kg} * \text{oK)}}$ =4890.5742 ^{o}K

When T_2 =273.15 ^{o}K, P_2 =6.11 mb. Substitute these values in the above equation, we obtain

$$P_1 = 6.11exp^{17.92\frac{T_1-273.15}{T_1}} \tag{6}$$

where $T_1$is temperature in ^{o}K

When the temperature $T_1$is measured in ^{o}C, the above equation becomes

$$P_1 = 6.11exp^{\frac{17.92xT_1}{273.15+T_1}} \tag{7}$$

Depending on whether the ground temperature is reported in ^{o}K or ^{o}C, the Clausius-Clapeyron Equation (6) or (7) will be used in the model.

<u>The following steps are used to compute the saturation water vapor concentration at the surface in units of parts per million (ppm):</u>

1. Obtain the ground temperature T_g in units of ^{o}C. The ground temperature can be obtained from other ancillary support data.

2. Compute saturation water vapor pressure P_0 in units of mb using the Clausius-Clapeyron equation.

   $$P_0 = C_0exp^{\frac{C_1T_g}{C_2+T_g}}$$

   where

   C_0=6.11 mb
   C_1=17.92
   C_2=273.15 ^{o}K
   T_g the ground temperature in units of ^{o}C

3. Convert saturation water vapor pressure P_0 in units of mb to saturation water vapor pressure P_1 in units of pascal:

   $$P_1 = P_0 * 100$$

4. Compute saturation water vapor density D_1 in units of kg/m^3 using the following equation derived from the ideal gas law.

   $$D_1 = \frac{P_1}{461.495 * T_g}$$

   where

   P_1 is the saturation water vapor pressure in pascal: J/m^3 (from Step 3)
   461.491 is the gas constant for water vapor in units of J/(kg * ^{o}K)
   T_g is the ground temperature in ^{o}K (^{o}K= ^{o}C+273.15) (from Step 1)

5. Convert saturation water vapor density D_1 in units of kg/m^3 to saturation water vapor density D_2 in units of mol/m^3.

$$D_2 = \frac{D_1 * 1000}{18.016}$$

where

18.016 is the molecular weight of water vapor in units of gram/mol

6. Obtain the total pressure near the ground. If it is in units of mmHg, convert it to total ground pressure P_{total} in units of pascal by multiplying by 133.322.

7. Since the total pressure is the sum of the saturation water vapor pressure and the dry air pressure, compute dry air pressure P_3 in units of pascal:

$$P_3 = P_{total} - P_1$$

8. Compute dry air density D_3 in units of kg/m^3 using the following equation derived from the ideal gas law.

$$D_3 = \frac{P_3}{287.05 * T_g}$$

where

P_3 is the dry air pressure in pascal: J/m^3 (from Step 7)
287.05 is the gas constant for dry air in units of J/(kg * ^{o}K)
T_g is the ground temperature in ^{o}K (^{o}K= ^{o}C+273.15) (from Step 1)

9. Convert dry air density D_3 in units of kg/m^3 to dry air density D_4 in units of mol/m^3.

$$D_4 = \frac{D_3 * 1000}{28.964}$$

where

28.964 is the molecular weight of dry air in units of gram/mol

10. Compute the density D of mixture of dry air molecules and saturation water vapor molecules as

$$D = D_2 + D_4$$

11. Compute the saturation water vapor concentration C_w in units of ppm.

$$C_w = \frac{D_2}{D} * 1000000$$

5.1.5 Estimation of Saturation Water Vapor Concentration for Each of the Ten 100-meter Atmospheric Intervals

The overall procedure used to estimate the saturation water vapor concentration is the same for all atmospheric intervals. Note that the temperature, saturation water vapor pressure, and dry air pressure are different for each of the 10 100-meter atmospheric intervals and are estimated separately.

The following are steps used to compute the saturation water vapor concentration in each of the 10 intervals above ground in units of parts per million (ppm):

12. Assume the air temperature decreases by 7 ^{o}C as the altitude increases by 1 km (the lapse rate). Therefore, the air temperature is assumed to decrease by 0.7 ^{o}C for each 100-meter interval from the ground to the airborne sensor at 1000 meters AGL. Assume that the air temperature for the first interval T_{a1} is the temperature at the middle of the interval. In other words, $T_{a1} = T_g - 0.35$ in units of ^{o}C. The temperature of each successive interval is 0.7 ^{o}C lower than the previous interval: $T_{a\,i+1} = T_{ai} - 0.7$ ^{o}C for i=1, ……,9.

    Use the air temperature provided by the radiosonde data corresponding to the altitude of each atmospheric interval. Denote the air temperature for interval i by T_{ai}. Since the radiosonde data records the elevation information in MSL, the elevation of the collection site needs to be factored in when computing the altitude in AGL of each atmospheric interval (and finding the correct corresponding air temperature for that interval)..

13. Repeat Steps 2 to 5 to compute the saturation water vapor pressure and the saturation water vapor density D_{2i} for each of the 10 intervals using the air temperature T_{ai} of that interval in place of the ground temperature T_g.

14. Assume that the dry air pressure decreases according to the Barometric model. Compute the dry air pressure P_{ai} for each of the 10 intervals using the following Barometric model.

    $$P_{ai} = P_3 e^{-\frac{mgh_i}{RT_{ai}}}$$

    where

    P_{ai} is the dry air pressure in units of pascal of the ith interval
    P_3 is ground dry air pressure in units of pascal computed in Step 7.
    m is the molecular weight of dry air = 0.029 kg/mol
    g is the acceleration = 9.8 m/sec^2
    h_i is the a scale height of the ith interval = i*100 meters
    R is the universal gas constant = 8.314 J/mol ^{o}K
    T_{ai} is the temperature of the ith interval in units of ^{o}K (^{o}K= ^{o}C+273.15) (from Step 12)

    Use the total pressure provided by the radiosonde data corresponding to the altitude of each atmospheric interval. Since the radiosonde data reports the total pressures in units of mb, convert them to units of pascal. Denote the total pressure for interval i by $P_{total\ i}$. Repeat Step 7 to compute the dry air pressure P_{ai} in units of pascal for the ith interval using the total pressure $P_{total\ i}$ and the saturation water vapor pressure for the ith interval from Step 13.

15. Repeat Steps 8 and 9 to compute the dry air density D_{4i} in units of mol/m3 for each of the 10 intervals using the air temperature T_{ai} from Step 12 in place of the ground temperature T_g and the dry air pressure P_{ai} from Step 14 in place of P_3.

16. Repeat Steps 10 and 11 to compute the saturation water vapor concentration in units of ppm for each of the 10 intervals.

5.1.6 Estimation of Actual Water Vapor Concentration for Each of the Ten 100-meter Atmospheric Intervals

The amount of water vapor actually present can be estimated if the relative humidity is known. Relative humidity is defined as the amount of water vapor actually present relative to the amount that would be present at saturation expressed in percentage. Our initial model uses the same relative humidity for all 10 atmospheric intervals. But, if the relative humidity is available from radiosode data for each interval, they can be used.

The following are steps used to compute, for a given relative humidity, the actual water vapor concentration in each of the 10 intervals above ground in units of parts per million (ppm):

17. For a given relative humidity RH, compute the density D_i of the mixture of dry air molecules and the actual water vapor molecules for each of the 10 intervals using the saturation water vapor density D_{2i} from Step 13 and the dry air density D_{4i} from Step 15.

$$D_i = RH * D_{2i} + D_{4i}$$

Use the relative humidity provided by the radiosonde data corresponding to the altitude of each atmospheric interval. Denote the relative humidity for the ith interval by RH_i. Compute the density D_i of the mixture of dry air molecules and the actual water vapor molecules for each of the ith interval using the saturation water vapor density D_{2i} from Step 13 and the dry air density D_{4i} from Step 15.

$$D_i = RH_i * D_{2i} + D_{4i}$$

18. Compute the actual water vapor concentration C_{wi} in units of ppm for each of the 10 intervals as follows.

$$C_{wi} = \frac{RH * D_{2i}}{D_i} * 1000000$$

Compute the actual water vapor concentration C_{wi} in units of ppm for each of the 10 intervals as follows.

$$C_{wi} = \frac{RH_i * D_{2i}}{D_i} * 1000000$$

Sections 5.1.5 to 5.1.6 describe the steps to estimate the actual water vapor concentration for each of the 10 intervals. Using these values, the atmospheric transmittance $\tau_{ai}(\lambda)$ and the emissivity of the atmospheric constituents $\varepsilon_{ai}(\lambda)$ for each of the 10 intervals can be computed using Equations (3) and (4) respectively. Thus, we have computed all the necessary terms needed to estimate the at-sensor radiance spectrum $L(\lambda)$ using Equation (2).

5.1.7 SUMMARY

When the ground temperature T_g, the total pressure at the surface P_{total}, and the relative humidity RH are known, the temperature, saturation water vapor pressure, dry air pressure at the surface and in each of the ten 100-meter atmospheric intervals can be estimated using the lapse rate, the Clausius-Clapeyron equation, and the Barometric Model. Then, the actual water vapor concentration in each interval from the ground to the airborne sensor at 1000 meters AGL can be estimated. The estimation steps are described in detail in Section 5.1.4 through 5.1.6. CO_2, ozone, and methane are assumed to be well mixed gases and therefore their concentrations are the same for all 10 intervals (see Section 2). The path length of each interval is 100 meters. Using the actual water vapor concentration estimated for each of the 10 intervals and the CO_2, ozone, and methane concentration values (see Section 5.1.2), the atmospheric transmittance $\tau_{ai}(\lambda)$ in the ith interval can be computed using Equation (3) for all i=1, …., 10. The emissivity $\varepsilon_{ai}(\lambda)$ of the atmospheric constituents in the ith interval can be computed using Equation (4) for all i=1, …., 10.

This revised report discuss the case when the air temperature, total pressure, and relative humidity for each of the 100-meter intervals are available from the radiosonde data, they are used in place of the estimated air temperature and pressure for each interval in the model. These measured values from radiosonde data can also be used to determine the accuracy of the saturation water vapor pressure and the dry air pressure estimated from using the Clausius-Clapeyron equation and the Barometric Model.

Next, the emissivity of the ground ε_g is assumed to be known and assumed to be a constant value (i.e. do not vary as a function of wavelength). The air temperature of the ith interval T_{ai} is either estimated based on the lapse rate as described in Step 12, or provided by the radiosonde data. Given these values along with the estimated $\tau_{ai}(\lambda)$ and $\varepsilon_{ai}(\lambda)$, the at-sensor radiance spectrum is estimated using Equation (2).

Note: All calculations described in this report can be expanded for an aircraft altitude of greater than 1000 meters AGL. When the aircraft altitude is higher than 1000 meters AGL, the number of 100-meter atmospheric intervals used in the model will increase accordingly. But all calculations remain the same.

The objective is to use this model iteratively to estimate the at-sensor LWIR radiance spectrum by varying the concentration of CO_2 until the modeled at-sensor spectrum matches the spectrum sensed by the nadir looking FTIS instrument on-board the study aircraft. The gas concentration of CO_2 used in the model that produces a match provides an estimate of the amount of CO_2 in the column of atmosphere at the time of data collection. The CO_2 estimates derived from this method can then be compared to the estimates generated from atmospheric profile retrievals using ground-based upward looking and spaceborne downward looking infrared data, thereby providing additional insights into the boundary layer greenhouse gas estimation problem.

5.2 INTRODUCTION OF SECOND RADIATIVE TRANSFER MODEL

In order to examine a Radiative Transfer Model's ability to replicate the ASSIST and AIRS measurements, with sonde and other atmospherically determined components as input, Line-by-Line (LBL) codes may provide the best approach. However, a recent version of MODTRAN® has been adopted (only as a place-holder, with inputs similar to the prior discussion, but intended for Local Thermodynamic Equilibrium (LTE) conditions between 0-100km). It is fully recognized that testing MODTRAN®5 (MOD5) **(**references 1- 3, Section 5.2**)** capabilities within the CAMP program only provides a transfer for up- and down-looking simulations of ASSIST and AIRS measurements, respectively, and is not intended to replace the LBL efforts; (see the discussion and references 27-29 in Appendix G for previous applications of MODTRAN for up-down RT simultaneity simulations, and reference 1 for Sections 5.1 and 6 for previous work on spatially and temporally concurrent ground based upward looking (e.g., ASSIST-II) and space based downward looking (e.g., AIRS) passive LWIR atmospheric spectra). In particular, the ASSIST team has incorporated an LBL approach to produce a collection of inverted layer amounts for: alt(km), pres(mb), H2O, O3, CO2, CO, CH4, N2O, O2, NH3, NO, the latter all in units of 'atm cm/km'; see discussion in Section 3.

The ground and satellite state-of-the-art radiance measurements, as emulated by the modeling capabilities of the advanced version of MODTRAN®5, permits sensitivity analyses of the residuals. In all cases the model results are not being held as truth, but can provide, given a 1-3% RMS fitting (Brightness Temperature, BT(K)) of a limited subset of clear-sky measurements, a sense of the magnitude of each contributing atmospheric driver. It is important to note that MODTRAN is not a line-by-line radiative transfer code, as proposed and described in Section 5.1. Its virtue for this application is that it does replicate sensitivities realistically, while using a molecular band model approach, at 0.1 cm-1 spectral resolution. Since MODTRAN includes all the atmospheric components (Ref 4, Section 5.2) described in Section 2.1, a subset of those components has been isolated to determine their relative importance.

Only two dates have been analyzed in both the uplooking (ASSIST) and down-looking (AIRS) modes, for April 16 and May 20, 2013. A new solar irradiance has been acquired from an ultra-narrow calculation of a new solar source irradiance, extending over the full MOD5 spectral range, from 0.2 um to far-IR (ref 5, Section 5.2). Near-coincident sonde data was available for the 5/20 measurements [see discussion in Section 2.8: CAMP Sonde and AIRS Temperature and Specific Humidity Comparison]. The detailed mathematical layering analysis of the sonde profiles (developed (see section 4.4) for use in the prior Section 5 model discussion) has been directly ported to MODTRAN input and serves as the standard. Both dates also employed the inverted results from ASSIST as model input, circuitously. Additionally, because the April 16 AIRS collection exhibited broken clouds, only the ASSIST inverted profiles for a single clear-sky measurement were used, as noted above.

5.2.1 Overview of MODTRAN®: CODE DESCRIPTION

MODTRAN® is a moderate resolution atmospheric transmission, radiance and irradiance model developed as the Department of Defense (DoD) standard for arbitrary (0.2 cm^{-1} to spectrally broad) bandwidth radiative transfer applications. The code is unclassified and used by the general US Government, academia and corporations, as well as international scientific communities. MODTRAN's spectral range covers 0 to 50,000 cm^{-1}, which spans the UV through far infrared wavelengths (from 0.2 to greater than 30 µm; its spectral resolution is insufficient to support microwave research). MODTRAN has the capability for rapid calculations of atmospheric extinction, absorption, and emission, using molecular band model techniques (developed in conjunction with Spectral Sciences, Inc.). The band model is based on 0.1 cm^{-1} (also 1.0, 5.0 and 15.0 cm^{-1}) statistical binning for line centers within the interval, captured through an exact formulation of the full Voigt line shape, and accurately includes effects of far-wing contributions.

Continuum molecular absorption features (e.g., ozone in the ultraviolet [UV] and visible, plus chlorofluorocarbons [CFCs] in the infrared) are equally well accommodated. The transmission accuracy over the entire spectral range is typically of order 1% (at all resolutions) when compared to line-by-line calculations. Solar irradiance at the top of the atmosphere is defined for the same binning, such that correlations in telluric and solar line structure can be correctly convolved.

For ease of operation, MODTRAN provides relatively simple selection for default specifications of surface type and temperature, vertical profiles for ~30 molecular species (related to the HIgh-resolution TRANsmission (2008) molecular absorption database [HITRAN, Ref 8, Section 5.2] library and updated accordingly), temperature, pressure, plus a primitive set of aerosols and clouds (described both by their vertical profiles as well as their optical properties). Alternatively, user-defined options for all layered quantities are also accepted as a function of altitude or pressure, as might be collected by a typical radiosonde, at the **boundaries**, rather than integrated across the layer.

The current radiative transfer equations include full multiple scattering options (based on DISORT [ref 7, Section 5.2]) and improved vertical specification of the aerosol types, amounts and optical properties. These atmospheric profiles not only help determine the extinction due to water vapor and other absorbing molecules but are also used to calculate the (optical) slant path as a function of wavelength and user-specified path or viewing geometries associated with atmospheric refraction for altitudes up to 100 km. While the MODTRAN solar irradiances and geometries are well-defined, the lunar source and phase specifications remain rather primitive. MODTRAN has been developed and advanced through several model versions and is now in its 5th generation, referred to as MODTRAN®5, the current version being MODTRAN®5.3.0.

Because MODTRAN only includes approximations for local thermodynamic equilibrium terms associated with molecular, cloud, aerosol and surface components for emission, scattering, and reflectance, including multiple scattering, refraction and a statistical implementation of Correlated-k averaging. Spectroscopic parameters are from HITRAN 2008 with user-defined options for additional gases. Prior validation studies show that MOD5 can replicate other radiative transfer model simulations of AIRS responses, including line-by-line (LBL) brightness temperatures (BT) to within ~0.05ºK average and <.35ºK RMS, [based on MODTRAN5.3 vs R. Saunders et al., **A comparison of radiative transfer models for simulating Atmospheric Infrared Sounder (AIRS) radiances**, 2007, Ref 8, Section 5.2]. This level of agreement was reached for a single case comparison where boundary quantities are identically specified; the temperature statistics for the total of 46 cases is quite similar. **However, when comparing actual measurements to a model specified with a sonde at a distance from acquisition, the agreement is not expected to be of that fidelity.** For this limited number of CAMP cases MODTRAN®5 was found to have ~1% replication in Brightness Temperature (BT), depending upon the coincidence of the supporting measurements. For the single best case of May 20, 2013 (where both a sonde, plus the AIRS-inferred skin-temperature were available), the BT agreement was <.2% or .4K against the ASSIST instrument.

5.2.2 Radiance Equation in MODTRAN5®5

Repeating the equations of Section 5.1:

The following basic radiance equation is used in the original model (Equation 1).

$$L(\lambda) = \tau_a(\lambda)\varepsilon_g(\lambda)B(\lambda,T_g) + \varepsilon_a(\lambda)B(\lambda,T_a) \tag{1}$$

where

L is the observed radiance
λ is the wavelength
τ_a is the atmospheric transmittance
ε_g is the emissivity of the ground
B(λ,T) is the Planck function at temperature T
ε_a is the emissivity of the atmospheric constituents
T_g is the ground temperature

T_a is the air temperature

As noted, the equation is fundamental to the calculation of line-of-sight radiance calculations. The terms in MODTRAN must, of physical necessity, accomplish the same integration, but the nomenclature is different, since τ_a , the atmospheric transmittance term is built upon a bandmodel approach, (ref) where τ_a is the atmospheric transmittance, as represented by a statistical formulation at 0.1cm-1 binning; the RT equations are separated into line tails and an equivalent width formulation based on Ladenburg and Reiche functions, as discussed with respect to radiative transfer in two text books: 'An Introduction to Atmospheric Radiation, Second Edition, Liou, K.N., 2002, or Goody and Yung (1989). For the details of the mathematical approach implemented in the MODTRAN band model, see a more recent publication: Berk, A., (ref 3, Section 5.2)

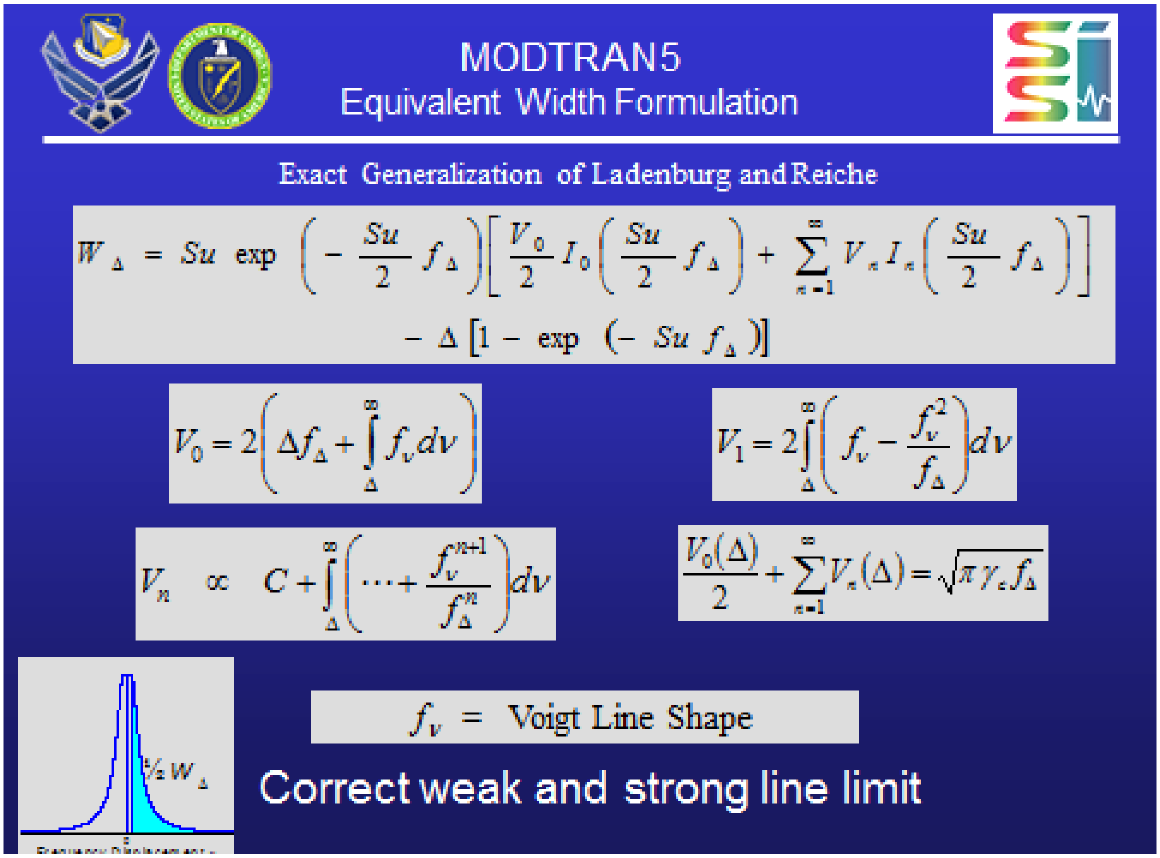

MODTRAN5
Equivalent Width Formulation

Exact Generalization of Ladenburg and Reiche

$$W_\Delta = Su \exp\left(-\frac{Su}{2} f_\Delta\right)\left[\frac{V_0}{2} I_0\left(\frac{Su}{2} f_\Delta\right) + \sum_{n=1}^{\infty} V_n I_n\left(\frac{Su}{2} f_\Delta\right)\right] - \Delta\left[1 - \exp\left(- Su\, f_\Delta\right)\right]$$

$$V_0 = 2\left(\Delta f_\Delta + \int_\Delta^\infty f_\nu d\nu\right)$$

$$V_1 = 2\int_\Delta^\infty \left(f_\nu - \frac{f_\nu^2}{f_\Delta}\right) d\nu$$

$$V_n \propto C + \int_\Delta^\infty \left(\cdots + \frac{f_\nu^{n+1}}{f_\Delta^n}\right) d\nu$$

$$\frac{V_0(\Delta)}{2} + \sum_{n=1}^{\infty} V_n(\Delta) = \sqrt{\pi \gamma_c f_\Delta}$$

f_ν = Voigt Line Shape

Correct weak and strong line limit

Figure 5.2.1 MODTRAN 5 Equivalent Width Formulation

The Figure 5.2.1 is representative of the mathematical implementation of line centers within MODTRAN. There is a rich historical basis, prior to the references above (e.g Varanasi, etal., 1972, ref 9, Section 5.2) . Within MODTRAN, line wings are matched using Padé approximates; (ref: see, for instance: Patent number: 7593835: "Reformulated atmospheric band model method for modeling atmospheric propagation at arbitrarily fine spectral resolution and expanded capabilities", issued May 6, 2010). The Patent Abstract describes the intention of the code: "A radiative transport band model method for prediction and analysis of high spectral resolution radiometric measurements. Atomic and molecular line center absorption is determined from finite spectral bin equivalent widths. A mathematically exact expansion for finite bin equivalent widths provides high accuracy at any desired spectral resolution. The temperature and pressure dependent Voigt line tail spectral absorption contributing to each spectral bin is pre-computed and fit to Padé approximants for rapid and accurate accounting of neighboring-to-distant lines. A specific embodiment has been incorporated into the MODTRAN™ radiation transport model."

It is important to note and emphasize that 'layer transmittances' are NOT multiplicative when using a bandmodel, so while 'layer boundary' quantities are supplied on input, output is only 'end-to-end' across the path. Layer-specific fluxes and energy deposition [Note: as required for energy deposition studies as summarized in Appendix C: "What constitutes the "greenhouse effect"] are generated from multiple end-to-end calculations from H1 to H2(i), where each H2(i) is the next layer boundary. Subtraction of these full 'ith' path radiances can provide an equivalent of layer-specific path quantities for flux-divergences, hemispherically integrated, as depicted in Figure 5.2.2. More recent versions of MODTRAN has an output mode (*.clr) which directly yields the derivative cooling rates.

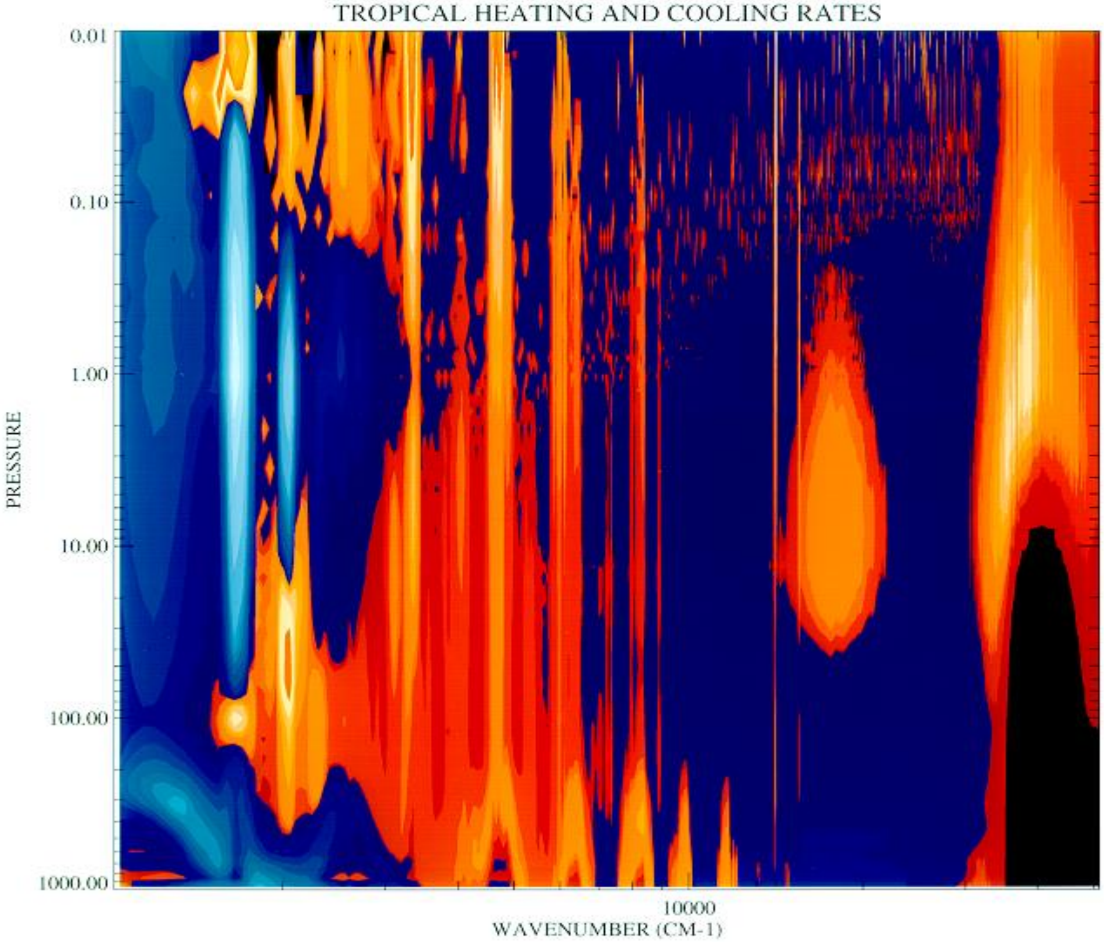

Figure 5.2.2 MODTRAN output mode for derivative cooling rates. Ref: (Bernstein, L. S., A. Berk, P. K. Acharya, D. C. Robertson, G. P. Anderson, J. H. Chetwynd, L. M. Kimball, 1996: Very Narrow Band Model Calculations of Atmospheric Fluxes and Cooling Rates. *J. Atmos. Sci.*, 53, 2887–2904.)

MOD5 can then serve as a surrogate for a variety of perturbation studies, including the solar source function, Io, with matching 0.1cm-1 spectral resolution. The 16 April data set was in the early morning, without a solar component, while 20 May incorporated a solar irradiance appropriate for the date, time of day and lat/lon location. Additionally, MOD5 calculations, using 'truth' data and satellite measurements supplied by the AIRS community, provide closure for this abbreviated study. All ~2400 AIRS spectral response functions (ISRFs) are supplied with MODTRAN®5. However, the ASSIST ISRFs have not yet been defined for automated MODTRAN integrations; the ASSIST team actually transformed some of the 0.1cm-1 MODTRAN radiance calculations on a one-by-one basis. Otherwise an embedded MODTRAN 'sinc slit' function was substituted at the specified spectral intervals; see, for instance, **MODTRAN®5.3.0.0 USER'S MANUAL**, ref 10, Section 5.2.

More specifically, the path radiance algorithm used in MODTRAN is based on an improved sublayer integration approach (ref 11, Section 5.2) that more accurately accounts for the temperature gradient within a single layer. Because band model transmittance functions are not equivalent to the Beer's law products, (eq.2, Section5.1.2), the simple and accurate approximation formulas developed for LBL sublayer integration (as stated in the earlier introduction to Section 5) do not apply. The approach adopted for MODTRAN is based on the development of a convenient analytical representation of the full range of equivalent width behaviors (Lorentz, Doppler, and Voigt) for atmospheric molecular absorption lines. The key features of this approach are summarized in a suite of earlier papers, e.g. by Berstein et al, 1996, (ref 12, Section 5.2)

5.2.3 Comparison for paired AIRS and ASSIST Calculations based on MODTRAN5®5: Input Specifications

Because MODTRAN can accommodate many (a variable definition, where 60-100 is typical) layers, the first requirement for modeling the paired AIRS and ASSIST data was to down-sample the 20 May sonde. Because a similar sonde was not available for the 16 April data set, a circular approach (using the ASSIST-retrieved results as input to MODTRAN) to then reproduce a MOD5 fit to ASSIST, was adopted.

Initial steps, then, were to decide how best to fit the MODTRAN-input requirements of layer boundaries vs. layer-thickness definitions. There is ample discussion of the layering definitions in earlier sections of this report.

Figure 5.2.3 is an example of layering options when a sonde is available, MODTRAN permits easy joining with default atmospheric profiles. In this case, mid-latitude summer was chosen for all defaults.

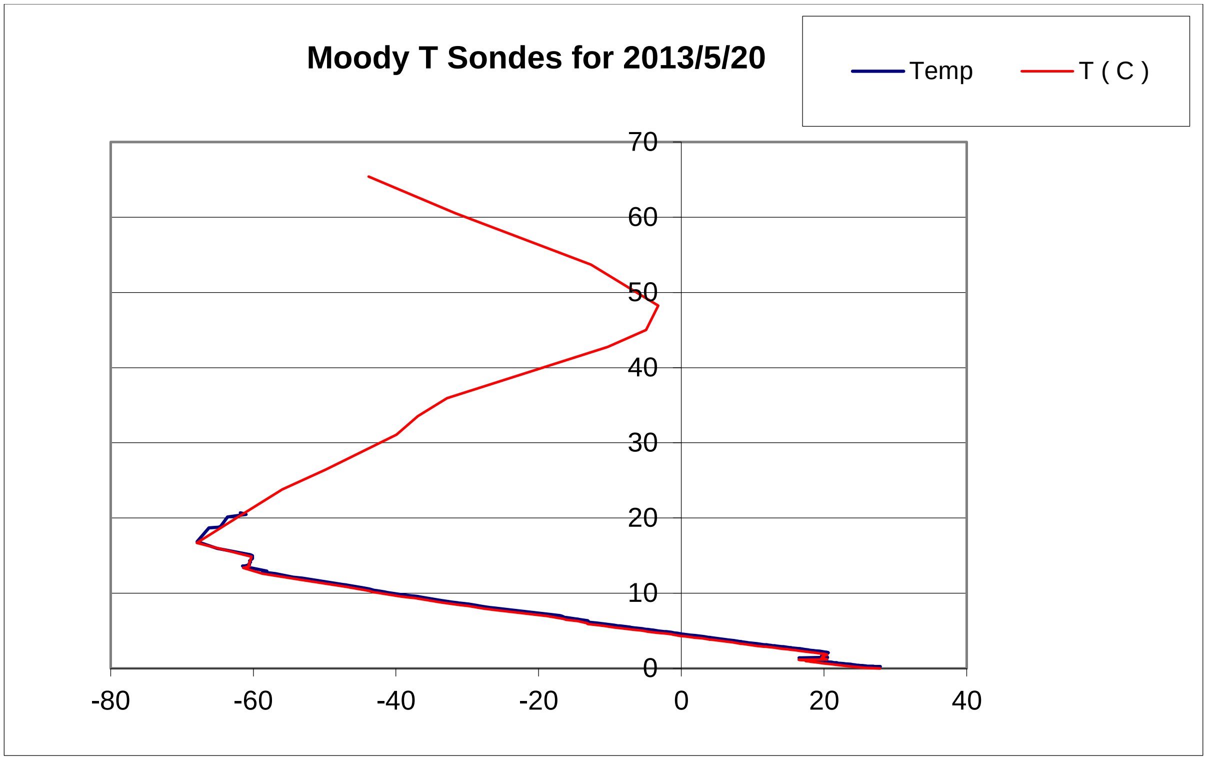

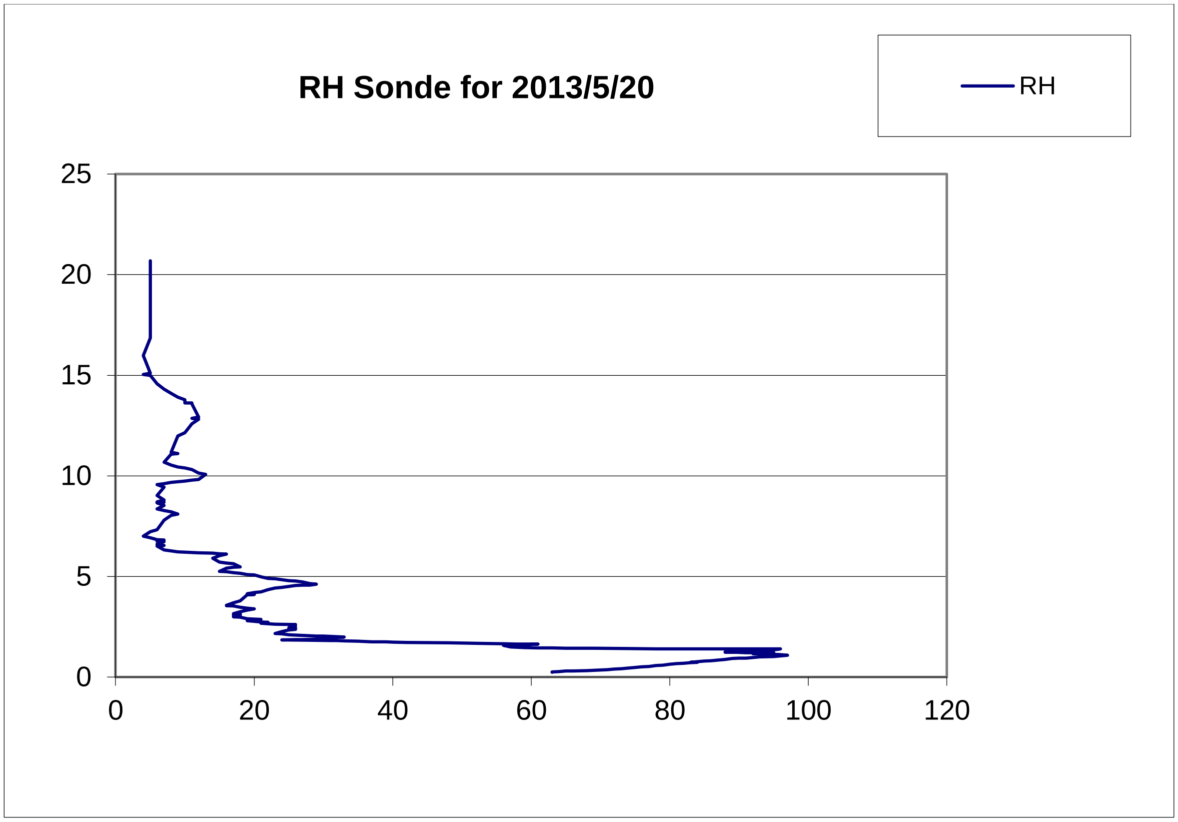

Figure 5.2.3 The pair of slides demonstrate how the detailed structure of the fine scale sonde can overlap with the default values provided within MODTRAN. The upper atmosphere is defined by built-in MOD5 profiles (ref 4, Section 5.)

For the 2013/4/16 comparisons, the layer quantities were obtained from the ASSIST retrievals. These are layer thicknesses rather than layer boundaries, leading to less MOD5 fidelity. [Aside: the loss of fidelity could easily be overcome by interpolating to layer boundaries but this has not yet been done.]

5.2.4 Comparison for paired AIRS and ASSIST Calculations based on MODTRAN5®5: Output Specifications

For the 2013 analysis, there were myriad options on input and ways to view the output. ASSIST and AIRS calculations were paired for 14 April 2013 and 20 May 2013. For 20 May data the actual 'coincident' AIRS measurements were obtained for the afternoon collect. These also included the inferred profiles. The resulting plots mimic those found in Appendix G Sections 1.10-1.14. Spatially and temporally concurrent ground based upward looking (e.g., ASSIST-II) and space based downward looking (e.g., AIRS) passive LWIR atmospheric spectra), G 1.10. Figure 5.2.4 is a detailed look at concurrent upward looking and downward looking passive LWIR hyperspectral atmospheric data.] ASSIST replaces AERI, but the intent is identical.

5.2.5 Sensitivity Studies for paired AIRS and ASSIST Calculations based on MODTRAN5®5: 4/16/2013 and 5/20/2013

In order to assure that MODTRAN5 can replicate other measurements, a second clear-sky test was undertaken, for April 16, 2013. [Note that at this time no analysis using MODTRAN's cloud and smoke capabilities has been implemented for CAMP; this has been done for other studies. [ref 13, Section 5.2] Additionally, this was an early morning case, without the need to incorporate the solar component. From an examination of the residuals for both May 20 (included in the Figure below, multiplied by -1 for visual separation) and April 16, it is apparent that the residuals are highly correlated.

The source of the residuals is under investigation. Examining the Transmittances, by species, seems to indicate that the water vapor continuum (CKD, ref14, Sections 5.2), which is known to be outdated (1989) may be at fault. MT-CKD [refs 15, 16, Section5.2] was used by all the participants in the Saunders Intercomparison (2007). It is expected to be included in the next version of MODTRAN®. As can be seen in the pair of Figures 5.3.2, the relative importance of the continuum (in red), compared to other significant absorption features, is a major spectral feature. The black line in Figure 5.3.2(a) is the 'total path transmittance' and obviously is most opaque when the continuum dominates.

An initial attempt to convert MODTRAN4 to MT-CKD was not completed and will be accomplished for MODTRAN-next. Figure 5.3.3, shows a preliminary comparison of the two continua, indicating the potential importance of the switch. Additionally, much recent effort has gone into appropriately extending the continua below 600 cm-1. See, for instance, ref 17, Section 5.2)

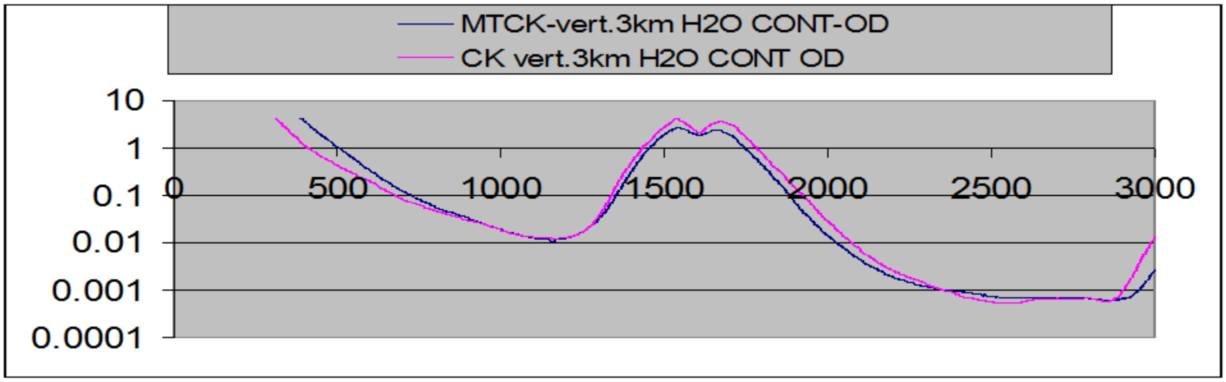

Figure 5.3.3 The two H2O continua (CKD and MT-CKD, in units of Optical Depth) are plotted over a broader spectral range and logarithmic optical depth. The relative magnitude differences between 500 and 2000 cm-1 will be critical to improving the correlation between model prediction and measurement.

Other sensitivities have been examined using modeled spectral residuals. Small perturbations on H2O and O3 (5% increment), CO2 (7 ppmv, from 402 to 395ppmv), zero CFC's vs. default, with and without the 'sun', etc. Each perturbation was made by removing the constituent from the full UP and DOWN radiance calculations, one at a time. Directionality determines the sense (+/-) of the change, resulting from the basic RT equations. The resulting radiances were then subtracted, to determine the relative sensitivity to these small perturbations. Note that each scaling is different because water so dominates the spectral response.

5.2.6 Conclusions for MODTRAN simulations of paired AIRS and ASSIST Measurements

As with prior simulation studies (see Section 6 and references), MODTRAN is a useful, simple, and fast resource. It is limited to ~1% spectral accuracy in replicating the measurements, but its ability to use the same atmosphere for up-down pairings, as well as other viewing geometries (off-nadir to tangent, etc.), while incorporating solar variability (and lunar) source functions, make it a useful tool. Instruments may be preliminarily designed with a MODTRAN-type code, but when the calibration and analyses require excellent replication and Jacobian inversions [see 3.3.1. Retrieval of Atmospheric Profiles from ASSIST Radiance Measurements; for instance, Figure 3.2 ASSIST radiance Jacobians (i.e., Sensitivity functions) for temperature, water vapor, ozone, methane, nitrous oxide, carbon monoxide, carbon dioxide, and aerosol MODTRAN can ***NOT*** undertake that step. [Final aside: Although not mentioned in this LWIR report, MODTRAN also has the flexibillity to move spectrally, through the visible and into the ultraviolet, as demonstrated by the cooling rate image.]

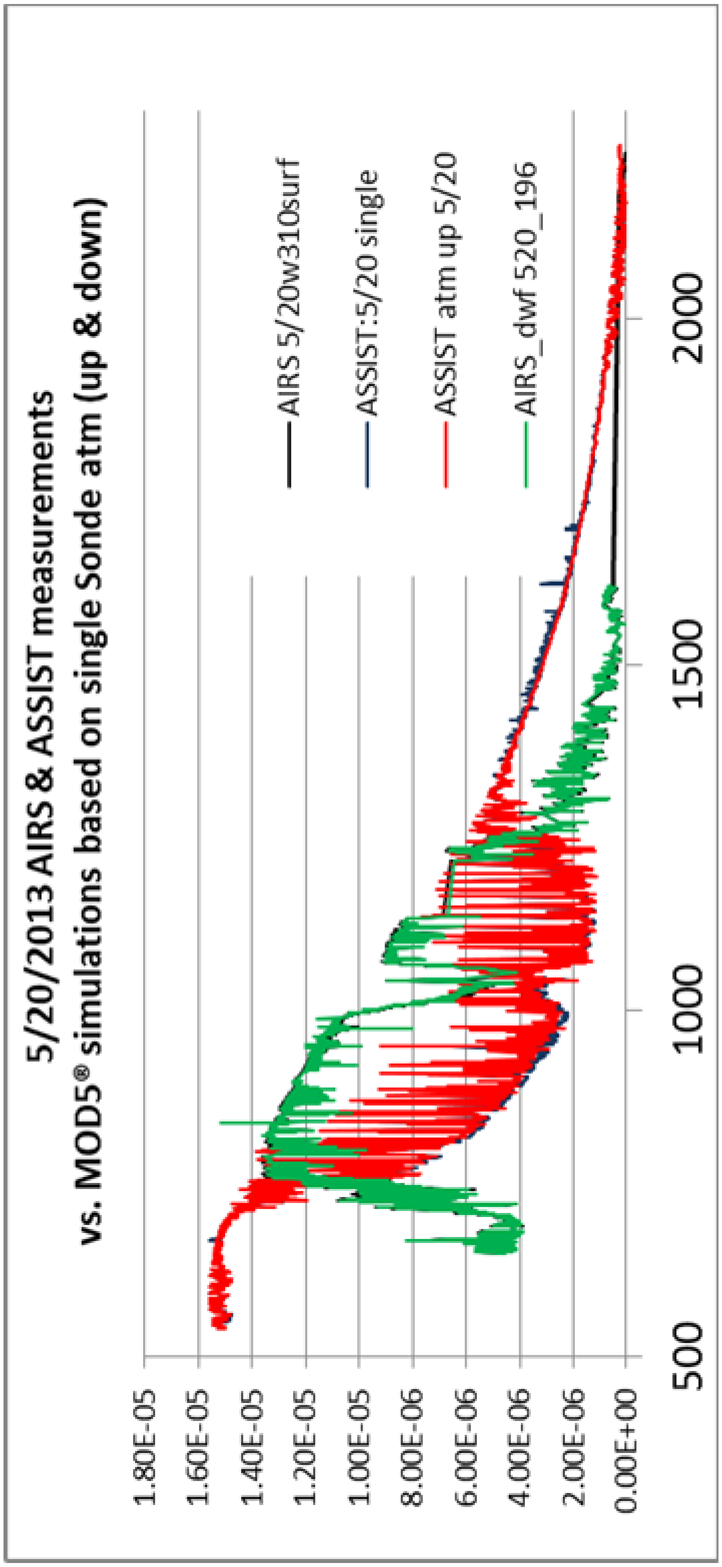

Figure 5.2.4 For May 20, 2013, both AIRS and ASSIST measurements for the same time and location. The MODTRAN simulations used the sonde data for May 20, as described earlier in Section 5, and the T-skin retrieved by the AIRS team.

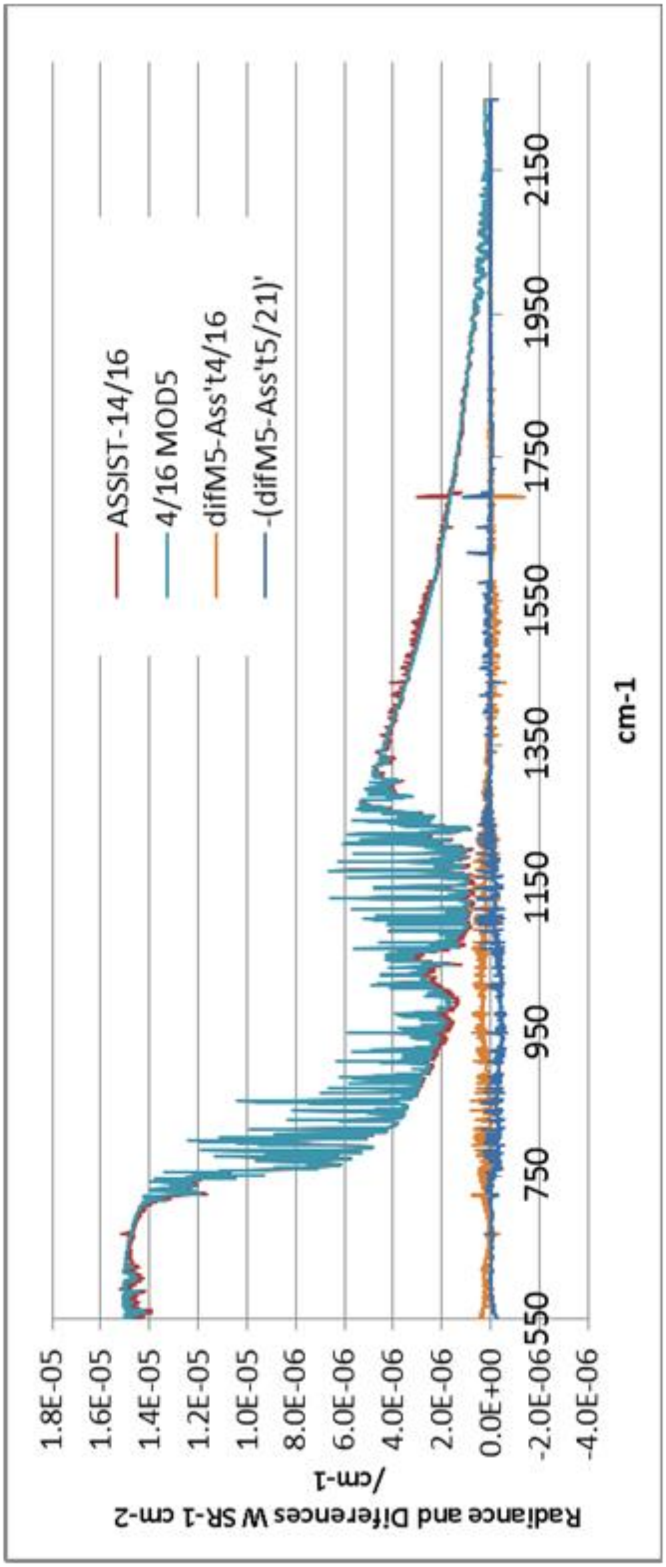

5.3.1 For April 16, 2013, only the ASSIST measurements were simulated, using the ASSIST retrieved atmospheric components. The residuals for both May 20 (multiplied by '-1') and April 16 are plotted at the bottom.

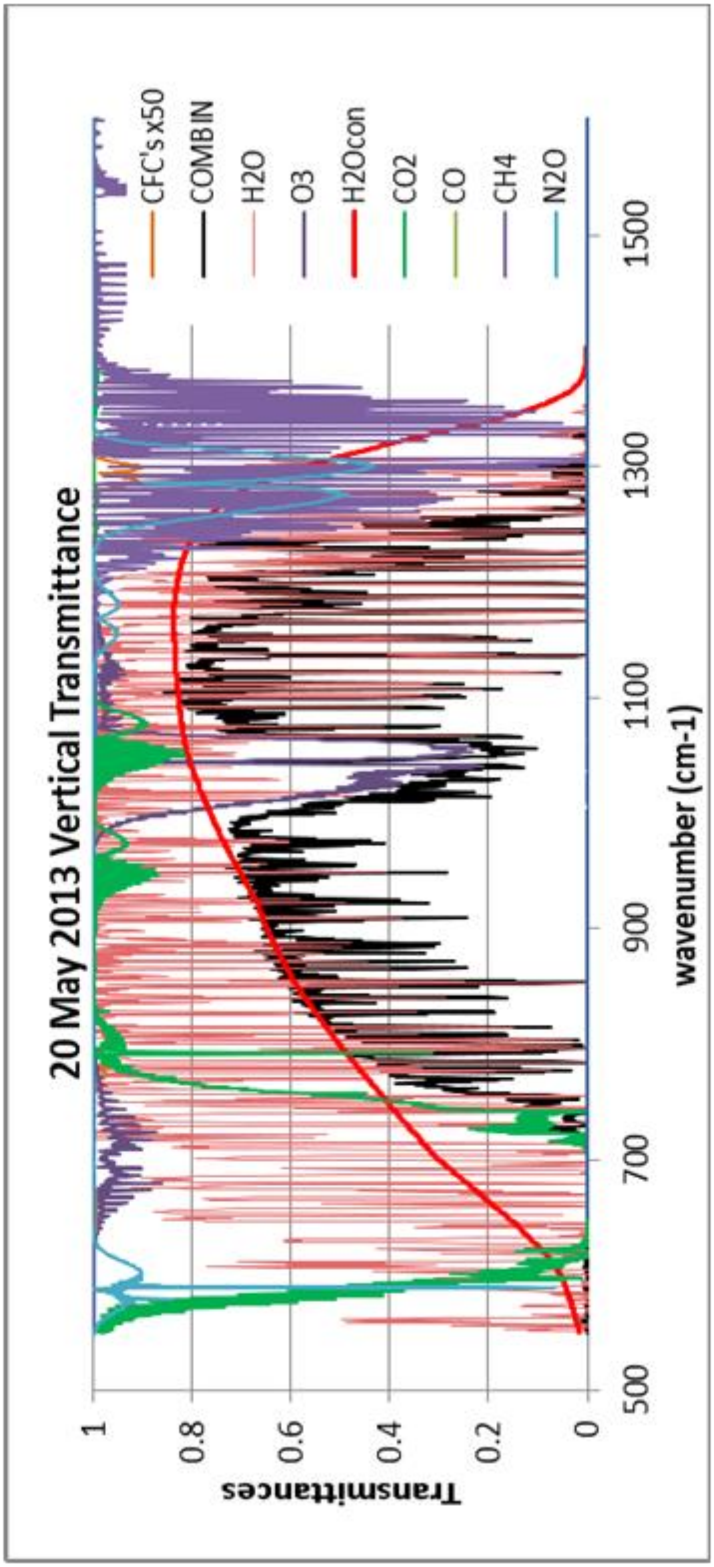

Figure 5.3.2a Transmittances for a number of atmospheric gases, between 0 and 100km, are plotted in Fig. a. In both Figs. a and Fig. b, the 'CKD' H2O continuum contribution is denoted in red.

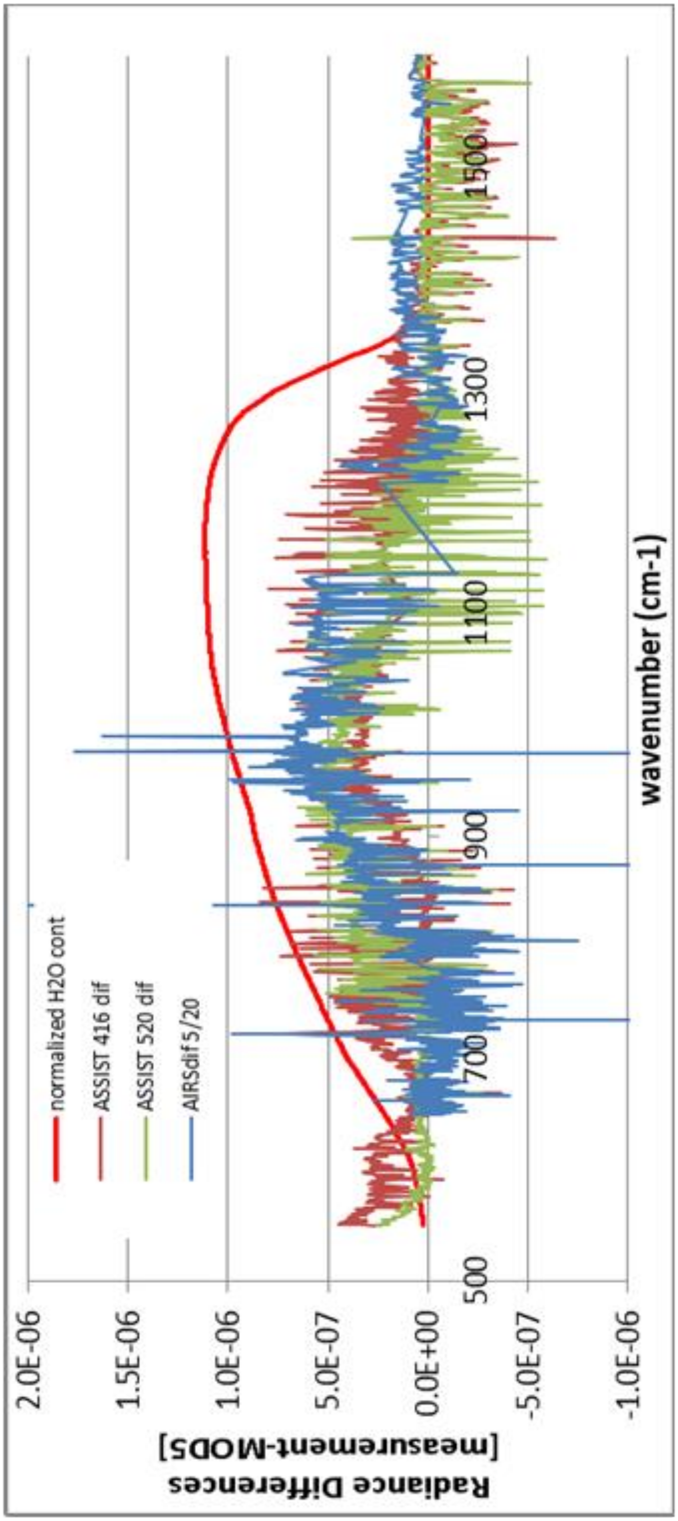

Figure 5.3.2bTResiduals: A scaled 'CKD' H2O continuum contribution is again denoted in red. Since the 'full path' transmittance is identical in the up (ASSIST) and down (AIRS) looking modes, the envelope of the CKD continuum has the highest correlation with the shape of the residual misfits between measurement and MODTRAN5. Of course there are other molecular sources for the finer scale misfits, including some due to wavelength alignment differences.

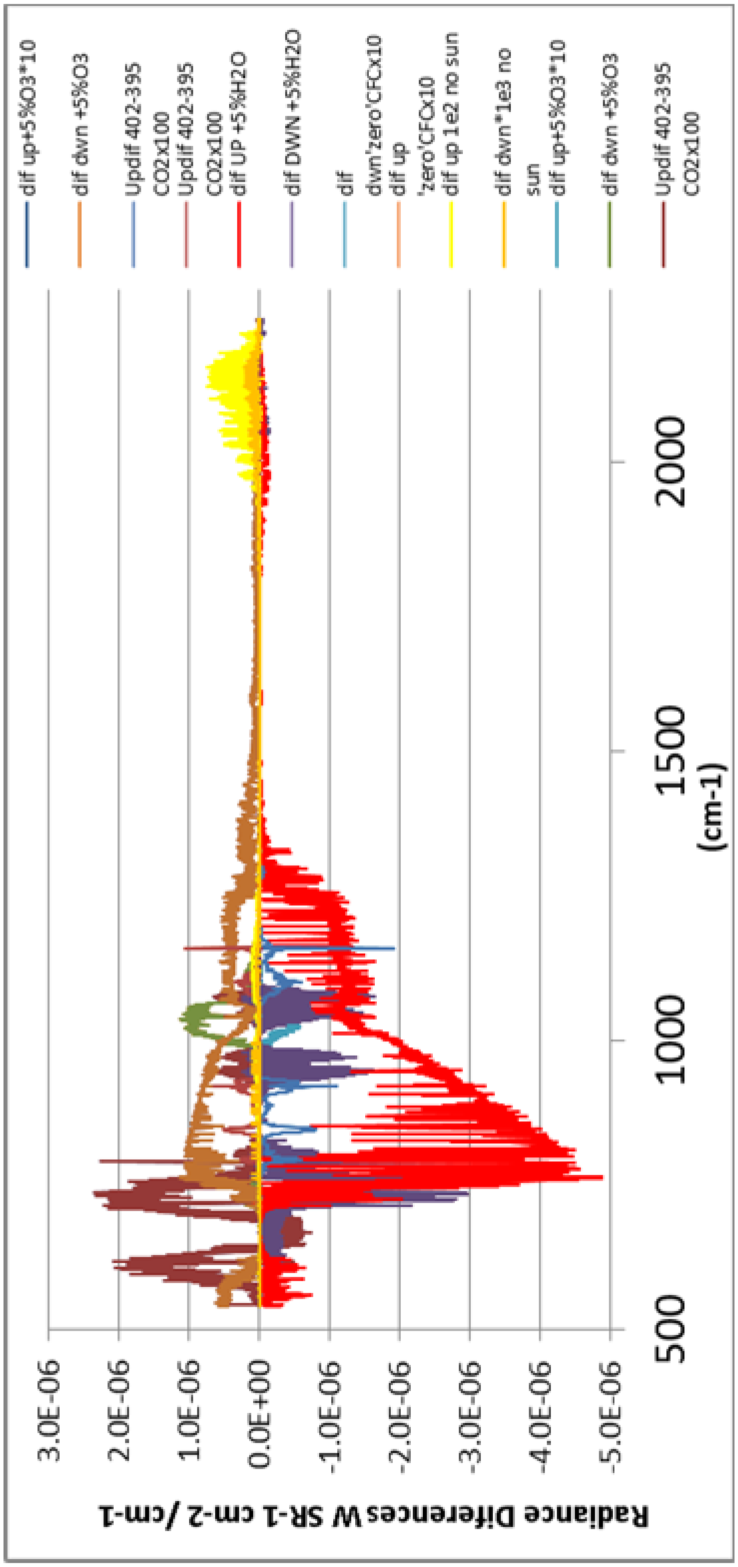

Figure 5.3.4a Figure a. shows the results of an inconsistent sensitivity test, where each molecule was perturbed uniquely within a pair of up-down MODTRAN simulations, with each such calculation subtracted from the two (up & down) control cases.

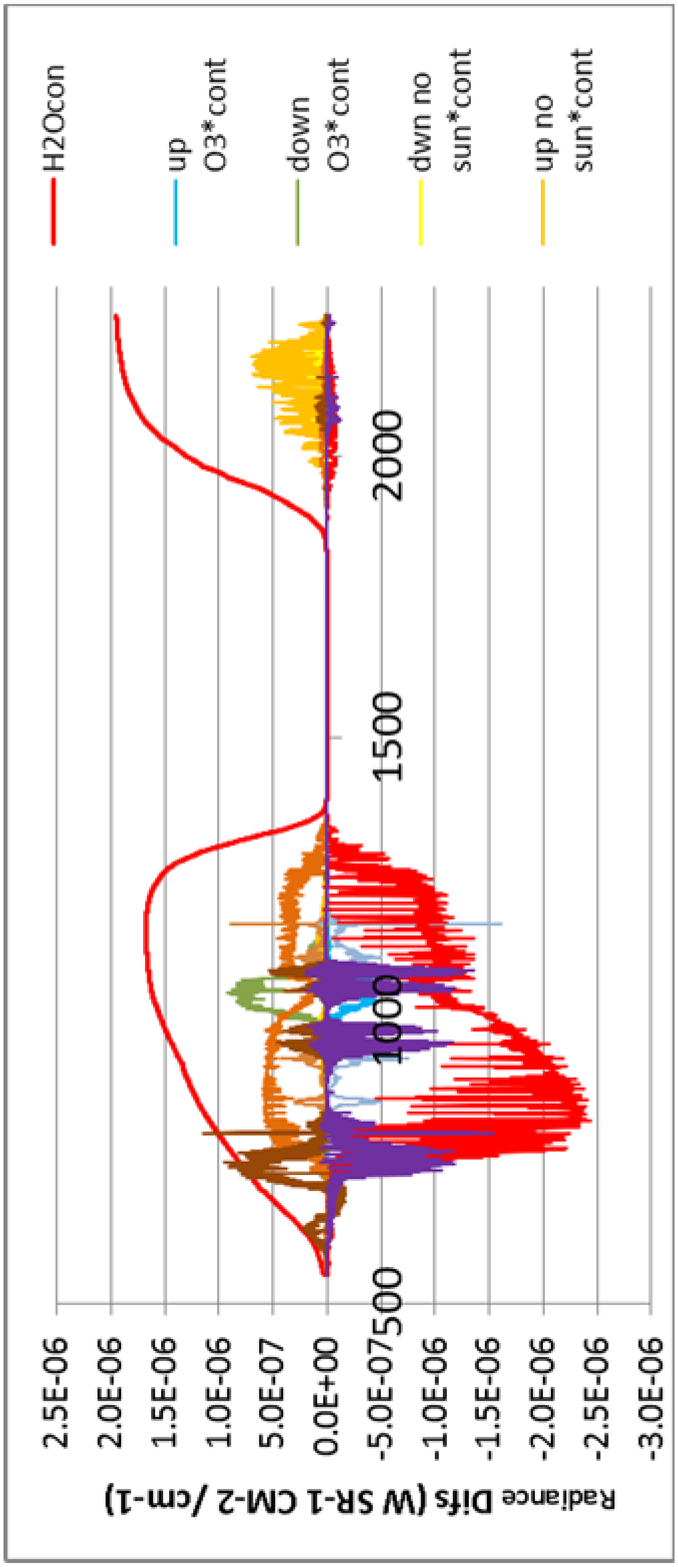

Figure 5.3.4b In Figure b. the unique sensitivity curves in Figure a. were convolved with the H2O continuum transmittance, to further demonstrate the importance of updating the current CKD implementation. Any change is the H2O continuum will impact the accuracy of MODTRAN.

5.2.7 References (Section 5.2)

1. Berk, A., P.K. Acharya, L.S. Bernstein, G.P. Anderson, P. Lewis, J.H. Chetwynd, M.L. Hoke, "Band Model Method for Modeling Atmospheric Propagation at Arbitrarily Fine Spectral Resolution," U.S. Patent #7433806, issued October 7, 2008.
2. Berk, A., G.P. Anderson, P.K. Acharya, L.S. Bernstein, L. Muratov, J. Lee, M. Fox, S.M. Adler-Golden, J.H. Chetwynd, M.L. Hoke, R.B Lockwood, J.A. Gardner, T.W. Cooley, C.C. Borel, P.E. Lewis and E.P. Shettle, "MODTRAN5: 2006 Update," Proc. SPIE, Vol. 6233, 62331F, 2006
3. Berk, A., "Voigt equivalent widths and spectral-bin single-line transmittances: Exact expansions and the MODTRAN®5 implementation", Journal of Quantitative Spectroscopy and Radiative Transfer, Volume 118, March 2013, Pages 102–120.
4. Anderson, G.P., S.A. Clough, F.X. Kneizys, J.H. Chetwynd,E. P. Shettle, AFGL atmospheric constituent profiles (0-120 km), Technical Report AFGL-TR-86-0110, AFGL, Hanscom AFB, MA. 01736, 1986.
5. Fontenla, J. M., J. Harder, W. Livingston, M. Snow, and T. Woods (2011), High-resolution solar spectral irradiance from extreme ultraviolet to far infrared, J. Geophys. Res., 116, D20108, doi:10.1029/2011JD016032.
6. Rothman, L., etal. "The HITRAN 2008 molecular spectroscopic database", Journal of Quantitative Spectroscopy & Radiative Transfer, 110, 2009, Pages 533–572.
7. Stamnes, K., Tsay, S.-C.,Wiscombe,W., and Laszlo, I.: DISORT, a General-Purpose Fortran Program for Discrete-Ordinate-Method Radiative Transfer in Scattering and Emitting Layered Media: Documentation of Methodology, Tech. rep., Dept. of Physics and Engineering Physics, Stevens Institute of Technology, Hoboken, NJ 07030, 2000.
8. Saunders, R., et al. (2007), A comparison of radiative transfer models for simulating Atmospheric Infrared Sounder (AIRS) radiances, J. Geophys. Res., 112, D01S90, doi:10.1029/2006JD007088.
9. Varanasi, etal., (1972), Line Shaper Parameters for HCl and HF in a CO2 Atmosphere, 972, JQSRT, 12, pp 857-872.
10. Berk, A , G.P. Anderson, P.K. Acharya, E.P. Shettle, MODTRAN®5.3.0.0 USER'S MANUAL, Spectral Sciences, Inc., Burlington, MA & Air Force Research Laboratory Space Vehicles Directorate, Albuquerque, NM, 2008.
11. Bernstein, L.S., Treatment of the Layer Temperature-Gradient Problem in Band Model Emission Codes, Appl. Opt., 34, pages 507-513, 1995.
12. Bernstein, L. S., A. Berk, P. K. Acharya, D. C. Robertson, G. P. Anderson, J. H. Chetwynd, L. M. Kimball, 1996: Very Narrow Band Model Calculations of Atmospheric Fluxes and Cooling Rates. J. Atmos. Sci., 53, 2887–2904.
13. Stone, R.S., et al., Radiative impact of boreal smoke in the Arctic: Observed and modeled, J. Gephys. Res., 113, D14S16, 2008.
14. Clough, S.A., F.X. Kneizys, and R.W. Davies, Line shape and the water vapor continuum, At,os. Res., 23, 29-241, 1989.

15. Mlawer, E. J., V. H. Payne, J.-L. Moncet, J. S. Delamere, M. J. Alvarado and D. D. Tobin, Development and recent evaluation of the MT_CKD model of continuum absorption, *Phil. Trans. Roy. Soc. A*, *370*, 1-37, doi:10.1098:rsta.2011.0295, 2012.]
16. Payne, V. H., E. J. Mlawer, K.E. Cady-Pereira and J-L. Moncet, Water vapor continuum absorption in the microwave, IEEE Trans. Geosci. Remote Sens, 49(6), 2194-2208, doi 10.1109/TGRS.2010.209141, 2011.
17. Delamere, J.S., S.A. Clough, V.H. Payne, E.J. Mlawer, D.D. Turner, and R.R. Gamache, A far-infrared radiative closure study in the Arctic: Application to water vapor, J. Geophys. Res., 115, D17106, doi: 10.1029/2009JD012968, 2010.

6 Assessment of Instrument Accuracy Requirement For Greenhouse Gas Concentration Retrieval

6.1 INTRODUCTION

The authors have developed the theory and process to estimate the LWIR radiance spectrum reaching to a sensor on-board an aircraft. This At-Sensor Radiance Modeling capability was developed in support of NGA's Collaborative Atmospheric Measurement Program (CAMP). The goal of the CAMP program is to obtain a thorough understanding of the quantitative accuracy of boundary layer greenhouse gas (GHG) concentration estimation derived from passive infrared remotely sensed measurement data. The CAMP study utilized spaceborne and airborne down-looking, as well as ground-based up-looking passive infrared instruments to collect near simultaneous data for quantitative GHG estimation in the lower troposphere.

The objective of the At-Sensor Radiance Modeling capability development is to use this model iteratively to estimate the at-sensor LWIR radiance spectrum by varying the concentration of CO_2 until the modeled at-sensor spectrum matches the spectrum sensed by the ASPECT's nadir looking Fourier transform infrared spectrometer (FTIS) on-board the study aircraft. The gas concentration of CO_2 used in the model that produces a match provides an estimate of the amount of CO_2 in the column of atmosphere at the time of data collection.

This report describes a study conducted to determine the effects of FTIS instrument error on the retrieved CO_2 concentration through the use of this at-sensor radiance model. The goal is to determine the FTIS instrument radiometric accuracy required to produce a CO_2 concentration estimate to within a specific percent error.

6.2 BACKGROUND

This section provides a brief description of the At-Sensor Radiance Model developed by the authors for the CAMP Program. Refer to Section 5 for detailed description of the theory and process of this forward model.

Using known or measured ground temperature, total atmospheric pressure near the ground, relative humidity, and ground emissivity, a model has been developed to generate an estimated at-sensor LWIR radiance spectrum as a function of the concentration values for four major atmospheric constituents (water vapor, CO_2, ozone, and methane). For the initial testing and evaluation, the study aircraft is assumed to be at 1000 meters AGL. The at-sensor radiance spectrum is modeled by propagating the ground radiance through 10 intervals of 100 meters of atmosphere above ground and also propagating the atmospheric radiance in each 100-meter atmospheric interval through all intervals above that interval reaching the sensor. The 1000-meter aircraft altitude and the 10 atmospheric intervals of 100 meters were used for initialization of the model. When the aircraft altitude is different from 1000 meters, the number of 100-meter atmospheric intervals used in the model will be adjusted accordingly.

Using known or measured ground temperature, total pressure near the ground, and relative humidity, this model estimates the water vapor concentration in each of the 10 atmospheric intervals based on the Clausius-Clapeyron equation and the ideal gas law. The concentrations of ozone and methane are assumed to be relatively unchanged in these 10 intervals. The objective is to use this model iteratively to estimate the at-sensor LWIR radiance spectrum by varying the concentration of CO_2 until the modeled at-sensor spectrum matches the spectrum sensed by ASPECT's nadir looking Fourier transform infrared spectrometer (FTIS) on-board the study aircraft. The gas concentration of CO_2 used in the model that produces a match provides an estimate of the amount of CO_2 in the column of atmosphere at the time of data collection. The authors have prepared and submitted a report entitled "At-Sensor Radiance Modeling Report" on October 24, 2011. This report describes in detail the theory and process of the model.

The authors subsequently prepared and submitted a revised report on December 11, 2012. This revision describes the process to estimate the LWIR radiance spectrum reaching to a sensor on-board an aircraft when the necessary ancillary information is provided by the radiosonde data. More specifically, this revision describes the process to estimate the water vapor amount in each of the 100-meter atmospheric intervals from the ground to the airborne sensor when the air temperature, total pressure, and relative humidity for each 100-meter atmospheric interval are provided by the radiosonde data.

6.3 EFFECT OF INSTRUMENT ERROR ON CO_2 CONCENRATION RETRIEVAL

Since the At-Sensor Radiance Model developed for CO_2 concentration retrieval is a forward model, the effect of Fourier Transform Infrared Spectrometer (FTIS) instrument error is determined by investigating the changes of the modeled at-sensor radiance when the input concentration of CO_2 changes. More specifically, the modeled at-sensor radiance values are converted to temperatures (as a function of wavelength), and the changes of the temperature are investigated.

Radiosonde data was not available as this study preceded the CAMP collection campaign. For this study, the ground temperature is assumed to be 25 ^{o}C, the total air pressure near the ground is assumed to be 760 mmHg, and the relative humidity is assumed to be 80%. Using these values, the saturation water vapor pressure in each of the 10 atmospheric intervals is computed based on the Clausius-Clapeyron equation and the ideal gas law. The dry air pressure for each of the 10 atmospheric intervals is computed using the Barometric model. The temperature for each of the 10 atmospheric intervals is computed using the lapse rate. Using these computed values, the water vapor concentration in each of the 10 atmospheric intervals is computed. The temperature and water vapor concentration values used as inputs to the At-Sensor Radiance Model are given in Table 6.1.

	Temperature (in ºK)	**Water Vapor Concentration (in ppm)**
Ground	298.15	21775.3106
Atmospheric Interval 1	297.8	21609.5648
Atmospheric Interval 2	297.1	21042.2946
Atmospheric Interval 3	296.4	20487.0273
Atmospheric Interval 4	295.7	19943.5866
Atmospheric Interval 5	295	19411.7967
Atmospheric Interval 6	294.3	18891.4825
Atmospheric Interval 7	293.6	18382.4698
Atmospheric Interval 8	292.9	17884.585
Atmospheric Interval 9	292.2	17397.6556
Atmospheric Interval 10	291.5	16921.5099

Table 6.1 Input Parameter Values for At-Sensor Radiance

For initial development of the model, CO_2, ozone, and methane are assumed to be well mixed gases and their concentrations are therefore assumed to be the same for all 10 intervals. Their concentrations are assumed to be:

Concentration for CO_2: C_{2i} = 387 ppm
Concentration for ozone: C_{3i} = 0.01 ppm
Concentration for methane: C_{4i} = 2.8 ppm

The At-Sensor Radiance Model generates an estimated at-sensor LWIR radiance spectrum in the 7.5 to 14.5 µm wavelength region at a sampling of approximately 0.0068 µm, resulting in 1024 spectral bands.

The At-Sensor Radiance Model first used 387 ppm as the CO_2 concentration to generate a LWIR radiance spectrum. The radiance spectrum was converted to temperature as a function of wavelength using the inverse Planck function. The process was then repeated for increased concentration levels of CO_2. The starting 387 ppm CO_2 concentration was increased by 1%, 10%, 20% and 30%. The temperature values at two wavelengths (9.55279 and 12.63196 µm) are reported. These two wavelengths were chosen because CO_2 has relatively strong absorption at these wavelengths. Although CO_2 has stronger absorption at several wavelengths higher than 13.5 µm, the available aircraft FTIS instrument has significant noise in the higher wavelength region. Therefore the two wavelengths, 9.55279 and 12.63196 µm, were chosen. Figure 6.1 shows the CO2 absorbance as a function of wavelength from 7.5 to 14.5 µm. Figure 6.2 shows the same CO2 absorbance in a different y-scale and also shows the two selected wavelengths.

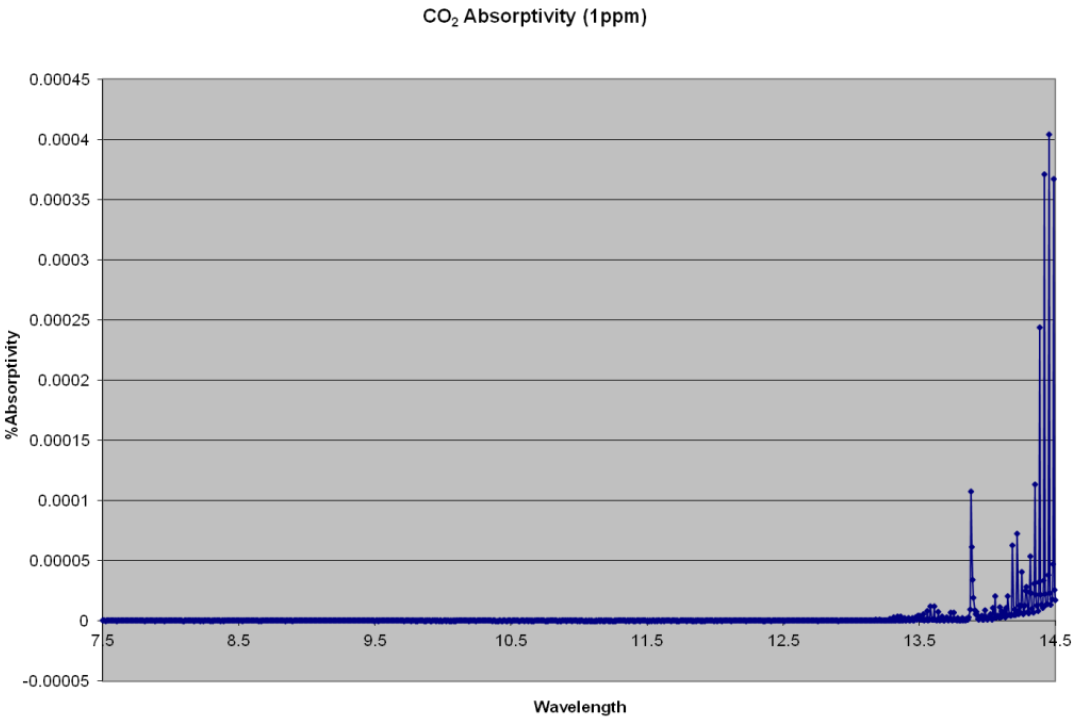
CO_2 Absorptivity (1ppm)

Figure 6.1 CO_2 Absorbance vs. Wavelength

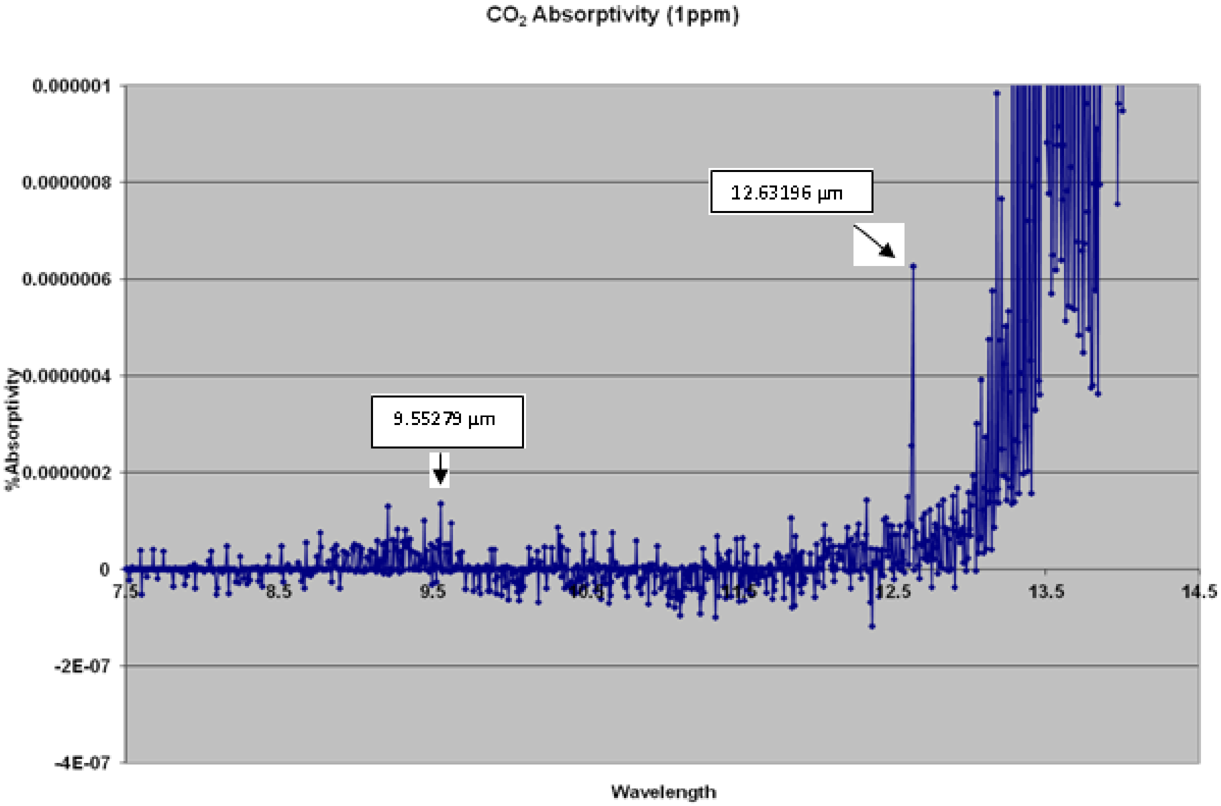
CO_2 Absorptivity (1ppm)

12.63196 µm

9.55279 µm

Figure 6.2 CO_2 Absorbance vs. Wavelength (Different y-Scale)

Table 6.2 shows the CO_2 concentration values that were used as inputs to the At-Sensor Radiance Model. Table 6.2 also shows the temperature values computed from the LWIR radiance spectrum generated by the At-Sensor Radiance Model. The temperature values reported in Table 6.2 are the temperatures computed from the modeled at-sensor radiance spectrum at 9.55279 and 12.63196 µm.

		Temperature Computed from At-Sensor Radiance Model (in ^{o}K)	
CO_2 Concentration (in ppm)	% Increase from 387 ppm	At 9.5528 µm	At 12.6320 µm
387		292.5157728	292.0462079
391	1%	292.5168468	292.0514723
426	10%	292.5262054	292.0967283
464	20%	292.5362879	292.1442521
503	30%	292.5465517	292.1913297

Table 6.2 Temperature Values Calculated from Modeled Radiance Spectra

Since CO2 has stronger absorption at 12.6320 µm than at 9.5528 µm, the temperature values calculated at 12.6320 µm are deemed more accurate. The analysis results showed that if the CO_2 concentration value is increased by 20% while all other input parameter values to the At-Sensor Radiance Model are unchanged, the temperature computed from the modeled at-sensor radiance spectrum is increased from 292.0462079 ^{o}K to 292.1442521 ^{o}K. This indicates that if the ASPECT's FTIS instrument has an error on the order of 0.1 ^{o}K, the retrieved CO_2 concentration could have an error of 20%.

6.3.1 Summary

For an accuracy of CO_2 concentration retrieval to be within 20%, the FTIS instrument accuracy requirement is 0.1 ^{o}K. If the accuracy of CO_2 concentration retrieval needs to be within 10%, the instrument accuracy requirement is 0.05 ^{o}K

6.4 References (Atmospheric Modeling and Simulation Support section 5.1 and section 6)

Paul E. Lewis, Sylvia S. Shen, David P. Miller, Gail P. Anderson, James Chetwynd, Robert Kroutil, "Analysis of concurrent space based and ground based atmospheric infrared spectrometer measurements", in Imaging Spectrometry XIII, Sylvia S. Shen; Paul E. Lewis, Editors, Proceedings of SPIE Vol. 7086 (SPIE, Bellingham, WA 2008), 70860F.

Paul E. Lewis, Gail P. Anderson, Sylvia S. Shen, James Chetwynd, Miguel Roman III, Crystal Schaaf, David D. Turner, David A. Rutan, Alexander Berk, David P. Miller, Robert Kroutil, "MODTRAN5 analysis of clear-sky, co-located space- and ground-based infrared atmospheric measurements: AERI, AIRS, CERES, MODIS", in Algorithms and Technologies for Multispectral, Hyperspectral, and Ultraspectral Imagery XV, Sylvia S. Shen; Paul E. Lewis, Editors, Proceedings of SPIE Vol. 7334 (SPIE, Bellingham, WA 2009), 733410.

P. Hanst, Infrared Spectra for Quantitative Analysis of Gases, Infrared Analysis Inc. A collection of 296 vapor-phase infrared spectra supplied in digital format. Infrared Analysis Corporation, Anaheim, CA. Available on the World Wide Web at http://www.infrared-analysis.com.

Weast, R.C. (Ed.). (1975). Handbook of Chemistry and Physics 55th edition. CRC Press.

Houghton, J.T. (1986). The Physics of Atmospheres, second edition. Cambridge University Press.

Goody, R.M. (1964). Atmospheric Radiation I. Oxford at the Clarendon Press.

Wallace, J. M. Hobbs, P.V. (1977). Atmospheric Science An Introductory Survey. Academic Press Inc.

Appendices A-J contain relevant background and supplementary information

Appendix A Issues surrounding data collection-analysis and reducing emissions of greenhouse gases (GHG)

Appendix A-1.0 CAMP data collection analysis objective

The explicit objective of the United States Environmental Protection Agency (US-EPA) Mandatory Reporting of GHG Rule is to collect accurate and timely emissions data to inform future policy decisions. This objective is considered to be an essential and responsible approach to addressing the issue of global warming associated with GHG emissions. Participation by the United States in a collaborative monitoring and verification role in future greenhouse gas emission related treaties between the United States of America and other participating countries will necessitate the use and enhancement of civil assets and internationally accepted measurement methodologies.

It is not clear at this time if or in what form monitoring and verification will be specified as part of any “treaty”. Nevertheless, NGA anticipates that remotely sensed measurements of GHG emissions from ground based, airborne, and space based civil platforms will become increasingly important future measurement sources and tools for the monitoring of GHG emissions from regional sources, to augment the global physical measurement grid (see Appendix F).

To this end, NGA and its CAMP authors have endeavored to obtain a parametric understanding of the quantitative accuracy of GHG estimation derived from remotely sensed passive LWIR infrared spectral data. The research presented in this report focuses on the following areas:

- Identification of the parametric variables associated with GHG estimation derived from laboratory and field (i.e. ground, airborne, and space) remotely sensed infrared spectral data.

- Assessment of the magnitude of individual and cumulative errors associated with these parametric variables on the quantitative accuracy associated with GHG estimation derived from remotely sensed laboratory and field (i.e., ground, airborne, and space) spectral data (within the limitations of CAMP resources).

- Determining useful quantitative accuracy ranges associated with GHG estimation derived from remotely sensed laboratory and field (i.e., ground, airborne, space) infrared spectral data through careful experimental designs, in which remotely sensed infrared spectral data derived quantitative GHG estimations in ppm are compared to physical sample measurements taken concurrently and converted to ppm (within the limitations of CAMP resources).

Finally, the goal of the CAMP activity and this final report is to provide a compendium to the literature on the assessment of derivation of greenhouse gases (GHG) estimation from passive LWIR spectral data, recommended methodologies, technical issues, and regional applications. The CAMP final report is offered as scientific evidence in support of the next generation passive LWIR remote sensing technologies needed by GHG/Climatology modelers and our policy and decision makers in addressing global warming.

Appendix A-1.1 Issues surrounding reducing emissions of greenhouse gases (GHG)

The following paragraphs provide insight into the struggle to find a basis for regulation of GHG emissions in the United States. Implicitly, they illustrate the struggle between economic and environmental needs in the United States and the rest of the world.

Pragmatic:

The major obstacle to progress in addressing global warming is the debate/struggle between economic and environmental interests which revolves around the following questions:

1. First, is global climate change real?
2. Second, if it is real, is global climate change due to the anthropogenic generation of greenhouse gases?

In the face of extensive scientific evidence, a country's debate position over the regulation of greenhouse gases (GHG) will take different postures based on their laws and industrial stage of development, dependencies, etc. At present, the key to international cooperation in addressing the danger do to the effect of global warming on each country still requires extensive negotiations and skilled diplomacy before significant reduction measures will be taken by the major GHG producing countries.

Political:

In August of 2003, the US Administration reversed the 1998 decision of the previous administration, which had classified carbon dioxide as a pollutant, and made it subject to the provisions of the Clean Air Act. As a result of the reversal of the 1998 decision, automobile manufacturers and power plants have been able to avoid making costly modifications that would have been required under the 1998 ruling.

Legislative:

In 2006, environmental groups pushed for legislation that would reinstate carbon dioxide as a pollutant. In August of 2006, EPA General Counsel Robert Fabricant concluded that since the Clean Air Act does not specifically authorize regulation to address climate change, CO_2 is not a pollutant.

On April 2, 2007, after a four-year court battle, the Supreme Court of the United States ruled 5-4 that carbon dioxide and other heat-trapping emissions are “air pollutants” under the Clean Air Act, and that the U.S. government already has authority to start curbing them.

Subsequently, the US-EPA has issued the Final Mandatory Reporting of Greenhouse Gases Rule. The rule requires reporting of GHG emissions from large sources and suppliers in the United States, and is intended to collect accurate and timely emissions data to inform future policy decisions.

Under the rule, suppliers of fossil fuels or industrial greenhouse gases, manufacturers of vehicles and engines, and facilities that emit 25,000 metric tons or more per year of GHG emissions are required to submit annual reports to EPA. The gases covered by the proposed rule are carbon dioxide (CO_2), methane (CH_4), nitrous oxide (N_2O), hydrofluorocarbons (HFC), perfluorocarbons (PFC), sulfur hexafluoride (SF_6), and other fluorinated gases including nitrogen trifluoride (NF_3) and hydrofluorinated ethers (HFE).

The final rule was signed by the EPA Administrator on September 22, 2009. On October 30, 2009, the final rule was published in the *Federal Register* (www.regulations.gov) under Docket ID No. EPA-HQ-OAR-2008-0508-2278. The rule will be effective December 29, 2009. This action includes final reporting requirements for 31 of the 42 emission sources listed. At this time, EPA is not finalizing the remaining source categories as they further consider comments and options.

Arguments:
Opposition to curbing of GHG in the United States has been from dozens of states and industry groups (there were more than 60 lawsuits all told). Opposition has challenged EPA’s actions on three grounds:

> First, they argue that the EPA’s determination that greenhouse gases “threaten the health and welfare of current and future generations” was wrongly decided. Second, the groups argued against individual EPA rules, like the fuel-economy standards for cars and light trucks. Third, plaintiffs also argued that the agency’s “Tailoring Rule”, in which the EPA limited its regulations to *only* the biggest power plants and facilities, was a misreading of the Clean Air Act.
>
> On Tuesday June 26, 2012 , the U.S. Court of Appeals for the District of Columbia Circuit ruled that the Environmental Protection Agency (EPA) was “unambiguously correct” in moving ahead to set limits on greenhouse gas emissions from power plants and automobiles.
>
> The three-judge panel rejected all three of these arguments. On the first, the court ruled that the EPA had “substantial record evidence” that greenhouse gases are heating up the planet. The judges essentially deferred to the EPA’s in-house expertise on this matter. “In

> the end, petitioners are asking us to re-weigh the scientific evidence before EPA and reach our own conclusion," the panel wrote. "This is not our role." [1]

Progress:
It should be noted that the Supreme Court ruling of 2007 that the U.S. Government has the authority to regulate GHG under the Clean Air Act is the basis upon which the EPA moved ahead with crafting new fuel-economy standards for cars and light trucks. The U.S. is experiencing the positive effects of this legislation manifested in the efficiency improvements of today's automobiles and their affect on fossil fuel consumption.

Appendix A-1.2 Intergovernmental Panel on Climate Change (IPCC)

To address the first question, "Is global climate change real?" The Intergovernmental Panel on Climate Change (IPCC) position of January 2001 managed to establish a consensus, phrased so cautiously that scarcely any expert or government representative dissented. It states:
An increasing body of observations gives a collective picture of a warming world and other changes in the climate system... There is new and stronger evidence that most of the warming observed over the last 50 years is attribuTable to human activities.[2]

The main conclusions of the IPCC on global warming were the following:

1. The global average surface temperature has risen 0.6 ± 0.2 °C since the late 19th century, and 0.17 °C per decade in the last 30 years.[3]
2. There is new and stronger evidence that most of the warming observed over the last 50 years is attribuTable to human activities, in particular emissions of the greenhouse gases carbon dioxide and methane.[4]
3. If greenhouse gas emissions continue, the warming will also continue, with temperatures projected to increase by 1.4 °C to 5.8 °C between 1990 and 2100. Accompanying this temperature increase will be increases in some types of extreme weather and a projected sea level rise.[5] On balance the impacts of global warming will be significantly negative, especially for larger values of warming.[6]

No scientific body of national or international standing has maintained a dissenting opinion; the last was the American Association of Petroleum Geologists, which in 2007 updated its 1999 statement rejecting the likelihood of human influence on recent climate with its current non-committal position.[7, 8]

Appendix B Overview of CAMP atmospheric measurement campaign, regional study areas, and schedule

Appendix B-1.0 Atmospheric measurement campaign

The CAMP has facilitated the coordination of spatially and temporally concurrent collection of passive LWIR spectral data from ground based (see Section 3), aircraft based (see Section 4), and space based (see Section 2) platforms from July 2012 through August 2013. Ground based zenith looking and space based nadir looking passive LWIR spectral data was collected on a continuous basis at the Department of Energy Atmospheric Radiance Measurement (ARM) site in Lamont, OK and at the McKinney TX Municipal Airport North-North-East of the Dallas-Fort Worth metropolitan area. In addition, ancillary measurement support data from the ARM site has been obtained on a continuous basis for this time period and used in support of the ground based and space based GHG profile retrievals for the Lamont, OK region. Available weather data was obtained and assimilated on a continuous basis for this time period and used in the generation of ground based and space based GHG profile retrievals for the McKinney TX, Dallas-Fort Worth metropolitan region. These continuous regional collections were augmented periodically (see section 4) with aircraft based nadir looking passive LWIR spectral and physical gas sampling data collection at altitudes of 1000, 2500, 5000, 7500, and 10000 ft. AGL. The aircraft based LWIR spectral and physical gas sampling data was conducted within +/- one hour of satellite regional overpass and served as water vapor and carbon dioxide validation and verification data for the lower troposphere. Note: Aircraft validation and verification flights were limited due to cost. During aircraft flights, calibrated radiosondes were released to coincide (+/- one hour) with satellite regional overpass.

Detailed discussions of instrumentation, technical approaches, measurements, methodologies, retrieval algorithms, and data can be found throughout this report and its references.

Appendix B-1.1 Regional study areas

The CAMP project collected measurement data over a large regional CO_2 source Dallas - Fort Worth Texas (DFW) and a rural region Lamont Oklahoma (LOK) in Grant County and Moody Texas. LOK represents an area that is geographically distant from any specific large CO_2 emission source.

Figure B-1 shows the area of the United States where the CAMP regional data has been collected. Historical climatology data was compiled for the study area and regions and evaluated by the CAMP team for use in the design of the study and subsequently in understanding analysis results from the collected data (see Appendix I & J). Analysis of the climatological data shows that seasonal variation in the direction of prevailing surface and upper level winds should provide an opportunity to measure and characterize the DFW CO_2 regional source and to correlate its effect on CO_2 measurements in the LOK area. Demonstration of the ability to measure and characterize a large regional CO_2 emitter has been identified as an essential step in increasing the fidelity of the input to global climate prediction models, as well as the determination of the effectiveness of GHG reduction activities on a regional scale. The CAMP project will also serve as a baseline for determining the feasible, cost effective, and best practice passive LWIR spectral data collection procedures for characterization of regional GHG source and sinks.

Figure B-1. CAMP Regional Study Area

Figure B-2a and B-2b show the CO_2 emission source locations and size for the CAMP study regions based on EPA documentation. This information was used in order to determine the placement of in situ ground based ASSIST II zenith infrared measurement instrument described in Section 3 of this document and to determine the best geographical locations for collection of whole gas samples and nadir infrared measurements from the CAMP study aircraft.

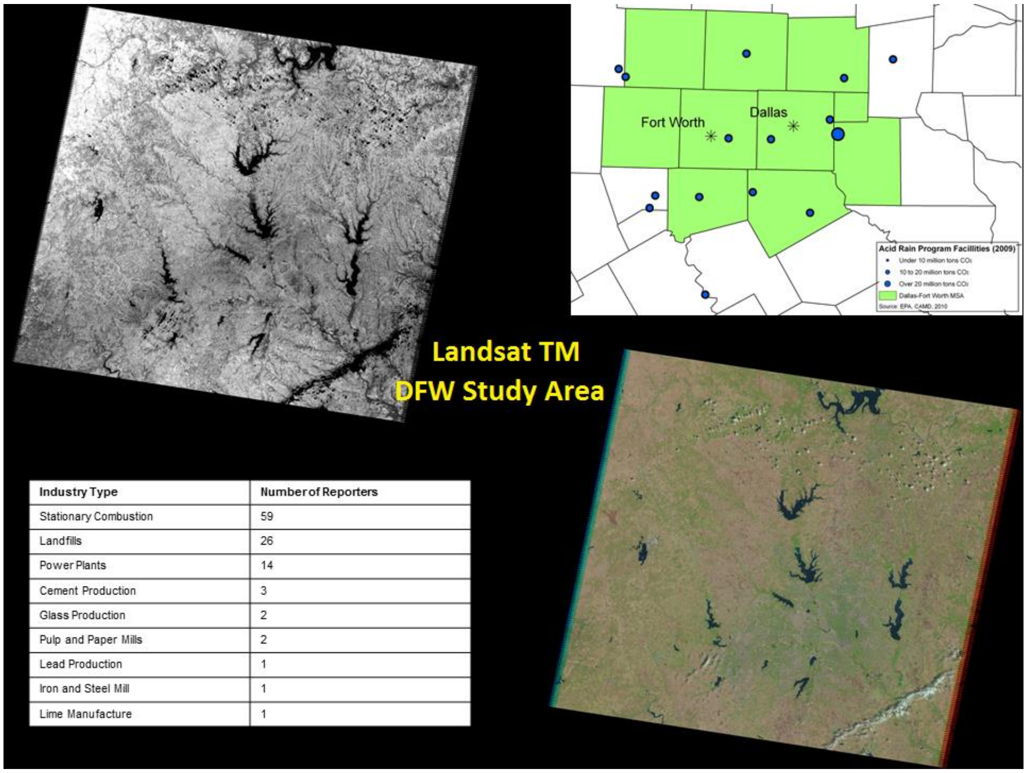

Industry Type	Number of Reporters
Stationary Combustion	59
Landfills	26
Power Plants	14
Cement Production	3
Glass Production	2
Pulp and Paper Mills	2
Lead Production	1
Iron and Steel Mill	1
Lime Manufacture	1

Figure B-2a. CO_2 emission sources, locations, sizes for the Dallas-Fort Worth, TX (DFW) area. Courtesy EPA Climate Change Division-Office of Atmospheric Programs

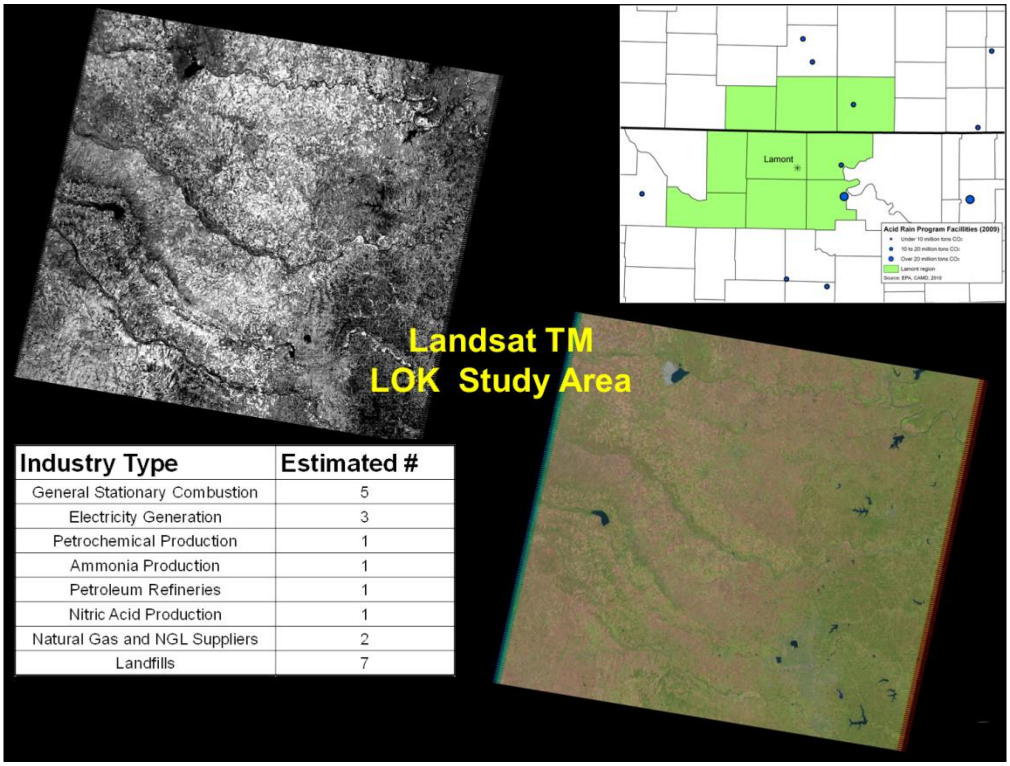

Industry Type	Estimated #
General Stationary Combustion	5
Electricity Generation	3
Petrochemical Production	1
Ammonia Production	1
Petroleum Refineries	1
Nitric Acid Production	1
Natural Gas and NGL Suppliers	2
Landfills	7

Figure B-2b. CO_2 emission sources, locations, sizes for the Grant County, OK area. Courtesy EPA Climate Change Division-Office of Atmospheric Programs

Appendix B-1.2 Collection schedule

The duration of the CAMP project study was initially planned for one year (See Figure B-3). This provides a sufficient time frame to assess the seasonal effect of climate on the transport of CO_2 from the source region DFW, TX along with seasonal comparison to the measurements taken in Grant Count, OK (LOK a non-CO_2 emitter) as well as data and measurements from the NOAA Carbon Tracker facility in Moody, TX. Figure B-3 depicts the general synchronization process for collection. This schedule was altered to include spring April and May 2013 collections. Note: Due to the unexpected timelines encountered for procurement of equipment, development and assembly of the required equipment and instrumentation, collection, and measurement procedures presented in Section 4 a statistically significant number of physical measurement collections over the period depicted in Figure B-3 was not achieved. Nevertheless, the validated and verified collection and measurement procedures and instrumentation presented in section 4 was achieved along with a limited number coordinated physical measurement collections over the Moody, TX site during April and May of 2013.

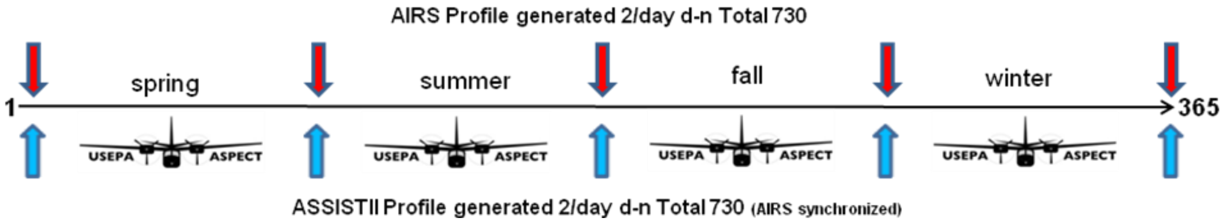

Figure B-3 Data collection and synchronization process for the regional area measurement data

Appendix C What constitutes the “greenhouse effect”

Appendix C-1.0 Temperature and heat transfer

Temperature is a measure of the internal heat energy of a substance like Earth’s Atmosphere. The motion of the molecules of a substance is faster at a higher temperature. Heat transfer can be accomplished in four ways: (1) conduction – where faster moving warmer molecules of substance #1 collide with the slower moving molecules of substance #2, which becomes hotter. Heat transfer via conduction occurs between the atmosphere and the Earth’s surface and is referred to as sensible heat flux; (2) phase changes – where a liquid absorbs energy and evaporates into the adjacent or surrounding gas removing heat from the liquid and cooling it. Heat transfer via phase change occurs between Earth’s surface water and the adjacent atmosphere and is referred to as latent heat flux; (3) convection – when a liquid or gas is heated, typically from below, energetic molecules of the heated substance are less dense rise and are replaced by cooler state molecules of the same substance. This is referred to as circulation of heat and it occurs in Earth’s atmosphere and oceans; (4) radiation – all materials emit electromagnetic field waves referred to as radiation, which propagate at a speed of 3.0×10^8 meters/second like the waves on the surface of a pond when a stone is dropped. This emitted radiation interacts with the molecules of a substance like the Earth's surface and atmosphere raising its temperature.

Appendix C-1.1 Earth's energy budget

Temperature on Earth and hence climate is determined by the amount and distribution of incoming solar radiation. Solar radiation is either, scattered and reflected by clouds and aerosols, absorbed by earth's atmosphere, or transmitted to the surface of the earth, where it is subsequently absorbed or reflected. Absorbed shortwave solar radiant energy is transformed into sensible heat, latent heat, potential energy, and kinetic energy before being emitted as long-wave infrared radiant energy by the earth and its atmosphere. Solar energy may be stored for some time, transported in various forms, and converted amongst the different forms, giving rise to a variety of weather or turbulent phenomena in the atmosphere and ocean. Using multiple sources of measured solar radiance data coupled with radiative transfer and climate model calculations Trenberth, Fasullo, and Kiehl[9] present a concise picture of the global annual mean energy budget from 2000 to 2004 (see Figure C-1). This picture is most useful in showing the complex interactions of solar energy as it passes into and out of the realm of the earth and its atmosphere.

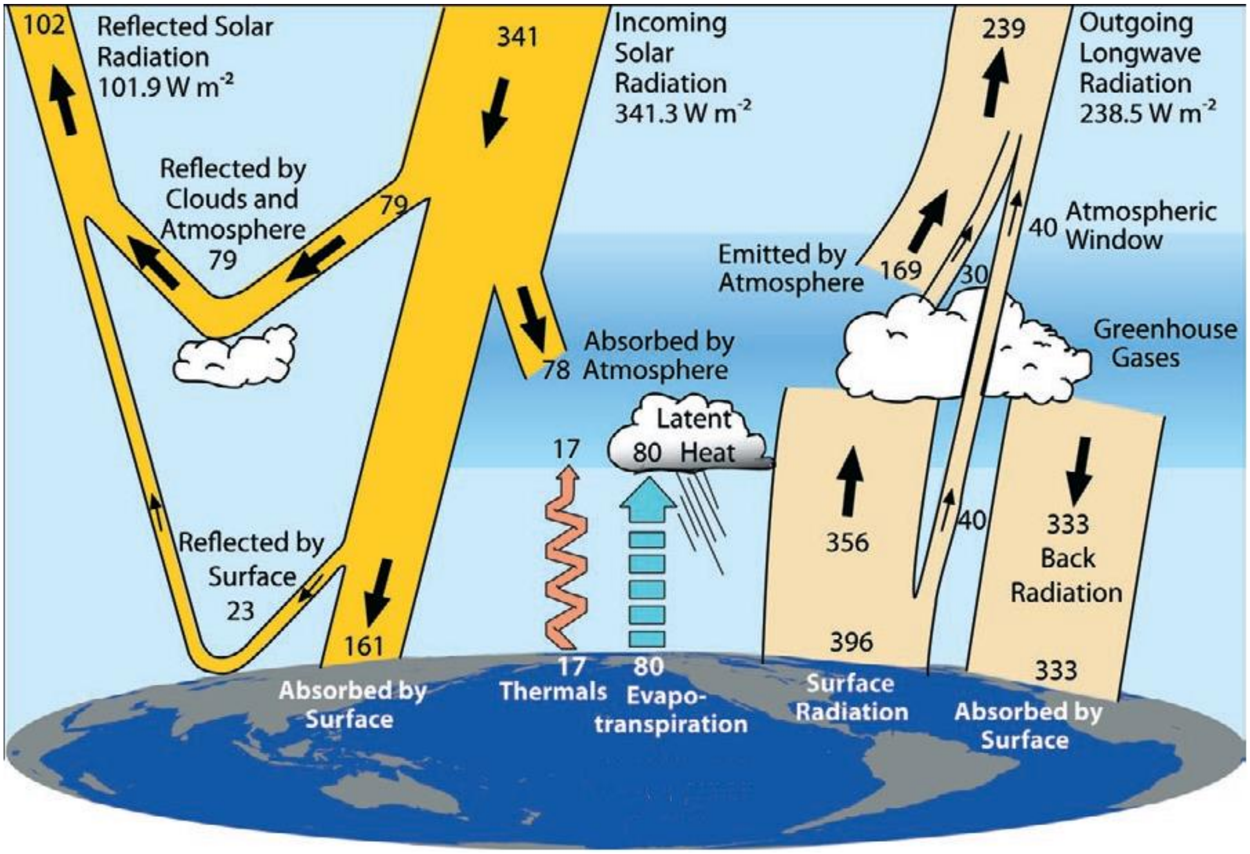

Figure C-1. Earth's global annual mean energy budget (Wm^{-2}) for March 2000 to May 2004. Illustration from Trenberth, Fasullo, and Kiehl[9]

Appendix C-1.2 The greenhouse effect

The greenhouse effect is the process by which absorption and emission of infrared radiation by gases in the atmosphere warm a planet's lower atmosphere and surface. It was proposed by Joseph Fourier in 1824 and was first investigated quantitatively by Svante Arrhenius[10] in 1896. Figure C-1 is also most useful to illustrate the greenhouse effect. Consider the topmost set of black arrows as depicting an equilibrium climate, where the effective radiating temperature of the earth T_e is governed by the balance between absorbed solar radiation and emitted LWIR radiation in a state of equilibrium. Essentially, the earth receives a total amount of radiation referred to as the solar constant $S_0 \approx 1366$ W/m^2, determined by earth's cross section ($\pi \cdot R_E^2$). As the earth rotates, this energy is distributed across the entire area of earth's sphere ($4 \cdot \pi \cdot R_E^2$). Hence the average incoming solar radiation is one-fourth the solar constant ≈341 W/m^2. If we assume the average reflective value for the earth surface and its atmosphere (albedo) to be 0.3, we obtain the values shown for Reflected Solar Radiation 102 W/m^2, Incoming Solar Radiation 341 W/m^2 , and outgoing Longwave Radiation 239 W/m^2 respectively in Figure 4. Again, for this system in equilibrium we can set the total absorbed solar radiation equal to the total emitted radiation invoking the Stefan-Boltzmann law and calculate the effective radiating temperature of the earth T_e:

$$\pi R^2(1-A)S_0 = 4\pi R^2 \sigma T_e$$

$$T_e = \left[\frac{S_0(1-A)}{4\sigma}\right]^{1/4}$$

where, R=radius of the earth, A=earth albedo (≈0.3), S_0=solar constant (1366 W/m^2), σ=Stephen-Boltzmann constant (5.67x10^{-8}Wm^{-2}K^{-4}).

$$T_e = \left[\frac{1366(.7)}{4 * 5.67\text{x}10-8}\right]^{1/4}$$

T_e=254K or -19.15C

An estimation of the average measured surface temperature of the earth $T_s \approx 288$K. The excess temperature:

$$T_s - T_e = the\ greenhouse\ effect$$

The gases and clouds making up earth's atmosphere are responsible for $T_s - T_e > 0$ resulting in the greenhouse effect. The greenhouse effect is a naturally occurring phenomenon on earth, which enables life as we know it. However, the enhancement of this effect by anthropogenic activities resulting in increasing atmospheric concentrations of GHG and related changes in surface reflective properties are the basis for concern about climate change. Climate change is different from weather change. Weather is the short-time scale (on the order of a few days) evolution of the atmosphere. The evolution of the state variables in the atmosphere is dynamic and non-linear making weather prediction beyond a short time scale unreliable. Climate is a statistical representation of the weather in terms of its deviation from a mean value over a long time scale. There is no reason to doubt climate prediction based on the statics of weather.

Appendix D The solar radiation spectrum and greenhouse gases (GHG)

Appendix D-1.0 The solar radiation spectrum

The solid blue curve in Figure D-1 shows the solar radiation spectrum for the sun modeled as a Black Body radiator at 5250 degrees Celsius. The yellow and red plotted data show the spectrum of solar radiation reaching the top of earth's atmosphere and at sea level respectively. The solar radiance energy in a wavelength region around 0.4-0.7 microns termed the visible region in Figure D-1 and is both the region of highest solar energy output of the sun and the region that is least absorbed by the earth's atmosphere and for these reasons the principle contributor to warming of the earth's surface.

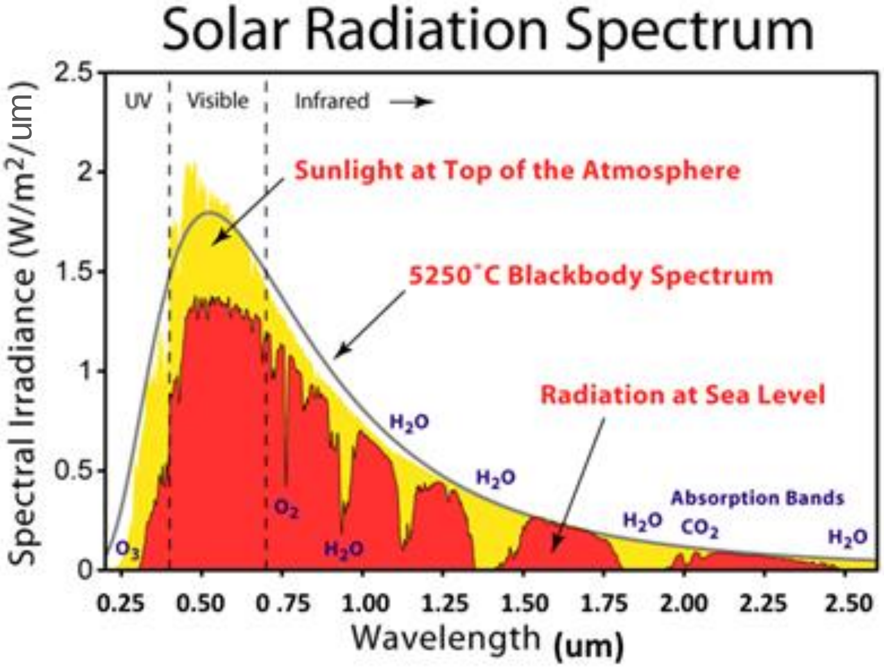

Figure D-1 Modeled 5250 deg. C solar radiance and atmospheric absorption by water vapor (H_2O),Carbon Dioxide(CO_2) [11].

Appendix D-1.1 Greenhouse gasses (GHG)

The layer of earth's atmosphere from the surface to around 15 kilometers in altitude accounts for over 80% of the mass of all atmospheric gases and almost all of the water vapor. This is the layer where the greenhouse effect is most pronounced trapping emitted LWIR radiation and causing T_s to rise. Earth's atmosphere below 100km by mass contains roughly 78% Nitrogen (N_2), 21% Oxygen (O_2), 1% to 4% quite variable water vapor, as well as percent fractions of carbon dioxide (CO_2), methane (CH_4), nitrous oxide (N_2O), and stratospheric Ozone (O_3).

Absorbed solar radiance energy is subsequently emitted as terrestrial or LWIR energy (see Appendix G-1.0 and G-1.4). Certain atmospheric constituent gas molecules that significantly absorb the terrestrial or infrared radiation emitted by the earth and its atmosphere are referred to as greenhouse gases (GHG). The approximate concentrations (in ppm by Volume) of the principal GHG in the Earth's atmosphere are as follows:

Water Vapor H2O: 0.1 to 40,000ppm; Carbon Dioxide CO_2: 375ppm;
Methane: 1.7 ppm; Ozone: 0 to12ppm.

Water vapor is the most abundant greenhouse gas in the atmosphere. Water vapor is not well mixed in the atmosphere and concentration is highly varied. Additionally, Water vapor has a profound effect on the accuracy of GHG estimates derived from remotely sensed infrared spectral data. As the air temperature increases, the same volume of air can hold more water vapor. The measure of the amount of water vapor in the air compared to the maximum amount of water vapor the air can hold is called relative humidity. As a GHG, the higher concentration of water vapor is able to absorb more thermal IR energy radiated from the Earth, thus further warming the atmosphere. This is referred to as a positive feedback loop. However, huge scientific uncertainty exists in understanding and defining the extent and importance of this feedback loop. Nevertheless, the future monitoring of atmospheric processes that involve water vapor will be critical to fully understand the feedbacks in the climate system leading to global climate change. The CAMP Committee has chosen to focus particular attention to water vapor measurement assessment. To date we have sparse measurements of global water vapor. Focused scientific validation to correlate satellite measured estimations of water vapor with balloon data and some in-situ ground measurements must be achieved in order to utilize the global potential of satellite data in understanding the role of water vapor in global warming.

Appendix E Scientific observations indicating global temperature change

Appendix E-1.0 Historical observation records

Since the 1970s accurate temperatures of the air near the surface have been measured on land, sea and by satellite instruments, these recorded temperatures starting in the latter part of the 20th century are depicted in Figure E-1a (black curve). Four of the main influences on global temperature are: irregular "El Niño" fluctuations in the upwelling of deep cold waters in the tropical Pacific Ocean, which cool or warm the air for a few years in Figure E-b (purple curve); sulfate smog particles emitted in volcanic eruptions, such as El Chichón in 1982 and Pinatubo in 1991, which bring temporary cooling Figure E-1b (blue curve); a quasi-regular cycle in the Sun's activity that changes the radiation received at Earth Figure E-1b (green curve); and human ("anthropogenic") changes — primarily emission of carbon dioxide from fossil fuels, but also other greenhouse gases and pollution, such as smoke, and land-use changes such as deforestation Figure E-1b (red curve) [12].

Climate prediction models such as the El Nino/Southern Oscillation (ENSO) are used to calculate and approximate the combined interactive effects of each of these factors. Model analysis is depicted below in Figure E-1a (orange curve) with adjusted weights to give the best fit to global observations. Note, for example, how the temperature trend in the first decade of the 21st century was generally flat because an upward push by anthropogenic forces was temporarily offset by a downward pull as solar activity decreased and the oceans absorbed more heat than usual from the atmosphere (sea water temperatures continued to rise). The combination gives quite a good match to the observations in Figure E-1a (orange curve) [12].

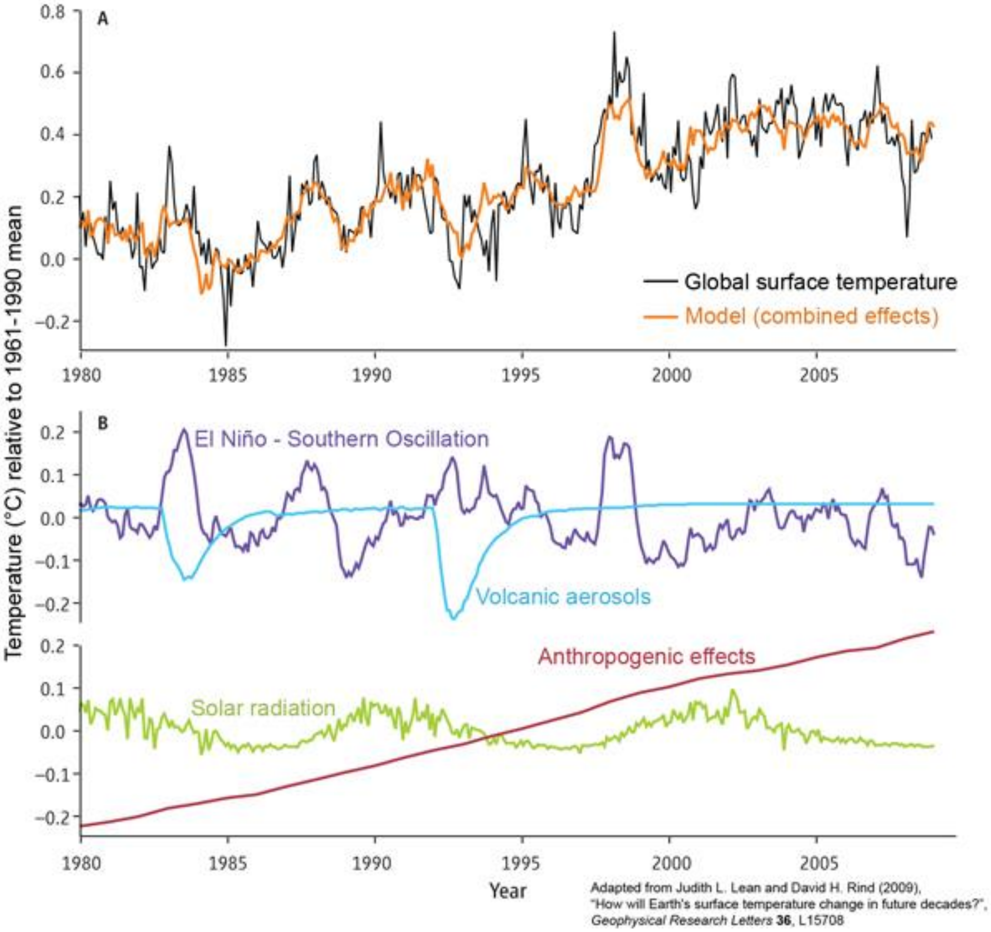

Adapted from Judith L. Lean and David H. Rind (2009), "How will Earth's surface temperature change in future decades?", *Geophysical Research Letters* **36**, L15708

Figure E-1a (top) E-1b (bottom). ENSO model calculation of factors influencing temperature[12]

The combination of better measurement technology input to climate models such as ENSO show that global heating since the 1970s can be explained only by anthropogenic GHG emissions. Figure E-2 is a graph of the mean carbon dioxide emissions record from Mauna Loa, HI. It shows a 0.53% or two parts per million by volume (ppmv) per year increase in the amount of atmospheric carbon dioxide from the beginning of measurements in 1958 to the present. According to NOAA's Earth System Research Lab, CO_2 is responsible for 63% of the global warming attribuTable all GHG. Other researchers estimate percent contributions to global warming by GHG at 36 to 70 % for water vapor, 9 to 26% for carbon dioxide (CO_2), 4 to 9% for methane (CH_4), and 3 to 7% for ozone (O_3)[13,14,15]. Clouds also affect the radiation balance through cloud forcing similar to greenhouse gases.

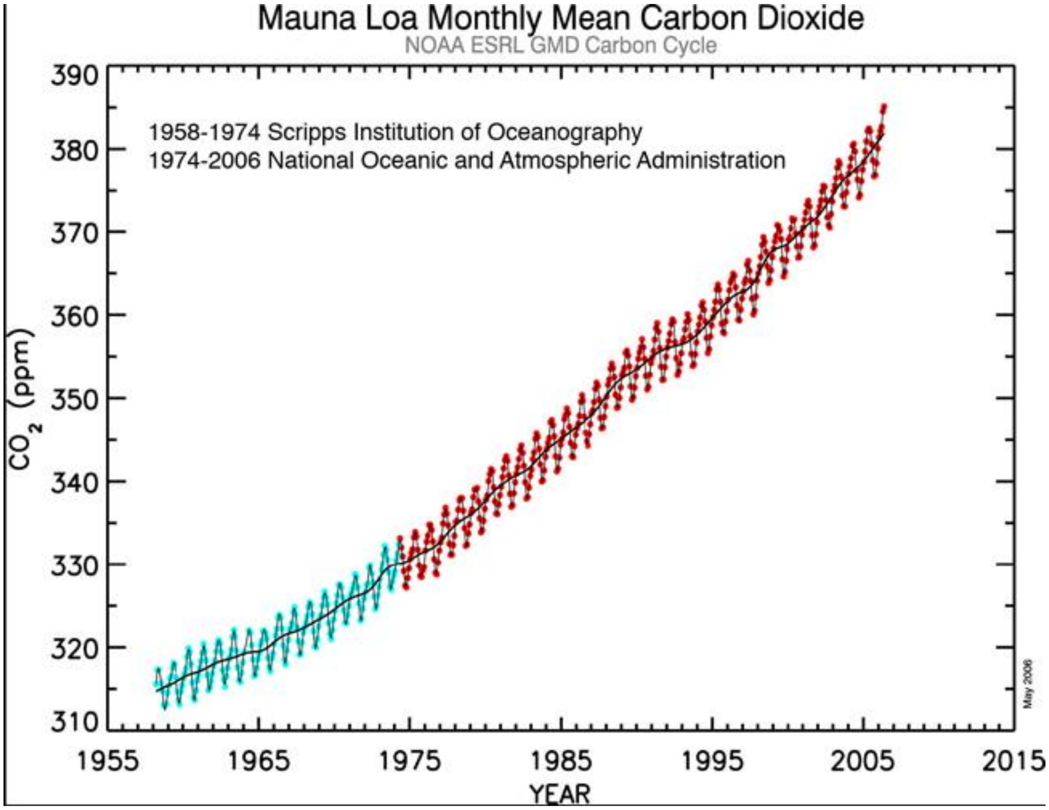

Figure E-2 Mauna Loa Carbon Dioxide Record from the beginning of measurements to present

There is a convincing body of scientific evidence supporting the explanation that the global warming trend is in fact due to anthropogenic activity. The burden of proof has now shifted to those who would still argue that natural causes are solely or mainly responsible for this trend. The consensus amongst scientists is that the global temperature is warming in the 21st century and that the effects of the warming will have predicTable demographic, geographic, and economic outcomes for all countries.

Appendix F Overview of GHG global grid measurement data

Appendix F-1.0 Global Atmospheric Watch

The World Meteorological Organization, Global Atmospheric Watch (GAW), maintains the World Data Centre for Greenhouse Gases (WDCGG)[16]. Nationally and internationally many organizations and programs maintain and operate a finite number of measurement stations, which contribute to the global system for tracking the levels of greenhouse gases in our atmosphere. The resulting data archive consists of physical sample measurements made using a specified calibration protocol. Airborne physical measurements augment this data base as well, but to a statistically significant lesser extent.

The measurement data consists of gas mole fractions and relevant data (data flag, standard deviation, the number of data used to average, etc.) and coincident ancillary data (associated meteorological data). In the case of observation by mobile platforms, measurement locations (latitude and longitude, etc.) are also included in the measurement data. The WDCGG requires that the measurement data units should not be in concentrations such as µg/m3 but in mole fractions such as ppm (µmol/mol), ppb (nmol/mol), and ppt (pmol/mol). Measurement data consist of gas mole fraction data files and coincident ancillary data (associated meteorological data) files (optional). Metadata are additional information for observation such as observatory locations, sampling conditions, measurement methods, calibrations, traceability of employed scale, quality management information, etc. Metadata is essential to utilize measurement data, therefore, the WDCGG requests contributors to keep their metadata up-to-date.

Appendix F-1.1 Carbon Tracker

The authors wish to thank Ms. Arlyn Andrews and Mr. Jonathan Kofler of NOAA for providing assistance in helping with the setup of the ASSIST-II instrumentation and data during the execution of the CAMP activity at their Carbon Tracker Facility in Moody, TX.

The United States Department of Commerce National Oceanic & Atmospheric Administration (NOAA) Earth System Research Laboratory (ESRL) Global Monitoring Division operates and maintains Carbon Tracker. Carbon Tracker is the NOAA CO_2 measurement and modeling system. Carbon Tracker is designed to keep track of sources (emissions to the atmosphere) and sinks (removal from the atmosphere of carbon dioxide around the world, using atmospheric CO_2 observations. Carbon Tracker is a cooperative worldwide measurement effort a host of organizations and researchers that maintain facilities and contribute data[17].

Appendix G Fundamental PROPERTIES for LWIR measurement of the atmosphere

Appendix G-1.0 Atmospheric temperature structure

Temperature in the lower atmosphere decreases with altitude up to the tropopause at approximately 15 km (see Figure G-1). This decrease, termed lapse rate, is approximately 7 deg per km. The layer from the earth's surface to the tropopause accounts for over 80% of the mass and almost all of the water vapor. The next region from the 15 km tropopause to the 50km stratopause is characterized by a predominance of ozone with the maximum concentration occurring near 25km. In this region the temperature increases with altitude making it difficult to simply associate the depth of penetration as a unique function of the radiance L_λ with the temperature at a given level of the atmosphere. The strongest portion of the ozone measured typically comes from a region between 15 and 30 km, whether viewing from a satellite or surface platform.

> Property 1. Temperature in the lower atmosphere decreases with altitude up to the tropopause at approximately 15 km (see Figure G-1). This decrease, termed lapse rate, is approximately 7 deg per km. The layer from the earth's surface to the tropopause accounts for over 80% of the atmospheric mass and almost all of the water vapor.

Together the troposphere and stratosphere account for about 99.9% of the mass of the atmosphere. Above the tropopause in the stratosphere the temperature increases as a function of altitude due to radiative processes involving the absorption of solar radiation by ozone and is balanced by infrared emissions from carbon dioxide. Careful examination of simultaneous upward and downward looking infrared spectrometer radiance measurement spectra reveals the differing mechanisms behind the temperature-driven emission-absorption features against the temperature structure as a function of height that occurs throughout the lower atmosphere, e.g. below 100km (see Appendix G 1.10).

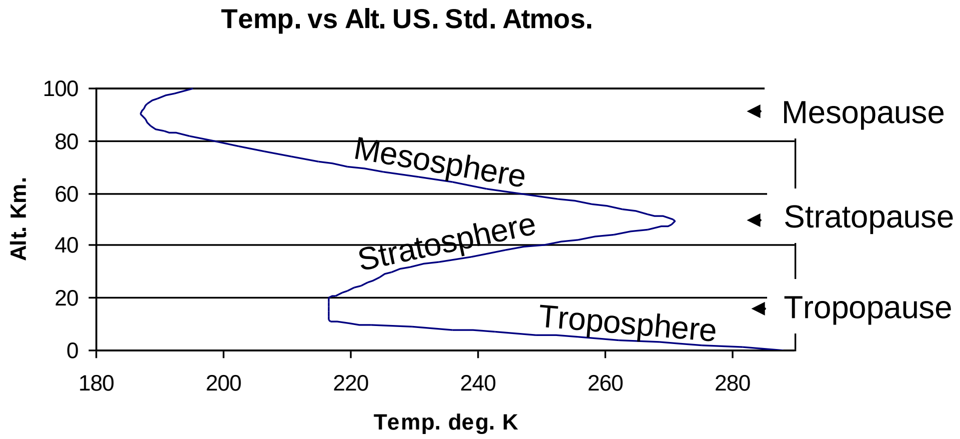

Figure G-1. Temperature vs altitude US Standard Atmosphere

Appendix G-1.1 Analysis of pressure and density

In earth's atmosphere, the vertical variability of pressure and density is much larger than its horizontal variability. At any given level, up to around 100km, the logarithm of the atmospheric pressure in (mb) drops off approximately linearly with height see Figure G-2.

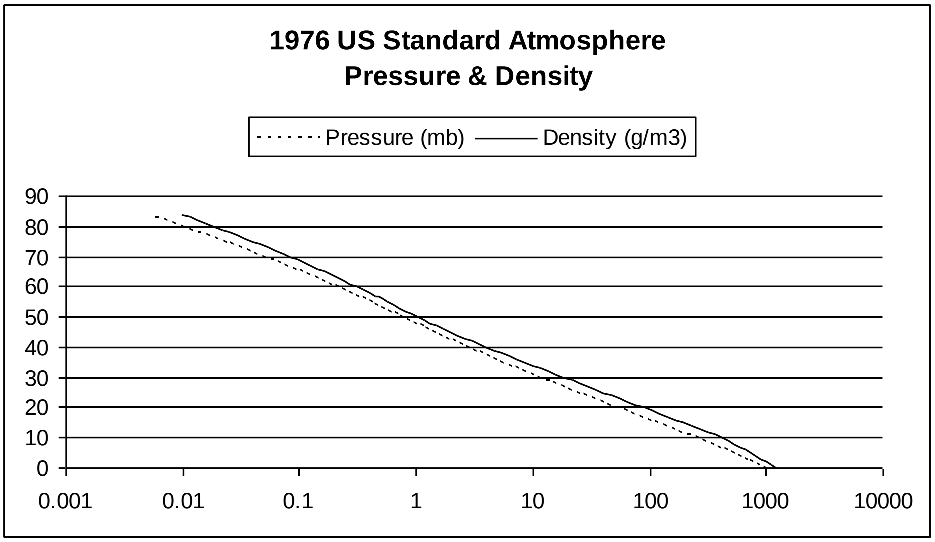

Figure G-2 Verticle profile of pressure in millibars(---), density in grams per cubic meter(—), plotted on a logarithmic scale [18 P-F193]

Let z represent height, then the log of pressure at height z can be represented as

$$\log\left(p(z)\right) \cong \log\left(p(0)\right) - Bz \qquad 1$$

where *p(z)* represents the pressure at height *z*, *p(0)* is the pressure at sea level, and *B* is a constant related to the average slope of an empirical pressure curve for this sea level to 100km region. Equation one can be rewritten as

$$\ln \frac{p(z)}{p(0)} \cong -\tfrac{z}{H}\text{, where H}\equiv 1/(2.3\text{B}). \qquad 2$$

Taking the antilog

$$p(z) \cong p(0)e^{-z/H} \qquad 3$$

This gives rise to what is called the scale height of the atmosphere H, which states that pressure drops off by a factor of e through an ascending layer depth of H. Empirically the log (p) decreases by 6.3 in the lowest 100km of the atmosphere. If you substitute -6.3 into equation 1, a value for *B* of 0.063 is calculated, and subsequently the value for the scale height of H ≅ 7km.

> Property 2. A unit volume of atmosphere will contain more gas molecules at a higher temperature in a lower region of the troposphere than in a higher region. This is easily explained by the ideal gas law.

Appendix G-1.2 Ozone

Ozone is formed in the stratosphere (10-50km) and mesosphere (50-80km). At altitudes above 100km. solar radiation *hv* ($0.1< \lambda <0.25$um; O_2 Herzberg bands and continua) is almost completely absorbed in the following photo-disassociation reaction

$$O_2 + hv \Rightarrow 2O. \qquad (R1)$$

The highly reactive atomic oxygen produced by R1 is a major constituent in this region of the atmosphere. The formation and persistence of atomic oxygen is a function of low density in the mesosphere. In the higher density stratosphere, atomic oxygen combines rapidly to form ozone in the following manner

$$O_2 + O + M \Rightarrow O_3 + M. \quad \text{(R2)}$$

Solar radiation *hv* in the ultraviolet region around 0.2um (O_3 Hartley-Huggins bands) is not strongly absorbed by the R1 reaction and penetrates into the stratosphere, where it is absorbed in following photo-disassociation reaction

$$O_3 + hv \Rightarrow O_2 + O. \quad \text{(R3)}$$

The atomic oxygen resulting from R3 rapidly combines to form another molecule of ozone [19 P66]. The trace amounts of ozone present in the stratosphere are capable of absorbing almost all the solar radiation from 0.2-3.1um, which is then converted to kinetic energy and is responsible for the heating of the atmosphere as a function of altitude in the stratosphere. The temperature maximum produced by this phenomenon takes place at around 50km and defines the stratopause. The level of maximum ozone concentration is located somewhat lower at around 25km.

> Property 3. The increase in temperature as a function of altitude in the stratosphere is due to the absorption of solar radiation and its conversion to kinetic energy by ozone. The majority of atmospheric ozone is confined to this region.

Appendix G-1.3 Atmospheric processes

Earth's atmosphere below 100km by mass contains roughly 78% Nitrogen(N_2), 21% Oxygen(O_2), 4% quite variable water vapor, with atmospheric concentrations of uniformly mixed Carbon Dioxide (CO_2) of 375 parts per million and Ozone(O_3) at 0 to12 parts per million in the stratosphere. For the purposes of this discussion, the ratios of various gaseous constituents at any level in the atmosphere are governed by two competing processes; molecular diffusion and mixing due to fluid motions.

Molecular diffusion:

Gaseous diffusion results in an atmospheric distribution in which the average molecular weight of constituent gases gradually decreases until only the lightest are present (helium and hydrogen) at the highest elevations. This translates to the densities of lighter gasses decreasing at a slower rate than heavier gasses. However, it turns out that empirically, the plot of the atmospheric density in (g m^{-3}) as a function of height in the lowest 100km of the atmosphere follows the same curve as pressure (see Figure G-2). Therefore, the density of a gas as a function of height ρ(z) can also be approximated using Equation 3 substituting density for pressure

$$\rho(z) \cong \rho(0)e^{-z/H} \qquad 4$$

This indicates that most gaseous constituents are uniformly mixed in the homosphere where such mixing dominates, having similar scale heights (e.g. CO_2, O_2, etc.). However, for the more photochemically controlled species (e.g. ozone) and/or dynamically variable (e.g. water vapor), the density of each gas may not follow the scale height according to equation 4. The scale height H for water is ~ 3km, while that for ozone is ill-defined, as it increases with altitude from the tropopause up to ~25km.

Mixing due to fluid motions:

The mixing of atmospheric gases due to fluid motions of macro-scale air parcels is independent of molecular weight and predominates in the lower atmosphere up to approximately 80km; this region of the atmosphere is called the homosphere. Once the mixing of gases breaks down because of lack of collisions, each gas can assume its own scale height, inversely proportional to its molecular weight. The transition to diffusive control generally occurs above the turbopause, near 100km.This translates to the densities of lighter gasses decreasing at a slower rate than heavier gasses.

> Property 4. The troposphere and stratosphere contain all of our principal infrared absorbers, which do not significantly vary in concentration as a function of height, with the exception of ozone which is confined to the stratosphere.

Appendix G-1.4 Solar vs terrestrial radiation

Figure G-3 is most intuitive in terms of understanding the behavior of the atmosphere in terms of the infrared. Observe that the solar radiation occurs in the visible and near infrared regions of the spectrum, while radiation from the earth and its atmosphere resides in the infrared. The fact that there is nearly complete absence of overlap between these curves is justification for separating thermal (surface and atmospheric) from solar radiation. However, in the midwave infrared, the contributions from solar and thermal regimes are about equal during sunlit conditions, making this a more complex spectral regime.

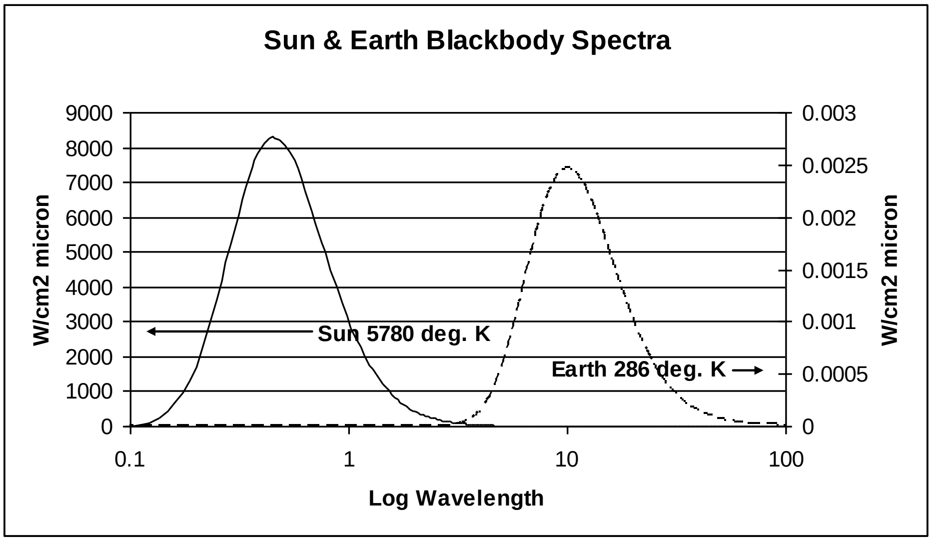

Figure G-3 The plot of the blackbody spectra representative of the sun (5780 deg K) and earth (286 deg K) on a logarithmic wavelength scale[20 P4]

Property 5. Solar irradiation and terrestrial radiation have almost no overlap in the LWIR wavelength regions in which our infrared spectrometers are measuring. Therefore the source must be terrestrial or kinetic.

Appendix G-1.5 Optical density Beer's law

At the wavelengths of solar radiation, only absorption (and extinction due to scattering) needs to be considered. However, at the wavelengths of terrestrial radiation both absorption and emission are equally important and must be considered simultaneously.

The absorption of terrestrial radiation as a function of wavelength *da*$_\lambda$ along an upward path through the atmosphere is proportional to the number of molecules per unit area or unit layer that are absorbing radiation along the path and described by an equation of this form

$$da_\lambda \equiv -\frac{dL_\lambda}{L_\lambda} = -k_\lambda \rho \sec\theta dz \qquad 5$$

where ρ is the density of the gas, *L* is radiance, and *secϑdz* is an expression of the upward path volume. k_λ the absorption coefficient, is a measure of the fraction of the gas molecules per unit wavelength that are absorbing radiation at a particular wavelength. Note: k_λ is a function of temperature and pressure of the gas in a layer, and is in units of square meters per kilogram. Therefore, $k_\lambda \rho dz$ is dimensionless. Integration of 5 from a level *z* to the top of the atmosphere ∞ or to the top of a particular layer results in

$$\ln L_{\lambda\infty} - \ln L_\lambda = \sec\theta \int_z^\infty k_\lambda \rho dz\,. \qquad 6$$

Taking the antilog of both sides results in

$$L_\lambda = L_{\lambda\infty} e^{-\sigma_\lambda} \quad 7$$

where

$$\sigma_\lambda = \sec\theta \int_z^\infty k_\lambda \rho dz\,. \qquad 8$$

This derivation is often referred to as Beer's Law, which shows how radiance decreases with path length through a layer. σ_λ is called the optical depth or optical thickness, and is a measure of the attenuation of the radiation as a function of wavelength as a result of its passage through a layer. Again, analogous to scale height, if the optical depth or thickness is identically one (unity) the attenuation of radiation as a function of wavelength is *e*. Analyzing concurrent upward and downward looking spectrometer data provides additional insight in determining where, as a function of wavelength and path length, does the optical depth or thickness approach ∞ (see Appendix G-1.10).

Appendix G-1.6 Transmissivity, absorptivity, and Schwartzchild's equation

Two useful terms can now be defined. The transmissivity of a layer of gas is

$$\tau_\lambda \equiv \frac{L_\lambda}{L_{\lambda\infty}} = e^{-\sigma_\lambda} \qquad 9$$

and for the long wave infrared region LWIR, where scattering is not of concern, the absorptivity is defined as

$$a_\lambda = 1 - \tau_\lambda = 1 - e^{-\sigma_\lambda} \quad 10$$

At wavelengths close to the center of absorption lines, k_λ (the absorption coefficient) may become quite large so that very short path lengths are sufficient to absorb virtually all the radiation. On the other hand, at wavelengths away from absorption lines, a path length many orders of magnitude longer may be required to produce significant absorption. Gas molecules possess discrete energy levels associated with their vibrational-rotational states. These vibration-rotation states manifest themselves as absorption/emission lines in the infrared portion of the spectrum. An absorption/emission band is made up of thousands of individual absorption/emission lines. The line structure associated with any particular atmospheric gas component is complex. This line structure is affected by both collision and or Doppler broadening mechanisms that vary as a function of temperature and pressure. Thus, individual lines and resulting bands broaden as the path length traverses the atmosphere.

Kirchoff's law states that absorption a_λ is equal to ε_λ. This law applies to gases as well provided that the frequency of molecular collisions is large in comparison to the frequency of individual absorption and emission events. It turns out that this condition is fulfilled up to altitudes of 60km. Therefore, at the wavelengths of terrestrial radiation, absorption and emission must be considered simultaneously.

> Property 6**.** for our atmosphere and its constituents, absorption is equal to emission in the LWIR.

Appendix G-1.7 Absorption and emission

The absorption of terrestrial radiation along an upward path through the atmosphere is described by equation 5 with a sign change. Therefore, the emission of radiation by a gas can be written in the form

$$dL_\lambda = L_\lambda{}^* d\varepsilon_\lambda = L_\lambda{}^* da_\lambda = L_\lambda{}^* k_\lambda \rho \sec\theta dz \qquad 11$$

where $L_\lambda*$ is the blackbody radiance specified by Planck's Law. If we subtract a_λ from ε_λ we obtain equation 12, which describes the net contribution of the layer to the radiance passing upward through it.

$$dL_\lambda = -k_\lambda (L_\lambda - L_\lambda{}^*) \rho \sec\theta dz \qquad 12$$

Equation 12 is Schwarzchild's equation and is the basis for computations of infrared radiation transfer, be they for a single layer or the cumulative affects of multiple layers (e.g. as simulated with atmospheric Radiative Transfer Codes, particularly Line-by-Line codes). For a constant temperature gas, equation 12 can be integrated to obtain

$$(L_\lambda - L_\lambda{}^*) = (L_{\lambda 0} - L_\lambda{}^*)e^{(-\sigma_\lambda)} \qquad 13$$

where $L_{\lambda 0}$ is the radiance incident on the layer from below.

Note: this expression shows that L_λ should exponentially approach L_λ* as the optical thickness of the layer increases [21 P302].

> Property 7. A for a layer of infinite optical thickness the radiance emitted is L_λ*, the black body radiance regardless of the value of $L_{\lambda 0}$. Stated another way an optically thick layer behaves as a black body at the temperature of that layer.

The understanding that radiance approaches that of a black body of a given temperature as opacity approaches ∞ in combination with the knowledge of the behavior of temperature as a function of altitude provides key insight required in order to interpret depth of penetration from empirical infrared spectrometer radiance data and reveals useful information for the infrared remote sensing practitioner.

In the atmosphere there are only a few entire spectral regions where the atmospheric path becomes truly opaque, the set of water bands beyond 1.8um, which includes the 6.3um region, the CO_2 15um region, and portions of the microwave region, again due to water vapor, etc. See Figure G-5 for 'absorptance plots' (1-Transmittance) in the infrared spectral range for the major GHG. As the absorptance approaches 'unity', then the gas is optically thick over that spectral range. Other spectral regions that nicely turn into simple temperature indicators are the 'window regions' when looking in the nadir direction, such that the surface radiance emitted at the surface temperature is transmitted almost directly to the sensor. Ozone, which is never truly opaque in the IR, only represents an average temperature over the span of the ozone feature, and the maximum or minimum temperature viewed in nadir or up-looking modes will be different.

The previously unsolvable depth of penetration issues caused by the increase of temperature as a function of altitude in the stratosphere can be addressed by the careful application of these 8 points to concurrent upward and downward spectrometer data in combination with the empirical measurement or basic knowledge of the atmospheric temperature profile.

Appendix G-1.8 Absorption characteristics of optical depth σ in the vertical profile of the atmosphere

The following analysis helps to understand the vertical penetration of the sun's radiation into a well-mixed atmosphere or in our case the lower approximately 100km of the atmosphere (see Figure G-1 and G-2) where the absorption coefficient k_λ is independent of height. Substituting irradiance for radiance and density for optical depth in equation 4 gives the following

$$\sigma_\lambda = k_\lambda \rho_0 \int_z^\infty e^{-z/H} dz$$

Integration provides a useful expression for the optical depth as a function of height

$$\sigma_\lambda = Hk_\lambda \rho_0 e^{-z/H}. \qquad 14$$

The expression for the change in irradiance caused by the differential absorption of any layer in the atmosphere can be expressed as

$$dE_\lambda = E_{\lambda\infty} \tau_\lambda da_\lambda \qquad 15$$

where τ_λ is the transmission of the atmosphere above a differentially absorbing layer. Equation 15 can be rewritten after substituting equations 9 for τ_λ, 5 for da_λ and 4 for ρ respectively as

$$dE_\lambda = (E_{\lambda\infty} k_\lambda \rho_\lambda) e^{-z/H} e^{-\rho_\lambda} dz.$$

After the substitution for e $^{(-z/H)}$ from equation 14 we obtain the expression for absorption per unit layer thickness as a function of optical depth

$$\frac{dE_\lambda}{dz} = \frac{E_{\lambda\infty}}{H} \sigma_\lambda e^{-\sigma_\lambda} \qquad 16$$

Taking the derivative of equation 16 and setting it equal to 0 allows us to determine what optical depth results in the maximum absorption. It turns out that this occurs at an optical depth $\sigma_\lambda=1$. This is an important revelation in terms of understanding how the atmosphere behaves relative to what we see in our infrared spectrometer measurements.

> Property 8. most of the absorption (or emission) for gases that are neither transparent or opaque takes place along/over a path length through the atmosphere equivalent to the spatial region around the range where the optical depth is approximately one; ozone at 9.6um is a primary example, but CO_2 and H_2O also exhibit the same sensitivity to altitude over portions of their spectral signatures.

Appendix G-1.9 Remote sensing of temperature

For simplicity, one can examine the downward looking measurement. However, the following analysis can be applied to upward looking measurement as well. The relationship between the atmospheric vertical temperature profile and the emitted infrared spectrum of its gaseous constituents as a function of each incremental layer *dz* in a well-mixed atmosphere is depicted by the following approximations.

The incident radiation absorbed within any differential layer of the atmosphere is given by

$$dL_\lambda = L_\lambda^* \tau_\lambda da_\lambda. \qquad 17$$

$$dE_\lambda = E_{\lambda\infty} \tau_\lambda da_\lambda \qquad 17a$$

This is nothing more than equation 11 multiplied by τ_λ , which represents the transmission of the layer immediately in front of the layer represented by Equation 17. Substitution of irradiance for radiance results in Equation 17a. As previously shown, dL_λ/dz is a maximum when $\sigma_\lambda = 1$. Stated another way, looking through the atmosphere, most of the radiance measured is emitted by layers near the level of unit optical depth for a particular wavelength. Well above unit optical depth, the mass of the gaseous constituents is too small to produce significant radiation, and radiation originating from layers well below unit optical depth is absorbed. If we integrate Equation 17 with respect to depth z we obtain

$$L_\lambda = \tau_{\lambda 0} a_{\lambda 0} L^*_{\lambda 0} + \int_0^\infty \tau_\lambda L^*_\lambda k_\lambda \rho dz \qquad 18$$

where 0 represents the earth's surface. Equation 18 can be expressed as a sum of the contributions of N layers. If each separate layer is considered to be isothermal then Equation 18 becomes

$$L_\lambda = \alpha_0 L^*_{\lambda 0} + \alpha_1 L^*_{\lambda 1} + \alpha_2 L^*_{\lambda 2} + \ldots + \alpha_N L^*_{\lambda N} \qquad 18a$$

where

$$\alpha_0 = \tau_{\lambda 0} a_{\lambda 0}$$

$$\alpha_i = \tau_{\lambda i} \int k_{\lambda i} \rho_i dz_i$$

Where *(i=1,N)*and $\tau_{\lambda i}$ represents the transmissivity of the atmosphere lying above the ith layer. From equation 7 the coefficients α can be expressed in terms of optical thickness

$$\alpha_i = \tau_{\lambda i} \sigma_{\lambda i} .$$

These coefficients α_i can be accurately determined from data on average atmospheric composition as a function of height. For each of the layers in equation 18a the black body radiance as a function of wavelength L^*_λ. is measured by our upward and downward looking spectrometers. The temperatures associated with L^*_λ can readily be determined by Planck's law. Therefore, theoretically it is possible to solve the resulting set of simultaneous equations to obtain L^*_λ and a subsequent temperature for each layer [22 P306].

In practice, the solution can only be obtained if the set of equations is non-singular, which for many situations they are not due to temperature increase in the stratosphere; thus the same temperatures can occur above or below the tropopause. This non-uniqueness, coupled with the altitudes at which the optical depth is near unity, can help distinguish where the emission/absorption actually occurs. The careful application of Properties 1-8 to either empirical or statistical measurements of the profile of atmospheric temperature as a function of height T(z) in combination with the radiance measurements from upward and downward looking spectrometers facilitates a solution for the optical depth of a radiance measurement as a function of wavelength. This process is fundamental to the analysis of upward and downward looking LWIR atmospheric spectrometer measurement data and subsequent retrieval of GHG profile information.

Appendix G-1.10 A detailed look at spatially and temporally concurrent upward looking and downward looking passive LWIR hyperspectral atmospheric spectra

Figure G 4 shows January 24 2005 AIRS / AERI data plotted with black body radiance curves for the measured ground surface air temperature of 286 deg K along with radiance curves at -7 deg K (i.e., Scale Height temperature decrease for the troposphere) increments up through the 15 km tropopause, continuing on to the mesopause temperatures ~180 deg K. The AIRS/AERI data fits within this envelope because the atmosphere being sensed through in either direction can be adequately characterized by our discussion in Sections 2 and 3. Let's take a closer look at the three LWIR atmospheric spectral regions that are outlined in Figure G-4 MODTRAN®5 was used to illustrate in Figure 12 the four major atmospheric absorbing and emitting constituents and their relative wavelength by wavelength spectral effect on the radiance values measured by both AIRS and AERI for the three LWIR Regions from 6.2 to 15 um. For the analysis of regions one through three refer back to the eight properties that were outlined in Appendices G-1 through G-8 along with Figure G-4

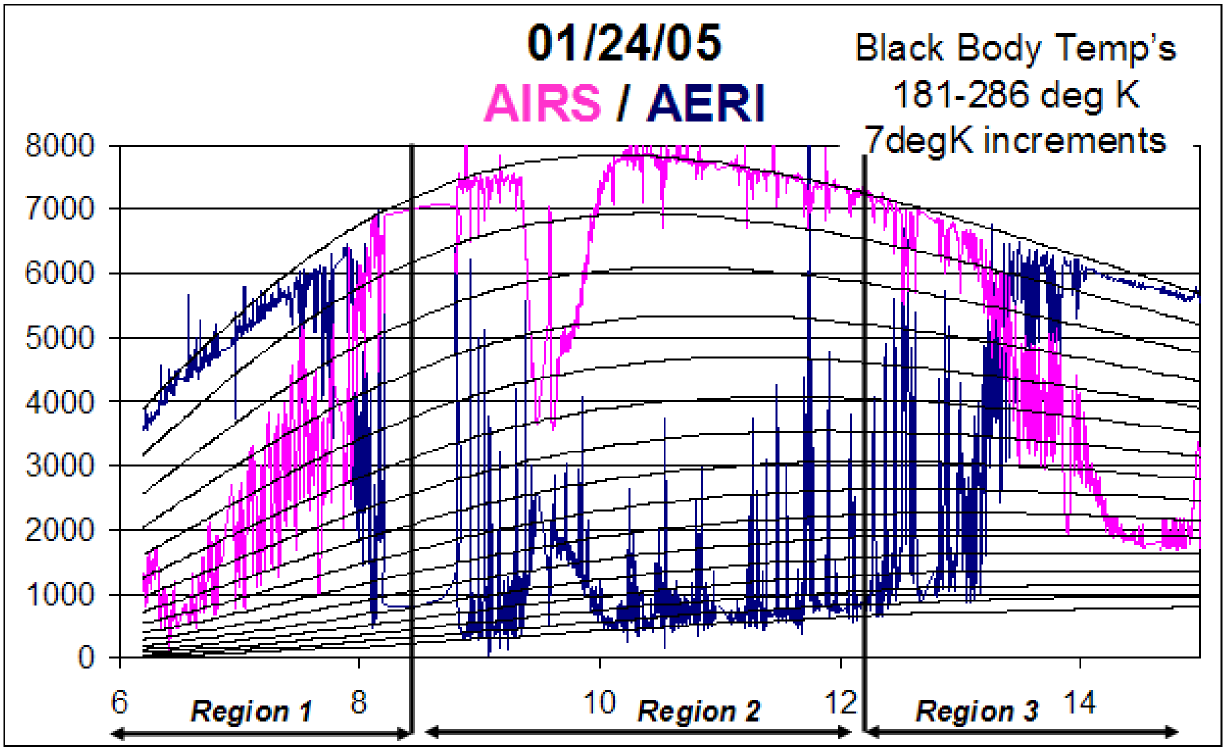

Figure G-4 Spatially and Temporally concurrent AIRS/AERI atmospheric spectra over Lamont, OK

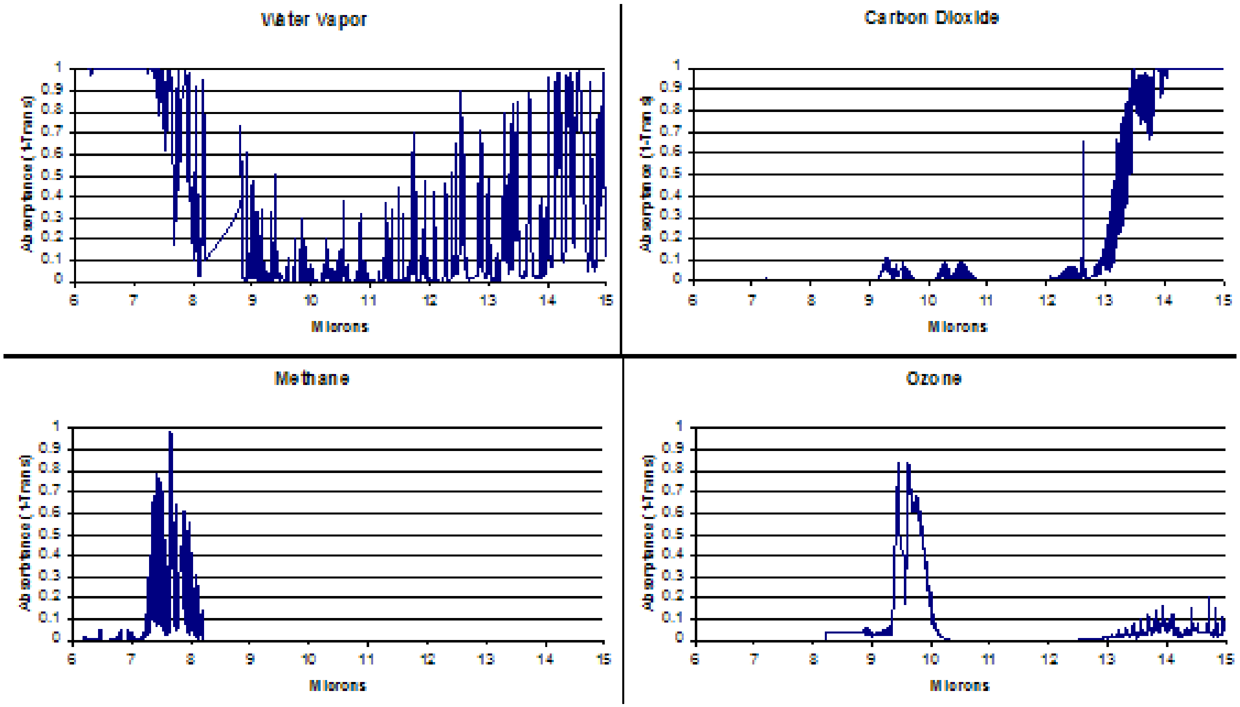

Figure G-5 MODTRAN®5 generated spectra of major atmospheric GHG constituents

Appendix G-1.11 Atmospheric Region “1” 6.2-8.8 um

Figure G-6shows Region 1 from 6.2 to 8.7 um. The first thing to notice is that the AIRS and AERI radiance data are well separated from 6.2 to around 7.5 microns, dominated by water vapor and methane. This radiance separation is because both sensors are measuring two different optically thick ($\sigma_\lambda=\infty$) path lengths consisting mainly of water vapor and methane (see Figure G-4) from two opposite directions. We know that they are different optically thick path lengths because we understand the -7 deg K behavior of temperature as a function of altitude in this well mixed constituent region of the atmosphere, and that the number of gas molecules per unit volume increases with pressure. The AERI sensor is looking at an optically thick path length from the ground level up, and most of the radiance being sensed is coming from lower levels of the atmosphere at or around 286 deg K which was the measured ground air temperature on that day. The AIRS sensor is looking down from space at a similar constituent mixture at temperatures that are twenty to fifty degrees cooler than those at the surface.

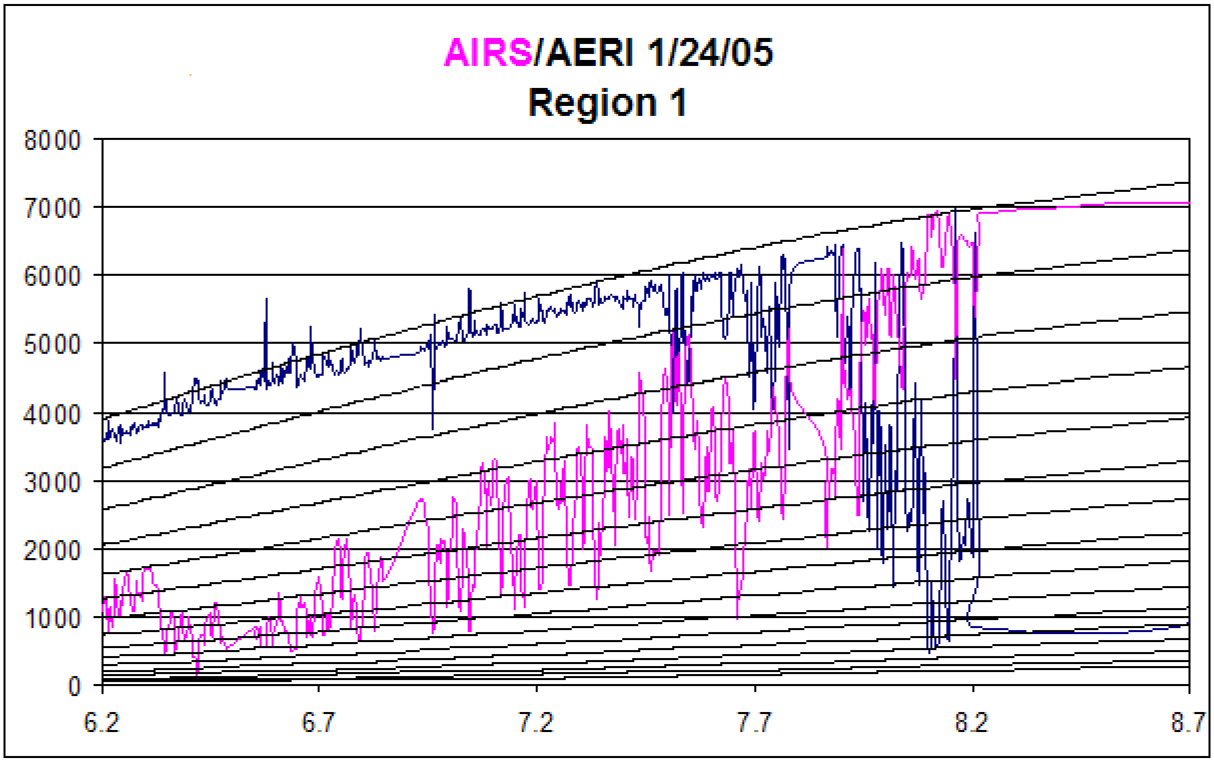

Figure G-6 AIRS/AERI spatially and temporally concurrent atmospheric spectra Region 1

Around 7.8 um both sensors are measuring similar radiance values and therefore are measuring to the same atmospheric levels. At around 7.94 um the radiance value plots for AIRS and AERI have crossed over and begin once more to become well separated. AERI radiance values are now at temperatures associated with the colder upper levels of the troposphere/mesopause. AIRS radiance values are now at temperatures associated with the warmer surface levels of the troposphere. In this region from 7.94 to 8.7 um path lengths and their associated radiance values (i.e., temperatures) constituting optical thickness have changed. Both sensors are seeing further through the total atmosphere (i.e., ground to space or space to ground). For clarification review “Properties 1, 4, 7, and 8” in Appendices G-1 through G-8.

Appendix G-1.12 Atmospheric Region “2” 8.7-12.2 um

Figure G-7 shows Region 2 from 8.7 to 12.2 um. Interpretation of the empirical data in Region 2 is the most difficult due to the presence of ozone from approximately 9.3 to 10.18 um. Therefore in order to simplify our interpretation, and to follow the same format, let’s address the 9.3 to 10.18 um ozone region separately in Appendix G-1.13.

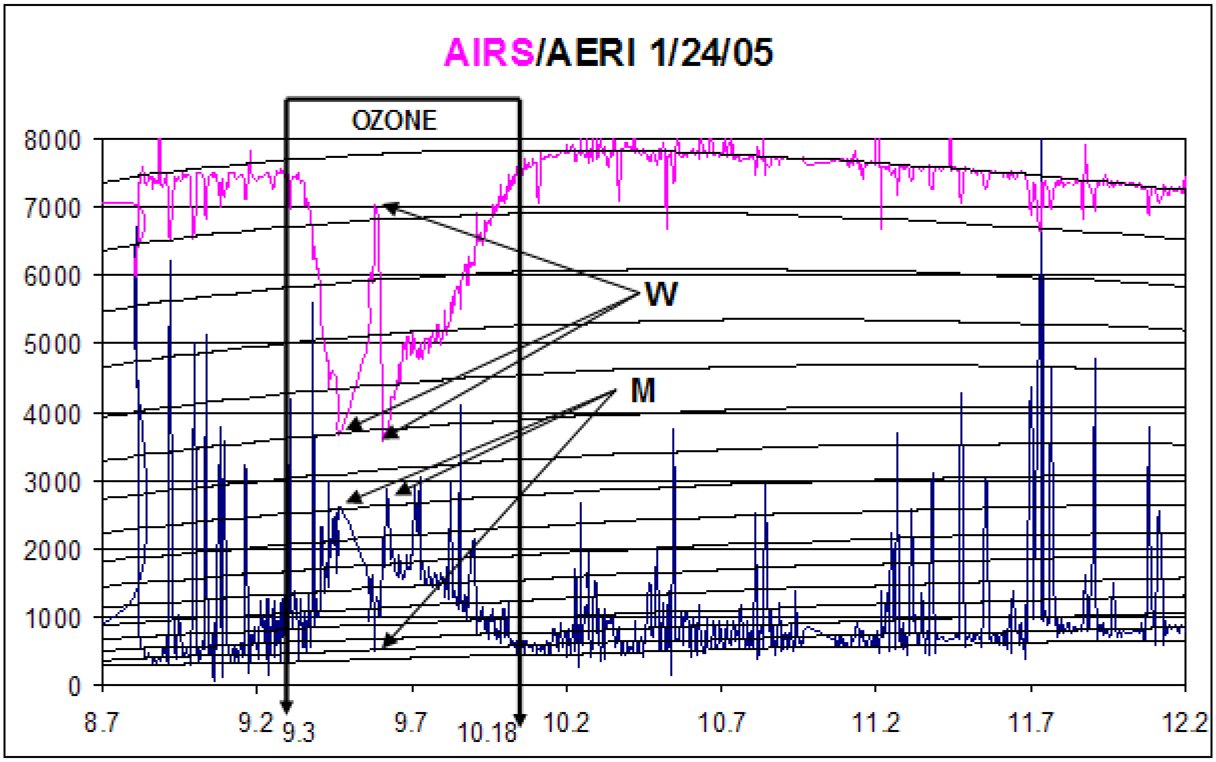

Figure G-7 AIRS/AERI spatially and temporally concurrent atmospheric spectra Ozone region

The first thing to notice is that the, the AIRS and AERI radiance data are very well separated from 8.7 to around 12.2 microns. This radiance separation is because both sensors are measuring two different path lengths consisting mainly of water vapor, carbon dioxide, and ozone (see Figure G-4) from two opposite directions. Radiance values measured by both sensors indicate that for the majority of the wavelengths, their path lengths are not opaque and traverse the entire lower atmosphere in which these constituents are present. This is manifested in the radiance values measured by AIRS, which represent temperatures at the 286 deg K surface level region, and by AERI radiance values, which represent temperatures at the much cooler higher altitude levels of the troposphere/mesopause.

The obvious magnitude and direction differences between the radiance values measured by AIRS and AERI at the same wavelength throughout this region, is an example of Kirchoff’s law ($a_\lambda = \varepsilon_\lambda$.). For AIRS, radiance values indicate that the majority of absorbing and emitting radiance contributions are from gases that we know originate from an optical depth $\sigma_\lambda=1$, which are absorbing and emitting radiance values at surface air or actual ground temperatures.

For AERI, the same explanation can be applied, however, due to the opposite path direction radiance contributions originating from an optical depth $\sigma_\lambda=1$ are absorbing and emitting radiance values at upper tropospheric temperatures. The phenomena appear in the measured data as absorption features or dips as a function of wavelength from the 286 deg K blackbody boundary temperature profile structure of the AIRS data. In the AERI data they appear as emission features or spikes. For clarification review "Properties 1, 2, 7, and 8,."

Appendix G-1.13 Atmospheric Region "2" (9.3-10.18 um) Ozone

In Figure G-7, the 9.3 to 10.18 um ozone region requires the careful application of additional knowledge of what is happening because of ozone in the stratosphere in order to correctly interpret what is seen in the empirical radiance data. Ozone, residing in the stratosphere, absorbs solar radiation and converts that radiation to kinetic energy, subsequently absorbing and emitting the radiation that is indicative of the stratospheric temperature profile. Figure G-1 shows that the temperature in the stratosphere begins to heat back up as a function of increasing altitude, reaching temperatures near those of the surface air or ground temperatures.

The first thing to notice is that the presence of ozone causes AIRS and AERI radiance values to diverge from their characteristic surface and tropospheric black body temperature boundary values respectively. This radiance diversion is indicative of sensing path lengths associated with the temperature altitude profile of ozone in the stratosphere. In both situations the total path length sensed by AIRS and AERI is significantly different in length, gas constituent content, and temperature; these differences in retrieved altitude regimes relate to whether the instrument is viewing ozone from above the peak contribution zone ($\sigma_\lambda=1$) or below, as previously discussed. Because the optical depth σ_λ due to the presence of ozone in the stratosphere becomes large, but not opaque, the viewing direction determines where the greatest radiometric contribution occurs, at higher altitudes and temperatures for AIRS and generally lower altitudes and temperatures for AERI; see Figure G-4, where the absorptance of the vertical O_3 column is ~0.8, so the transmittance is ~0.2, and the optical depth is ~0.8. It is just the fact that ozone is approaching being optically thick that makes its vertical profile determination more difficult, and why higher resolution measurements can be helpful, since some lines are much more opaque than others. Careful examination of the radiance values measured by both AIRS and AERI for three distinctive ozone features at 9.47, 9.59, and 9.62 um (see Figure G-6) provides key evidence into the relative path lengths associated with σ_λ approaching unity for remote sensing in this region.

In the AIRS data these radiance values appear as dip, spike and dip or "W" (see Figure G-7). AIRS looking down from space is measuring a path length containing ozone at the higher stratospheric temperatures. Ozone produces the two dips at and around 9.47 and 9.62 um respectively, indicative of path lengths from space to these respective temperature layers in the stratosphere. The AIRS radiance values at and around 9.59 um are near surface temperatures indicating a longer downward path length sensing closer to the surface.

In the AERI data these radiance values appear as spike, dip and spike or "M" (see Figure G-7). AERI looking up from the surface is measuring a path length containing ozone at lower stratospheric temperatures, which are higher then the other tropospheric gas radiance values it is measuring in this path length. Here ozone produces two spikes at and around 9.47 and 9.62 um respectively, indicative of path lengths from the surface to these respective temperature layers in the stratosphere. The AERI radiance values at and around 9.59 um are near mesospheric temperatures once again indicating a much longer upward path length.

Ozone features appear either in absorption or emission depending on their temperature in relation to the temperature of the surface or tropospheric boundary layers, which can be reached by other wavelengths.

Appendix G-1.14 Atmospheric Region "3" 12.2-13.2um

Figure G-8 shows Region 3 from 12.2 to 15 um. From 12.2 to 13.2 um, AIRS and AERI are measuring radiance values associated with different temperature layers of well mixed tropospheric gases such as water vapor and CO_2. The features of these gases appear either in absorption or emission depending on their temperature in relation to the temperature of the surface or tropospheric boundary layers, which can be reached by other wavelengths. AIRS and AERI radiance values begin to converge from around 13.2 to 13.8 um. In this region both sensors are once again measuring radiance values from approximately the same level in the atmosphere, but from opposite directions. From 13.9 um on out to 15 um both sensors are

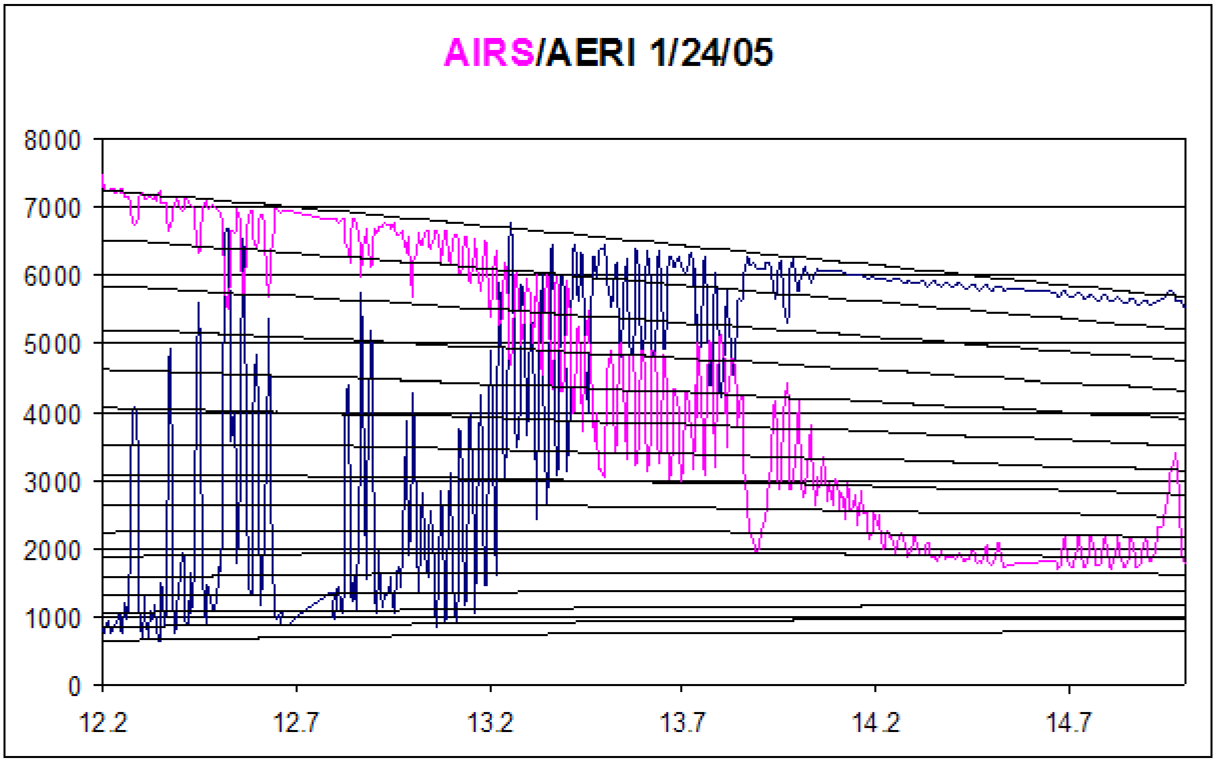

Figure G-8 AIRS/AERI spatially and temporally concurrent atmospheric spectra Region 3 measuring two different optically thick ($\sigma_\lambda=\infty$) path lengths consisting mainly of water vapor and CO2 (see Figure G-4) from two opposite directions. The atmosphere is once more for the most part opaque and AIRS once more sees tropospheric temperatures and AERI sees surface air temperatures.

References (Appendices A-G)

1. http://www.washingtonpost.com/blogs/ezra-klein/wp/2012/06/26/epas-climate-rules-upheld-in-court/,Posted by Brad Plumer on June 26, 2012 at 4:14 pm
2. Ipcc tar wg1 (2001). Houghton, J.T.; Ding, Y.; Griggs, D.J.; Noguer, M.; van der Linden, P.J.; Dai, X.; Maskell, K.; and Johnson, C.A.. ed. *Climate Change 2001: The Scientific Basis*. Contribution of Working Group I to the Third Assessment Report of the Intergovernmental Panel on Climate Change. Cambridge University Press. ISBN 0-521-80767-0 (pb: 0-521-01495-6).
3. ^"Climate Change 2001: The Scientific Basis". Grida.no. Retrieved 2012-07-30
4. ^"Climate Change 2001: The Scientific Basis". Grida.no. Retrieved 2012-07-30
5. "Climate Change 2001: The Scientific Basis". Grida.no. Retrieved 2012-07-30
6. Working Group II: Impacts, Adaptation and Vulnerability p.958 – IPCC
7. Brigham-Grette, Julie (September 2006). "Petroleum Geologists' Award to Novelist Crichton Is Inappropriate" (PDF). *Eos* **87** (36). Retrieved 2007-01-23. "The AAPG stands alone among scientific societies in its denial of human-induced effects on global warming."
8. Oreskes, Naomi (2007). "The Scientific Consensus on Climate Change: How Do We Know We're Not Wrong?". In DiMento, Joseph F. C.; Doughman, Pamela M.. *Climate Change: What It Means for Us, Our Children, and Our Grandchildren*. MIT Press. pp. 65–66. ISBN 978-0-262-54193-0.
9. Trenberth, K., J.T. Fasullo and J. Kiehl. 2009: Earth's Global Energy Budget. Bulletin of the American Meteorological Society, 90, 311-324, doi:10.1175/2008BAMS2634.1.
10. Weart, Spencer (2008). "The Carbon Dioxide Greenhouse Effect". *The Discovery of Global Warming*. American Institute of Physics. Retrieved 21 April 2009.
11. http://en.wikipedia.org/wiki/File:Solar_Spectrum.png
12. Lean, J.L., Rind, D.H., "How wil Earth's surface temperature change in future decades?", Geophysical Research Letters, vol. 36, L15708, doi:10.1029/2009GL038932
13. ^ Kiehl, J.T.; Trenberth, K.E. (1997). "Earth's Annual Global Mean Energy Budget" (PDF). *Bulletin of the American Meteorological Society* **78** (2): 197–208. Bibcode 1997BAMS...78..197K. doi:10.1175/1520-0477(1997)078<0197:EAGMEB>2.0.CO;2. ISSN 1520-0477. Archived from the original on 24 June 2008. Retrieved 21 April 2009.
14. Schmidt, Gavin (6 April 2005). "Water vapour: feedback or forcing?". RealClimate. Retrieved 21 April 2009.
15. Russell, Randy (16 May 2007). "The Greenhouse Effect & Greenhouse Gases". University Corporation for Atmospheric Research Windows to the Universe. Retrieved 27 December 2009.
16. World Meteorological Organization **http://www.wmo.int/pages/prog/arep/gaw/gaw-reports.html**

17. U.S Department of Commerce-National Oceanic & Atmospheric Administration-NOAA Research, Earth System Research Laboratory (ESRL) Global Monitoring Division, **http://www.esrl.noaa.gov/gmd/ccgg/carbontracker/**
18. Weast, R.C. (Ed.). (1975). Handbook of Chemistry and Physics 55th edition. CRC Press.
19. Houghton, J.T. (1986). The Physics of Atmospheres, second edition. Cambridge University Press.
20. Goody, R.M. (1964). Atmospheric Radiation I. Oxford at the Clarendon Press.
21. Wallace, J. M. Hobbs, P.V. (1977). Atmospheric Science An Introductory Survey. Academic Press Inc.
22. Wallace, J. M. Hobbs, P.V. (1977). Atmospheric Science An Introductory Survey. Academic Press Inc.
23. NASA Atmospheric Infrared Sounder website, http://disc.sci.gsfc.nasa.gov/AIRS/
24. DOE Atmospherically Emitted Radiance Interferometer website, http://www.arm.gov/instruments/instrument/instrument.php?id=aeri
25. http://www.arm.gov/data/vap_process.php?id=qmeaerilb
26. Shen, S. Miller, D. Lewis, P. (2007). Analysis of SO2 Point Source Emissions Using NASA Atmospheric Infrared Sounder Data. Proceedings of SPIE , Vol. 6565 65651L-1.
27. Berk, A.. Cooley, T. W., Anderson, G. P., Acharya, P. K., Bernstein, L. S., Muratov, L., Lee, J., Fox, M. J., Adler-Golden, S. M., Chetwynd, J. H., Hoke, M. L., Lockwood, R. B., Gardner, J. A., and Lewis, P. E. (2004), MODTRAN5: a reformulated atmospheric band model with auxiliary species and practical multiple scattering options, Sensors, Systems, and Next-Generation Satellites VIII, Edited by Meynart, Roland; Neeck, Steven P.; Shimoda, Haruhisa, Proceedings of the SPIE, 5571, 78-85.
28. Anderson, G.P., A. Berk., J. H. Chetwynd., J. Harder., J. M. Fontenla., E. P. Shettle., R.. Saunders., H. E. Snell, P. Pilewskie., B. C. Kindel., J. A. Gardner., M. L. Hoke., G. W. Felde, R. B. Lockwood., P. K. Acharya (2007), Using the MODTRAN™5 radiative transfer algorithm with NASA satellite data: AIRS and SORCE,, Proceedings of SPIE, Algorithms and Technologies for Multispectral, Hyperspectral, and Ultraspectral Imagery XIII, 6565, Edited by Sylvia S. Shen, Paul E. Lewis.
29. Saunders, R., P. Rayer, P. Brunel, A. von Engeln, N. Bormann, L. Strow, S. Hannon, S. Heilliette, Xu Liu, F. Miskolczi, Y. Han, G. Masiello, J.-L. Moncet, Gennady Uymin, V. Sherlock, and D. S. Turner (2007), A comparison of radiative transfer models for simulating Atmospheric Infrared Sounder (AIRS) radiances, J. Geophys. Res., VOL. 112.

Appendix H Complete documentation of the ASTM Standard laboratory methodologies D1945 and D3416 outlined in section 4.3.5 for measurement of CO_2 samples collected from the aircraft.

Appendix H-1.0 ASTM D1945-(03)Primary Methodology

Designation: D1945 – 03 (Reapproved 2010)

Standard Test Method for Analysis of Natural Gas by Gas Chromatography[1]

This standard is issued under the fixed designation D1945; the number immediately following the designation indicates the year of original adoption or, in the case of revision, the year of last revision. A number in parentheses indicates the year of last reapproval. A superscript epsilon (ε) indicates an editorial change since the last revision or reapproval.

1. Scope*

1.1 This test method covers the determination of the chemical composition of natural gases and similar gaseous mixtures within the range of composition shown in Table 1. This test method may be abbreviated for the analysis of lean natural gases containing negligible amounts of hexanes and higher hydrocarbons, or for the determination of one or more components, as required.

1.2 The values stated in inch-pound units are to be regarded as standard. The values given in parentheses are mathematical conversions to SI units that are provided for information only and are not considered standard.

1.3 *This standard does not purport to address all of the safety concerns, if any, associated with its use. It is the responsibility of the user of this standard to establish appropriate safety and health practices and determine the applicability of regulatory limitations prior to use.*

2. Referenced Documents

2.1 *ASTM Standards:*[2]

D2597 Test Method for Analysis of Demethanized Hydrocarbon Liquid Mixtures Containing Nitrogen and Carbon Dioxide by Gas Chromatography

D3588 Practice for Calculating Heat Value, Compressibility Factor, and Relative Density of Gaseous Fuels

E260 Practice for Packed Column Gas Chromatography

3. Summary of Test Method

3.1 Components in a representative sample are physically separated by gas chromatography (GC) and compared to calibration data obtained under identical operating conditions from a reference standard mixture of known composition. The numerous heavy-end components of a sample can be grouped into irregular peaks by reversing the direction of the carrier gas through the column at such time as to group the heavy ends either as C_5 and heavier, C_6 and heavier, or C_7 and heavier. The composition of the sample is calculated by comparing either the peak heights, or the peak areas, or both, with the corresponding values obtained with the reference standard.

4. Significance and Use

4.1 This test method is of significance for providing data for calculating physical properties of the sample, such as heating value and relative density, or for monitoring the concentrations of one or more of the components in a mixture.

5. Apparatus

5.1 *Detector*—The detector shall be a thermal-conductivity type, or its equivalent in sensitivity and stability. The thermal conductivity detector must be sufficiently sensitive to produce a signal of at least 0.5 mV for 1 mol % *n*-butane in a 0.25-mL sample.

5.2 *Recording Instruments*—Either strip-chart recorders or electronic integrators, or both, are used to display the separated components. Although a strip-chart recorder is not required when using electronic integration, it is highly desirable for evaluation of instrument performance.

5.2.1 The recorder shall be a strip-chart recorder with a full-range scale of 5 mV or less (1 mV preferred). The width of the chart shall be not less than 150 mm. A maximum pen response time of 2 s (1 s preferred) and a minimum chart speed of 10 mm/min shall be required. Faster speeds up to 100 mm/min are desirable if the chromatogram is to be interpreted using manual methods to obtain areas.

5.2.2 *Electronic or Computing Integrators*—Proof of separation and response equivalent to that for a recorder is required for displays other than by chart recorder. Baseline tracking with tangent skim peak detection is recommended.

5.3 *Attenuator*—If the chromatogram is to be interpreted using manual methods, an attenuator must be used with the detector output signal to maintain maximum peaks within the recorder chart range. The attenuator must be accurate to within 0.5 % between the attenuator range steps.

5.4 *Sample Inlet System:*

5.4.1 The sample inlet system shall be constructed of materials that are inert and nonadsorptive with respect to the

---

[1] This test method is under the jurisdiction of ASTM Committee D03 on Gaseous Fuels and is the direct responsibility of Subcommittee D03.07 on Analysis of Chemical Composition of Gaseous Fuels.

Current edition approved Jan. 1, 2010. Published March 2010. Originally approved in 1962. Last previous edition approved in 2003 as D1945–96(2003). DOI: 10.1520/D1945-03R10.

[2] For referenced ASTM standards, visit the ASTM website, www.astm.org, or contact ASTM Customer Service at service@astm.org. For *Annual Book of ASTM Standards* volume information, refer to the standard's Document Summary page on the ASTM website.

***A Summary of Changes section appears at the end of this standard**

TABLE 1 Natural Gas Components and Range of Composition Covered

Component	Mol %
Helium	0.01 to 10
Hydrogen	0.01 to 10
Oxygen	0.01 to 20
Nitrogen	0.01 to 100
Carbon dioxide	0.01 to 20
Methane	0.01 to 100
Ethane	0.01 to 100
Hydrogen sulfide	0.3 to 30
Propane	0.01 to 100
Isobutane	0.01 to 10
n-Butane	0.01 to 10
Neopentane	0.01 to 2
Isopentane	0.01 to 2
n-Pentane	0.01 to 2
Hexane isomers	0.01 to 2
Heptanes+	0.01 to 1

components in the sample. The preferred material of construction is stainless steel. Copper, brass, and other copper-bearing alloys are unacceptable. The sample inlet system from the cylinder valve to the GC column inlet must be maintained at a temperature constant to ±1°C.

5.4.2 Provision must be made to introduce into the carrier gas ahead of the analyzing column a gas-phase sample that has been entrapped in a fixed volume loop or tubular section. The fixed loop or section shall be so constructed that the total volume, including dead space, shall not normally exceed 0.5 mL at 1 atm. If increased accuracy of the hexanes and heavier portions of the analysis is required, a larger sample size may be used (see Test Method D2597). The sample volume must be reproducible such that successive runs agree within 1 % on each component. A flowing sample inlet system is acceptable as long as viscosity effects are accounted for.

NOTE 1—The sample size limitation of 0.5 mL or smaller is selected relative to linearity of detector response, and efficiency of column separation. Larger samples may be used to determine low-quantity components to increase measurement accuracy.

5.4.3 An optional manifold arrangement for entering vacuum samples is shown in Fig. 1.

5.5 *Column Temperature Control:*

5.5.1 *Isothermal*—When isothermal operation is used, maintain the analyzer columns at a temperature constant to 0.3°C during the course of the sample run and corresponding reference run.

5.5.2 *Temperature Programming*—Temperature programming may be used, as feasible. The oven temperature shall not exceed the recommended temperature limit for the materials in the column.

5.6 *Detector Temperature Control*—Maintain the detector temperature at a temperature constant to 0.3°C during the course of the sample run and the corresponding reference run. The detector temperature shall be equal to or greater than the maximum column temperature.

5.7 *Carrier Gas Controls*—The instrument shall be equipped with suitable facilities to provide a flow of carrier gas through the analyzer and detector at a flow rate that is constant to 1 % throughout the analysis of the sample and the reference standard. The purity of the carrier gas may be improved by flowing the carrier gas through selective filters prior to its entry into the chromatograph.

5.8 *Columns:*

5.8.1 The columns shall be constructed of materials that are inert and nonadsorptive with respect to the components in the sample. The preferred material of construction is stainless steel. Copper and copper-bearing alloys are unacceptable.

5.8.2 An adsorption-type column and a partition-type column may be used to make the analysis.

NOTE 2—See Practice E260.

5.8.2.1 *Adsorption Column*—This column must completely separate oxygen, nitrogen, and methane. A 13X molecular sieve 80/100 mesh is recommended for direct injection. A 5A column can be used if a pre-cut column is present to remove interfering hydrocarbons. If a recorder is used, the recorder pen must return to the baseline between each successive peak. The resolution (R) must be 1.5 or greater as calculated in the following equation:

$$R(1,2) = \frac{x_2 - x_1}{y_2 + y_1} \times 2, \qquad (1)$$

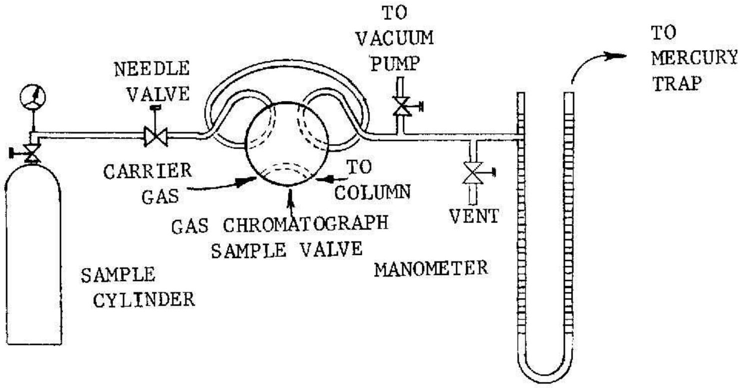

FIG. 1 Suggested Manifold Arrangement for Entering Vacuum Samples

where x_1, x_2 are the retention times and y_1, y_2 are the peak widths. Fig. 2 illustrates the calculation for resolution. Fig. 3 is a chromatogram obtained with an adsorption column.

5.8.2.2 *Partition Column*—This column must separate ethane through pentanes, and carbon dioxide. If a recorder is used, the recorder pen must return to the base line between each peak for propane and succeeding peaks, and to base line within 2 % of full-scale deflection for components eluted ahead of propane, with measurements being at the attenuation of the peak. Separation of carbon dioxide must be sufficient so that a 0.25-mL sample containing 0.1-mol % carbon dioxide will produce a clearly measurable response. The resolution (*R*) must be 1.5 or greater as calculated in the above equation. The separation should be completed within 40 min, including reversal of flow after *n*-pentane to yield a group response for hexanes and heavier components. Figs. 4-6 are examples of chromatograms obtained on some of the suitable partition columns.

5.8.3 *General*—Other column packing materials that provide satisfactory separation of components of interest may be used (see Fig. 7). In multicolumn applications, it is preferred to use front-end backflush of the heavy ends.

NOTE 3—The chromatograms in Figs. 3-8 are only illustrations of typical separations. The operating conditions, including columns, are also typical and are subject to optimization by competent personnel.

5.9 *Drier*—Unless water is known not to interfere in the analysis, a drier must be provided in the sample entering system, ahead of the sample valve. The drier must remove moisture without removing selective components to be determined in the analysis.

NOTE 4—See A2.2 for preparation of a suitable drier.

5.10 *Valves*—Valves or sample splitters, or both, are required to permit switching, backflushing, or for simultaneous analysis.

5.11 *Manometer*—May be either U-tube type or well type equipped with an accurately graduated and easily read scale covering the range 0 to 900 mm (36 in.) of mercury or larger. The U-tube type is useful, since it permits filling the sample loop with up to two atmospheres of sample pressure, thus extending the range of all components. The well type inherently offers better precision and is preferred when calibrating with pure components. Samples with up to one atmosphere of pressure can be entered. With either type manometer the mm scale can be read more accurately than the inch scale. Caution should be used handling mercury because of its toxic nature. Avoid contact with the skin as much as possible. Wash thoroughly after contact.

5.12 *Vacuum Pump*—Must have the capability of producing a vacuum of 1 mm of mercury absolute or less.

6. Preparation of Apparatus

6.1 *Linearity Check*—To establish linearity of response for the thermal conductivity detector, it is necessary to complete the following procedure:

6.1.1 The major component of interest (methane for natural gas) is charged to the chromatograph by way of the fixed-size sample loop at partial pressure increments of 13 kPa (100 mm Hg) from 13 to 100 kPa (100 to 760 mm Hg) or the prevailing atmospheric pressure.

6.1.2 The integrated peak responses for the area generated at each of the pressure increments are plotted versus their partial pressure (see Fig. 9).

6.1.3 The plotted results should yield a straight line. A perfectly linear response would display a straight line at a 45° angle using the logarithmic values.

6.1.4 Any curved line indicates the fixed volume sample loop is too large. A smaller loop size should replace the fixed volume loop and 6.1.1 through 6.1.4 should be repeated (see Fig. 9).

6.1.5 The linearity over the range of interest must be known for each component. It is useful to construct a table noting the response factor deviation in changing concentration. (See Table 2 and Table 3).

6.1.6 It should be noted that nitrogen, methane, and ethane exhibit less than 1 % compressibility at atmospheric pressure. Other natural gas components do exhibit a significant compressibility at pressures less than atmospheric.

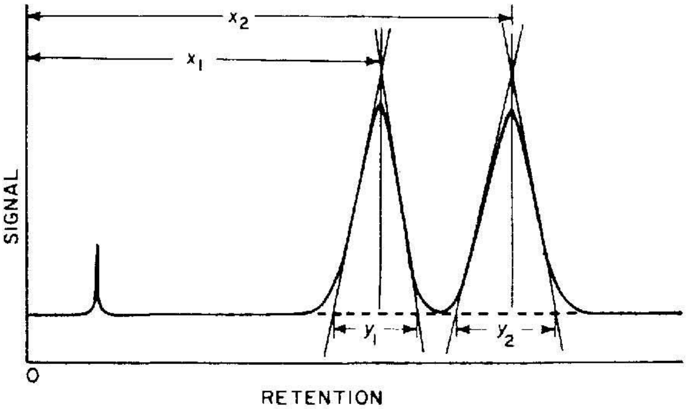

FIG. 2 Calculation for Resolution

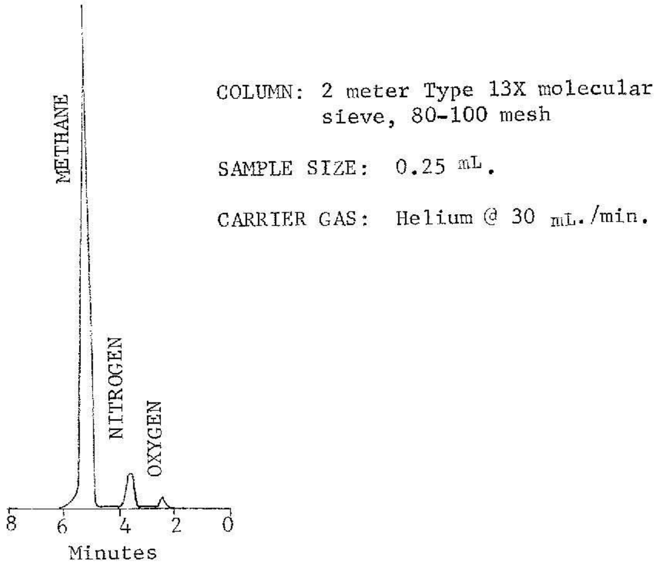

FIG. 3 Separation Column for Oxygen, Nitrogen, and Methane (See Annex A2)

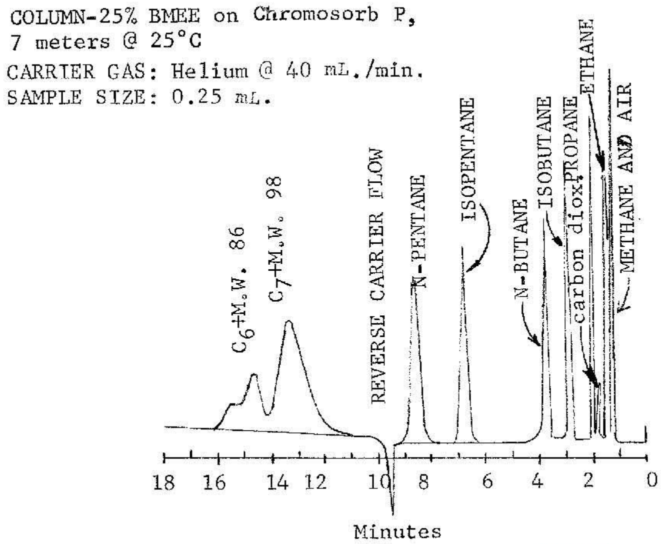

FIG. 4 Chromatogram of Natural Gas (BMEE Column) (See Annex A2)

6.1.7 Most components that have vapor pressures of less than 100 kPa (15 psia) cannot be used as a pure gas for a linearity study because they will not exhibit sufficient vapor pressure for a manometer reading to 100 kPa (760 mm Hg). For these components, a mixture with nitrogen or methane can be used to establish a partial pressure that can extend the total pressure to 100 kPa (760 mm Hg). Using Table 4 for vapor pressures at 38°C (100°F), calculate the maximum pressure to which a given component can be blended with nitrogen as follows:

$$B = (100 \times V)/i \qquad (2)$$

$$P = (i \times M)/100 \qquad (3)$$

where:

B = blend pressure, max, kPa (mm Hg);
V = vapor pressure, kPa (mm Hg);
i = mol %;
P = partial pressure, kPa (mm Hg); and
M = manometer pressure, kPa (mm Hg).

6.2 . *Procedure for Linearity Check:*

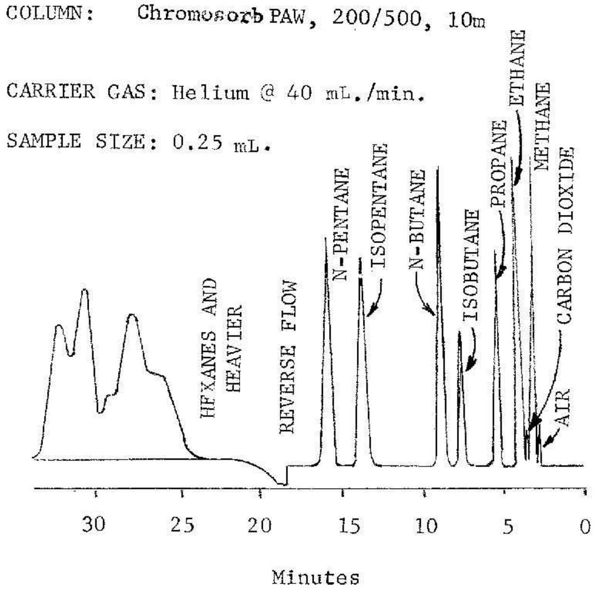

FIG. 5 Chromatogram of Natural Gas (Silicone 200/500 Column) (See Annex A2)

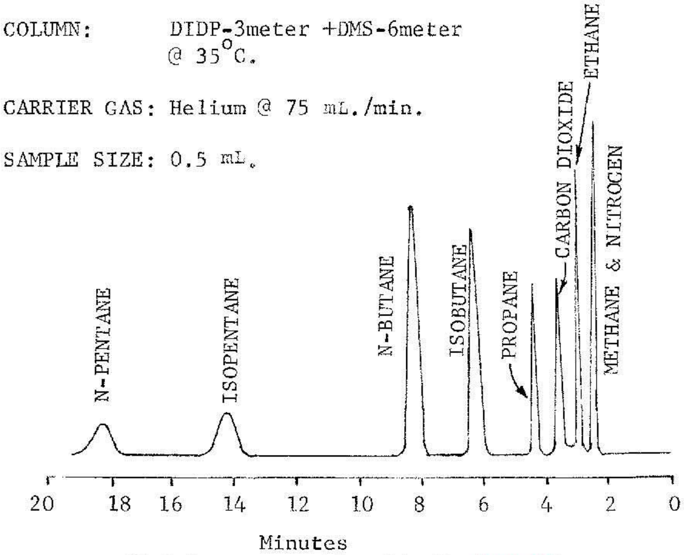

FIG. 6 Chromatogram of Natural Gas (See Annex A2)

6.2.1 Connect the pure-component source to the sample-entry system. Evacuate the sample-entry system and observe the manometer for leaks. (See Fig. 1 for a suggested manifold arrangement.) The sample-entry system must be vacuum tight.

6.2.2 Carefully open the needle valve to admit the pure component up to 13 kPa (100 mm Hg) of partial pressure.

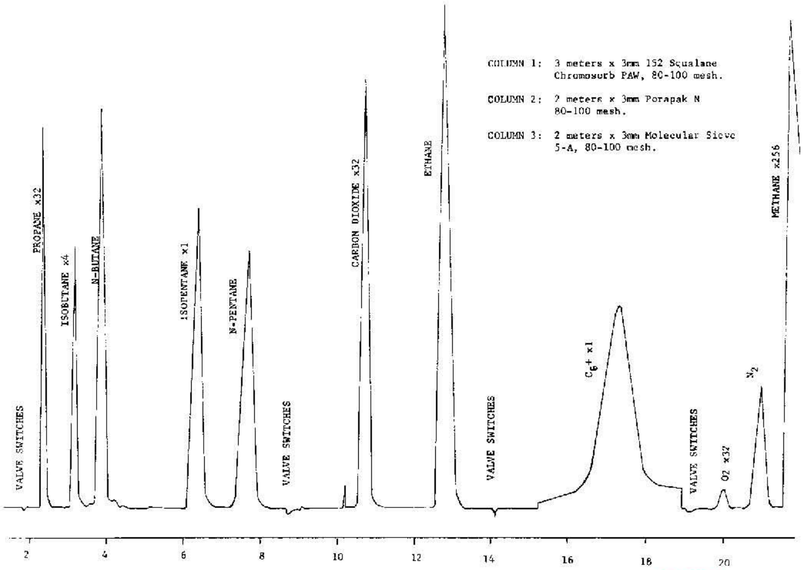

COLUMN 1: 3 meters x 3mm 152 Squalane Chromosorb PAW, 80-100 mesh.

COLUMN 2: 2 meters x 3mm Porapak N 80-100 mesh.

COLUMN 3: 2 meters x 3mm Molecular Sieve 5-A, 80-100 mesh.

FIG. 7 Chromatogram of Natural Gas (Multi-Column Application) (See Annex A2)

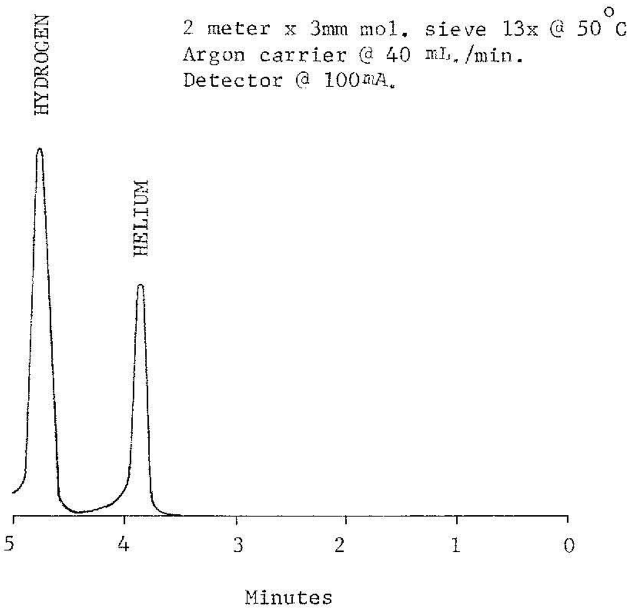

2 meter x 3mm mol. sieve 13x @ 50 °C
Argon carrier @ 40 mL./min.
Detector @ 100mA.

FIG. 8 Separation of Helium and Hydrogen

6.2.3 Record the exact partial pressure and actuate the sample valve to place the sample onto the column. Record the peak area of the pure component.

6.2.4 Repeat 6.2.3 for 26, 39, 52, 65, 78, and 91 kPa (200, 300, 400, 500, 600, and 700 mm Hg) on the manometer, recording the peak area obtained for sample analysis at each of these pressures.

6.2.5 Plot the area data (*x* axis) versus the partial pressures (*y* axis) on a linear graph as shown in Fig. 9.

6.2.6 An alternative method is to obtain a blend of all the components and charge the sample loop at partial pressure over the range of interest. If a gas blender is available, the mixture can be diluted with methane thereby giving response curves for all the components. (**Warning**—If it is not possible to obtain

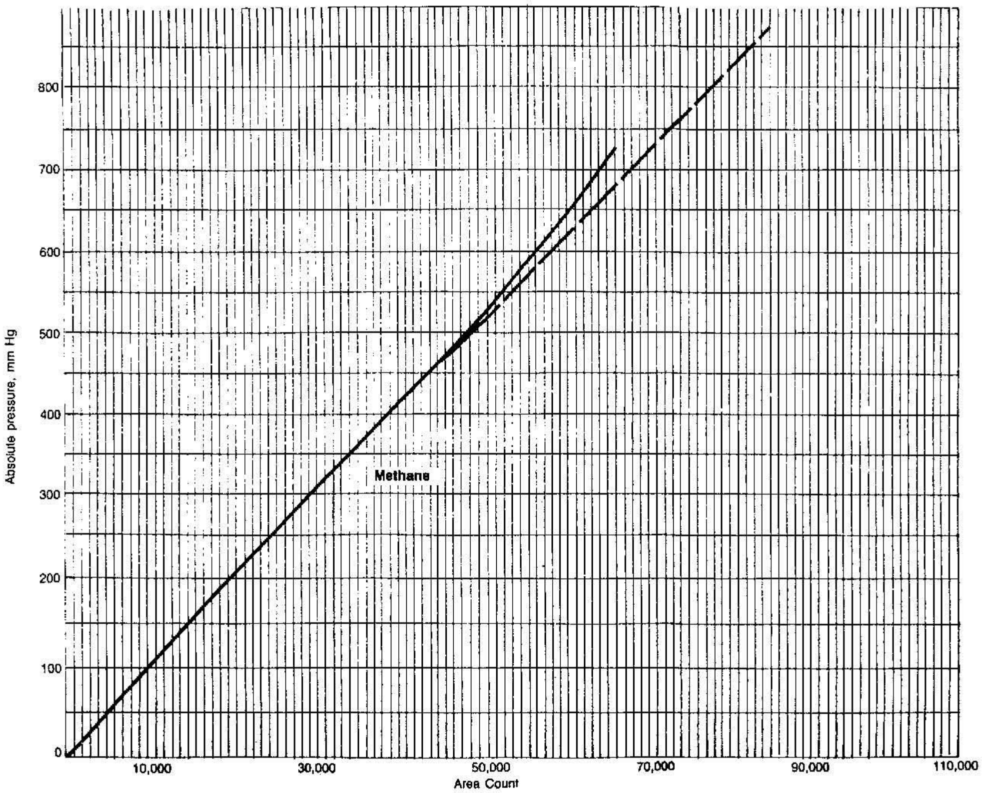

FIG. 9 Linearity of Detector Response

TABLE 2 Linearity Evaluation of Methane

S/B diff = (low mole % – high mole %)/low mole % × 100

B area	S mole %	S/B mole %/area	S/B diff., % on low value
223 119 392	51	2.2858e-07	
242 610 272	56	2.3082e-07	–0.98
261 785 320	61	2.3302e-07	–0.95
280 494 912	66	2.3530e-07	–0.98
299 145 504	71	2.3734e-07	–0.87
317 987 328	76	2.3900e-07	–0.70
336 489 056	81	2.4072e-07	–0.72
351 120 721	85	2.4208e-07	–0.57

TABLE 3 Linearity Evaluation for Nitrogen

S/B diff = (low mole % – high mole %)/low mole % × 100

B area	S mole %	S/B mole %/area	S/B diff., % on low value
5 879 836	1	1.7007e-07	
29 137 066	5	1.7160e-07	–0.89
57 452 364	10	1.7046e-07	–1.43
84 953 192	15	1.7657e-07	–1.44
111 491 232	20	1.7939e-07	–1.60
137 268 784	25	1.8212e-07	–1.53
162 852 288	30	1.8422e-07	–1.15
187 232 496	35	1.8693e-07	–1.48

information on the linearity of the available gas chromatograph detector for all of the test gas components, then as a minimum requirement the linearity data must be obtained for any gas component that exceeds a concentration of 5 mol%. Chromatographs are not truly linear over wide concentration ranges and linearity should be established over the range of interest.)

7. Reference Standards

7.1 Moisture-free gas mixtures of known composition are required for comparison with the test sample. They must contain known percents of the components, except oxygen (Note 5), that are to be determined in the unknown sample. All components in the reference standard must be homogenous in the vapor state at the time of use. The concentration of a component in the reference standard gas should not be less than one half nor more than twice the concentration of the corresponding component in the test gas.

NOTE 5—Unless the reference standard is stored in a container that has been tested and proved for inertness to oxygen, it is preferable to calibrate

TABLE 4 Vapor Pressure at 38°C (100°F)[A]

Component	kPa absolute	psia
Nitrogen	>34 500	>5000
Methane	>34 500	>5000
Carbon dioxide	>5 520	>800
Ethane	>5 520	>800
Hydrogen sulfide	2 720	395
Propane	1 300	189
Isobutane	501	72.6
n-Butane	356	51.7
Isopentane	141	20.5
n-Pentane	108	15.6
n-Hexane	34.2	4.96
n-Heptane	11.2	1.62

[A] The most recent data for the vapor pressures listed are available from the Thermodynamics Research Center, Texas A&M University System, College Station, TX 77843.

for oxygen by an alternative method.

7.2 *Preparation*—A reference standard may be prepared by blending pure components. Diluted dry air is a suitable standard for oxygen and nitrogen (see 8.5.1).[3,4]

8. Procedure

8.1 *Instrument Preparation*—Place the proper column(s) in operation as needed for the desired run (as described in either 8.4, 8.5, or 8.6). Adjust the operating conditions and allow the chromatograph to stabilize.

8.1.1 For hexanes and higher, heat the sample loop.

NOTE 6—Most modern chromatographs have valve ovens that can be temperature controlled. It is strongly recommended in the absence of valve ovens to mount the gas sampling valve in the chromatograph oven and operate at the column temperature.

8.1.2 After the instrument has apparently stabilized, make check runs on the reference standard to establish instrument repeatability. Two consecutive checks must agree within the repeatability limits for the mol % amount present of each component. Either the average of the two consecutive checks, or the latest check agreeing within the repeatability limits of the previous check on each component may be used as the reference standard for all subsequent runs until there is a change in instrument operating conditions. Daily calibrations are recommended.

8.2 *Sample Preparation*—If desired, hydrogen sulfide may be removed by at least two methods (see Annex A2.3A2.3).

8.2.1 *Preparation and Introduction of Sample*—Samples must be equilibrated in the laboratory at 20 to 50°F above the source temperature of the field sampling. The higher the temperature the shorter the equilibration time (approximately 2 h for small sample containers of 300 mL or less). This analysis method assumes field sampling methods have removed entrained liquids. If the hydrocarbon dewpoint of the sample is known to be lower than the lowest temperature to which the sample has been exposed, it is not necessary to heat the sample.

8.2.2 Connections from the sample container to the sample inlet of the instrument should be made with stainless steel or with short pieces of TFE-fluorocarbon. Copper, vinyl, or rubber connections are not acceptable. Heated lines may be necessary for high hydrocarbon content samples.

8.3 *Sample Introduction*—The size of the sample introduced to the chromatographic columns shall not exceed 0.5 mL. (This small sample size is necessary to obtain a linear detector response for methane.) Sufficient accuracy can be obtained for the determination of all but the minor constituents by the use of this sample size. When increased response is required for the determination of components present in concentrations not exceeding 5 mol %, it is permissible to use sample and reference standard volumes not exceeding 5 mL. (Avoid introduction of liquids into the sample system.)

8.3.1 *Purging Method*—Open the outlet valve of the sample cylinder and purge the sample through the inlet system and sample loop or tube. The amount of purging required must be established and verified for each instrument. The sample loop pressure should be near atmospheric. Close the cylinder valve and allow the pressure of the sample in the loop or tube to stabilize. Then immediately inject the contents of the loop or tube into the chromatographic column to avoid infiltration of contaminants.

8.3.2 *Water Displacement*—If the sample was obtained by water displacement, then water displacement may be used to purge and fill the sample loop or tube. (**Warning**—Some components, such as carbon dioxide, hydrogen sulfide, and hexanes and higher hydrocarbons, may be partially or completely removed by the water.)

8.3.3 *Evacuation Method*—Evacuate the charging system, including the sample loop, and the sample line back to the valve on the sample cylinder, to less than 0.1 kPa (1 mm Hg) absolute pressure. Close the valve to the vacuum source and carefully meter the fuel-gas sample from the sample cylinder until the sample loop is filled to the desired pressure, as indicated on the manometer (see Fig. 1). Inject the sample into the chromatograph.

8.4 *Partition Column Run for Ethane and Heavier Hydrocarbons and Carbon Dioxide*—This run is made using either helium or hydrogen as the carrier gas; if other than a thermal conductivity detector is used, select a suitable carrier gas for that detector. Select a sample size in accordance with 8.1. Enter the sample, and backflush heavy components when appropriate. Obtain a corresponding response on the reference standard.

8.4.1 Methane may also be determined on this column if the column will separate the methane from nitrogen and oxygen (such as with silicone 200/500 as shown in Fig. 5), and the sample size does not exceed 0.5 mL.

8.5 *Adsorption Column Run for Oxygen, Nitrogen, and Methane*—Make this run using helium or hydrogen as the carrier gas. The sample size must not exceed 0.5 mL for the determination of methane. Enter the sample and obtain a response through methane (Note 5). Likewise, obtain a response on the reference standard for nitrogen and methane. Obtain a response on dry air for nitrogen and oxygen, if desired. The air must be either entered at an accurately measured reduced pressure, or from a helium-diluted mixture.

---

[3] A suitable reference standard is available from Scott Specialty Gases Inc., Plumsteadville, PA.

[4] A ten-component reference standard traceable to the National Institute of Standards and Technology (NIST) is available from Institute of Gas Technology (IGT), 3424 S. State St., Chicago, IL 60616.

8.5.1 A mixture containing approximately 1 % of oxygen can be prepared by pressurizing a container of dry air at atmospheric pressure to 2 MPa (20 atm) with pure helium. This pressure need not be measured precisely, as the concentration of nitrogen in the mixture thus prepared must be determined by comparison to nitrogen in the reference standard. The percent nitrogen is multiplied by 0.268 to obtain the mole percent of oxygen or by 0.280 to obtain the mole percent total of oxygen and argon. Do not rely on oxygen standards that have been prepared for more than a few days. It is permissible to use a response factor for oxygen that is relative to a stable constituent.

8.6 *Adsorption Column Run for Helium and Hydrogen*—Make this run using either nitrogen or argon as the carrier gas. Enter a 1- to 5-mL sample and record the response for helium, followed by hydrogen, which will be just ahead of oxygen (Note 5). Obtain a corresponding response on a reference standard containing suitable concentrations of helium and hydrogen (see Fig. 8).

9. Calculation

9.1 The number of significant digits retained for the quantitative value of each component shall be such that accuracy is neither sacrificed or exaggerated. The expressed numerical value of any component in the sample should not be presumed to be more accurate than the corresponding certified value of that component in the calibration standard.

9.2 *External Standard Method:*

9.2.1 *Pentanes and Lighter Components*—Measure the height of each component peak for pentanes and lighter, convert to the same attenuation for corresponding components in the sample and reference standard, and calculate the concentration of each component in the sample as follows:

$$C = S \times (A/B) \tag{4}$$

where:

C = component concentration in the sample, mol %;
A = peak height of component in the sample, mm;
B = peak height of component in the standard, mm; and
S = component concentration in the reference standard, mol %.

9.2.1.1 If air has been run at reduced pressure for oxygen or nitrogen calibration, or both, correct the equation for pressure as follows:

$$C = S \times (A/B) \times (P_a/P_b) \tag{5}$$

where:

P_a = pressure at which air is run and
P_b = true barometric pressure during the run, with both pressures being expressed in the same units.

9.2.1.2 Use composition values of 78.1 % nitrogen and 21.9 % oxygen for dry air, because argon elutes with oxygen on a molecular sieves column under the normal conditions of this test method.

9.2.2 *Hexanes and Heavier Components*—Measure the areas of the hexanes portion and the heptanes and heavier portion of the reverse-flow peak (see Annex A1, Fig. A1.1, and X3.6). Also measure the areas of both pentane peaks on the sample chromatogram, and adjust all measured areas to the same attenuation basis.

9.2.3 Calculate corrected areas of the reverse flow peaks as follows:

$$\text{Corrected } C_6 \text{ area} = 72/86 \times \text{measured } C_6 \text{ area} \tag{6}$$

$$\text{Corrected } C_7 \text{ and heavier area} \tag{7}$$

$$= 72/A \times \text{measured } C_7 \text{ and heavier area}$$

where A = average molecular weight of the C_7 and heavier fraction.

NOTE 7—The value of 98 is usually sufficiently accurate for use as the C_7 and heavier fraction average molecular weight; the small amount of C_8 and heavier present is usually offset by the lighter methyl cyclopentane and cyclohexane that occur in this fraction. A more accurate value for the molecular weight of C_7 and heavier can be obtained as described in Annex A1.3.

9.2.4 Calculate the concentration of the two fractions in the sample as follows:

$$\text{Mol \% C6} = (\text{corrected } C_6 \text{ area}) \tag{8}$$

$$\times (\text{mol \% } iC_5 + nC_5)/(iC_5 + nC_5 \text{ area}).$$

$$\text{Mol \% } C_7+ = (\text{corrected } C_7 \text{ area}) \tag{9}$$

$$\times (\text{mol \% } iC_5 + nC_5)/(iC_5 + nC_5 \text{ area}).$$

9.2.4.1 If the mole percent of $iC_5 + nC_5$ has been determined by a separate run with a smaller sized sample, this value need not be redetermined.

9.2.5 The entire reverse flow area may be calculated in this manner as C_6 and heavier, or as C_5 and heavier should the carrier gas reversal be made after *n*-butane. The measured area should be corrected by using the average molecular weights of the entire reverse-flow components for the value of A. The mole percent and area of the iC_5 and nC_5 reverse flow peak of an identically sized sample of reference standard (free of C_6 and heavier) shall then be used for calculating the final mole percent value.

9.2.6 Normalize the mole percent values by multiplying each value by 100 and dividing by the sum of the original values. The sum of the original values should not differ from 100.0 % by more than 1.0 %.

9.2.7 See sample calculations in Appendix X2.

10. Precision

10.1 *Precision*—The precision of this test method, as determined by the statistical examination of the interlaboratory test results, for gas samples of pipeline quality 38 MJ/m^3 (1000 Btu/SCF) is as follows:

10.1.1 *Repeatability*—The difference between two successive results obtained by the same operator with the same apparatus under constant operating conditions on identical test materials should be considered suspect if they differ by more than the following amounts:

Component, mol %	Repeatability
0 to 0.09	0.01
0.1 to 0.9	0.04
1.0 to 4.9	0.07
5.0 to 10	0.08
Over 10	0.10

10.1.2 *Reproducibility*—The difference between two results obtained by different operators in different laboratories on identical test materials should be considered suspect if they differ by more than the following amounts:

Component, mol %	Reproducibility
0 to 0.09	0.02
0.1 to 0.9	0.07
1.0 to 4.9	0.10
5.0 to 10	0.12
Over 10	0.15

11. Keywords

11.1 gas analysis; gas chromatography; natural gas composition

ANNEXES

(Mandatory Information)

A1. SUPPLEMENTARY PROCEDURES

A1.1 Analysis for Only Propane and Heavier Components

A1.1.1 This determination can be made in 10- to 15-min run time by using column conditions to separate propane, isobutane, *n*-butane, isopentane, *n*-pentane, hexanes, and heptanes, and heavier, but disregarding separation on ethane and lighter.

A1.1.2 Use a 5-m bis-(2(2-methoxyethoxy) ethyl)ether (BMEE) column at about 30°C, or a suitable length of another partition column that will separate propane through *n*-pentane in about 5 min. Enter a 1- to 5-mL sample into the column and reverse the carrier gas flow after *n*-pentane is separated. Obtain a corresponding chromatogram on the reference standard, which can be accomplished in about 5-min run time, as there is no need to reverse the flow on the reference standard. Make calculations in the same manner as for the complete analysis method.

A1.1.3 A determination of propane, isobutane, *n*-butane, and pentanes and heavier can be made in about 5-min run time by reversing the carrier-gas flow after *n*-butane. However, it is necessary to know the average molecular weight of the pentanes and heavier components.

A1.2 Single-Run Analysis for Ethane and Heavier Components

A1.2.1 In many cases, a single partition run using a sample size in the order of 1 to 5 mL will be adequate for determining all components except methane, which cannot be determined accurately using this size sample with peak height measurements, because of its high concentration.

A1.2.2 Enter a 1- to 5-mL sample into the partition column and reverse the carrier gas flow after *n*-pentane is separated. Obtain a corresponding chromatogram of the reference standard. Measure the peak heights of ethane through *n* -pentane and the areas of the pentane peaks of the standard. Make calculations on ethane and heavier components in the same manner as for the complete analysis method. Methane and lighter may be expressed as the difference between 100 and the sum of the determined components.

A1.3 Special Analysis to Determine Hexanes and Heavier Components

A1.3.1 A short partition column can be used advantageously to separate heavy-end components and obtain a more detailed breakdown on composition of the reverse-flow fractions. This information provides quality data and a basis for calculating physical properties such as molecular weight on these fractions.

A1.3.2 Fig. A1.1 is a chromatogram that shows components that are separated by a 2-m BMEE column in 20 min. To make this determination, enter a 5-mL sample into the short column and reverse the carrier gas after the separation of *n*-heptane. Measure areas of all peaks eluted after *n*-pentane. Correct each peak area to the mol basis by dividing each peak area by the molecular weight of the component. A value of 120 may be used for the molecular weight of the octanes and heavier reverse-flow peak. Calculate the mole percent of the hexanes and heavier components by adding the corrected areas and dividing to make the total 100 %.

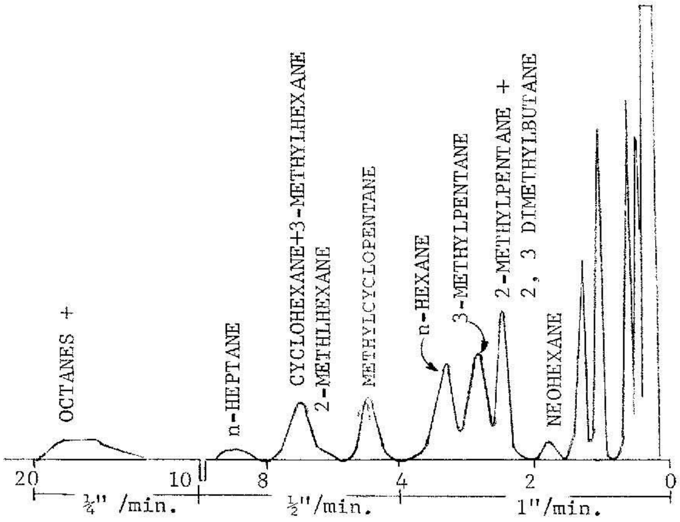

FIG. A1.1 Composition of Hexanes and Heavier Fraction

A2. PREPARATION OF COLUMNS AND DRIER

A2.1 *Preparation of Columns*—See Practice E260.

A2.2 *Preparation of Drier*—Fill a 10-mm diameter by 100-mm length glass tube with granular phosphorus pentoxide or magnesium perchlorate, observing all proper safety precautions. Mount as required to dry the sample. Replace the drying agent after about one half of the material has become spent.

A2.3 *Removal of Hydrogen Sulfide:*

A2.3.1 For samples containing more than about 300 ppm by mass hydrogen sulfide, remove the hydrogen sulfide by connecting a tube of sodium hydrate absorbent (Ascarite) ahead of the sample container during sampling, or ahead of the drying tube when entering the sample into the chromatograph. This procedure also removes carbon dioxide, and the results obtained will be on the acid-gas free basis.

A2.3.2 Hydrogen sulfide may also be removed by connecting a tube of pumice that has been impregnated with cupric sulfate in the line upstream of both the chromatograph and drying tube. This procedure will remove small amounts of hydrogen sulfide while having but minimal effect on the carbon dioxide in the sample.

A2.4 *Column Arrangement*—For analyses in which hexanes and heavier components are to be determined, Fig. A2.1shows an arrangement whereby columns can be quickly and easily changed by the turn of a selector valve. Two columns are necessary to determine all of the components covered in this test method. However, short and long partition columns provide the flexibility of three partition column lengths, by using them either singly or in series. The connection between V_1 and V_2 in Fig. A2.1 should be as short as possible (20 mm is practical) to minimize dead space between the columns when used in series. If all columns are chosen to operate at the same temperature, then stabilization time between changing columns will be minimized.

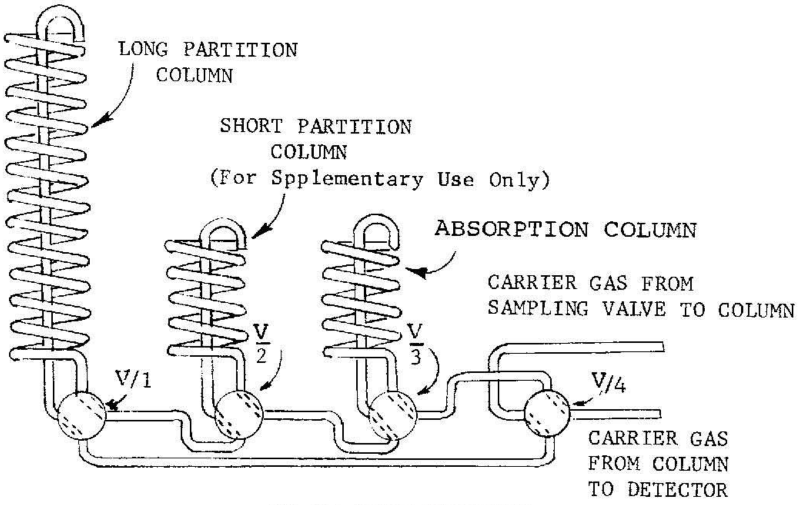

FIG. A2.1 Column Arrangement

APPENDIXES

(Nonmandatory Information)

X1. REFERENCE STANDARD MIXTURE

X1.1 Preparation

X1.1.1 Gas mixtures of the following typical compositions will suffice for use as reference standards for most analytical requirements (Note X1.1):

Component	Lean Gas, mol %	Rich Gas, mol %
Helium	1.0	0.5
Hydrogen	3.0	0.5
Nitrogen	4.0	0.5
Methane (maximum)	85	74
Ethane	6.0	10
Carbon dioxide	1.0	1.0
Propane	4.0	7.0
Isobutane	2.0	3.0
n-Butane	2.0	3.0
Neopentane	0.5	1.0
Isopentane	0.5	1.0
n-Pentane	0.5	1.0
Hexanes+	0.1	0.2

NOTE X1.1—If the mixture is stored under pressure, take care to ensure that the partial pressure of any component does not exceed its vapor pressure at the temperature and pressure at which the sample is stored and used. The lean mixture has a cricondentherm at 60°F and the rich mixture has a cricondentherm at 100°F.

X1.1.2 A useful method for preparation of a reference standard by weight is as follows:[3]

X1.1.2.1 Obtain the following equipment and material:

Cylinder, 20 L
Pressure Cylinders, two 100 mL (*A* and *B*)
Balance, 2000-g capacity, sensitivity of 10 mg.
Pure Components, methane through *n*-pentane, and carbon dioxide. The pure components should be 99+ % pure. Methane should be in a 1-L cylinder at 10-MPa (100-atm) pressure. Run a chromatogram of each component to check on its given composition.

X1.1.2.2 Evacuate the 20-L cylinder for several hours. Evacuate 100-mL Cylinder *A*, and obtain its true weight. Connect Cylinder *A* to a cylinder of pure *n*-pentane with a metal connection of calculated length to contain approximately the amount of *n*-pentane to be added. Flush the connection with the *n*-pentane by loosening the fitting at the valve on Cylinder *A*. Tighten the fitting. Close the *n*-pentane cylinder valve and open Cylinder *A* valve to admit the *n*-pentane from the connection and then close the valve on Cylinder *A*. Disconnect and weigh Cylinder *A* to obtain the weight of *n*-pentane added.

X1.1.2.3 Similarly, add isopentane, *n*-butane, isobutane, propane, ethane, and carbon dioxide, in that order, as desired, in the reference standard. Weigh Cylinder *A* after each addition to obtain the weight of the component added. Connect Cylinder *A* to the evacuated 20-L cylinder with as short a clean, small-diameter connector as possible. Open the valve on the 20-L cylinder, then open the valve on Cylinder *A*. This will result in the transfer of nearly all of the contents of Cylinder *A* into the 20-L cylinder. Close the cylinder valves, disconnect, and weigh Cylinder *A* to determine the weight of mixture that was not transferred to the 20-L cylinder.

X1.1.2.4 Evacuate and weigh 100-mL Cylinder *B*. Then fill Cylinder *B* with helium and hydrogen respectively to the pressures required to provide the desired concentrations of these components in the final blend. (Helium and hydrogen are prepared and measured separately from the other components to prevent their pressures, while in the 100-mL cylinder, from causing condensation of the higher hydrocarbons.) Weigh Cylinder *B* after each addition to obtain the weight of the component added. Connect Cylinder *B* to the 20-L cylinder with as short a clean, small-diameter connector as possible. Open the valve on the 20-L cylinder, then open the valve on Cylinder *B*, which will result in the transfer of nearly all of the contents of Cylinder *B* into the 20-L cylinder. Close the cylinder valves, disconnect, and weigh Cylinder *B* to obtain the weight of the mixture that was not transferred to the 20-L cylinder.

X1.1.2.5 Weigh a 1-L cylinder containing pure methane at about 10-MPa (100-atm) pressure. Transfer the methane to the 20-L cylinder until the pressure equalizes. Weigh the 1-L cylinder to determine the weight of methane transferred.

X1.1.2.6 Thoroughly mix the contents of the 20-L cylinder by heating at the bottom by a convenient means such as hot water or a heat lamp, and leaving the cylinder in a vertical position for at least 6 h.

X1.1.2.7 Use the weights and purities of all components added to calculate the weight composition of the mixture. Convert the weight percent to mole percent.

X1.2 Calibration with Pure Components

X1.2.1 Use helium carrier gas to admit a sample volume of 0.25 to 0.5 mL into the adsorption column, providing methane at 50-kPa (375-mm Hg) and nitrogen at 10-kPa (75-mm Hg) absolute pressure. Run a sample of the standard mixture at 70-kPa (525-mm Hg) pressure and obtain peaks for methane and nitrogen.

NOTE X1.2—Each run made throughout this procedure should be repeated to ensure that peak heights are reproducible after correction for pressure differences to within 1 mm or 1 % of the mean value. All peaks should be recorded at an instrument attenuation that gives the maximum measurable peak height.

X1.2.2 Change the carrier gas to argon or nitrogen and, after the base line has stabilized, enter a sample of pure helium at 7-kPa (50-mm Hg) absolute pressure, recording the peak at an attenuation that allows maximum peak height. Run a sample of the mixture at 70-kPa (525-mm Hg) absolute pressure and obtain the helium peak.

X1.2.3 Switch to the partition column with helium carrier gas, and run the gas mixture at 70-kPa (525-mm Hg) absolute pressure. Then admit samples of pure ethane and propane at 10-kPa (75-mm Hg) absolute pressure, and butanes, pentanes, and carbon dioxide at 5-kPa (38-mm Hg) absolute pressure.

X1.2.4 Run the gas mixture at 70-kPa (525-mm Hg) absolute pressure.

X1.2.5 Calculate the composition of the prepared gas mixture as follows:

X1.2.5.1 Correct peak heights of all pure components and the respective components in the blend to the same attenuation (Note X1.2).

X1.2.5.2 Calculate the concentration of each component as follows:

$$C = (100V_f)(A/B)(P_b/P_a) \tag{X1.1}$$

where:

C = component concentration, mol;
A = peak height of component in blend;
B = peak height of pure component;
P_a = pressure at which blend is run, kPa (mm Hg);
P_b = pressure at which component is run, kPa (mm Hg); and
V_f = volume fraction of pure component.

NOTE X1.3—V_f = 1.000 if the calibration component is free of impurities.

X1.2.5.3 Normalize values to 100.0 %.

X1.3 Calibration using Relative Molar Response Values

X1.3.1 Relative response ratios can be derived from linearity data and used for calculating response factors. This eliminates the need for a multicomponent standard for daily calibration. The test method can be used on any gas chromatograph using a thermal conductivity or thermistor detector.

X1.3.2 Obtain a blend that brackets the expected concentration the instrument will be analyzing. The major component (methane) is used as the balance gas and may fall below the expected concentration. This component is present in the daily calibration standard and linearity is assured from previous tests.

X1.3.3 Inject the sample at reduced pressures using the apparatus in Fig. 1 or using a mechanical gas blender. Obtain repeatable peak areas or height at 90, 75, 60, 45, 30, and 15 % of absolute pressure. For 100 kPa (760 mm Hg), the pressures used are 90 kPa (684 mm Hg), 75 kPa (570 mm Hg), 60 kPa (456 mm Hg), 45 Kpa (342 mm Hg), 30 kPa (228 mm Hg), 15 kPa (114 mm Hg).

X1.3.4 Plot the area or height (attenuated at the same height as the reference component) versus concentration and calculate the slope of the line by the least squares method. Given the equation of the line as $Y = a_O + a_1 X$ where Y represents the area or height points and X the concentration points. The line is assumed to intersect through the origin and $a_0 = 0$. The slope a_1 can be calculated by:

$$a_1 = \frac{\sum XY}{\left(\sum Y\right)^2} \tag{X1.2}$$

X1.3.5 Ratio the slopes of the referenced components (*i*) to the slopes of the reference components (*r*) present in the daily calibration standard. This gives the Relative Molar Response factor (RMR_i) for component (*i*). The reference component must be present in the same instrumental sequence (except Hexanes+) as the referenced components. For instance, propane can be the reference component for the butanes and pentanes if propane is separated on the same column in the same sequence as the butanes and pentanes. Ethane can be the reference component for carbon dioxide if it elutes in the same sequence as carbon dioxide. The hexanes + peak can be referenced to propane or calculated as mentioned in the body of the standard.

X1.3.6 For daily calibration, a four-component standard is used containing nitrogen, methane, ethane, and propane. The fewer components eliminates dew point problems, reactivity, is more accurate and can be blended at a higher pressure. The

TABLE X1.1 Least Square Calculation for Slope of Iso-Butane

	Area Y	Mole % X	XY	Y^2
	984 515	1	984 515	9.693e + 11
	900 410	0.9	810 369	8.107e + 11
	758 917	0.75	569 187.75	5.670e + 11
	611 488	0.6	366 892.8	3.739e + 11
	466 037	0.45	209 716.65	2.172e + 11
	314 649	0.3	94 394.7	9.900e + 10
	159 303	0.15	23 895.45	2.538e + 10
sum =	4 195 319	4.15	3 058 971.35	3.071 452e + 12
	slope =	$\sum XY/\sum Y^2$	9.9594e-07	

referenced components' response factors are calculated from the current reference factor and the Relative Molar Response factor. Following is a description of the basic calculations, an example of deriving a Relative Molar Response factor (Fig. X1.1), and a table showing how response factors are calculated (Table X1.2).

$$\text{Response Factor (R)} = \frac{\text{Mole \%}}{\text{Area}}, \tag{X1.3}$$

$$\text{Relative Molar Response } (RMR_i) = \frac{\text{Mole \%}(i)/\text{Area}(i)}{\text{Mole \%}(r)/\text{Area}(r)} \tag{X1.4}$$

$$R_{iC_4} = RMR_{iC_4} \times R_{C_3} \tag{X1.5}$$

X1.3.7 Periodic checks of the RMR relationship is recommended. The relationship is independent of temperature, sample size, and carrier gas flow rate. If changes occur in these operating conditions, all of the components will be affected equally and the calculated response factors will shift accordingly. See Table X1.1 and Fig. X1.1 and Table X1.2.

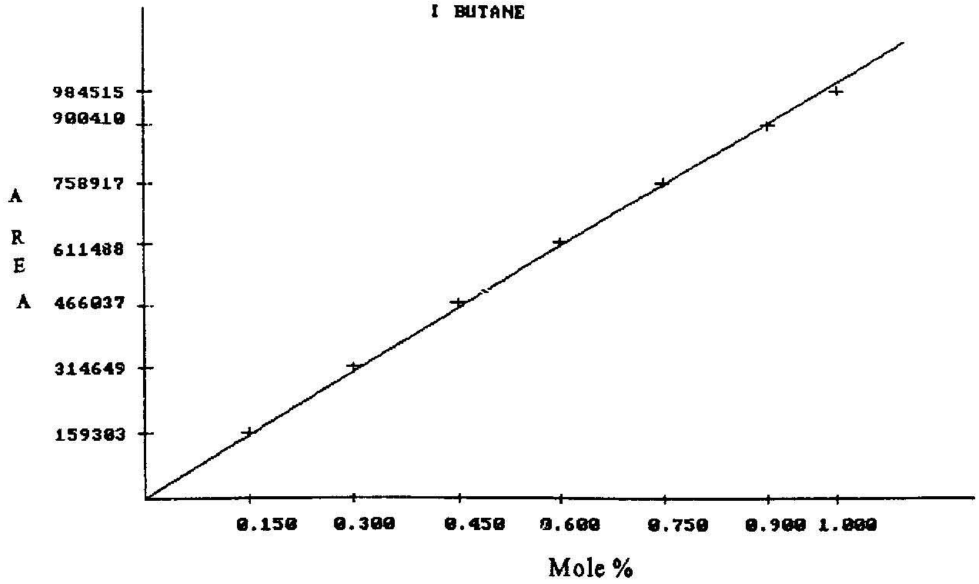

FIG. X1.1 Example of Deriving a Relative Molar Response Factor

TABLE X1.2 Calculation of Response Factors Using Relative Molar Response Values

Component	Mole % in Reference Standard S	Response of Reference Standard B	Response Factor From Reference Standard S/B,K	Relative Molar[A] Response from $\text{Slope}_i/\text{K}_i$ RMR_i	Response Factor of Referenced Components $(\text{RMR}_i)\text{x}(\text{K}_i)$
Nitrogen	5.08	2 685 885	1.8914E-6		
Methane	82.15	36 642 384	2.2419E-6		
Ethane	8.75	6 328 524	1.3826E-6		
Propane	4.02	3 552 767	1.1315E-6		
Carbon dioxide				$1.116\,07_{c2}$	1.5429E-6
Isobutane				$0.729\,58_{c3}$	9.9594E-7
n-Butane				$0.693\,10_{c3}$	9.1142E-7
Neopentane				$0.682\,71_{c3}$	8.9776E-7
Isopentane				$0.638\,74_{c3}$	8.3994E-7
n-Pentane				$0.600\,41_{c3}$	7.8953E-7
Hexanes+				$0.547\,62_{c3}$	7.2012E-7

[A] The Relative Molar Response is a constant that is calculated by dividing the slope of the referenced component by the component that is present in the reference standard. For example:

$$\text{RMR}_{ic_4} = (\text{slope}\,ic_4)/(\text{K}\,c_3) = 9.9594E-7\ 1.1315E-6 = 0.729\,58$$

X2. SAMPLE CALCULATIONS (SEE SECTION 9)

X3. PRECAUTIONS FOR AVOIDING COMMON CAUSES OF ERRORS

TABLE X2.1 Sample Calculations

Component	Mol % in Reference Standard, *S*	Response of Reference Standard, *B*	Response Factor, *S/B*	Response for Sample,[A] *A*	Percent *C* = *(S × A)/B*	Normalized, %
Helium	0.50	41.1	0.0122	12.6	0.154	0.15
Hydrogen	0.74	90.2	0.0082	1.5	0.012	0.01
Oxygen	0.27	35.5	0.0076	2.1	0.016	0.02
Nitrogen	4.89	77.8	0.0629	75.6	4.755	4.75
Methane	70.27	76.4	0.9198	90.4	83.150	83.07
Ethane	9.07	96.5	0.0940	79.0	7.426	7.42
Carbon dioxide	0.98	57.5	0.0170	21.2	0.360	0.36
Propane	6.65	55.2	0.1205	20.6	2.482	2.48
Isobutane	2.88	73.2	0.0393	11.0	0.432	0.43
n-Butane	2.87	60.3	0.0476	15.0	0.714	0.71
Neopentane	0.59	10.4	0.0567	0.1	0.006	0.01
Isopentane	0.87	96.0	0.0091	24.0	0.218	0.22
n-Pentane	0.86	86.8	0.0099	20.5	0.203	0.20
Hexanes+[B]				72.1[C]	0.166[D]	0.17
					100.094 %	100.00 %

[A] The response for a constituent in the sample has been corrected to the same attenuation as for that constituent in the reference standard.

[B] Average molecular weight of $C_6+ = 92$.

[C] Corrected C_6 response = (original response of 92.1) × (72/92) = 72.1.

[D] Mol % $C_6+ = (0.218 + 0.203) \times (72.1)/(96.0 + 86.8) = 0.166$.

% iC_5 % nC_5 Areas $iC + nC_5$

X3.1 Hexane and Heavier Content Change

X3.1.1 The amounts of heavy-end compounds in natural gas are easily changed during handling and entering of samples to give seriously erroneous low or high values. Concentration of these components has been observed to occur in a number of cases because of collection of heavier components in the sample loop during purging of the system. The surface effect of small diameter tubing acts as a separating column and must not be used in the sampling and entering system when components heavier than pentanes are to be determined. An accumulation of oily film in the sampling system greatly aggravates this problem. Also, the richer the gas, the worse the problem. Periodically, check C_6 and heavier repeatability of the apparatus by making several check runs on the same sample. It is helpful to retain a sample containing some hexanes and heavier for periodic checking. When enlargement of the heavy end peaks is noted, thoroughly clean the sampling valve and loop with acetone. This trouble has been experienced with some inlet systems even when clean and with the specified sample loop size. This contamination can be minimized by such techniques as purging with inert gas, heating the sample loop, using a vacuum system, or other such effective means.

X3.2 Acid Gas Content Change

X3.2.1 The carbon dioxide and hydrogen sulfide contents of gas are easily altered during sampling and handling. If samples containing carbon dioxide or hydrogen sulfide, or both, are to be taken, use completely dry sample cylinders, connections, and lines, as moisture will selectively absorb appreciable amounts of the acid gases. If hydrogen is present, use aluminum, stainless steel, or other materials inert to hydrogen sulfide for the cylinder, valves, lines, and connections.

X3.3 Sample Dew Point

X3.3.1 Nonrepresentative samples frequently occur because of condensation of liquid. Maintain all samples above the hydrocarbon dew point. If cooled below this, heat 10°C or more above the dew point for several hours before using. If the dew point is unknown, heat above the sampling temperature.

X3.4 Sample Inlet System

X3.4.1 Do not use rubber or plastic that may preferentially adsorb sample components. Keep the system short and the drier small to minimize the purging required.

X3.5 Sample Size Repeatability

X3.5.1 Varying back pressures on the sample loop may impair sample size repeatability.

X3.5.2 Make it a practice to make all reverse flow determinations in the same carrier gas flow direction. All single-peak determinations and corresponding reference runs will then be made in the same carrier gas flow direction.

X3.5.3 Be sure that the inlet drier is in good condition. Moisture on the column will enlarge the reverse flow peak.

X3.5.4 Be sure the column is clean by occasionally giving it several hours sweep of carrier gas in reverse flow direction. A level baseline should be quickly attained in either flow direction if the column is clean.

X3.5.5 When the reverse flow valve is turned, there is a reversal of pressure conditions at the column ends that upsets the carrier gas flow. This flow should quickly return to the same flow rate and the baseline level out. If it does not, the cause may be a leak in the carrier gas system, faulty flow regulator, or an unbalanced condition of the column or plumbing.

X3.6 Reference Standard

X3.6.1 Maintain the reference standard at +15°C or a temperature that is above the hydrocarbon dew point. If the reference standard should be exposed to lower temperatures, heat at the bottom for several hours before removing a sample. If in doubt about the composition, check the *n*-pentane and isopentane values with pure components by the procedure prescribed in Annex A2.

X3.7 Measurements

X3.7.1 The baseline and tops of peaks should be plainly visible for making peak height measurements. Do not use a fixed zero line as the baseline, but use the actual observed baseline. On high sensitivity, this baseline may drift slightly without harm and it need not frequently be moved back to zero. A strip-chart recorder with an offset zero is desirable. The area of reverse flow peak may be measured by planimeter or geometric construction. The reverse flow area, and the pentanes peaks used for comparison, should be measured by the same method. That is, use either geometric construction or planimeter, but do not intermix. When a planimeter is used, carefully make several tracings and use the average. Check this average by a second group of tracings.

X3.8 Miscellaneous

X3.8.1 Moisture in the carrier gas that would cause trouble on the reverse flow may be safeguarded against by installing a cartridge of molecular sieves ahead of the instrument. Usually 1 m of 6-mm tubing packed with 30- to 60-mesh molecular sieves is adequate, if changed with each cylinder of carrier gas.

X3.8.2 Check the carrier gas flow system periodically for leaks with soap or leak detector solution.

X3.8.3 Use electrical contact cleaner on the attenuator if noisy contacts are indicated.

X3.8.4 Peaks with square tops with omission of small peaks can be caused by a sluggish recorder. If this condition cannot be remedied by adjustment of the gain, check the electronics in the recorder.

SUMMARY OF CHANGES

Committee D03 as identified the location of selected changes to this standard since the last issue (D1945–96 (Reapproved 2001)) that may impact the use of this standard.

*(1)*Updated Section 8.1.2 to replace the criteria of two consecutive checks agreeing within 1 % of the amount present of each component, since this requirement was much tighter to meet than the method "r" limits for all components with % mole concentrations > 0.1%, which resulted in labs performing multiple analyses to try and meet the tighter requirements to be in compliance with the method.

(2) Sections 10.1.1 and 10.1.2 were revised.

ASTM International takes no position respecting the validity of any patent rights asserted in connection with any item mentioned in this standard. Users of this standard are expressly advised that determination of the validity of any such patent rights, and the risk of infringement of such rights, are entirely their own responsibility.

This standard is subject to revision at any time by the responsible technical committee and must be reviewed every five years and if not revised, either reapproved or withdrawn. Your comments are invited either for revision of this standard or for additional standards and should be addressed to ASTM International Headquarters. Your comments will receive careful consideration at a meeting of the responsible technical committee, which you may attend. If you feel that your comments have not received a fair hearing you should make your views known to the ASTM Committee on Standards, at the address shown below.

This standard is copyrighted by ASTM International, 100 Barr Harbor Drive, PO Box C700, West Conshohocken, PA 19428-2959, United States. Individual reprints (single or multiple copies) of this standard may be obtained by contacting ASTM at the above address or at 610-832-9585 (phone), 610-832-9555 (fax), or service@astm.org (e-mail); or through the ASTM website (www.astm.org). Permission rights to photocopy the standard may also be secured from the ASTM website (www.astm.org/COPYRIGHT/).

--`,,,,,`,`,`,,`,`,`,`,`,`-`,`,,`,,`,`---

Copyright ASTM International
Provided by IHS under license with ASTM
No reproduction or networking permitted without license from IHS

Order Number: 01993911
Sold to:ROBERT KROUTIL [126446] - RTKROUTIL@GMAIL.COM,
Not for Resale,2014-01-27 16:52:57 UTC

Appendix H-1.1 ASTM D3416 Redundant Methodology

separation, the analyzer is designed with a stripper column. The stripper column separates the fast-eluting components (methane and carbon monoxide) from the slower-eluting components (carbon dioxide, water, and heavier hydrocarbons). Following the elution of methane and carbon monoxide, the stripper column is backflushed to remove the slower-eluting interferents.

6.2 Total hydrocarbon measurement includes any substance that ionizes in the hydrogen flame and gives a response in the detector. In ambient air samples, these include what is classified as an air peak. Interference due to air in the sample may be eliminated by using air as the carrier gas (in which hydrocarbons have been reduced to less than 0.1 ppm) by passing the air through a catalytic oxidation device.

6.3 The total hydrocarbon analysis is sensitive to all hydrocarbons, but it should be noted that it also will respond to almost all organic compounds and will yield responses more or less depending on the number of C-H bonds in the compound. Empirical data generally show that the relative sensitivity to various hydrocarbons is about equal on a mol percent carbon basis. Oxygenated and halogenated compounds give somewhat lower readings.

7. Apparatus

7.1 Commercially available total hydrocarbon, methane, and carbon monoxide analyzers of the type suitable for use with this method should be installed on location and demonstrated by the manufacturer. The specifications shall meet or exceed those described in this test method.

7.2 A diagram of the analyzer used in this method is shown in Fig. 1. The principal components are as follows:

7.2.1 *Gas Chromatograph*, with a hydrogen flame ionization detector and a suitable readout device.

7.2.2 *Particulate Filter (In-line)*—To protect the delicate valves, analytical column, and detector, the sample line shall be equipped with a particulate filter having a pore size of about 1 to 3 µm or less (not shown in Fig. 1).

7.2.3 *Sampling Pump*, with a noncontaminating diaphragm capable of providing a flow of sample air through

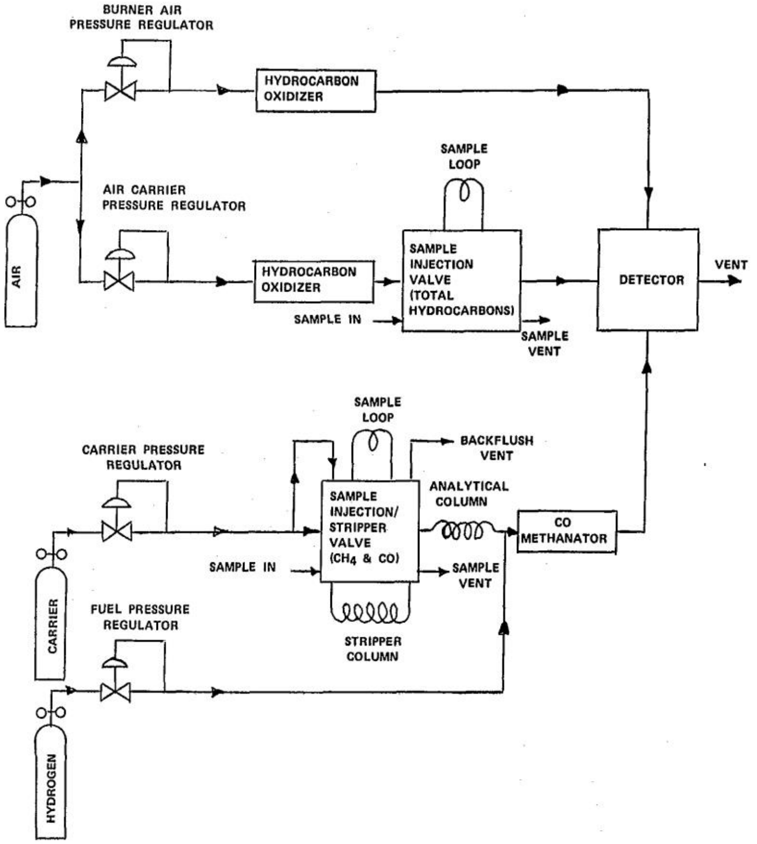

FIG. 1 Diagram of Total Hydrocarbon, Methane, and Carbon Monoxide Method

two small sample loops; one for total hydrocarbon measurement, and one for methane and carbon monoxide measurement (not shown in Fig. 1).

7.2.4 *Hydrocarbon Oxidizer*, for the oxidation of hydrocarbon contaminants normally present in even the cleanest available cylinder air. A catalytic oxidizer can be used with the subsequent conversion of most of the hydrocarbon contaminants in the burner air and, if used, in the carrier air, to carbon dioxide and water vapor.

7.2.5 *Multiport Valves*—One each for the methane and carbon monoxide analysis and for the total hydrocarbon analysis are required for trapping known volumes in a sample loop; sample injection into the stripper column, analytical column or the detector; and for backflushing the stripper column.

7.2.6 *Stripper Column*—Any suitable column (Note 1) that will separate the air, carbon monoxide and methane from other components; which will remove hydrocarbons other than methane, carbon dioxide and water; and which can be backflushed.

NOTE 1—Columns giving satisfactory results are: 12-in. (300 mm) long stainless steel tube, ¼ in. (6 mm) outside diameter packed with 5 in. (125 mm) of 10 % Carbowax on 60/80 mesh Chromosorb WHP; 5 in. (125 mm) of 60/80 mesh silica gel and 2 in. (50 mm) of Mallcosorb 8/20 mesh, or 6 ft. (2 m) of Porapak Q 50/60 mesh in ⅛-in. (3 mm) outside diameter stainless steel tubing.

7.2.7 *Analytical or Gas Chromatographic Column*—Any suitable column (Note 2) that will give base-line resolution between carbon monoxide and methane.

NOTE 2—A column giving satisfactory results is ¼-in. (6 mm) outside diameter stainless steel tubing of suitable length packed with 5A molecular sieve of 60/80 mesh.

7.2.8 *Catalytic Reactor*, 6 in. (150 mm) long, stainless steel tubing, outside diameter same as analytical column, packed with 10 % Ni on 42/60 mesh C-22 firebrick encased in a heating element for operation at elevated temperatures.

7.2.9 *Programmer*, not shown in Fig. 1, capable of controlling the automatic sequence of the measurement of total hydrocarbons, methane, and carbon monoxide is preferred over manual control. An override switch shall be provided for manual activation.

7.2.10 *Oven or Ovens*, for temperature-controlled housing of stripper and chromatographic columns, multiport injection valves, and detector.

8. Reagents and Materials

8.1 *Calibration Gas Mixture*—Mixture containing carbon monoxide and methane in air, each corresponding to 80 % of full scale.

8.1.1 The calibration gas shall be certified to be within ±2 % of the certified value. Replacement cylinders shall be verified by direct comparison with the old cylinder. If the replacement cylinder has a measured value within $\pm 1.02\ C_c$ ppm, (where C_c is the certified value of the replacement cylinder), it may be accepted. Otherwise, discard the cylinder.

8.2 *Carrier Gas*—High-purity air containing less than 1.3 mg/m^3 (2 ppm) hydrocarbon as methane.

8.3 *Catalytic Reactor*, packed with 10 % nickel on 40/60 mesh Chromosorb-P solid support. Preparation is identical to that of the hydrocarbon oxidizer catalyst except for an additional step for reducing the nickel oxide. Preparation is described in **Ref (2)**.

8.4 *Column Packings* that have been found to be satisfactory include the following:

8.4.1 10 % Carbowax liquid phase on 60/80 mesh Chromosorb WHP solid support[6]

8.4.2 C-22 firebrick 42/60 mesh[7]

8.4.3 5A Molecular sieve packing 60/80 mesh[8]

8.4.4 Mallcosorb 8/20 mesh[9]

8.4.5 60/80 mesh silica gel[10]

8.4.6 Porapak Q porous polymer 50/60 mesh[11]

8.5 *Combustion Air*—High-purity air containing less than 1.3 mg/m^3 (2 ppm) hydrocarbon as methane.

8.6 *Fuel*—Hydrogen or a hydrogen-inert gas mixture. When ordering specify electrolytic-grade hydrogen.

8.7 *Hydrocarbon Oxidizer*, packed with 12.7 % nickel oxide on 40/60 mesh Chromosorb-P. This solid support may be supplied with the instrument or prepared as described in **Ref (2)**.

8.8 *Zero Gas*—Air containing no more than 0.1 ppm total hydrocarbons and 0.1 ppm carbon monoxide.

9. Precautions

9.1 Operate the analyzer system in proper safety areas unless the equipment is explosion proof.

9.2 Vent analyzer exhaust into fume hood or out-of-doors.

9.3 The handling and storage of compressed gas cylinders and the installation and use of the analyzer shall follow Practice D 3249. Cylinders shall not be exposed to direct sunlight.

10. Sampling

10.1 Sample air by using an outside probe connected to a noncontaminating sample pump. The sampling probe shall be of material that does not affect the concentration of the components to be measured. A probe of polytetrafluoroethylene, ¼ in. in inside diameter, has proved satisfactory.

10.2 See Practices D 1357 and D 1605 for general sampling guidelines.

11. Calibration

11.1 To calibrate the analyzer, proceed as follows:

11.1.1 Introduce the zero gas, and adjust the various zero controls to the concentrations of carbon monoxide, methane, or total hydrocarbons in the zero gas (if any). Some commercial instruments have the capability for automatically adjusting for zero drift without using a zero gas.

11.1.2 Introduce the calibration gas, and adjust the span control to indicate the proper value on the recorder scale. (For carbon monoxide on a 0 to 58-mg/m^3 scale, set to 46

---

[6] Available from Supelco, Inc., Bellefonte, PA, and gives satisfactory results.

[7] Available from Coast Engineering Laboratories, Costa Mesa, CA and gives satisfactory results.

[8] Available from Linde Div., Union Carbide Co., New York, NY and gives satisfactory results.

[9] Available from Mallinckrodt, St. Louis, MO and gives satisfactory results.

[10] Available from Scott Research Laboratories, Plumstedville, PA and gives satisfactory results.

[11] Available from Waters Division, Millipore Corp., Milford, MA and gives satisfactory results.

mg/m^3 (40 ppm) standard at 80 % of the full recorder chart scale.)

11.1.3 Recheck the zero and the span controls until adjustments are no longer necessary.

11.2 See EPA-600/54/81-015 for additional guidelines.

12. Procedure

12.1 Calibrate the instrument as described in Section 11. For specific operating instructions refer to equipment manuals. Figure 1 shows a typical flow scheme.

12.2 If the instrument is equipped with a programmer for controlling the automatic sequence of steps of the procedure, the only manual steps required are activation of the valve, column, and detector controls; introduction of burner air, hydrogen fuel, and carrier gas; and introduction of the sample. Introduce the sample into the system under the same conditions of pressure and flow rates as are used in calibration.

12.3 An acceptable operating procedure would be as follows:

12.3.1 Referring to Fig. 1, with detector flame activated and carrier gases flowing, introduces the sample to the sample loops of each multiport valve.

12.3.2 Pass the sample aliquot in the sample injection/stripper valve through the stripper column until sufficient time is elapsed for the retention time of the methane and carbon monoxide. Isolate the stripper column from the analytical column prior to elution of carbon dioxide, water, and heavier hydrocarbon carbons and backflush the stripper column.

12.3.3 Pass the carrier gas stream containing the methane and carbon monoxide through the analytical column. The methane is eluted first and passes unchanged through the catalytic reactor to the detector. The carbon monoxide, after elution from the analytical column, reacts with hydrogen to form methane in the catalytic reactor. Pass the carrier gas containing the separated components into the detector. Each component is ionized in turn in the hydrogen flame of the detector and separate peak-value outputs of the electrometer are provided for readout.

12.3.4 Pass the sample aliquot in the total hydrocarbon sample injection valve to the detector.

12.4 For sequential analyses, repeat the procedure.

12.5 See Practice D 3249 for guidance on general ambient air analyzer procedures.

13. Calculation

13.1 Read the concentration of the total hydrocarbons determined as methane directly from the readout device.

13.2 To obtain measurement of the nonmethane constituents of the atmosphere, subtract the methane concentration from the total hydrocarbon concentration.

13.3 Carbon monoxide concentration in mg/m^3 can be converted to ppm at 25°C, and 1013 kPa (760 torr) as follows:

$$\text{ppm CO} = \text{mg CO/m}^3 \times 0.873$$

13.4 Methane concentration in mg/m^3 can be converted to ppm as follows:

$$\text{ppm CH}_4 = \text{mg CH}_4\text{/m}^3 \times 1.528$$

14. Precision and Bias

14.1 Precision with standard calibration gases is ±0.5 % of full-scale response.

14.2 Bias is dependent on the instrument linearity (Note 3) and the absolute concentration of the calibration gases used. Generally the accuracy for the calibration gases is ±1 % of full scale for the ranges given in 1.3.

NOTE 3—To determine the linearity of the instrument, proceed as follows:

With the instrument maintained as its recommended operating parameters introduce a sample of each of four calibration gas mixtures corresponding to 10, 20, 40, and 80 % of full scale. If the gases are under pressure bypass the pump.

With the calibration gas mixtures determine the linearity of the detector response for methane, carbon monoxide, and total hydrocarbons using peak height or peak area.

From the data obtained prepare calibration curves if instrument nonlinearity is greater than 1.0 % of full-scale response.

14.3 Bias of the method is dependent on the accuracy of the calibration of the calibration gases.

REFERENCES

(1) Stevens, R. K., O'Keefe, A. E., Ortman, G. C., "A Gas Chromatographic Approach to the Semi-Continuous Monitoring of Atmospheric Carbon Monoxide and Methane". Published in the Proceedings, Eighth Conference on Air Pollution Control, Purdue University.

(2) Villalobos, R. and Chapman, R. L., "A Gas Chromatographic Method for Automatic Monitoring of Pollutants in Ambient Air". ISA Proceedings, ISA/AID Symposium, 17th, Houston TX., April 19–21, 1971.

(3) Houben, W. P., "Hydrocarbon Analysis Auto Exhaust by Various Instrumental Methods". ISA Proceedings, ISA/AID Symposium, 17th, Houston, TX, April 19–21, 1971.

(4) Villalabos, R. "Role of Gas Chromatography in Air Pollution Monitoring," Chapter 1, pp 17–42. Published in *Analytical Methods Applied to Air Pollution Measurements*, Stevens, R. F. and Huget, W. F., eds, Ann Arbor Press, 1974.

(5) Stevens, R. K. and Herget, W. F., "Analytical Methods Applied to Air Pollution Measurements", Ann Arbor Science Publishers, 1974.

Appendix I Study Area Climatology

The Authors wish to thank Ryan J. Ippolito of the Defense Intelligence Agency for the climatology summaries of our study areas Appendices I and J.

1.0 Introduction

The CAMP project climatological study area consists of a portion of the Southern Great Plains between the following four major cities: San Antonio, TX; Houston, TX; Lake Charles, LA; and Norman, OK. San Antonio represents the western edge of the study area, and has a generally dry climate. Norman represents the northern edge of the study area with a predominantly rural landscape, and CO_2 emissions as evidenced in Figure 2b are quite low relative to the Dallas-Fort Worth area. Lake Charles represents the eastern edge of the study area, and due to its close proximity to Houston, they tend to have similar climates. Lake Charles sits next to a major lake as well as the Gulf of Mexico which contributes to the relatively humid environment found there.

1.1 Precipitation

Figure I-4 provides average precipitation values on a monthly basis for the four major cities bounding the study area. Detailed precipitation information is provided city by city in the paragraphs that follow.

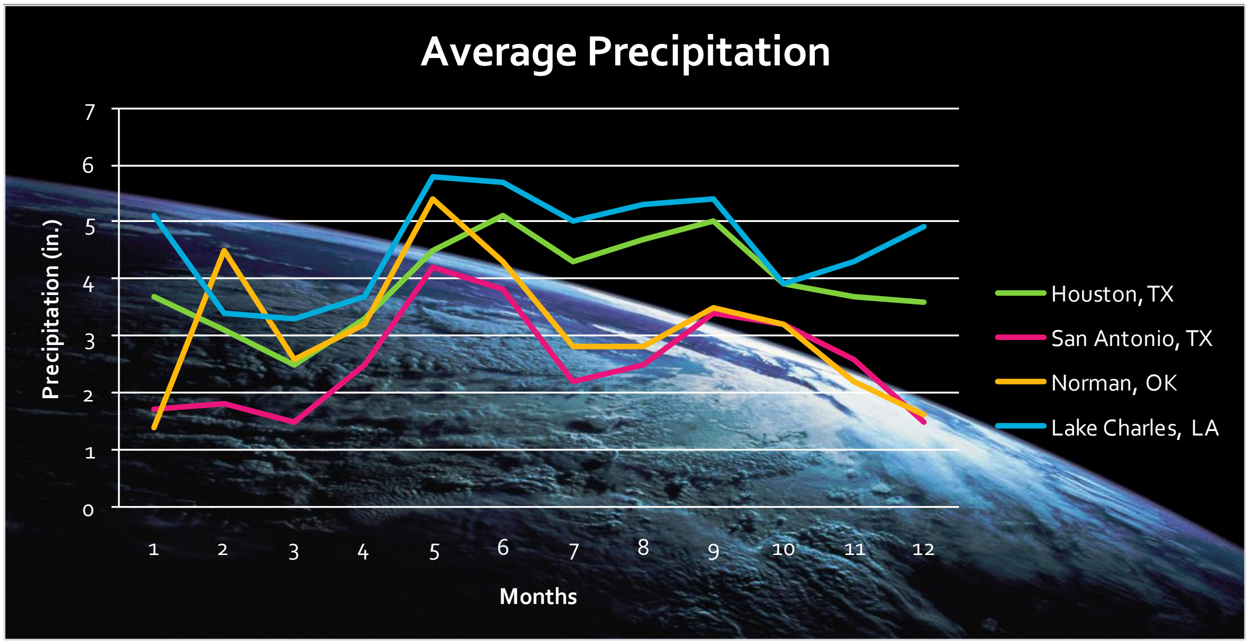

Figure I-4 Summary Average Annual Precipitation

Lake Charles, LA

The area experiences the greatest average amount of annual precipitation at 55.8 inches. Peak rainfall occurs between May and September, when monthly rainfall is greater than 5" and less than 6.0". December and January also experience a significant amount of precipitation, about 5" each month.

San Antonio, TX

The area averages the lowest amount of annual precipitation, receiving only 30.9". There are two significant periods of peak rainfall: May (4.2") and June (3.8"). September and October average slightly lower levels of rainfall at 3.4 and 3.2 inches, respectively. The lowest average rainfall amount occurs in March and December, at 1.5 inches each. The remaining months each average less than 2.5 inches of rainfall.

Norman, OK

The area experiences an average only 34.4 inches of precipitation annually. The three months receiving the greatest amount of average rainfall are February (4.5"), May (5.4"), and June (4.3"). The lowest amount of average precipitation was determined to occur in January, with only 1.4". The rest of the year from July to December and March to April precipitation is in the range of 1.6" (December) to 3.5" (September).

Houston, TX

The city experiences a fair amount of annual precipitation, about 47.3" on average. The heaviest rainfall occurs between May and September, with the two peak months being June (5.1") and September (5.0"). March averages the lowest amount of rainfall at 2.5". The remaining months average between 3.1" (February) and 3.9" (October).

1.2 Temperature

Figure I-5 provides average maximum temperature values on a monthly basis for the four major cities bounding the study area. Detailed average temperature information is provided city by city in the paragraphs that follow.

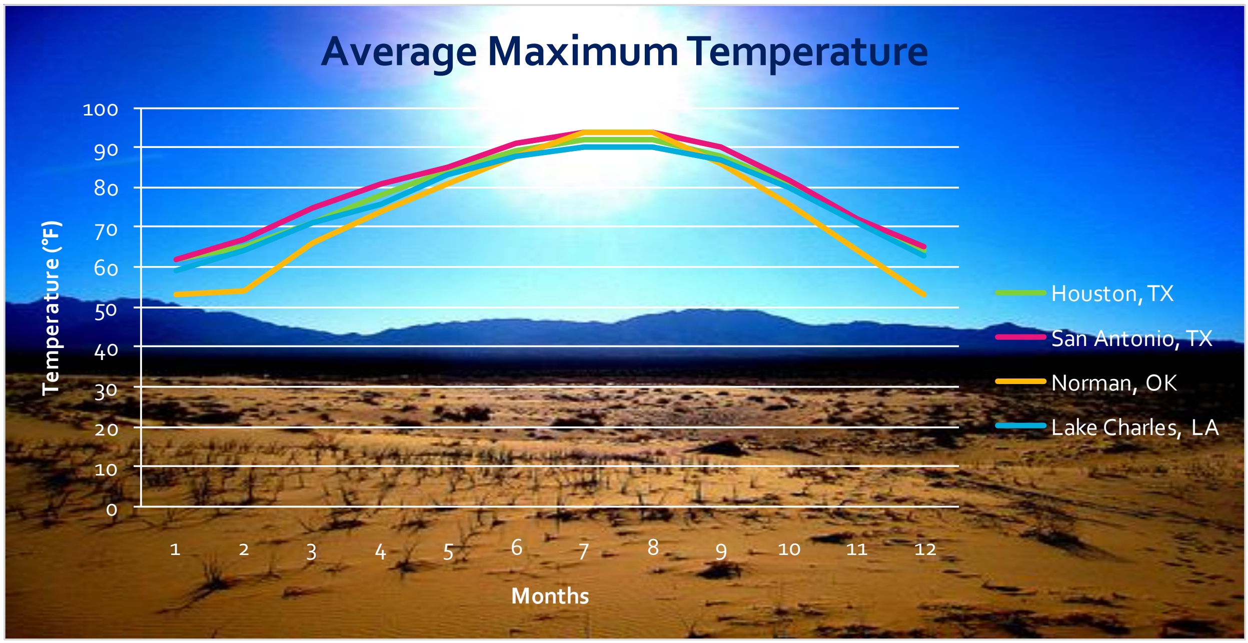

Figure I-5. Average daily maximum temperature

San Antonio, TX

Experiences the highest daily maximum temperatures on average, with an 80° F annual average maximum temperature. July and August tend to be the hottest months with an average daily maximum temperature of 94° F, while January was the coldest with an average daily maximum temperature of 62° F. The average daily minimum temperature is 59° F for the year. The lowest minimum temperatures occur in January with an average daily minimum temperature of 44° F.

Norman, OK

Averages the lowest overall daily maximum temperatures with an annual average temperature of 74° F. The two peak months are July and August, and both have an average daily maximum temperature of 94° F. The lowest daily maximum temperatures occur in December and January, with an average daily maximum temperature of 53° F, and also in February with an average temperature of 54° F. Norman's winter temperatures are on average 9° F lower than San Antonio's, despite both having identical summertime high temperatures. The average daily minimum temperature is 53° F for the year. The lowest temperatures occur in December and January with average daily minimum temperatures of 33° F. The minimum temperature remains just above freezing from December through February, where February's average daily minimum temperature is 35° F.

Houston, TX
Has an average maximum temperature of 78° F annually. The two warmest months are July and August with the average daily maximum temperature averaging 92° F for each. The lowest maximum temperature occurs in January with an average daily maximum temperature of 62° F. Houston has an average minimum temperature of 60° F for the year. January yields the lowest minimum temperatures with an average daily minimum temperature of 44° F.

Lake Charles, LA
Has an average annual maximum temperature of 77° F. The highest temperatures occur in July and August with an average daily maximum temperature of 90° F. January provides the lowest daily maximum temperatures with an average of 59° F. Lake Charles has an average minimum temperature of 60° F throughout the year. The lowest temperatures occur in January with an average daily minimum temperature of 44° F.

1.3 Relative Humidity

Figure I-6 provides average relative humidity values on a monthly basis for the four major cities bounding the study area. Detailed relative humidity information is provided city by city in the paragraphs that follow.

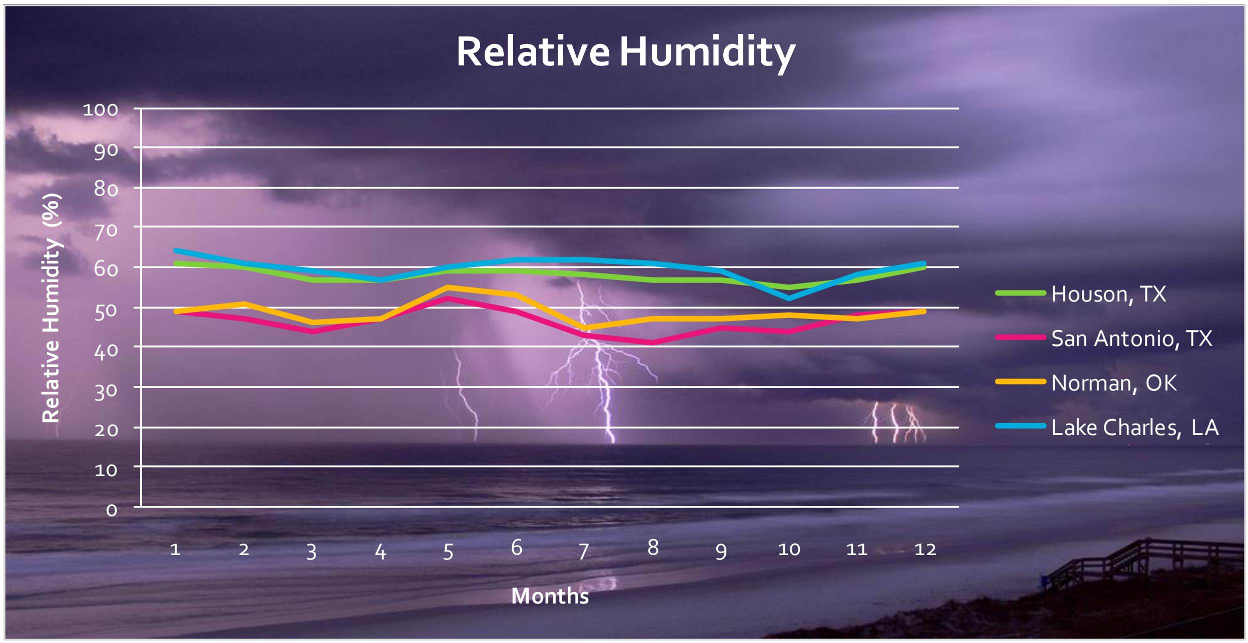

Figure I-6. Summary Relative Humidity

Lake Charles, LA
Has the highest overall relative humidity throughout the year, averaging 60% in the early afternoon (14 Local Standard Time (LST)). This is likely due to the close proximity to the Lake as well as the Gulf of Mexico. Relative humidity is highest in January (64%) with slightly lower

values observed from February (61%) through September (59%). Relative humidity was observed to be lowest in October (52%).

San Antonio, TX

Is the least humid, with an average relative humidity of just 47%. May is the most humid month with a relative humidity of 52%, while August is the least humid with a relative humidity of 41%. All other months have an average relative humidity range of 43-49%. These averages were derived from observations recorded in the mid-afternoon (16 LST).

Houston, TX

Is also relatively humid, averaging 58% relative humidity throughout the year. The most humid month is January with a relative humidity of 61% on average, although December and February are also nearly as humid with a relative humidity of 60% for each. The lowest observed relative humidity occurs in October averaging 55% for the month. All humidity observations were made in the early afternoon (14 LST).

Norman, OK

Has a relatively low relative humidity, averaging 49% throughout the year. May is the peak month, with an average relative humidity of 55%. The least humid month is July, with an average relative humidity of 45%. All other months have a relative humidity range of 46-53%, with 7 months ranging from 47-49%. These observations were made in the early to mid-afternoon (15 LST).

I 1.4 Surface and upper level winds

Figure I-7 provides average upper level wind circulation values on a monthly basis for the four major cities bounding the study area. Detailed wind information is provided on a monthly basis in the paragraphs that follow.

Wind Speed = knots
1knot = 1.15 mph

Average Upper Level Wind Circulations: JANUARY

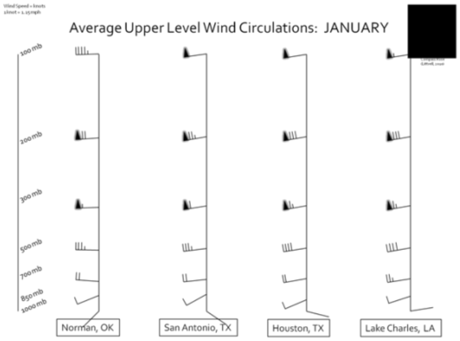

Average Upper Level Wind Circulations: FEBRUARY

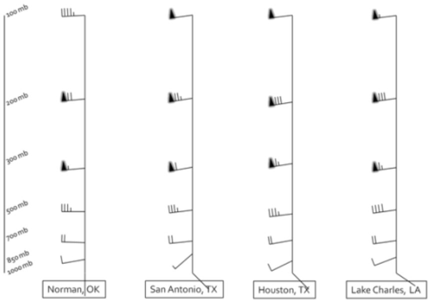

Average Upper Level Wind Circulations: MARCH

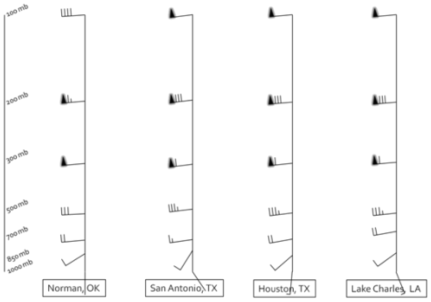

Average Upper Level Wind Circulations: APRIL

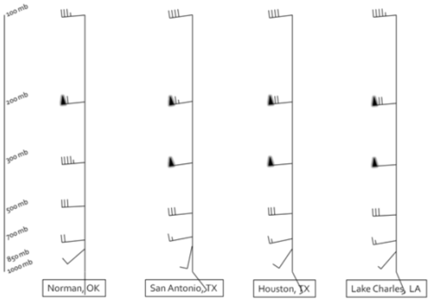

Average Upper Level Wind Circulations: MAY

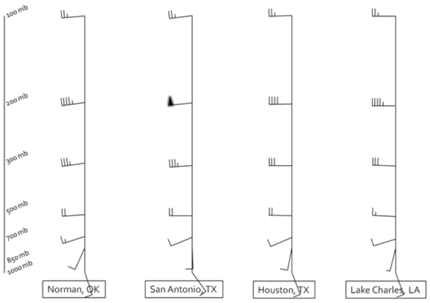

Average Upper Level Wind Circulations: JUNE

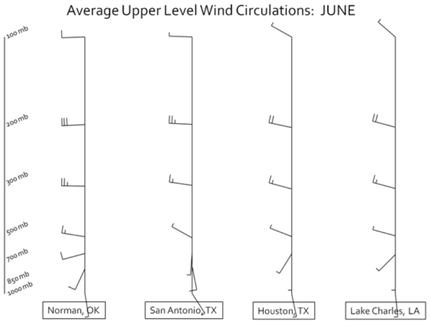

Average Upper Level Wind Circulations: JULY

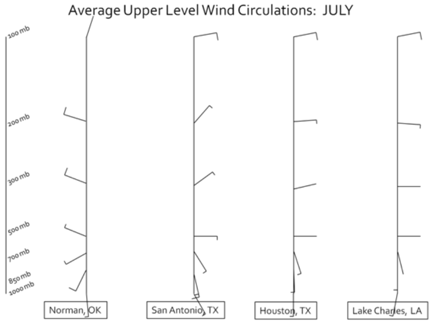

Average Upper Level Wind Circulations: AUGUST

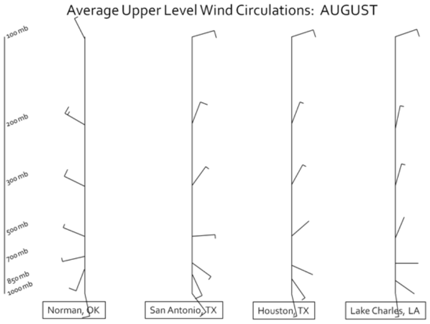

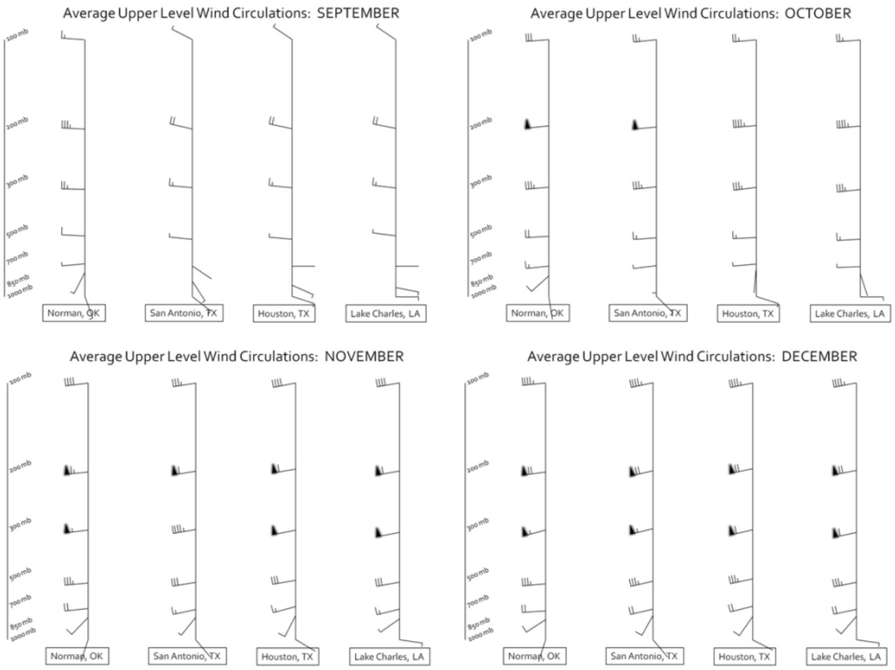

Figure I-7. Upper Level Wind Directions and Velocities

January

From the 700-mb pressure level up to the 100-mb pressure level, the prevailing winds are from a westerly direction at all sites, with the highest wind speeds (50-80 knots) occurring at the 300- to 100-mb pressure levels. The wind speed and direction at the 850-mb pressure level is around 10 knots from a WSW direction at all sites. The winds vary at the surface (1000-mb) with Norman showing a SW wind direction, San Antonio showing a SE wind direction, Houston showing an ESE wind direction, and Lake Charles an ENE wind direction. All sites have an average surface wind speed of 0 knots during the month of January.

February

The upper level winds (850-mb to 100-mb pressure levels) have not significantly changed from January to February. The surface winds at Norman appear to be southerly (or from the south), while the surface winds at San Antonio, Houston, and Lake Charles appear to come from the SE. Surface wind directions have changed slightly but wind speed remains at 0 knots for all sites during the month of February.

March

The upper level winds (700- to 100-mb pressure levels) have not significantly changed from February to March, although the 1000-mb (surface) and 850-mb level winds have slightly changed in both speed and direction. All 850-mb level winds have an average speed of 10 knots and a SW direction. Norman's surface level winds are southerly with an average speed of 0 knots. San Antonio's surface level winds are also blowing at 0 knots from the SE. Houston's surface level winds can be considered southerly with an average wind speed of 5 kts. The winds at Lake Charles blow from the SSE at an average speed of 5 kts.

April

The upper level winds (700- to 100-mb pressure levels) have not significantly changed from March to April in terms of wind direction, but wind speed has decreased between 5-10 kts at all heights and locations. At the 850-mb pressure level, wind speeds continue to blow at approximately 10 kts at all site locations, with winds at Norman, Houston, and Lake Charles blowing from the SW while San Antonio's come from a SSW direction. Surface level winds remain essentially identical to those observed in March, however, San Antonio's average wind speed has increased from 0 knots to 5 knots, and Houston's winds now come from a SSE direction.

May

The winds in the upper levels (700- to 100-mb pressure levels) continue from the West at all sites. Wind speed has dropped approximately 15-20 kts at all sites and levels from 700- to 100-mb. At the 850-mb pressure level, Norman's winds now have a more SSW flow direction, with San Antonio's winds are coming directly from the South, and the winds at Houston and Lake Charles from a SSW direction. At the surface, all sites have an average wind speed of 10 kts, with the winds at Norman, Houston, and Lake Charles blowing from the SSE and San Antonio's winds blowing from the SE.

June

The upper level winds (700- to 100-mb pressure levels) have decreased in speed by 15-25 knots at all sites. The winds at the 100-mb pressure level at Houston and Lake Charles have slowed to 5 kts and are now from the NW. The winds at the 500- to 200-mb pressure levels at Houston and Lake Charles are from the WNW direction. Winds at the 500-mb height at Norman and San Antonio are also from the WNW direction. At the 700-mb pressure level, the winds at San Antonio now blow from the South at 5 kts, while the winds at Houston and Lake Charles are from the SW at 5 kts. At the 850-mb pressure level, the winds at Houston and Lake Charles are from the South at a wind speed of 5 kts, while San Antonio winds blow at 10 kts from a SSE direction. At the surface, all wind speeds have slowed to 5 kts, with the winds at San Antonio from the SSE, and the winds at Norman, Houston, and Lake Charles coming predominantly from the South.

July

From June to July the upper level winds experience a substantial direction change as well as overall reduction in wind speeds. All wind speeds from 1000- to 100-mb have a range of 0-10 knots with the wind directions at San Antonio, Houston, and Lake Charles prevailing from the East and NE at the 500- to 100-mb pressure levels. At the 1000- to 700-mb pressure levels in Houston, San Antonio, and Lake Charles, the wind speeds are mostly around 5 knots with the prevailing winds coming from the S or SSE directions. At the 100-mb level, Norman's wind speed averages 0 knots coming from the NNE. At the 500- to 200-mb pressure levels, the prevailing winds at Norman are from the NNW at an average speed of 5-10 kts. From 700- to 1000-mb the winds at Norman gradually change direction from WSW to South, with wind speeds ranging from 5 to 10 kts.

August

From July to August the winds from the surface to the 100-mb pressure level are at an average speed of 0-10 kts. The winds at the 100-mb pressure level at Houston, San Antonio, and Lake Charles average 10 kts and blow from the ENE direction. At the 500- to 200-mb heights the winds at San Antonio, Houston, and Lake Charles blow at 5-10 kts from the NNE, except for the winds at San Antonio at the 500-mb height which blow from the East. The winds at San Antonio, Houston, and Charles at the 700-mb height prevail from the E and SE directions at 0-5 kts, with the winds at the 1000- to 850-mb heights prevailing from the SE and SSE directions at 0-10 kts. At the 100-mb pressure level at Norman the winds blow from the NNW at 5 kts. The wind speeds average 5-15 kts between the 500- and 200-mb pressure levels at Norman with prevailing winds from the NW. From the 700- to the 1000-mb pressure level at Norman, the winds gradually shift from a WSW direction to a SSE direction, with wind speeds between 5-10 kts.

September

From August to September there is a significant change in wind direction from Easterly to Westerly. The winds between 500- and 100-mb heights blow from the W and WNW directions at an average speed of 5-35 kts. The highest wind speeds occur and the 300- and 200mb heights. For San Antonio, Houston, and Lake Charles, winds speeds at the 700 to 1000mb pressure levels range between 0-5 kts with winds prevailing from the E and ESE directions. The winds at Norman between 700- and 1000mb pressure levels average 5 kts with a prevailing wind direction shifting from WSW (700mb) to SSE (1000mb).

October

From September to October the overall wind speed has increased in the 700- to the 100-mb pressure levels, with the prevailing winds coming unanimously from the West. The wind speeds range from 25 to 50 kts at the 300- to 100-mb heights, and 0-20 kts at the 1000- to 700-mb heights. The winds at the 850-mb heights are from the SW at Norman, from the South at San Antonio and Houston, and from the SSE at Lake Charles. At the surface, winds are from the South at Norman, SE at San Antonio, and SE and E at Houston and Lake Charles, respectively.

November

From October to November winds continue to blow from the West, with wind speeds increasing to 35-65 kts at the 300- to 100-mb heights, 15-35 kts at the 700- to 500-mb heights, and 0-20 kts at the 1000- to 850-mb heights. The wind blows from the SW in all sites at the 850-mb pressure level. At the surface, the wind blows from the SSW at Norman, SE at San Antonio and Houston, and from the E at Lake Charles.

December

From November to December there are no significant changes in wind direction at any height. However, wind speeds continue to increase with a range of 45-70 knots at the 300- to 100-mb heights, 20-35 kts at the 700- to 500-mb heights, and 0-10 kts at the 1000- to 850-mb heights.

1.5 Cloud ceiling and visibilities

In general, visibility tends to be best during the summer months at each site. A few factors influence visibility, such as cloud cover, cloud ceiling height, fog, and precipitation. However, only those conditions pertinent to this research will be analyzed here. These conditions are visibility and cloud ceiling height, assuming the plane will only be flown on clear days without fog or precipitation. Low-level clouds dictate how high the plane can fly and therefore what the sensor can see. The following analysis looks at 4 cloud height-visibility relationships that could negatively impact the flying missions.

The first condition consists of a cloud ceiling less than 3,000 ft with horizontal visibility of 3 miles. Between November and May, these conditions tend to occur 24-39% of the time at Houston, San Antonio, and Lake Charles. These conditions occur much less frequently between June and October, only between 6-29% of the time. Norman has those conditions most often in February as they tend to occur 22% of the time. July, these conditions happen the least, only 5% of the time, and less than 10% of the time between June and September. The remaining months experience these exact conditions only 14-18% of the time. The average annual occurrence of these conditions at each site is 23% Houston, 30% San Antonio, 13% Norman, and 24% Lake Charles.

The second condition consists of a cloud ceiling less than 1,500 ft with a horizontal visibility of 3 miles. San Antonio experiences these conditions most frequently throughout the year, with an average annual occurrence rate of 21%. Peak months are from November through May, with conditions occurring between 23-25% of the time. These conditions persist less frequently from June to October with an occurrence rate of 13-18%. Houston and Lake Charles see these conditions equally throughout the year, with peak months between December and April (19-29%) and minimum occurrences between May and November (2-20%). On average, Houston and Lake Charles experience these conditions 15-16% of the time throughout the year. These conditions occur approximately 8% of the time throughout the year at Norman. Peak months are February (16%), November (11%), and December (13%), with all other months experiencing a 3-9% occurrence rate.

The third condition consists of a cloud ceiling less than 1,000 ft and horizontal visibility of 2 miles. These conditions occur 13% of the time in San Antonio, 11% of the time in Lake Charles, 10% of the time in Houston, and 5% of the time in Norman, on average throughout the year. San Antonio experiences these conditions most often, with peak occurrences in September through May (10-19%) and minimal occurrences between June and August (5-9%). Houston and Lake Charles see these conditions the most between November and April (5-23%) and the least between May and October (1-10%). Norman experiences these conditions less than 12% of the time at any point throughout the year. Most of the spring, summer, and fall see these conditions 1-6% of the time.

The last condition consists of a cloud ceiling less than 200 ft and horizontal visibility of 0.5 miles. These conditions are extremely rare at any of the 4 sites, with average annual occurrences between 0.5 and 2%. Norman sees these conditions 0.5-1% of the time during the year, with Houston, San Antonio, and Lake Charles experiencing these conditions less than 7% of the time throughout the year. Peak months for these 3 sites are November-March, with an occurrence of these conditions 3-6% of the time. The remaining months (April-October) experience these conditions only 0.5-3% of the time.

Appendix J Dallas, TX (DFW) Climatology

Climate Overview - DFW, TX August 1948-January 1998

Precipitation
Dallas, TX, receives approximately 34.2 inches of precipitation annually. Seasonally, the heaviest rainfall takes place during the summer (12.1 inches); the least rainfall occurs during the winter (6.3 inches). May produces the most rainfall by month (5.0 inches); January produces the least rainfall by month (1.9 inches). The maximum recorded rainfall of 45.3 inches was recorded in June.

Snowfall
Average snowfall is 3.0 inches per year, with the majority of snow falling during the winter (2.0 inches) between January (1.0 inch) and February (1.0 inch). The maximum recorded snowfall is 16.0 inches, recorded in February. The second heaviest snowfall on record is 10.0 inches, recorded in January.

Temperature
Dallas, TX, has an average annual temperature range of 44 - 85°F. The warmest month is July, with an average temperature of 85°F, an average high temperature of 96°F, and an average low temperature of 76°F. The coolest month is January, with an average temperature of 44°F, an average high temperature of 56°F, and an average low temperature of 36°F. The highest recorded temperature is 111°F, recorded in June; the lowest recorded temperature is -2°F, recorded in December and January.

Relative Humidity
Dallas, TX has an average maximum relative humidity of 76%, and an average minimum relative humidity of 47%. The months with the highest relative humidity are May and June, with an average maximum relative humidity of 80% and an average minimum relative humidity of 52% and 48%, respectively. The month with the lowest relative humidity is August, with an average maximum relative humidity of 74%, and an average minimum relative humidity of 40%. Fall has the highest relative humidity on average (77% maximum; 46% minimum). Summer has the lowest relative humidity on average (76% maximum; 43% minimum).

Surface and Upper Level Winds
Wind speeds generally increase with altitude. The lowest wind speeds exist at the surface (1000 mb), with the highest wind speeds occurring at or near the 200 mb pressure level. Wind speeds tend to increase between the 1000 – 200 mb pressure levels, and quickly subside at

heights above the 200 mb pressure level. The winter season produces the strongest winds (at all heights), while the summer months produce the weakest winds. In order to minimize the influence of extreme outliers on mean wind conditions, wind speeds recorded slightly lower than maximum recorded wind speeds (99th percentile) were used instead of the highest recorded maximums on all subsequent Figures J-8→J-19.

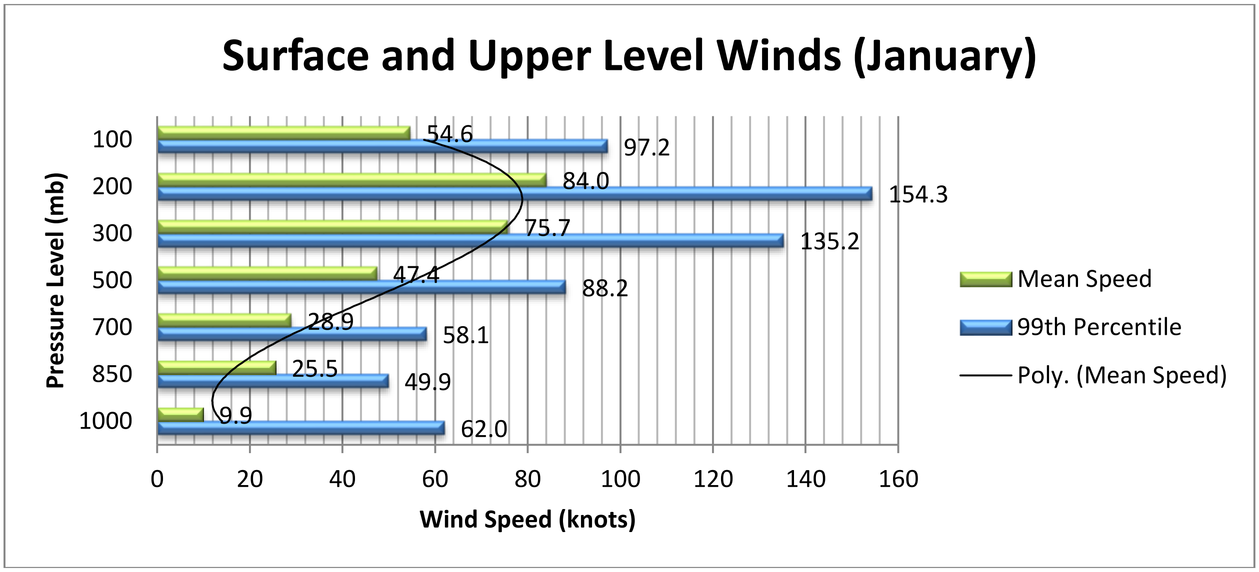

Figure J-8. Mean and near-maximum wind speeds by atmospheric pressure level – January

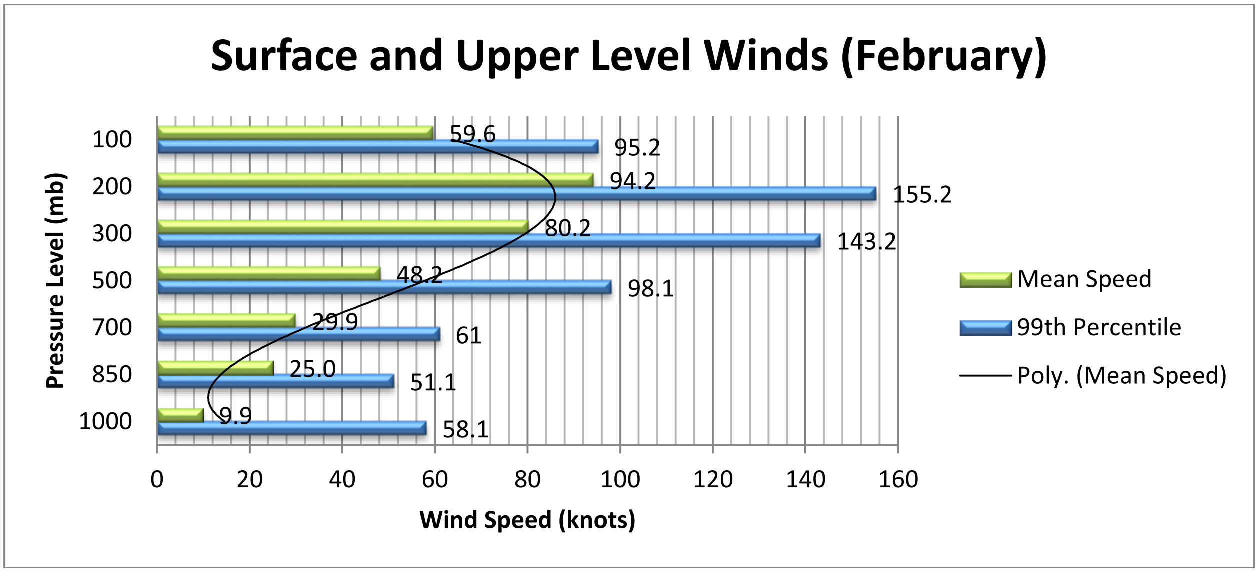

Figure J-9. Mean and near-maximum wind speeds by atmospheric pressure level – February

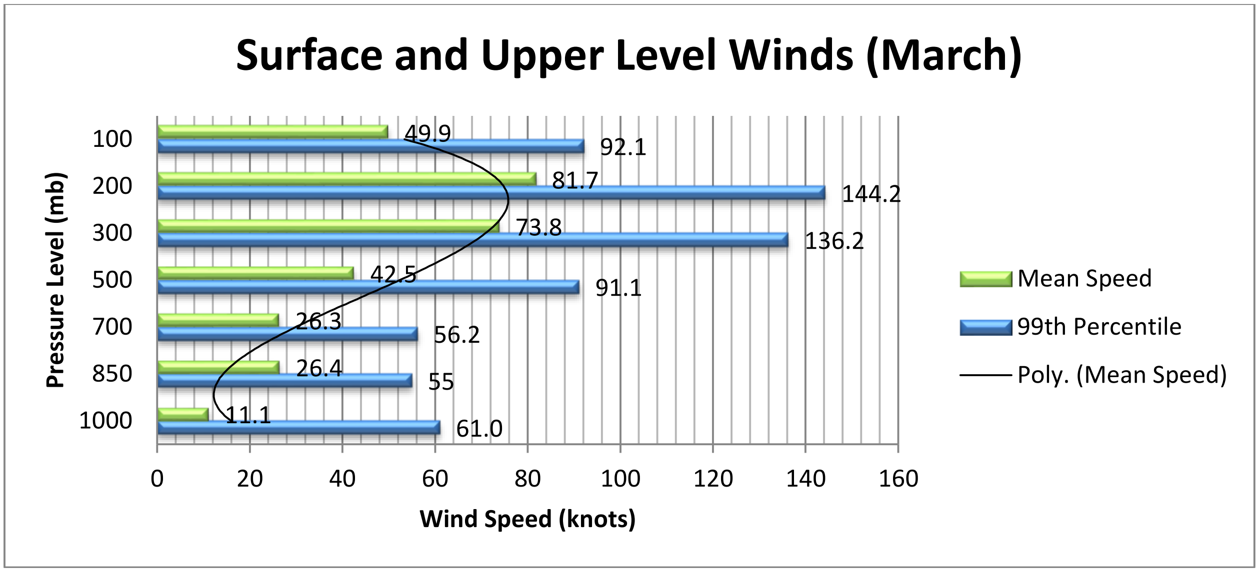

Figure J-10. Mean and near-maximum wind speeds by atmospheric pressure level – March

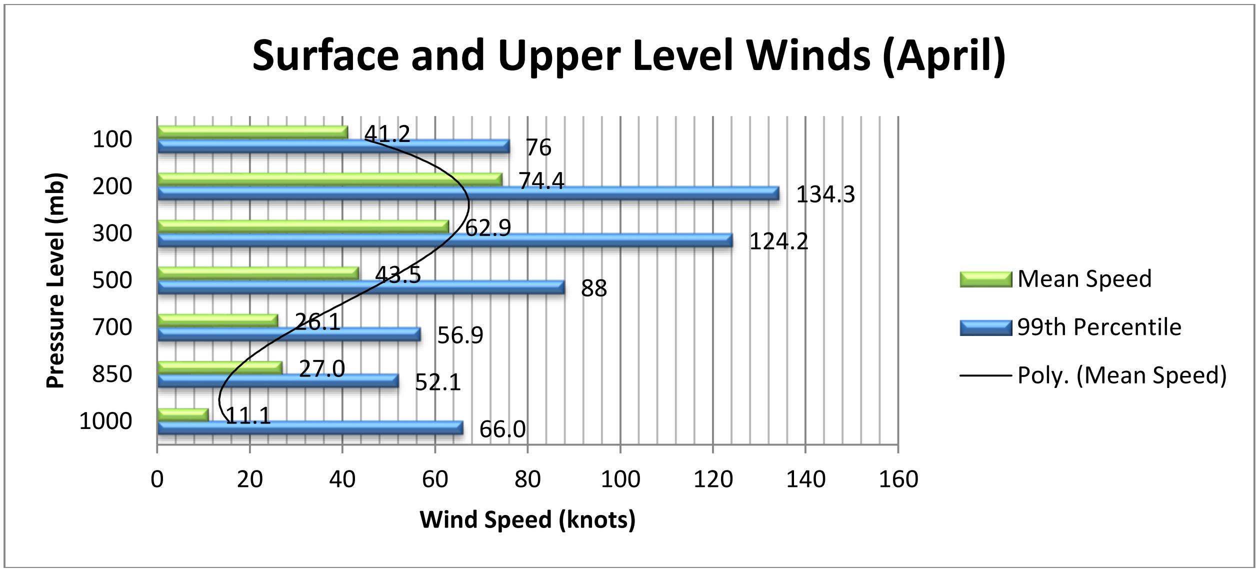

Figure J-11. Mean and near-maximum wind speeds by atmospheric pressure level – April

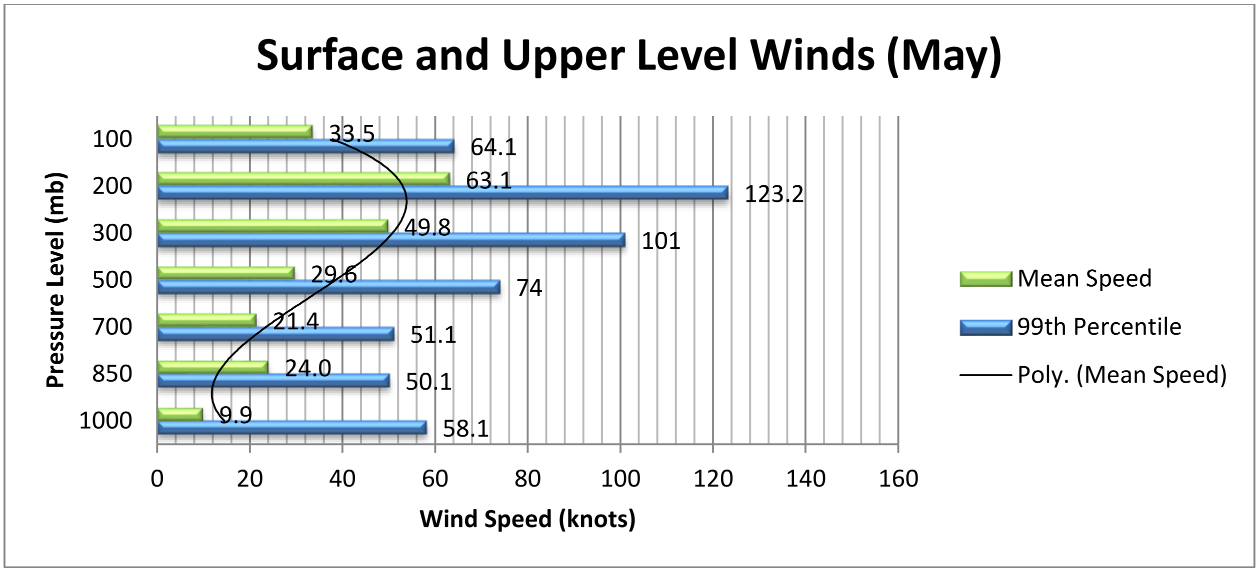

Figure J-12. Mean and near-maximum wind speeds by atmospheric pressure level – May

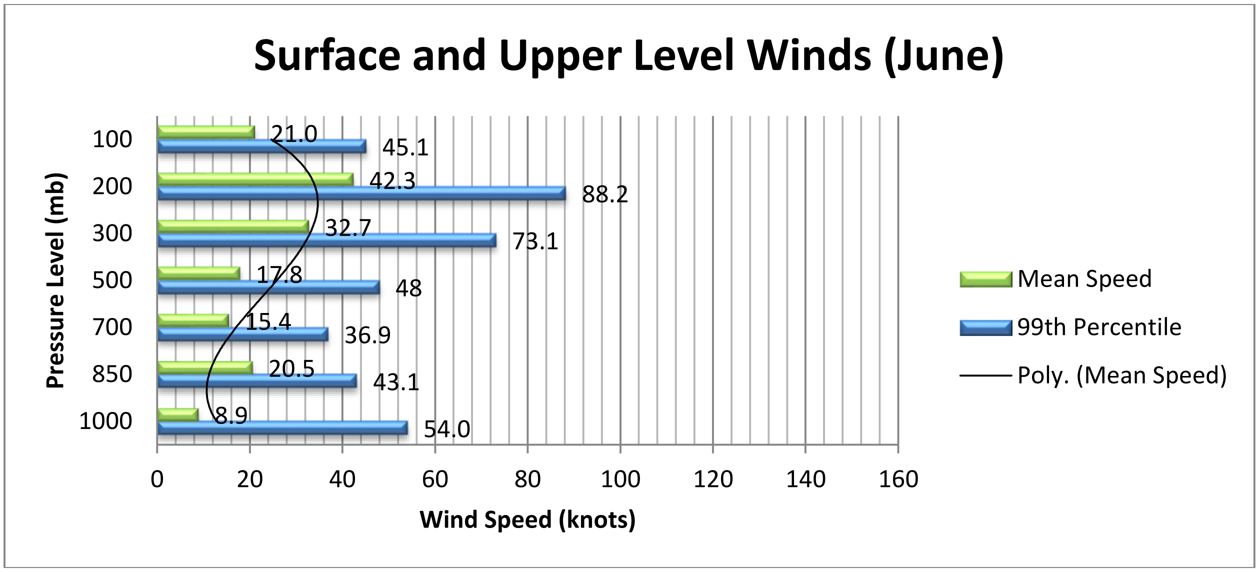

Figure J-13. Mean and near-maximum wind speeds by atmospheric pressure level – June

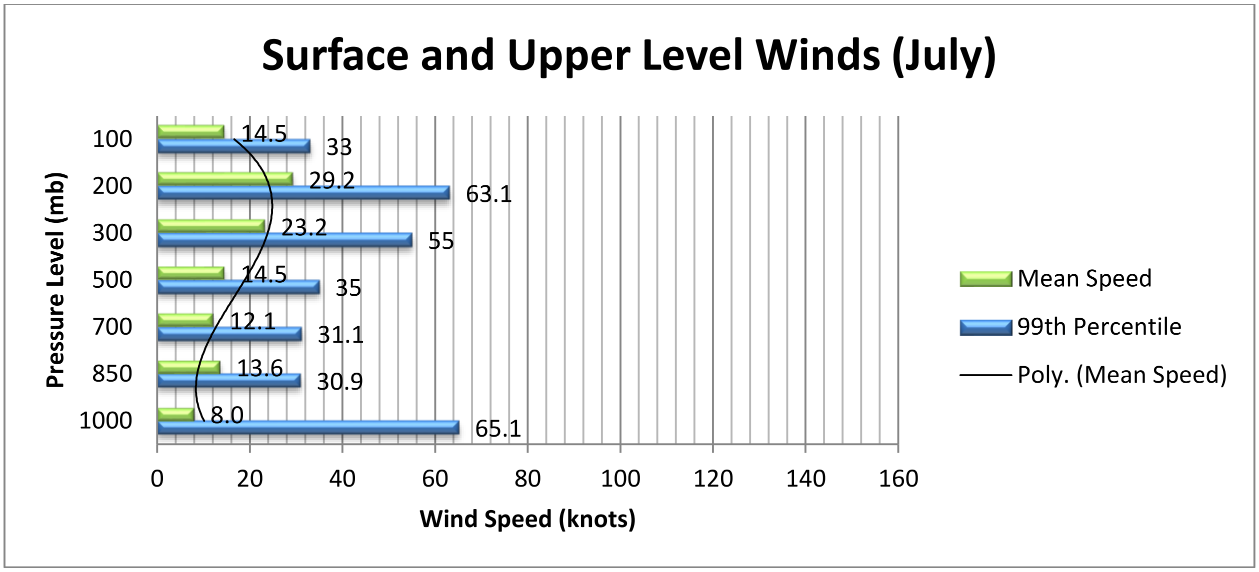

Figure J-14. Mean and near-maximum wind speeds by atmospheric pressure level – July

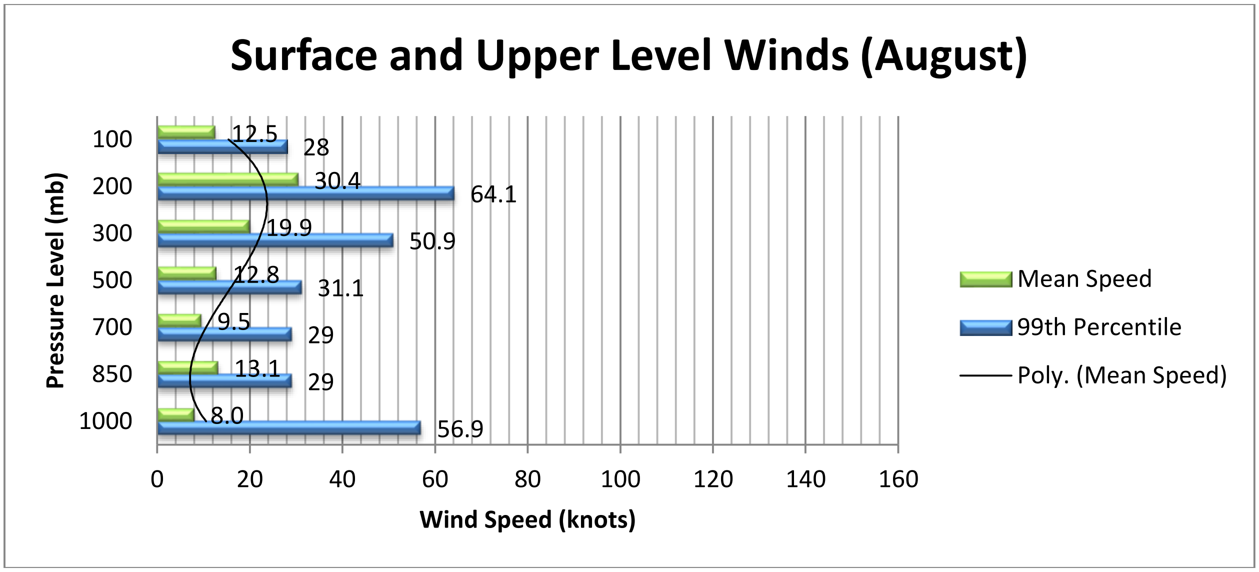

Figure J-15. Mean and near-maximum wind speeds by atmospheric pressure level – August

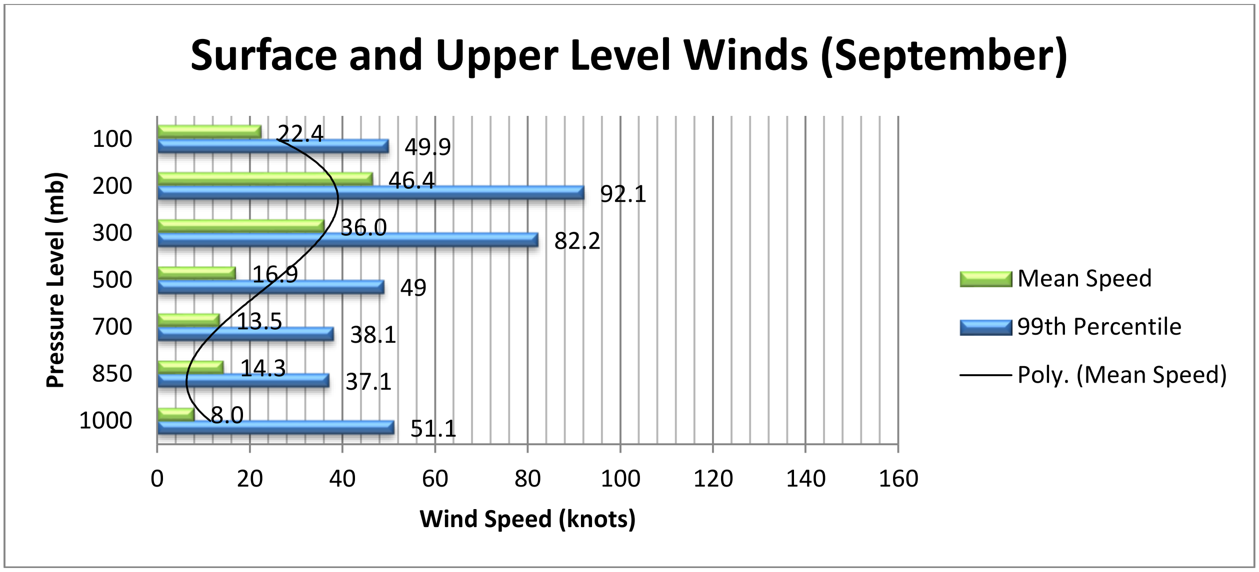

Figure A16. Mean and near-maximum wind speeds by atmospheric pressure level – September

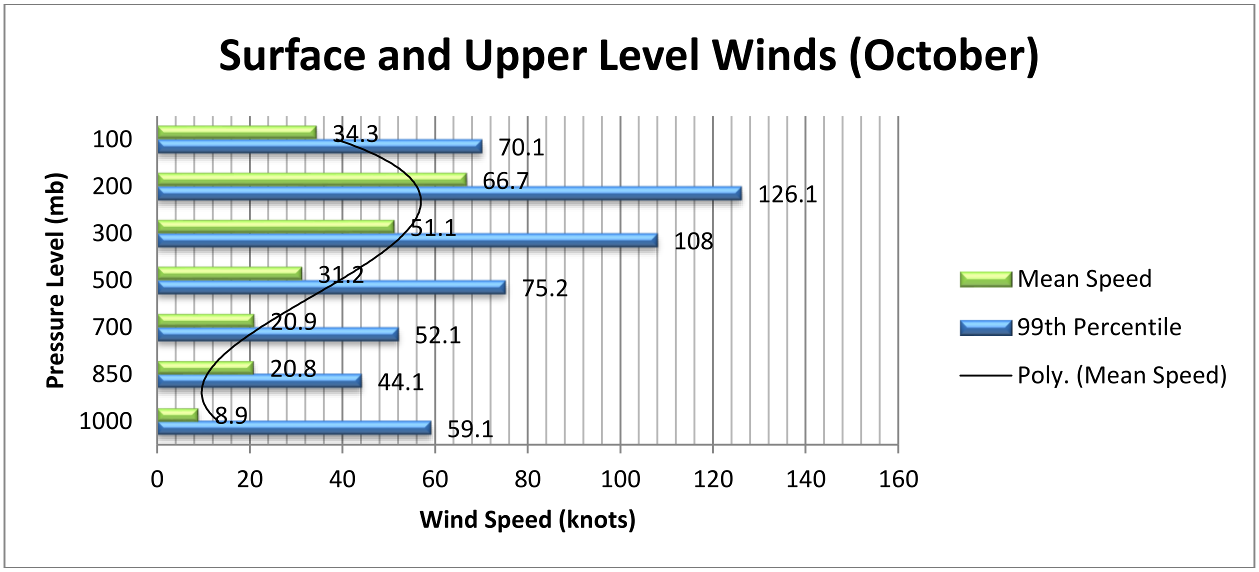

Figure J-17. Mean and near-maximum wind speeds by atmospheric pressure level – October

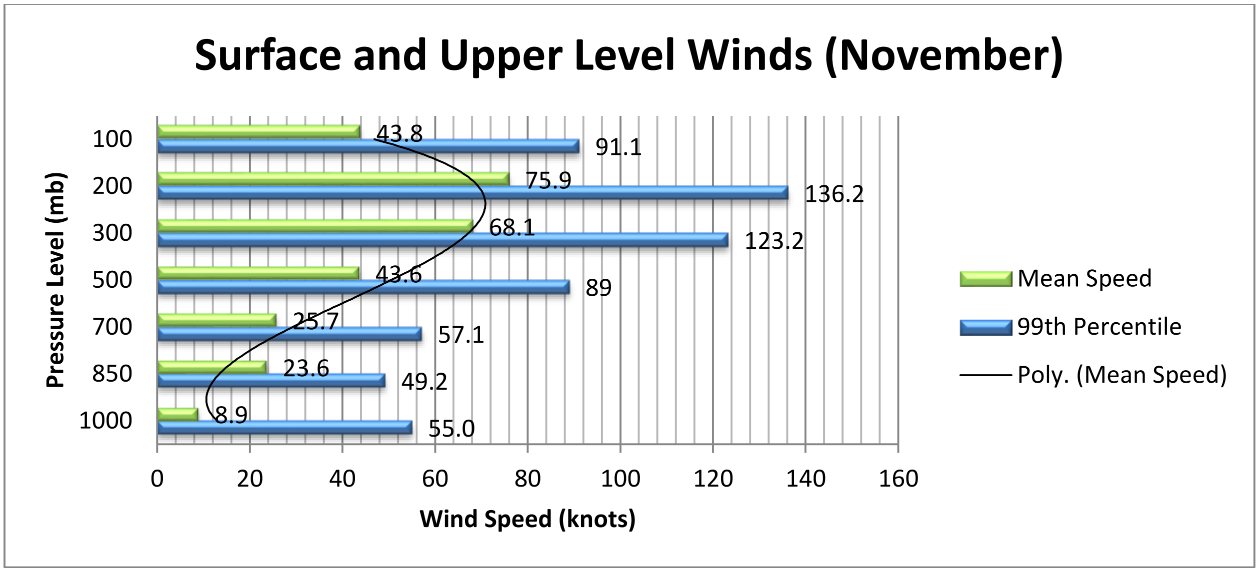

Figure J-18. Mean and near-maximum wind speeds by atmospheric pressure level – November

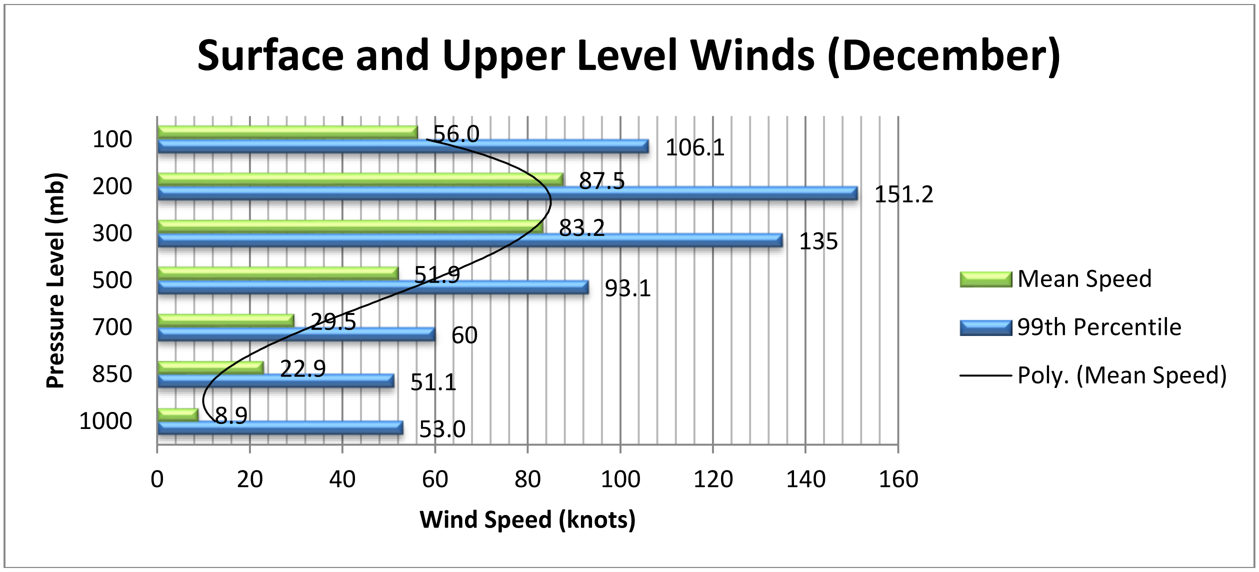

Figure J-19. Mean and near-maximum wind speeds by atmospheric pressure level – December

Cloud Ceiling and Visibility

Cloudy days most frequently occur during the winter (including late fall and early spring), and occur most infrequently during the summer (June – August). High altitude clouds are also more common than lower altitude clouds, suggesting there is a good chance for generally clear upper air visibility. The following 4 scenarios (Figures J-20→J-23) represent conditions in which cloud cover could potentially impede upper air visibility. Each condition is ordered in succession from best visibility to worst visibility (relative to one another).

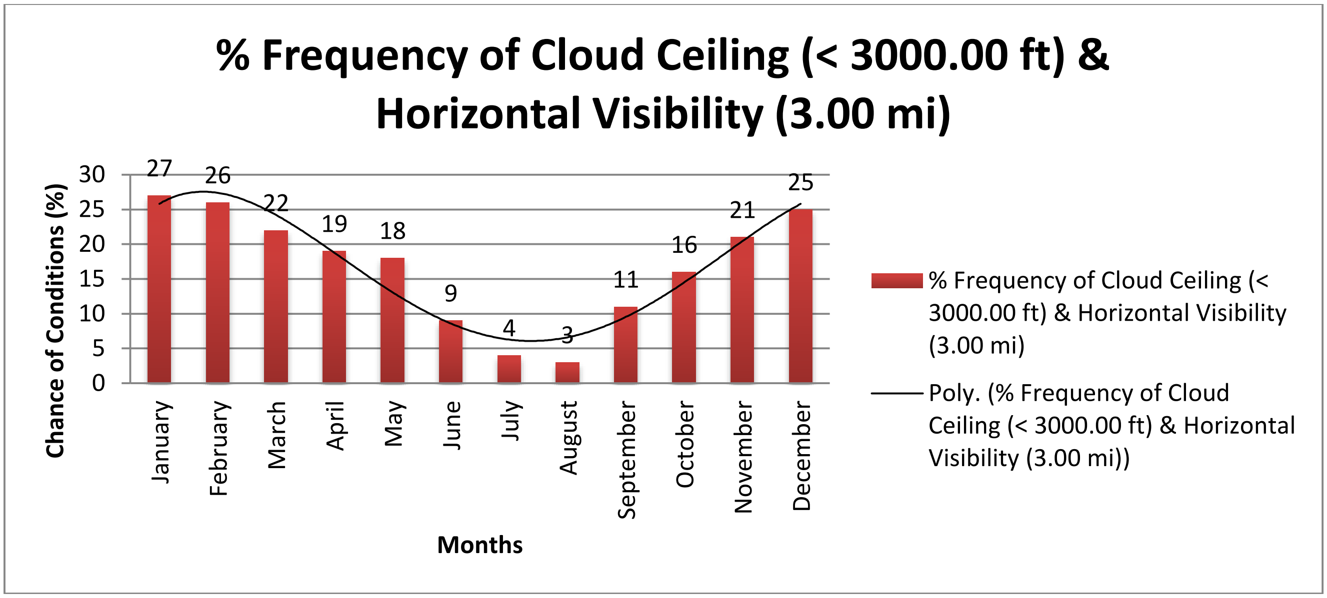

Figure J-20. Cloud ceiling < 3,000ft and horizontal visibility of 3.0 miles

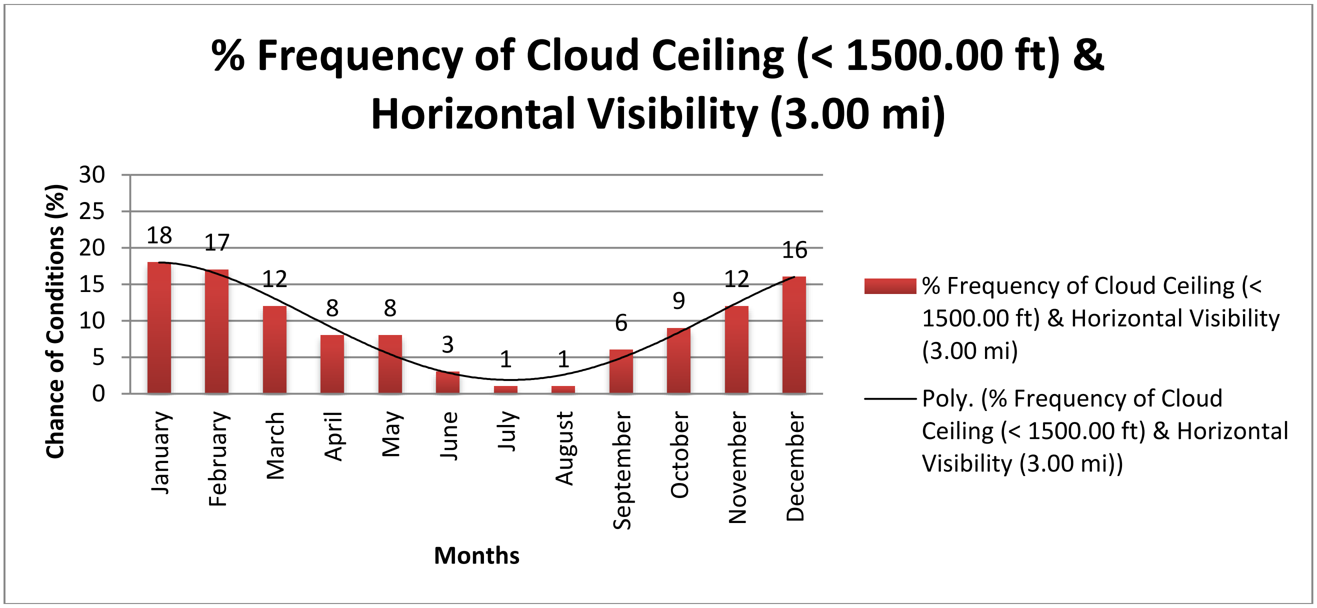

Figure J-21. Cloud ceiling < 1,500ft and horizontal visibility of 3.0 miles

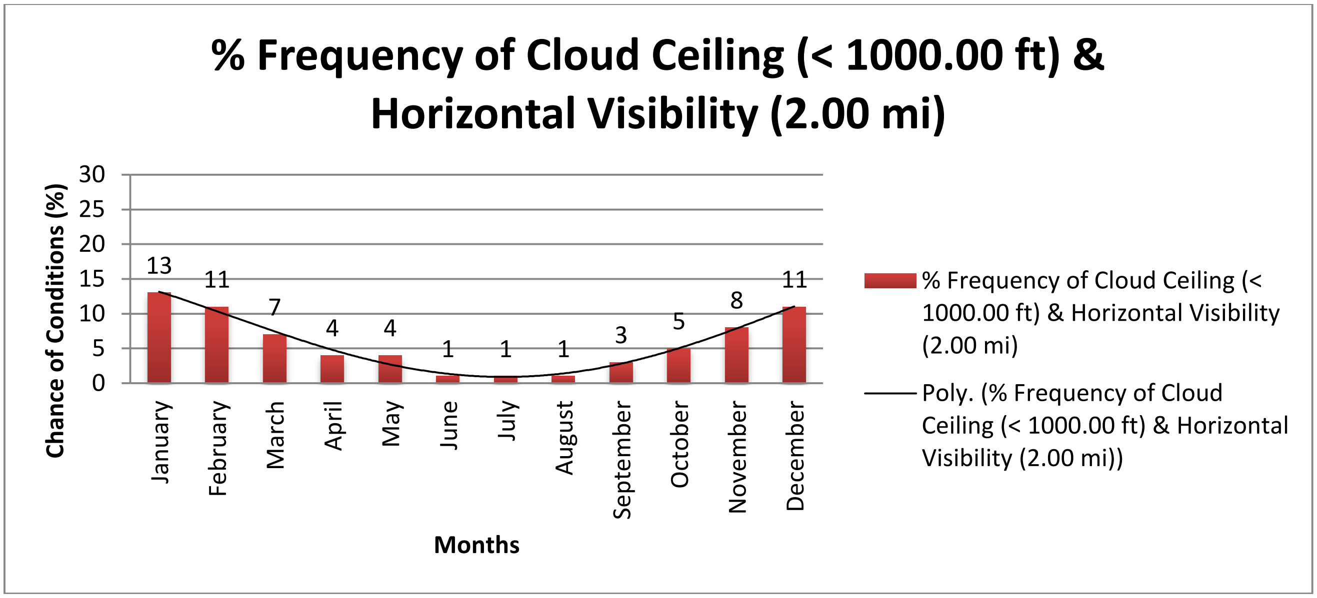

Figure J-22. Cloud ceiling < 1,000ft and horizontal visibility of 2.0 miles

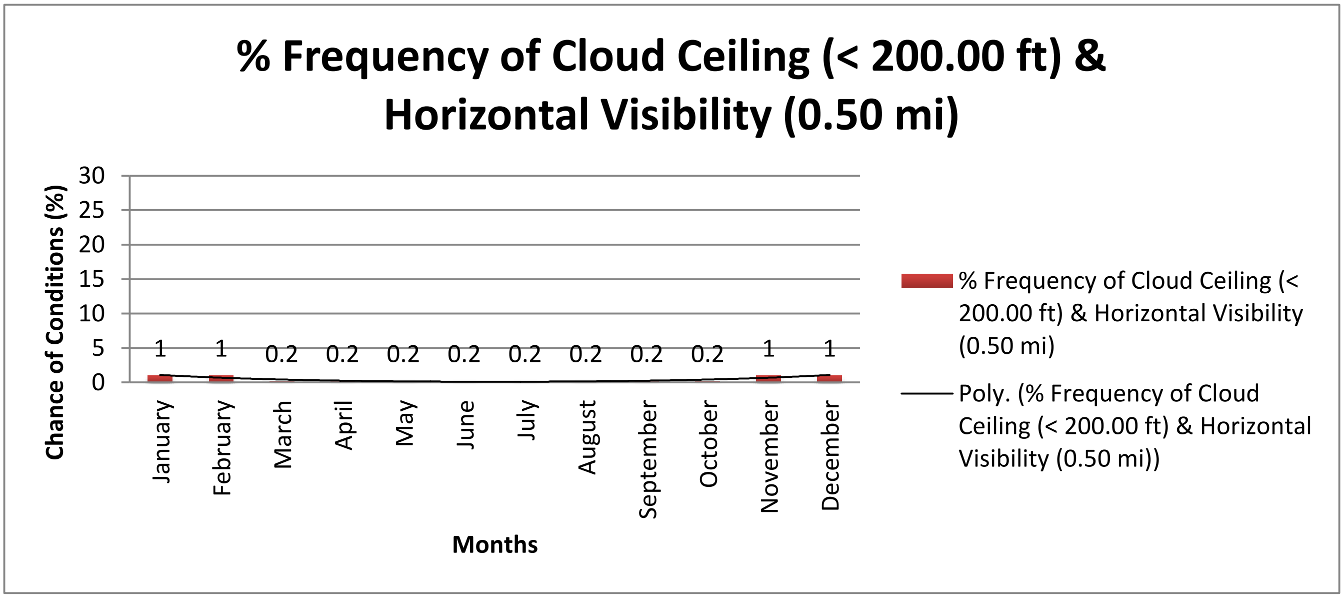

Figure J-23. Cloud ceiling < 200ft and horizontal visibility of 0.5 miles

J DFW Precipitation

Months	Max Precipitation (in)	Mean Precipitation (in)	Min Precipitation (In)
January	5.4	1.9	0
February	3.8	2.3	0.1
March	12.1	2.7	0.1
April	8.5	3.8	0.1
May	10.6	5.0	0.6
June	45.3	3.3	0
July	8.6	2.1	0

August	19.6	2.3	0
September	6.9	2.9	0
October	8.6	3.4	0
November	3.9	2.3	0.3
December	7.7	2.1	0.1
Annual	51.1	34.2	18.5

Seasons	Max Precipitation (in)	Mean Precipitation (in)	Min Precipitation (in)
Winter	16.90	6.30	0.20
Spring	31.20	11.50	0.80
Summer	73.50	12.10	0.00
Fall	19.40	10.40	0.30

Months	Max Snowfall (in)	Mean Snowfall (in)
January	10	1
February	16	1
March	2	0
April	0	0
May	0	0
June	0	0
July	0	0
August	0	0
September	0	0
October	0	0
November	6	0
December	4	0
Annual	25	3

J DFW Temperature

Months	Max Temperature (°F)	Mean High Temperature (°F)	Mean Temperature (°F)	Mean Low Temperature (°F)	Min Temperature (°F)
January	87	56	44	36	-2
February	94	61	49	41	7
March	99	70	58	49	12
April	97	76	66	57	30
May	101	83	73	65	43
June	111	91	81	72	55
July	110	96	85	76	62
August	108	95	85	75	58
September	106	88	77	69	40

October	99	79	68	59	24
November	90	67	56	48	16
December	87	59	48	40	0
Annual	111	77	66	57	-2

Seasons	**Max Temperature (°F)**	**Mean High Temp (°F)**	**Mean Temp (°F)**	**Mean Min Temp (°F)**	**Min Temperature (°F)**
Winter	89.33	58.67	47.00	39.00	1.67
Spring	99.00	76.33	65.67	57.00	28.33
Summer	109.67	94.00	83.67	74.33	58.33
Fall	98.33	78.00	67.00	58.67	26.67

J DFW Relative Humidity

Months	**Relative Humidity Max (%)**	**Relative Humidity Min (%)**
January	75	51
February	74	49
March	72	45
April	75	47
May	80	52
June	80	48
July	75	42
August	74	40
September	78	45
October	77	45
November	76	47
December	76	50
Annual	76	47

J DFW Surface and Upper Winds

Month	**Pressure (mb)**	**Prevailing Direction**	**Mean Speed - Prevailing Direction (knots)**	**99th Percentile (knots)**	**Max Speed (knots)**
JAN	1000	S	9.9	62.0	62.0
JAN	850	SW	25.5	49.9	55.2
JAN	700	W	28.9	58.1	133.3
JAN	500	W	47.4	88.2	103.0
JAN	300	W	75.7	135.2	174.1
JAN	200	W	84.0	154.3	235.3
JAN	100	W	54.6	97.2	165.3
FEB	1000	S	9.9	58.1	58.1

FEB	850	SW	25.0	51.1	72.1
FEB	700	W	29.9	61	78.1
FEB	500	W	48.2	98.1	114.2
FEB	300	W	80.2	143.2	168.3
FEB	200	W	94.2	155.2	166.3
FEB	100	W	59.6	95.2	137.2
MAR	1000	S	11.1	61.0	61.0
MAR	850	SSW	26.4	55	68.2
MAR	700	W	26.3	56.2	75.2
MAR	500	W	42.5	91.1	115.2
MAR	300	W	73.8	136.2	192.2
MAR	200	W	81.7	144.2	178.2
MAR	100	W	49.9	92.1	116.2
APR	1000	S	11.1	66.0	66.0
APR	850	SSW	27.0	52.1	64.1
APR	700	SW	26.1	56.9	72.1
APR	500	W	43.5	88	106.1
APR	300	W	62.9	124.2	143.2
APR	200	W	74.4	134.3	155.2
APR	100	W	41.2	76	117.2
MAY	1000	S	9.9	58.1	58.1
MAY	850	SSW	24.0	50.1	66.1
MAY	700	SW	21.4	51.1	69.0
MAY	500	W	29.6	74	95.2
MAY	300	W	49.8	101	135.2
MAY	200	W	63.1	123.2	155.2
MAY	100	W	33.5	64.1	81.0

Month	Pressure (mb)	Prevailing Direction	Mean Speed - Prevailing Direction (knots)	99th Percentile (knots)	Max Speed (knots)
JUN	1000	S	8.9	54.0	54.0
JUN	850	S	20.5	43.1	61.0
JUN	700	SW	15.4	36.9	48.0
JUN	500	W	17.8	48	63.0
JUN	300	W	32.7	73.1	104.1
JUN	200	W	42.3	88.2	107.1
JUN	100	W	21.0	45.1	61.0
JUL	1000	S	8.0	65.1	65.1
JUL	850	S	13.6	30.9	43.9
JUL	700	SSW	12.1	31.1	38.1
JUL	500	E	14.5	35	46.8
JUL	300	W	23.2	55	82.2

Month	Pressure (mb)	Prevailing Direction	Mean Speed - Prevailing Direction (knots)	99th Percentile (knots)	Max Speed (knots)
JUL	200	W	29.2	63.1	258.4
JUL	100	E	14.5	33	42.0
AUG	1000	S	8.0	56.9	56.9
AUG	850	S	13.1	29	36.9
AUG	700	SW	9.5	29	34.0
AUG	500	NNW	12.8	31.1	39.1
AUG	300	W	19.9	50.9	62.2
AUG	200	WNW	30.4	64.1	80.1
AUG	100	E	12.5	28	36.1
SEP	1000	S	8.0	51.1	51.1
SEP	850	S	14.3	37.1	51.1
SEP	700	N	13.5	38.1	52.1
SEP	500	W	16.9	49	70.9
SEP	300	W	36.0	82.2	93.8
SEP	200	W	46.4	92.1	104.1
SEP	100	W	22.4	49.9	69.0
OCT	1000	S	8.9	59.1	59.1
OCT	850	SSW	20.8	44.1	58.1
OCT	700	W	20.9	52.1	70.9
OCT	500	W	31.2	75.2	99.1
OCT	300	W	51.1	108	138.1
OCT	200	W	66.7	126.1	176.2
OCT	100	W	34.3	70.1	104.1
NOV	1000	S	8.9	55.0	55.0
NOV	850	SW	23.6	49.2	65.1
NOV	700	W	25.7	57.1	69.2
NOV	500	WSW	43.6	89	104.1
NOV	300	W	68.1	123.2	158.2
NOV	200	W	75.9	136.2	187.1
NOV	100	W	43.8	91.1	118.1
DEC	1000	S	8.9	53.0	53.0
DEC	850	SW	22.9	51.1	69.2
DEC	700	W	29.5	60	72.1
DEC	500	W	51.9	93.1	113.1
DEC	300	W	83.2	135	159.3
DEC	200	WSW	87.5	151.2	174.3
DEC	100	W	56.0	106.1	155.1

J DFW Cloud Ceiling and Visibility

Months	% Frequency of Cloud Ceiling (< 3000.00 ft) & Horizontal Visibility (3.00 mi)
January	27
February	26
March	22
April	19
May	18
June	9
July	4
August	3
September	11
October	16
November	21
December	25
Annual	17

Months	% Frequency of Cloud Ceiling (< 1500.00 ft) & Horizontal Visibility (3.00 mi)
January	18
February	17
March	12
April	8
May	8
June	3
July	1
August	1
September	6
October	9
November	12
December	16
Annual	9

Months	% Frequency of Cloud Ceiling (< 1000.00 ft) & Horizontal Visibility (2.00 mi)
January	13
February	11
March	7
April	4
May	4
June	1
July	1
August	1
September	3

October	5
November	8
December	11
Annual	6

Months	**% Frequency of Cloud Ceiling (< 200.00 ft) & Horizontal Visibility (0.50 mi)**
January	1
February	1
March	0.2
April	0.2
May	0.2
June	0.2
July	0.2
August	0.2
September	0.2
October	0.2
November	1
December	1
Annual	0.2

Appendix J Acknowledgements

Data provided by the 14th Weather Squadron, Asheville, NC.